Characterisation of normal human pleural mesothelium to understand malignant pleural mesothelioma

Samantha A. Arathimou

Lungs for Living Research Centre

UCL Respiratory

University College London

A thesis submitted for the degree of

Doctor of Philosophy

2020

Declaration:

I, Samantha A. Arathimou, confirm that the work presented in this thesis is my own. Where information has been derived from other sources, I confirm that this has been indicated in the thesis.

Acknowledgements:

I would like to thank my supervisor, Professor Sam Janes for his constant scientific optimism and belief in my project despite the many research challenges I encountered. I am grateful to my supervisors Associate Professors Steven Mutsaers and Cecilia Prêle for their support and for hosting me at the University of Western Australia, as well as Professor Robin McAnulty for his research advice. I would also like to thank Dr Rob Hynds for his research suggestions and for functioning as an informal supervisor throughout my PhD.

I would like to acknowledge the members of the mesothelioma team Dr Krishna Kolluri and Dr Doraid Alrifai. Most importantly, I would like to thank my lab supervisor Dr Yuki Ishii, for her humour, positivity and her experimental suggestions throughout my PhD. I would like to thank my collaborators; Dr Adam Pennycuick and Dr Ryan Arathimos for their bioinformatic analyses, Dr Vitor Teixeira and Dr Mary Falzon for their histopathology advice as well as Jemima Burden and Dr Tom Gregory for offering their expertise in SEM. I would like to acknowledge Dr Mariam Jamal-Hanjani and the PEACE consortium, with special thanks to Dr David Moore for his pathology expertise, Mita Akther for tissue acquisition as well as the CTC PEACE team for data collection. I am immensely grateful to the ASCENT team, Dr Sarah Clarke and Dr Helen Hall, for their collection of samples which allowed me to progress the research presented in this thesis.

I would also like to thank the members of the epithelial team, for their experimental advice and scientific enthusiasm - notably Sandra, Marie-Belle, Phie, Ersi, Jo and Kate. I am also very grateful for the help and friendship of fellow PhD students at UCL Respiratory; Rebecca, Giota, Zoe and Dave. Notably, I want to thank Rebecca Graham for patiently teaching me flow cytometry and for being my go-to-person for bouncing research ideas off over coffee, as well my post-lab wine drinking companion. I also want to thank Giota Chondrou for her friendship, positive attitude and humour through many late evenings in the lab. My colleagues have made my time at UCL Respiratory an enjoyable journey.

I am grateful to Liam McNeil for his encouragement during the inevitable troughs of PhD research and for supporting all my ideas and ambitions. I'm also thankful for the support and endless proof-reading help that my brother Ryan has given me over the years of my PhD.

Finally, I would like to thank the British Lung Foundation, for financing my PhD studentship.

Abstract:

Malignant pleural mesothelioma (MPM) is an aggressive and fatal malignancy. Gene expression analysis of MPM tumours and use of MPM *in vitro* cell models are established tools used to investigate the disease and identify potential therapeutic pathways. However, the study of MPM has been hindered by the lack of normal human pleura to utilise as a control for transcriptomic studies and to derive pre-clinical mesothelial cell models from.

Obtaining normal pleural tissue can be challenging and not accessible to many research laboratories. I present data to support the use of visceral pleura acquired from two distinct human tissue pipelines; routine lung resection surgery and post-mortem tissue from advanced cancer patients. Using these samples, I provide a full morphological and structural evaluation of human visceral mesothelium in homeostasis (n=18). Importantly, I found that pleural samples from both tissue pipelines offer a viable source of human visceral mesothelial cells (VMCs). These findings will enable the future adoption of these pipelines and the expansion of human-based pleural studies by the research field.

In the limited human studies of normal pleura, pleural fluid from effusions remains the main method of mesothelial cell isolation, although this produces a heterogeneous cell population of parietal and visceral mesothelial cells. Here, I developed a method to isolate VMCs using brushings of visceral pleura, which resulted in a VMC population with estimated purity of 92% based on Cytokeratin 5 (CK5) expression (n=4). Subsequently, by implementing negative selection for contaminating cell types, I purified pleural brushing cell populations by Fluorescence-Activated Cell Sorting (FACS). The combination of pleural brushing and FACS-purification enabled the elimination of immune cells, red blood cells, CD31-expressing endothelial cells and CD90-expressing fibroblasts, thus improving purity to an estimated 95% and yielding VMC cell counts of up to 25 x 10^3 (n=5). VMC populations were RNA Sequenced for the first time, which generated novel insights into this cell type in homeostasis (n=4).

Importantly, this normal VMC dataset allowed us to elucidate upregulated pathways in MPM using the MPM RNA sequencing dataset available through The Cancer Genome Atlas (TCGA). Pathway analysis revealed 30 significantly upregulated pathways in MPM compared to normal VMCs, including TGFβ and Hedgehog signalling. Further exploration of the TCGA MPM cohort showed higher expression of *GLI2* in a subset of MPM tumours when compared to other cancers and the association of *TGFB2* with *GLI1*. Subsequent stimulation of MPM cells *in vitro* with the cytokines TGFβ_1 and TGFβ_2 resulted in a significant increase of *GLI1* and *GLI2*

mRNA levels. These results suggest for the first time that there is an upregulation of GLI2 in MPM which can be partially explained by convergence of TGFβ signalling on Hedgehog transcription factors.

Finally, siRNA and shRNA-mediated knockdown of GLI2 in MPM cell models resulted in statistically significant reduction in cell viability and colony-forming capacity respectively. Pharmacological inhibition of Hedgehog signalling with currently available GLI inhibitors showed modest efficacy when tested in a panel of MPM cell lines (n=9). However, pathway analysis of differentially expressed genes identified by microarray of shRNA-mediated GLI2 knockdown in H2803 cells, indicated that GLI2 may play a role in cell cycle regulation. Therefore, the development of more potent and selective pharmacological agents for Hedgehog pathway inhibition at the level of the GLI2 protein is warranted.

Impact statement:

Malignant pleural mesothelioma (MPM) is a rare cancer which occurs in the lining of the lungs, the pleura. The pleura has two layers, the visceral layer is attached to the lung whilst the parietal layer covers the chest wall. The pleura is composed of pleural mesothelial cells (PMCs), which are called either visceral or parietal depending on the pleural layer from which they originate. Despite decades of research, our understanding of the pathogenesis and potential treatments for MPM remain poor. One of the limitations of MPM research is the lack of normal human pleura with which to compare malignant pleura. Historically, the research field has over relied on animal models for insights into PMC morphology and function. Therefore, studies of non-malignant human pleura and new methods to establish normal PMC models are urgently needed to better understand the differences between normal and malignant pleura.

The findings presented in this thesis address multiple important aspects of MPM research. Firstly, I explore and expand the opportunities for normal human visceral pleura acquisition by assessing two different tissue sources; samples from routine lung cancer surgery and post-mortem samples from a national trial called PEACE. I found that both these tissue pipelines are suitable for the study of visceral pleura, although each has distinct capabilities and limitations. These sources are far more common than acquisition of non-malignant pleura from MPM patients and thus offer a solution to the lack of human visceral pleura in research laboratories.

An additional limitation of the MPM field is the lack of knowledge surrounding the premalignant stage of MPM, referred to as malignant mesothelioma *in situ* (MMIS). Recently, the first official criteria for MMIS was published based on the loss of expression of an important tumour suppressor protein called BAP1, in the PMCs of 10 patients with no known pleural disease, of which 70% later developed MPM. I detected prominent loss of the protein BAP1 in proliferative mesothelial cells, in the non-malignant pleura of a kidney cancer patient. This pre-malignant finding solidifies the need for further investigation of BAP1 expression in parietal pleura biopsies. The post-mortem tissue resources outlined here could prove to be a useful tool to identify, examine and further understand MMIS.

In addition, the research field is hindered by flawed human PMC isolation methods due to the poor availability and limited study of normal human pleural tissue. To date, the most common methodology for studying and establishing human PMC cultures is to use the excess pleural fluid which occurs in many disease settings. However, in this thesis I describe a new isolation method which entails the use of a cytology brush to collect VMCs from human visceral pleura.

This offers an easy, fast and cheap way to isolate VMCs and could be used in all research laboratories with access to lung resection samples. Furthermore, this pleural brushing method could be applied to other mesothelial cell sites such as the parietal pleura and the peritoneum.

Finally, I implemented this new method to collect and analyse VMC populations by RNA sequencing, which allowed the transcriptomic comparison of normal VMCs to MPM for the first time. Based on insights from this transcriptomic comparison, I investigated Hedgehog signalling and found an upregulation in the transcription factor GLI2 which appears to be a pleiotropic regulator which may have therapeutic potential as a molecular target in MPM.

Table of Contents

Table of Figures

1 Introduction

1.1 The human pleural mesothelium

1.1.1 Location and composition of pleural mesothelium

There are three embryonic germ layers; the ectoderm, mesoderm and endoderm. The mesothelium is a single-cell epithelium-like serosal layer which originates from the lateral plate mesoderm (1). It was first described by Bichat nearly 200 years ago, although the term was coined later by Minot after his microscopic study of organs (2,3). All coelomic cavities are lined with mesothelium, for the protection of encapsulated organs (4). The mesothelium covers the heart, lungs, gut and tunica vaginalis (2–6) and is composed of specialised cells called mesothelial cells (2,3).

The mesothelium which encapsulates the lungs is referred to as the pleura and is thought to be a slowly renewing tissue composed of pleural mesothelial cells (PMCs) (3). The pleura consists of two single cell layers of mesothelium (4,7–10). The layer attached to the lung is the visceral pleura whereas the layer attached to the chest wall is the parietal pleura, as shown in Figure 1.1 (10). The gap between the layers is known as the pleural space and contains a small amount of liquid which consists of immune cells, blood components and enzymes (Figure 1.1).

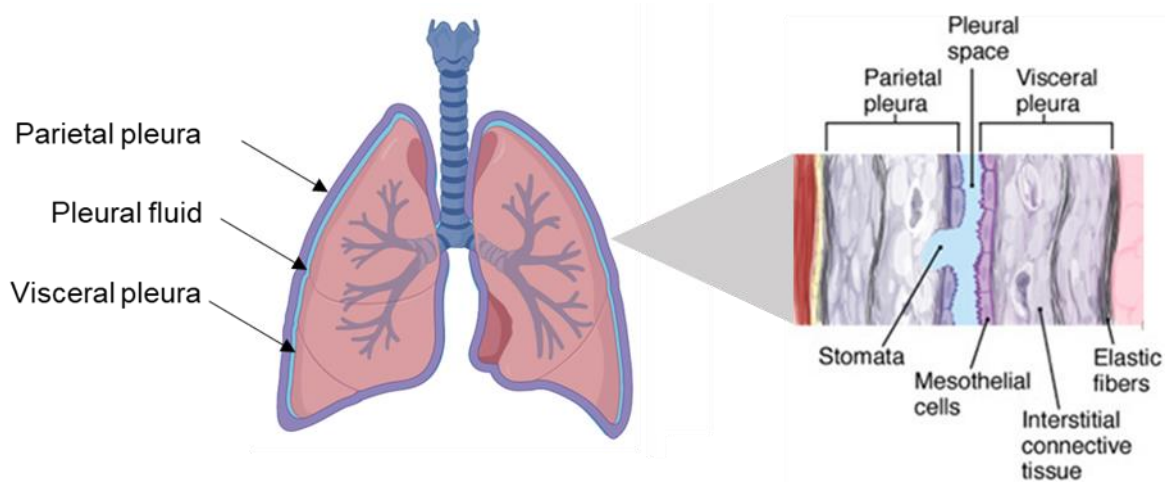

Figure 1.1 Structure of human pleura. The visceral pleura is attached to the lung while the parietal pleura is attached to the chest wall. The pleural space between the two pleural layers contains pleural fluid.

1.1.2 Ubiquitous functions of human mesothelial cells

Mesothelial cells in all human cavities share two key functions; to secrete lubricants forming a non-adhesive layer which enables underlying organ movement and to provide physical and mechanical protection of the underlying coelomic organ (2–4,11,12).

Notably, studies over the last two decades have elucidated an additional specialised function of mesothelial cells, although the precise mechanism by which they achieve this remains incompletely defined. Lineage tracing studies and extensive immunostaining in human and murine embryonic models have quantitatively shown that embryonic mesothelial cells of the heart, lungs and gut are able to undergo mesenchymal transition, migrate to underlying tissue and differentiate into vasculogenic cell types which become resident in sub-mesothelial locations (4,7,12–16).

Rinkevich *et al*. conducted a study of adult mouse mesothelial cells which supported the presence of a pluripotent lineage of mesothelin (MSLN)-expressing mesothelial cells which gave rise to fibroblast and smooth muscle cells *in vitro* and *in vivo* (16). In this study, MSLN was used as the only positive mesothelial cell marker. In parallel, endothelial and immune cell markers were used to eliminate contaminating cell populations by Fluorescence-Activated Cell Sorting (FACS). MSLN-positive mesothelial cells were extracted by FACS from mesothelium of the lungs, liver, kidney, intestine, spleen, peritoneal wall and diaphragm (16). These MSLN-expressing cells gave rise to fibroblast and smooth muscle cells in culture, which were found to express alpha Smooth-Muscle Actin (αSMA), Thy1 (CD90), Fibroblast-Specific Protein-1 (FSP-1) and vimentin (16). Although MSLN has been used as a marker of reactive and malignant mesothelial cells, it is unclear to what extent this is expressed in other cell types. Furthermore a report from human cytologic specimens indicated that MSLN is not selective enough to be used as a ubiquitous marker of mesothelial cells, with reported 73% sensitivity and 55% specificity (17). In addition, Dixit *et al.* found no expression of MSLN by immunohistochemistry (IHC) in embryonic mouse visceral pleura (7). Therefore, there are significant limitations in basing a PMC purification strategy on the presence of a positive marker, including bias toward a subset of mesothelial cells. Subsequently, it is difficult to discern if the fibroblast and stromal cells derived from MSLN-expressing cells in culture were due to a progenitor population of mesothelial cells or if marker limitations may have caused cell culture contamination with other cell types.

Interestingly, Dixit *et al.* showed in embryonic mouse pleura that Wilm's Tumour-1 (Wt1)-expressing visceral mesothelial cells (VMCs) contributed to cell populations of the lung parenchyma, including α-SMA expressing vascular smooth muscle cells in pulmonary arteries and veins as well as desmin positive peri-bronchiolar fibroblasts. These findings suggest that embryonic pleural mesothelium could be a source of essential cell types of the lung parenchyma in humans (7).

In summary, shared functions of mouse mesothelial cells from different cavities have been identified, yet their counterparts in humans are rarely compared. Although these studies indicate a pluripotent mesothelial lineage in murine models, the quantitative validation of this and identification of stem or progenitor cells in the pleura, is impeded by poor knowledge of mesothelial cell markers, biology and difficulty in obtaining human pleural tissue.

1.1.3 Pleural mesothelium in homeostasis, inflammation and thoracic pathologies

Transmission electron microscopy (TEM) has shown that PMCs have abundant intracellular organelles such as mitochondria, ribosomes, Golgi apparatus and rough endoplasmic reticulum (18). This intracellular view indicates that the mesothelial cell is capable of significant metabolic activity and may support the diverse functions of PMCs during pleural homeostasis.

PMCs are thought to be involved in the process of pleural fluid turnover, as they are hypothesised to regulate fluid transport and clearance of debris from the pleural space (19). PMCs are known to produce and secrete lubricants including glycosaminoglycans, glycoproteins and surfactant, which allow frictionless movement of the lung (Figure 1.2).

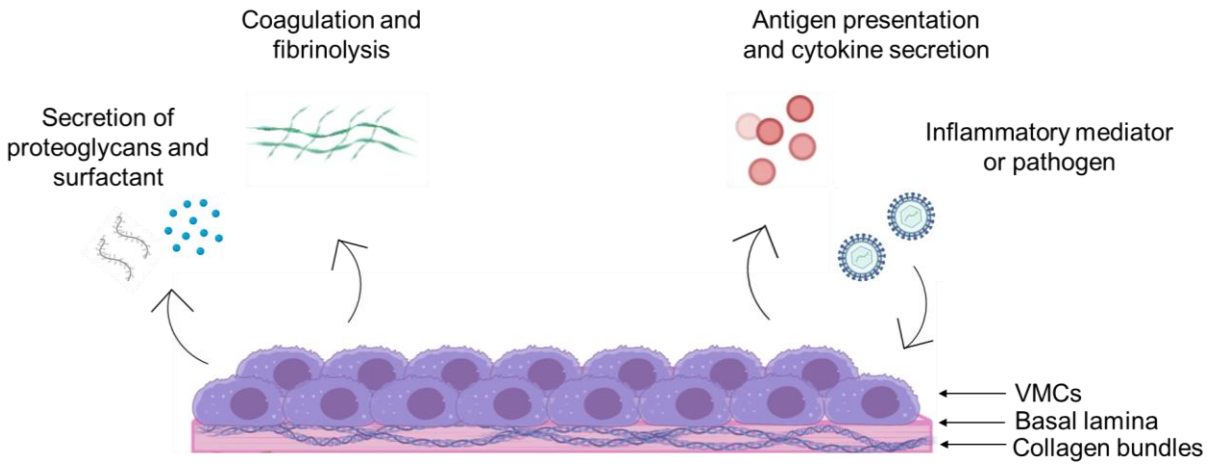

Figure 1.2 The functions of normal human visceral mesothelial cells. Visceral mesothelial cells form a protective cellular barrier over the lung and secrete proteins such as surfactant and proteoglycans. Mesothelial cells have also been shown to antigen present and secrete cytokines in response to inflammatory mediators or pathogen. Schematic created using BioRender.

Another important function of PMCs in homeostasis is to produce connective tissue macromolecules which form the sub-pleural connective tissue. A study of cultured rat PMCs revealed their ability to synthesise collagen types I, III and IV, elastin, laminin, proteoglycans and fibronectin (20). Similarly, cultured mouse MSLN-positive mesothelial cells secreted collagen I and IV as well as fibronectin in short-term cell cultures (16). Interestingly, the study of rat PMCs provided evidence that PMCs can organise macromolecules into structures

including fibres and the basal lamina, a finding which supports PMCs as the cell type responsible for sub-pleural connective tissue generation (2,3,8,10,20). Finally, PMCs have tight junctions and desmosomes which tether them to the underlying basal lamina. The formation of a continuous cellular layer of visceral mesothelium is thought to provide mechanical support to the underlying lung.

A key function of PMCs is protective, as they can facilitate regeneration at sites where denudation of mesothelium has been caused by an injurious agent (Figure 1.2). Multiple murine studies have investigated the mechanism by which PMCs mediate serosal repair (21). Exposure of normal murine pleural mesothelium to an injurious stimulus such as thermal injury or carcinogenic fibres including carbon nanotubes and asbestos, results in induction of inflammation (22–24). Stimulated PMCs are able to phagocytose, antigen present, recruit neutrophils and macrophages to the site of injury as well as secrete cytokines (2,3,23–30). Furthermore, in murine models, free-floating viable mesothelial cell numbers have been reported to increase following injury. These studies labelled the free-floating mesothelial cells and tracked their incorporation in repaired mesothelium (31,32). Thus, the mesothelium is considered to be a source of metabolically active cells which are able to dynamically respond to environmental cues and have wound healing and regenerative properties (1,33).

Importantly, study of the human pleural response to asbestos fibres has shown that mesothelial cells are able to secrete a suite of pro-inflammatory cytokines including Tumour Necrosis Factor alpha (TNFα), Interleukin (IL)-8 and IL-1β as well as growth factors Platelet-Derived Growth Factor (PDGF) and Vascular Endothelial Growth Factor (VEGF) (22,34–36). In a recent study of cultured mouse PMCs incubated with asbestos fibres for up to 48 hours, pro-inflammatory cytokines IL-1, IL-6 and the macrophage-recruiting cytokine MIP-2 were secreted. In addition, significant necrosis was present in asbestos treated cells when compared to the non-treated control cells (37). This supports a model of PMC immune cell recruitment in response to inflammation or injury of the mesothelium.

PMCs have been linked to several pathologies. PMCs have been suggested to contribute to the formation of pleural plaques and pleural effusions as well as idiopathic pulmonary fibrosis (IPF) (38–40). Transformation of PMCs into myofibroblasts by TGFβ signalling in a process referred to as mesothelial to mesenchymal transition (Meso-MT) has been proposed to contribute to IPF pathogenesis (38,41–43). The PMC is thought to be a key cell type as it is involved in the generation of increased amounts of collagen and fibrin in response to pleural injury as well as

increasing the population of fibroblast cells (44). The increase in production and deposition of components usually produced in wound repair, is thought to causes some of the hallmarks of IPF, including fibrinogenesis, scarring and restriction of the lung (33). In summary, the PMC is a clinically important cell type and thus the study of its functions and responses to stimuli require further investigation.

1.1.4 Morphology of pleural mesothelium

The development of scanning electron microscopy (SEM) allowed the study of the pleural surface of human and murine tissue for the first time in the 1970s. Many early studies reported that the pleura is characterised by microstructures, such as micropores which were postulated to be functional openings to underlying tissue (45). In murine pleural homeostasis, VMCs have been reported to measure 16 - 42 µm in diameter and imaging has shown both bushy and sparse microvilli of 0.5 - 2 µm covering their luminal surface (Figure 1.3A) (45,46). The visceral mesothelium is very thin at 1 - 4 µm and VMCs resemble either flattened endothelial or cuboidal epithelial cells in SEM imaging studies (45) (Figure 1.3). Diversity in VMC morphology has been observed in human studies of pleural mesothelium (45,46). VMC morphology is thought to be influenced by the characteristics of sub-mesothelial tissue such as the rigidity of underlying musculature (45). Similarly, microvilli presence and density has been reported to vary between samples and within pleural tissue from the same donor. One study reports that murine microvilli density is linked to wound healing response and thus microvilli density could be used as an indication of mesothelial cell functionality (27).

Imaging of the human parietal pleura has revealed small orifices called stomata, with documented openings of 3 – 12 µm (46). Peng *et al.* identified parietal pleural stomata in 2/11 patient tissues, although further investigation of their function was not conducted (Figure 1.3B). Many have suggested that parietal pleura stomata serve as a type of pleural ‘sink’, which connects with lymphatic vessels in sub-mesothelial tissue and enables clearance of debris and cell particles, although there is currently no quantitative evidence of this.

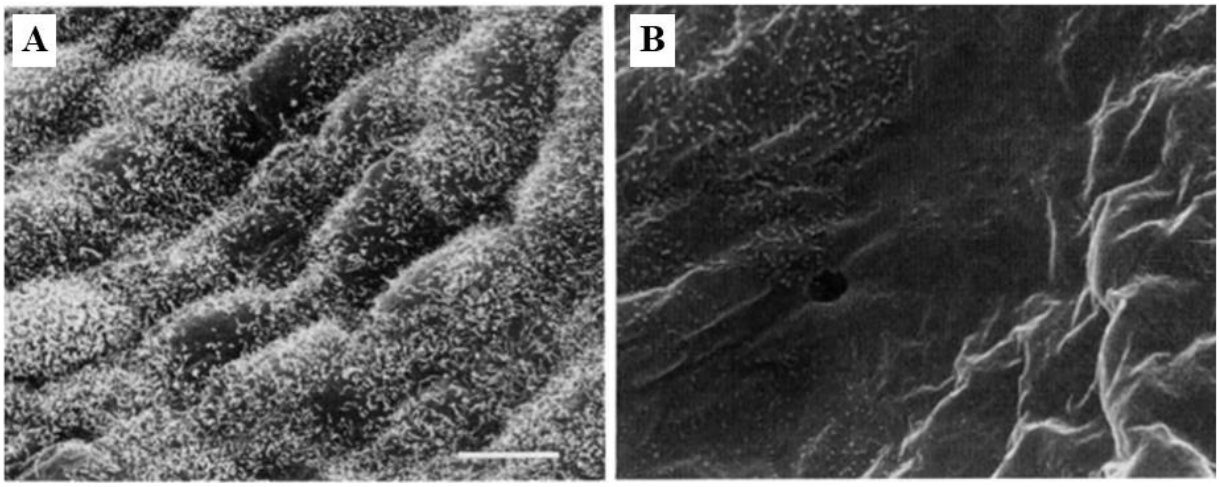

Figure 1.3 Scanning electron microscopy of human visceral and parietal pleura. A) Human visceral mesothelial cells from the mediastinal pleura have a larger surface area and more microvilli than diaphragmatic or parietal pleura (scale bar = 10 μm) (45). B) Human parietal pleura has visible surface openings (stomata), objective x 1,250 (46).

Animal studies have shown that in the days following injury of mesothelium, visible changes entailed a reactive mesothelium with elongation of individual mesothelial cells and localised macrophage recruitment (27).

In humans, frequent perturbation of the parietal pleura including mesothelial cell denudation and fibrin deposition was reported in 100% of the 11 pleural samples assessed despite the patients having no known pleural disease (46). This study suggests that the mesothelium is a reactive cell membrane which is sensitive to a range of stimuli and undergoes morphological changes when homeostasis is disrupted (46).

1.1.5 Anatomy and structure of sub-pleural tissue

Underpinning the visceral pleura is a thin layer of connective tissue composed of collagen bundles, elastin and other fibrous components many of which are known to be secreted by VMCs (1,25,47). This connective tissue also includes a basal lamina, to which mesothelial cells are attached (Figure 1.4). A network of endothelial and fibroblast-lined lymphatic vessels, arteries and capillaries are found in the sub-pleural connective tissue, which is also referred to as the pulmonary interstitium (Figure 1.4). In studies of human visceral pleura, endothelial cells are distinguished by their expression of Platelet Endothelial Cell Adhesion Molecule 1 (PECAM1/CD31) expression (12). Fibroblasts and pericytes in lung parenchyma have been detected by expression of Platelet Derived Growth Factor Receptors PDGFRα and PDGFRβ (7,12,16). Importantly, there is a large population of immune cells in the sub-pleural space, which patrol for pathogens and can be recruited to the lung surface by VMC-secreted cytokines

(48). Adjacent to the sub-mesothelial connective layer there is aerated space, composed of alveoli containing alveolar epithelial cells and immune cells (Figure 1.4). A recent imaging study of mouse lungs reported alveolar ducts at a depth of 1.5 mm below the visceral pleura (49). However, only one human lung sample was imaged and thus the sample size in this study is too small to accurately quantify the depth at which human alveoli are present in sub-pleural tissue (48,49).

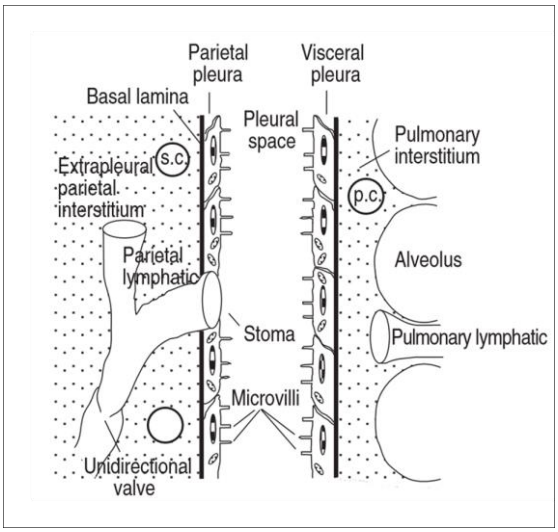

Figure 1.4 Schematic of the morphofunctional design of the pleural space. Systemic capillary (s.c.), pulmonary capillary (p.c.). Schematic taken from (50).

Between the visceral and parietal pleura there is a slim opening of 10 – 20 µm (Figure 1.4). This area is known as the pleural space and contains pleural fluid at a volume of 0.1 – 0.3 mL/kg during homeostasis (48). Pleural fluid provides a lubricated gap between the two serosal layers (48). An abnormal accumulation of pleural fluid between these two layers is referred to as a pleural effusion, which commonly occurs in a number of disease settings including respiratory infection, heart failure and cancer (51).

The process of fluid clearance in the pleural cavity has been studied extensively in sheep and rabbits (50,52). However, human studies are lacking, with pleural models based on animal studies commonly extrapolated to humans. Although lymphatic stomata have not been definitively shown as the filtering structures of the pleura, the parietal pleura is considered to be a permeable membrane with a pleural fluid turnover estimated at 0.15 mL/hour in sheep (50). In contrast, visceral pleura is thought to be less permeable. The process of pleural fluid filtration is proposed to be controlled by hydraulic pressure gradients, osmosis and the presence of Na+/K+ ATPase enzymes in parietal mesothelial cell membranes which facilitate transfer of

sodium and potassium (48,53). Dysregulation of this dynamic fluid filtration and clearance system results in the build-up of pleural fluid and development of a pleural effusion (40).

1.1.6 Limitations of pleural studies in animal models

Murine models as well as rabbit, sheep, hamster and dog have been used to characterise pleural mesothelium. The thickness and morphology of the parietal pleura is broadly similar between species. In contrast, the thickness of the visceral pleura and appearance of VMCs differs significantly between species, due to the variability in method of blood supply. In humans, the visceral pleura appears thick in histology sections whereas in mouse and rat pleura the thickness is drastically reduced (54). In mouse pleura, the sub-mesothelial connective tissue is almost indiscernible in comparison to humans, with alveoli much closer to the mesothelial basal lamina (55,56). Thick visceral pleura such as human and sheep pleura is thought to receive blood from systemic circulation, whereas thinner visceral pleura indicates blood supply from pulmonary circulation (50,54). Thus, murine models poorly mimic the structure of human visceral pleura.

In addition, mouse lungs have different lung size, architecture and capacity, pleural fluid volume, cellular organisation of airway epithelium and predisposition to MPM compared to human lungs (57). Furthermore, rodents do not exhibit the same symptoms of pleural pathologies including development of effusions and pleural malignancy. Thus, the insights into PMC morphology and functions in murine studies may provide a poor model when extrapolated to humans. These differences between animal and human pleura necessitate the identification and use of human tissue sources for mesothelial and mesothelioma research.

1.2 Malignant pleural mesothelioma

1.2.1 Classification and epidemiology

Mesothelioma can occur in several body cavities such as in the serosal lining of the peritoneum, pericardium and tunica vaginalis (25). However, malignant pleural mesothelioma (MPM) is the most common type of mesothelioma as it accounts for 60-80% of cases (58,59). MPM is a rare thoracic cancer, which can arise in either pleural layer but is thought to commonly originate in the parietal pleura and spread to the visceral pleura (10). In the UK, MPM is the 18th most common cancer and affects approximately 3 people per 100,000 annually (60).

MPM is mainly attributed to inhalation of the carcinogenic mineral asbestos. An estimated 75-90% of MPM cases are linked to asbestos exposure (25). Cases of MPM began to increase in the 1950s due to asbestos mining and widespread use in many industries (10). Wagner was the

first to discover the link between asbestos and MPM in 1956 and subsequently bans on asbestos imports into the UK were implemented in 1985 (10). Today, asbestos use is banned in only 55 countries, which leaves a significant proportion of the world population still exposed to the mining and industrial use of this carcinogenic mineral. Furthermore, due to its widespread use in previous decades, many buildings still have deposits of asbestos which were used for fire proofing and insulation. Due to the latency of the disease, there is an estimated incidence peak in MPM cases projected for 2020 (61), with complete remission of the malignancy not anticipated until many decades later due to the unabated use of asbestos in certain countries (62). MPM is commonly diagnosed in older patients due to long disease onset and statistically affects more men than women, a phenomenon which can only be partially explained by male occupational asbestos exposure (63).

There are three main histological subtypes of MPM; epithelioid constitutes ~60% of cases, whilst sarcomatoid and biphasic (which is also referred to as mixed) make up ~20% each of the remaining cases (10,64). Epithelioid MPM has a better prognosis than the other two types. However, case reports on histological variants are constantly emerging. For example, signet-like epithelioid mesothelioma and decidual mesothelioma are rare types of mesothelioma recently reported by Ordonez *et al*. (64,65).

1.2.2 Model of MPM pathogenesis

Asbestos has two main forms, the serpentine form which includes chrysotile fibres and the amphibole form which includes crocidolite and amosite (61). Of these asbestos types, crocidolite is considered the most carcinogenic. An elegant study using a rat model of aerosol asbestos inhalation, showed that asbestos fibres migrate rapidly from the airway epithelium, through the alveolar space to the surface of visceral pleura, as shown in Figure 1.5 (30). The study also showed gradual thickening of visceral pleura over a number of time points up to 365 days post-exposure of asbestos, as well as recruitment of neutrophils and macrophages to pleural areas (30). This study reported delayed clearance and persistence of asbestos fibres in the pleura. Once inhaled, asbestos is not biodegradable and thus it is possible that asbestos persists in the pleura for decades, although the limitations of animal model life cycles do not permit the long-term study of asbestos effects. In addition, the mechanism by which asbestos fibres, once inhaled, pass from the airway epithelium to the visceral pleura, remains unexplored.

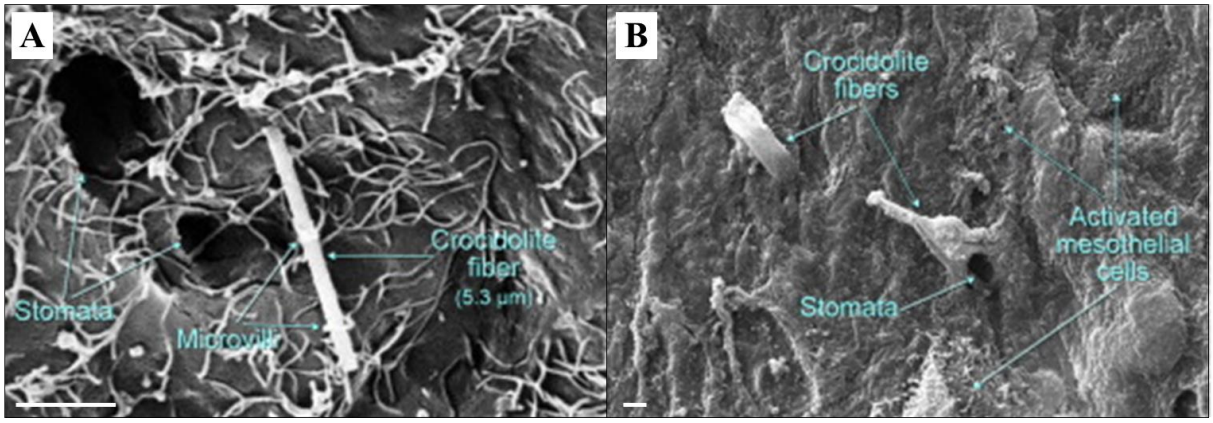

Figure 1.5 Aerosol asbestos inhalation in a rat model. Scanning electron micrographs show crocidolite asbestos lodged in the visceral pleura of rats, at 0 days post-cessation of aerosol asbestos inhalation. A) A crocidolite fibre measuring 5.3 µm is stuck to microvilli, adjacent to pleural stomata. B) Crocidolite fibres are wedged in the diaphragmatic pleural surface and activated mesothelial cells are visible. Adapted from Bernstein *et al.* (30)

The model for the development of mesothelioma is based on the hypothesis that mesothelial cells undergo long-term inflammation-inducing processes when exposed to asbestos. The pathogenesis of mesothelioma is thought to include induction of inflammation due to pleural irritation by asbestos fibres, production of reactive oxygen species (ROS) which cause mesothelial hyperplasia as well as accumulation of DNA damage, which gives rise to mutations, aneuploidy and genomic instability (22,29). Combined, these cancer-inducing processes lead to pleural malignancy after several decades. However, the precise mechanism by which asbestos induces pleural carcinogenesis is still not clearly elucidated.

1.2.3 Symptoms, diagnosis and therapy

MPM patients commonly present with dyspnoea and localised pain due to the development of pleural effusions. Pleural effusions often need to be drained multiple times to alleviate patient symptoms (10,40,66,67). Diagnosis is often made at a late stage because symptoms typically develop when there is a high disease burden. MPM is usually diagnosed by imaging, with Computed Tomography (CT) scans frequently used. Magnetic Resonance Imaging (MRI) and PET-CT scans are complementary and aid visualisation of MPM spread to thoracic structures. In asbestos-exposed patients, the presence of asbestos-mediated disease such as pleural thickening is also frequently diagnosed. As the malignancy progresses from sporadic nodules on the pleura, it forms a tough rind which restricts the heart and lungs (65,68).

MPM is an aggressive and chemotherapy resistant cancer with a poor prognosis (67). Median life expectancy depends on the MPM histological type but on average ranges from 8 – 36 months after diagnosis (63,69). Doublet chemotherapy with the platinum compound cisplatin

and the anti-metabolite pemetrexed has been reported to offer an overall patient survival of 12.1 months when compared to the 9.3 months achieved with the single agent cisplatin (70). Despite the limited efficacy of doublet chemotherapy, combination of cisplatin and pemetrexed is licensed by NICE as standard of care for MPM patients in the UK (71).

For a limited subset of patients, which account for approximately 15% of MPM cases, there are three surgical procedures available; pleurodesis, pleurectomy with decortication and extra-pleural pneumonectomy (EPP) (72–74). For patients experiencing recurring pleural effusions, pleurodesis inhibits their formation by the introduction of talc into the thoracic cavity which closes the space between the two pleural layers (73). Pleurectomy with decortication includes the removal of parietal pleura as well as excision of visible tumours (72). The most radical surgical approach is EPP, which entails removal of the parietal pleura, part of the diaphragm, pericardium and lung (69). Recent evidence from the MARS trial showed that radical surgery by EPP was not beneficial to patient overall survival and was associated with higher morbidity in the treated group compared to patients who did not undergo EPP (69). Subsequently, the approach of EPP surgery has been limited. To date, the optimal surgical method has not been established and no international agreement has been reached regarding MPM surgery with curative intent.

Although a plethora of small molecule inhibitors and cell therapies have been implemented in MPM clinical trials over the last few decades, the current treatment landscape remains reliant on primitive cytotoxic drugs (62,75). Notably, one of the major downfalls of small molecule inhibitor treatments, cell therapy and CAR-T cell approaches is that they do not take into consideration the heterogeneity of MPM patients. Thus, clinical trials such as the Phase II Mesothelioma Stratified Therapy (MiST) trial (NCT03654833), which aims to categorise patients into different treatment arms depending on the characteristics of their tumour histology, offer an essential tailored clinical trial approach in this disease setting.

Use of immunotherapy in combination with chemotherapy has shown some modest potential in early clinical trials. The MAPS-2 trial randomly categorised patients into two treatments arms. Treatment of 68 patients with the Programmed Death Receptor 1 (PD-1) inhibitor nivolumab and 64 patients with nivolumab and the CTLA-4 inhibitor ipilimumab, resulted in disease control at 12 weeks in 50% and 44% of the groups respectively (76). MAPS-2 median patient survival results were 11.9 months in the single agent group and 15.9 months in the nivolumab and ipilimumab group. Furthermore, the Japanese Phase II nivolumab trial, MERIT,

reported similar results to MAPS-2 with response rates up to 29% although low level toxicities were common in both trials (75). These results indicate some potency of checkpoint inhibitors in the treatment of MPM, although longer follow up and additional endpoints in larger patient cohorts are still required (75). The recent interim results of the Phase III CheckMate – 743 trial (NCT02899299) which tested nivolumab (Opdivo) and ipilumumab (Yervoy) as first line treatment for MPM compared to chemotherapy, showed potential in the ability of checkpoint inhibition to prolong median overall survival of MPM patients by 4 months (77). The results of currently active Phase II/III clinical trials are needed to conclude if immunotherapy efficacy and safety profiles, warrant the addition of checkpoint inhibitors to the current treatment paradigm for MPM (62,78).

1.2.4 Gene expression studies of normal pleura and MPM

1.2.4.1 Transcriptomic characterisation of normal visceral pleura

The genetic and transcriptomic landscape of normal PMCs remains poorly defined. A small study conducted Affymetrix microarray analysis of 7 normal parietal and 3 normal visceral tissue sections from human pleura and compared these to 5 malignant samples (79). This led to observations of increased cell cycle, anti-apoptosis, mitosis and replication gene expression in the malignant samples (79). However, this study was underpowered and thus is not able to reflect the heterogeneity of MPM tumours and identify transcriptomic changes therein. Furthermore, there was no histological data to support the presence of mesothelial cells in the normal samples, which is a frequent biopsy challenge (46). Finally, bulk sequencing of a heterogeneous tissue such as the visceral pleura does not allow the comprehensive characterisation of VMCs, as the predominant cell types in these samples are likely to be immune and stromal cells.

There is little transcriptomic information available on PMCs when compared with extensively characterised airway epithelial cell populations (80). Recently, there have been several key studies that have mapped the heterogeneity of cells in normal and IPF lungs using single cell RNA sequencing (scRNA-seq) (81–84). These scRNA-seq efforts include small populations of mesothelial cells that were derived from lung digestion and are therefore likely to be VMCs. Notably, the annotation and categorisation of scRNA-seq barcoded cells intro subgroups by UMAP analysis is based on known markers of each cell type. Therefore, as there is no ubiquitous marker of mesothelial cells, there is disparity between published scRNA-seq studies in the UMAP grouping of mesothelial cells. Adams *et al.* classed mesothelial cells as EpCAM+ epithelial cells (Figure 1.6A), whilst Reyfman *et al.* and Habermann *et al*. conducted grouping

of mesothelial cells as EpCAM- stromal and mesenchymal cell populations respectively. In addition, these datasets only contain a small number of mesothelial cells from a limited number of healthy donors. Notably, the scRNA-seq study by Travaglini *et al.* contained only 29 mesothelial cells identified in 1/3 donors (81). In contrast, the study by Adams *et al*. offered a larger scRNA-seq mesothelial dataset (n=550). However, a caveat of this dataset was that an average of 8 mesothelial cells and maximum of 54 mesothelial cells, were isolated from each donor and mesothelial cells were identified in only 51/79 donors. The samples in which mesothelial cells were identified, mainly constituted cases of COPD or IPF (Figure 1.6B). Therefore, this analysis although valuable, provides a limited view of mesothelial cells in homeostasis.

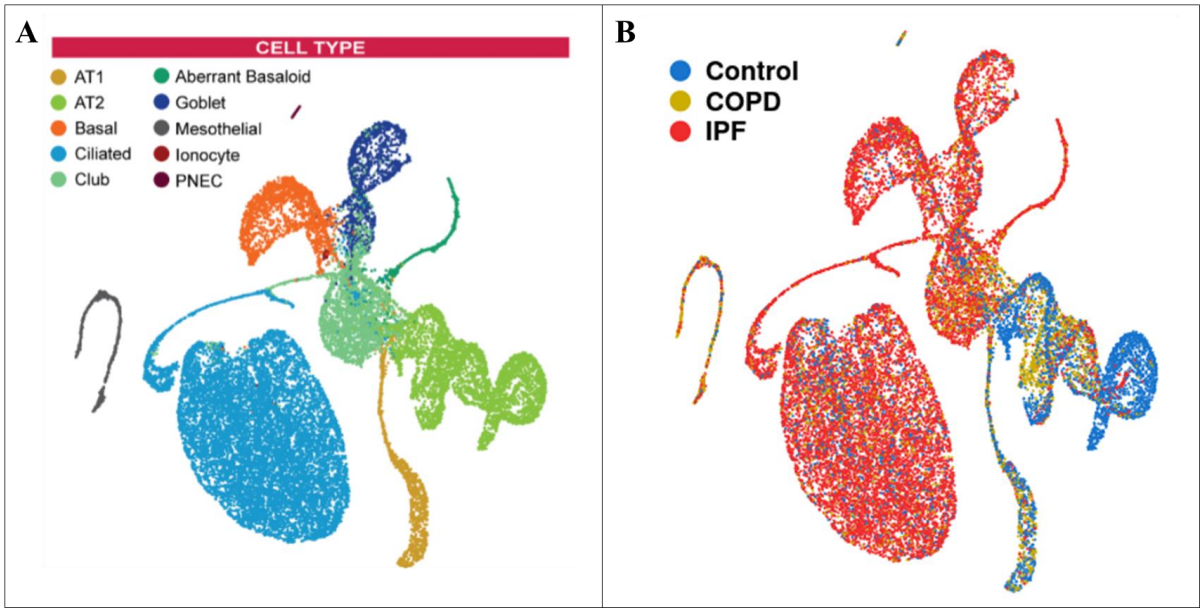

Figure 1.6 UMAP analysis of epithelial lung cell types and donor disease states, in a single-cell RNA sequencing study of human lung. A) Heterogeneity of human lung epithelial cells is shown by UMAP analysis of scRNA-seq dataset. AT1: alveolar type 1 cells, AT2: alveolar type 2 cells. B) UMAP of disease type of human lung samples used for scRNA-seq. The study included 29 healthy controls, 18 Chronic Obstructive Pulmonary Disease (COPD) and 32 IPF cases. UMAP plots are available through the IPF atlas (83).

Overall, the changes in transcriptional programmes between PMCs in homeostasis and pleural malignancy remain largely unknown due to the rare nature of normal VMCs in cell populations derived from lung digestion. As there is an unmet need to understand and develop better treatments for MPM, there is demand for a better understanding of PMCs in homeostasis and disease. Thus, there is significant value in isolating pure populations of human parietal and visceral mesothelial cells for gene expression studies, which will allow us to determine if these

cells differ, to understand their functions in homeostasis and to shed light on their role in pleural malignancy.

1.2.4.2 Transcriptomic characterisation of MPM

The main purpose of pleural sequencing studies has been to gain insight into MPM. Over the last decade the genetic and transcriptomic landscape of MPM has gradually been elucidated, with a low mutation burden described in multiple reports (85–89). The genomic study by Bueno *et al*. which analysed gene expression data from 216 MPM tumours, revealed recurring mutations which resulted in loss-of-function of key tumour suppressors. Frequently mutated tumour suppressors included Cyclin-Dependent Kinase Inhibitor 2A (*CDKN2A*) which is also known as p16 and regulates the cell cycle, Neurofibromatosis Type 2 (*NF2*) which produces the protein merlin, TP53 and the histone methyltransferase encoding gene SETD2 (85).

Several studies have reported mutations in BRCA1 Associated Protein-1 (*BAP1*), with up to 67% of MPM cases reported to harbour a *BAP1* mutation. *BAP1* is an important tumour suppressor gene due to its function as a deubiquitinating (DUB) enzyme. BAP1, through its DUB activity, regulates gene expression and cell processes ranging from DNA repair, chromatin accessibility and mitochondrial calcium flux to apoptosis. The importance of BAP1 in MPM has been highlighted further by reports of germline *BAP1* mutation inherited with an autosomal dominant pattern, predisposing individuals to a range of cancers including uveal melanoma, BCC and MPM (90). This finding combined with the frequent *BAP1* mutations reported in MPM, indicate a *BAP1* cancer syndrome and an important association between *BAP1* mutation and MPM (58,61,90–92).

A summary of common mutations identified by RNA Sequencing in The Cancer Genome Atlas (TCGA), a publicly available dataset of 86 MPM tumours, is shown in Figure 1.7A. Interestingly, characterisation of the transcriptome of MPM samples revealed a low number of coding alterations (Figure 1.7B). Overall, the genetic landscape of MPM is characterised by mutations in tumour suppressor genes and subsequent tumour suppressor protein loss-of-function (85,93,94).

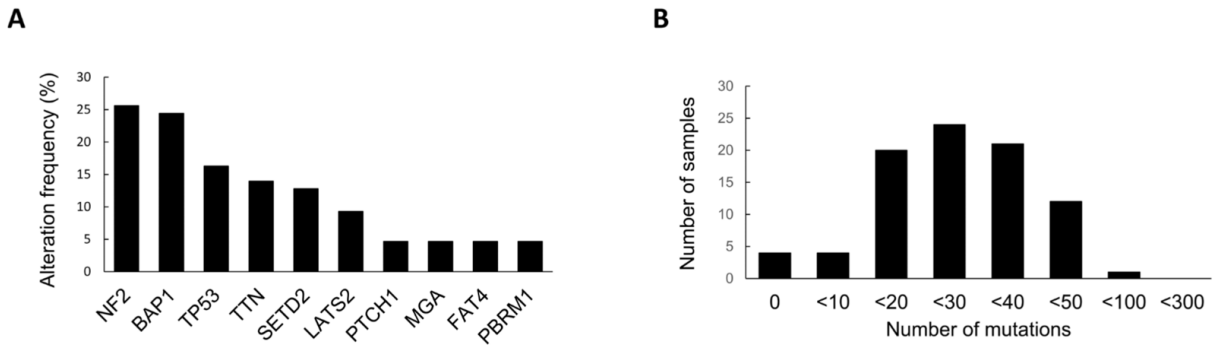

Figure 1.7 Mutations in MPM identified by whole genome sequencing. A) Most frequently mutated genes in TCGA PanCancer Atlas dataset of 86 MPM tumours; 62 epithelioid, 23 biphasic and 1 sarcomatoid. B) Number of mutations in the 86 MPM samples in the TCGA PanCancer Atlas cohort.

1.2.5 Markers of normal and malignant mesothelial cells

1.2.5.1 Markers of normal pleural mesothelial cells

Despite the lack of an established pan-mesothelial cell marker, one of the genes often used in studies of embryonic mesothelium is the transcription factor WT1 (4,7,95–97). WT1 is expressed in mesenchymal tissues which undergo a transition towards an epithelial phenotype (12,97). Mouse mesothelial cells from embryonic heart and intestine have been shown to express Wt1 (5,6,98). Dixit *et al.* used Wt1 expressing embryonic visceral pleura, ranging between E10.5 to E14.5, to study the differentiation and migration process of embryonic PMCs (7). Notably, Wt1 IHC expression reduced over the course of embryonic development and detectable expression in the visceral pleura was limited by embryonic stages E17.5 to E18.5. This raises questions regarding the utility of Wt1 as a marker of adult mesothelial cells. In addition, expression of MSLN was not identified in mouse embryonic pleura used in this study (7).

In human normal and reactive pleural mesothelium, a range of markers have shown modest specificity. Kachali *et al.* reported that MSLN showed a sensitivity of 73% and specificity of 55% in human cytologic specimens whilst calretinin exhibited superior staining performance with recorded sensitivity of 95% and specificity of 86% (17). Positive expression of a combination of calretinin and Cytokeratin 5/6 (CK5/6) has also been reported as strongly indicative of mesothelial cells, although these markers also label fibroblasts and airway epithelial cells respectively (99).

PMCs are tethered to sub-pleural connective tissue and are thus in close proximity to stromal cell types. In one study, the podoplanin antibody D2-40 was shown to have high sensitivity for normal mesothelial cells yet this also stained endothelial cells of the lymphatic system, which

are normally present in sub-pleural connective tissue (99,102). A separate study which focused on the differentiation of MPM from lung adenocarcinoma, described calretinin, CK5/6, HBME-1 as well as thrombomodulin and CD44 as useful markers of reactive pleural mesothelium (100). Notably, thrombomodulin stained endothelium and CD44 also stained lymphocytes, macrophages and fibroblasts (100). However, thrombomodulin and calretinin have been shown to be more specific than HBME-1 in several studies, yet neither is suitable as a diagnostic descriptor of mesothelial cells (101,102).

The bulk of IHC studies focus on the clinically significant challenge of differentiating MPM from other lung neoplasms and thus markers are typically assessed by their sensitivity and specificity to pleural malignancy. This has left the mesothelial marker field at a relatively primitive stage, with rare studies highlighting the differences between mesothelial marker expression in normal, reactive and malignant PMCs.

1.2.5.2 Markers of malignant mesothelial cells

MPM is a difficult to recognise malignancy due to its ability to grow in many histological patterns (103). MPM may also resemble a variety of other lung pathologies, including lung cancers which originate in the lung parenchyma but can grow over the pleural surface and thus emulate MPM (Figure 1.8), as well as certain types of pleuritis (104). Furthermore, malignant mesothelial cells have certain cytomorphological features such as nuclear atypia and multinucleation, which resemble adenocarcinoma (66). However, the key limitation is the current lack of a robust diagnostic marker for MPM (65,105,106).

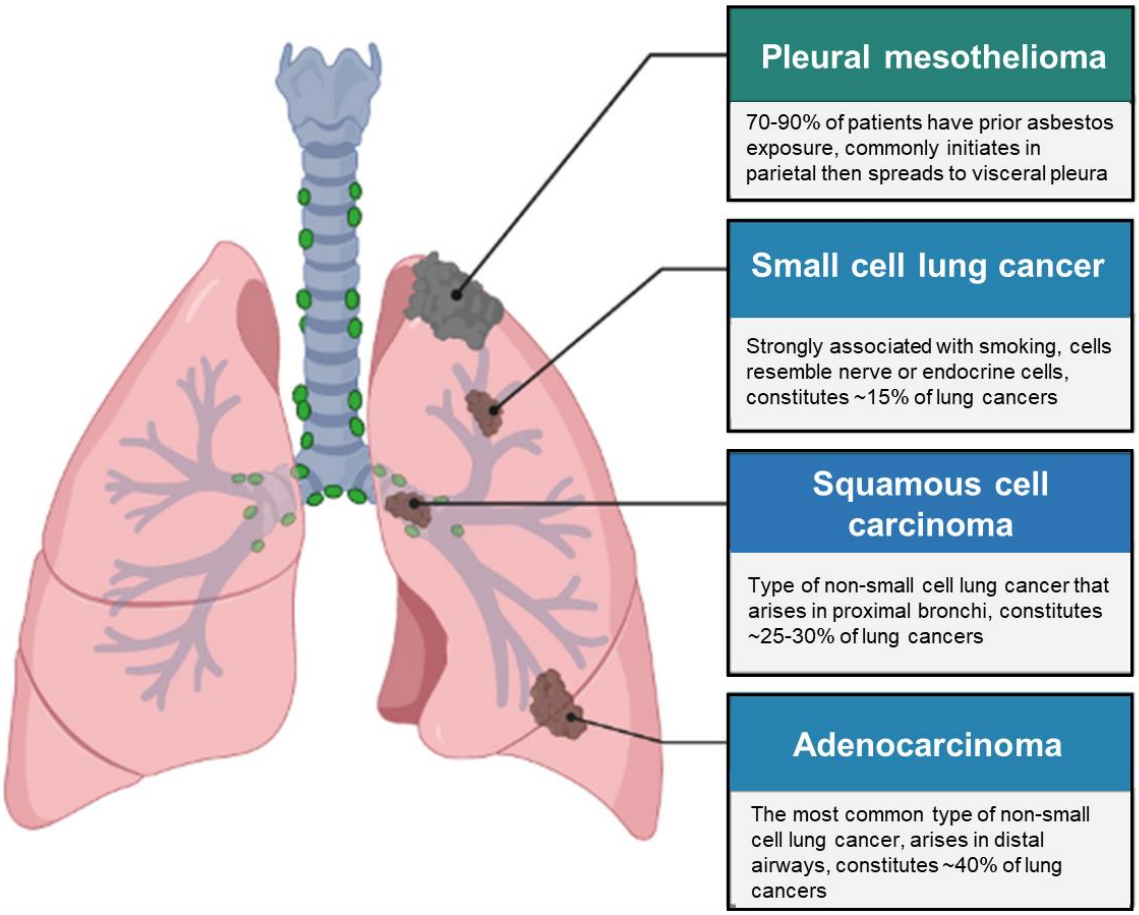

Figure 1.8 Comparison of pleural and lung malignancies. Schematic created using BioRender. Based on descriptions from (58,96).

IHC is widely recognised as the most useful diagnostic tool for MPM (58,96,103,107). A panel of IHC markers is typically used to differentiate MPM from similar malignancies such as adenocarcinoma and squamous carcinoma (68) (Figure 1.8). The panel of markers recommended by the International Mesothelioma Interest Group (iMig) for the differentiation of MPM from other lung malignancies, is summarised in Table 1.1 (96). These markers are used for analysis of suspect pleural effusions as well as tumour biopsies (96,105–108). Recently, an antibody for the mucin-like protein HEG homologue 1 (HEG1) has been shown to have high sensitivity for MPM, including desmoplastic and sarcomatoid subtypes (109). This gene was known for its function in zebrafish heart formation and recent studies report its involvement in the proliferation of MPM cells, indicating that HEG1 is an MPM-related antigen (110).

However, a caveat of the MPM positive markers is that they are not specific in labelling only one cell type (107,111). For example, the marker calretinin is expressed in 23 – 50% of squamous cell carcinomas, in normal tissues as well as in some types of MPM (111). One study

supported the use of podoplanin instead of a combination of CK5 5/6 and WT1, as it reported that strong cytoplasmic podoplanin expression was identified in 94 – 97% of reactive and malignant mesothelial cells but only in 7% of adenocarcinomas (1/14) (39). An analysis of HEG1 specificity showed that HEG1 was a highly sensitive marker for MPM although it stained reactive mesothelium and normal endothelial tissue (110,112). Collectively, it is apparent that correctly diagnosing MPM based on IHC is challenging and there is evident need for use of multiple mesothelial and epithelial markers to make a correct diagnosis.

Table 1.1 Positive and negative markers recommended by iMig for the differentiation of MPM from other malignancies. Wilms' tumour 1 (WT1), mesothelin (MSLN), cytokeratin 5 (KRT5), podoplanin (PDPN), calretinin (CALB2) are positive markers. Claudin 4 (CLDN4), thyroid transcription factor 1 (TTF-1), carcinoembryonic antigen (CEA), Epithelial cell adhesion molecule (EpCAM) often referred to as Ber-Ep4/MOC-31and Napsin A (NAPSA) are negative markers.

Positive markers	Negative markers
WT1	CLDN4
MSLN	TTF-1
KRT5	CEA
PDPN	EpCAM
CALB2	NAPSA

1.2.6 BAP1 expression in normal and malignant mesothelial cells

Genomic studies in MPM cohorts found that *BAP1* mutations resulted in protein truncation, disruption of the Nuclear Localisation Signal (NLS) domain or heterozygous loss, which caused BAP1 protein reduction or BAP1 loss-of-function (113,114). BAP1 loss-of-function is detectable by IHC and offers a potential biomarker for the differentiation and diagnosis of certain subtypes of MPM. A large-scale analysis of 212 mesotheliomas reported that 66% of tumours were BAP1-negative. In 100% of BAP1-negative samples there was detectable loss of nuclear BAP1 expression by IHC (58). In contrast, all 12 benign mesotheliomas assessed in the study retained nuclear expression of BAP1. Interestingly, of the 25 reactive mesothelial proliferations assessed, BAP1 loss was 100% specific for progression to malignancy as 6/22 samples were BAP1-negative and these patients progressed to BAP1-negative MPM (58). Thus, this study concluded that BAP1 IHC is 100% specific for *BAP1*-mutated MPM cases. A separate study in a smaller patient cohort showed identical BAP1 specificity results, providing confidence in BAP1 as a clinical tool. They reported *BAP1* mutations in 64% (14/22) of MPM

tumours investigated and out of these, BAP1 IHC showed nuclear loss of expression with 100% specificity (58,115).

Collectively, there is robust evidence indicating that quantification of nuclear BAP1 by IHC can provide evidence of BAP1 loss-of-function due to mutation, which supports the diagnosis of MPM and in certain cases indicates high risk of developing MPM (116). As *BAP1* mutations are common in epithelioid MPM, BAP1 staining offers a potentially useful tool for BAP1-negative epithelioid MPM differentiation from other malignancies.

Loss of nuclear BAP1 expression detected by IHC as well as homozygous detection of p16 (*CDKN2A*) by fluorescence *in situ* hybridisation (FISH) have shown 100% specificity for distinguishing MPM from reactive mesothelium (117). As with malignant PMCs, non-malignant PMCs do not show ubiquitous expression of a known marker. However, in patients without a germline *BAP1* mutation, positive BAP1 nuclear expression should be present in normal mesothelial cells and has been used previously to differentiate benign reactive mesothelium from MPM (58). Importantly, multiple reports have shown that reactive mesothelium retains BAP1 nuclear expression, as shown in Figure 1.9 (118).

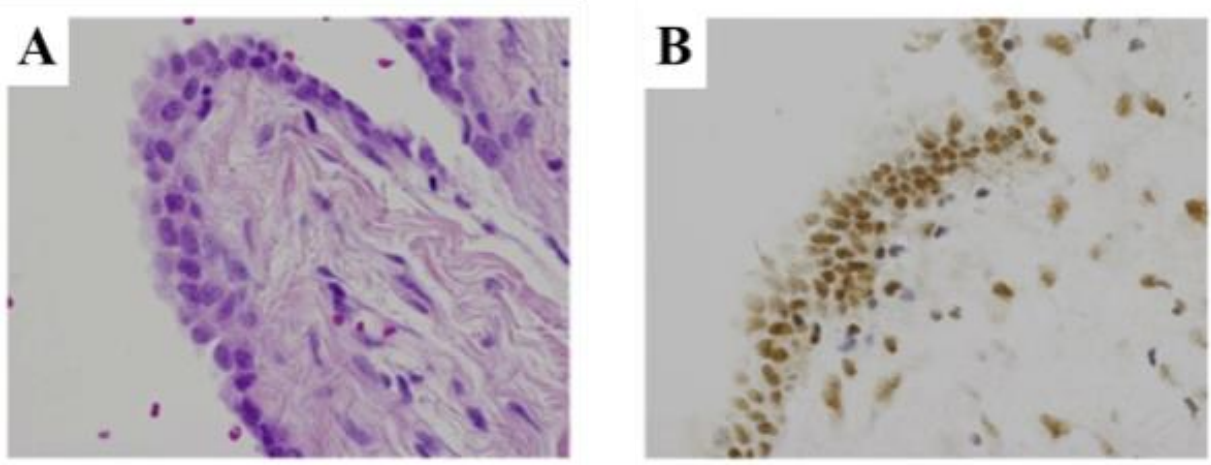

Figure 1.9 BAP1 immunohistochemistry in reactive pleural mesothelium. A) H&E stain of reactive mesothelium. B) IHC for BAP1 strongly stains nucleus and cytoplasm of reactive mesothelial cells. Reproduced from Yoshimura *et al.* (118).

1.2.7 Malignant mesothelioma in situ (MMIS)

Most malignancies have a pre-invasive stage before the onset of invasive cancer, referred to as carcinoma *in situ*. During this stage, cells harbour multiple mutations and exhibit cellular hyperplasia which is detectable by histology. In carcinoma *in situ* there is no invasion or spread to neighbouring tissue (119). This stage of malignancy is of clinical importance, as intervention can apprehend development of cancer in many instances (120). Especially in the disease setting

of MPM which is hindered by the lack of effective therapies, early diagnosis of pre-malignant pleural areas and subsequent ablation or excision of these lesions could provide a vital curative treatment for asbestos-exposed individuals.

Although small case reports have previously postulated the presence of mesothelioma *in situ* (121,122), until recently MPM was not considered to have a pre-invasive stage as there was no conclusive supporting evidence. This remains the case for UK clinical histopathology guidelines stipulated by NICE.

A seminal study by Churg *et al*. conclusively proved the existence of mesothelioma *in situ* (MMIS). In a cohort of 10 patients with MMIS, which consisted of 9 pleural cases and 1 peritoneal case, complete BAP1 loss-of-expression was demonstrated by IHC in surface mesothelial cells (Figure 1.10). These cases showed no local invasion of mesothelial cells and patients had no diagnosis of pleural malignancy or pleural pathologies, although one pleural case presented with recurring pleural effusions (123). Interestingly, cytologic atypia was present in only one MMIS case and thus was not considered a prerequisite for MMIS (Figure 1.10C). Surprisingly, only 1 case showed hyperproliferation in a papillary pattern, yet the remaining 9 cases of MMIS cases formed a bland mesothelial cell monolayer on the pleural surface which would not appear suspicious during routine histological examination. Collectively, three criteria were selected as prerequisites for diagnosis of a pleural biopsy with MMIS. The three criteria for MMIS are: the complete loss of BAP1 expression in the surface mesothelium, no visible invasion of reactive mesothelium and no diagnosed pleural disease.

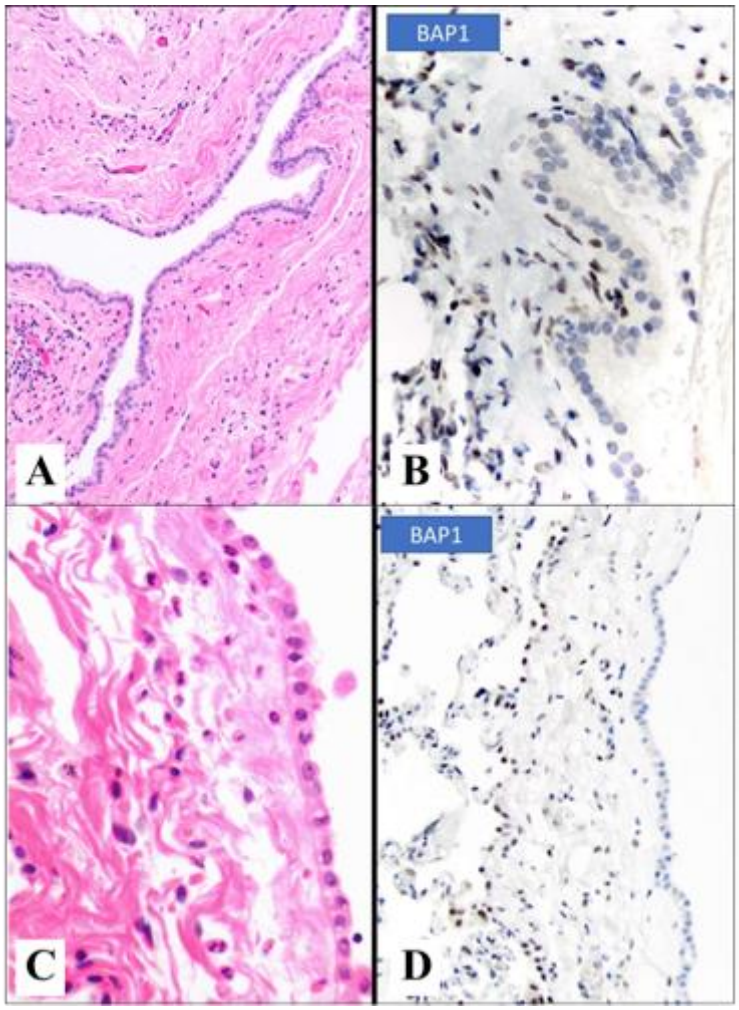

Figure 1.10 Pleural cases of MMIS demonstrated by loss of nuclear BAP1 in mesothelial cells. A) H&E stain demonstrates a monolayer of cuboidal, bland mesothelial cells. B) Loss of BAP1 expression detected in the surface mesothelium by IHC. C) H&E stain of moderately atypical cuboidal mesothelial cells. D) Loss of BAP1 in cuboidal mesothelial cells. Adapted from Churg *et al*. (123).

Mesothelial cytological changes and hyperplasia have been well documented and are usually referred to as atypical or typical reactive mesothelium (124). This nomenclature has been used to avoid overdiagnosis of pre-malignancy. Notably, although the study by Churg *et al*. is a valuable contribution to the field, as it cements MMIS as a precursor stage to MPM, the scope of 10 cases, of which 8 are morphologically identical, presents a limited view of an undoubtedly varied pre-malignancy stage. Thus, further histological exploration of pleural tissues by investigation of BAP1 expression is required to understand this asymptomatic but undoubtedly overlooked pre-invasive stage of MPM.

Strikingly, in the study by Churg *et al*. 70% of MMIS cases progressed to invasive pleural malignancy. This indicates that MMIS is a key stage in the progression to MPM and that the simple assessment of pleural tissues described above, could support early patient diagnosis. Early detection of MPM is not currently possible due to a lack of imaging sensitivity and the

absence of a diagnostic biomarker (68). Therefore, the clinical translation of histopathological MMIS findings would be particularly valuable. This warrants the further investigation of BAP1 loss-of-expression by IHC as a diagnostic tool, with which to identify MMIS.

In summary, pre-invasive MPM should be an important focus of bench-side research, as the ability to accurately diagnose MMIS and intervene at an earlier stage in MPM patient treatment could drastically improve patient prognosis. Although the investigation of pre-malignancy by assessment of BAP1-loss has rarely been considered until now, this simple IHC experiment should be included in studies which detect reactive mesothelium in human cases with no known pleural disease as well as in routine pleural biopsies from patients experiencing recurring pleural effusions or other thoracic abnormalities. Further study of MMIS will allow us to enhance our understanding of MPM carcinogenesis and ideally also enable patients with early preinvasive disease to be streamlined for management and monitoring to prevent the onset of incurable, invasive MPM.

1.3 Mesothelial cell culture

1.3.1 Pleural mesothelial cell isolation and culture methods

The rising incidence of MPM in the 1950s drove investigation into the clinically important interaction of asbestos and mesothelial cells. Early reports recorded migration of inhaled asbestos fibres to the pleura and the ability of mesothelial cells to phagocytose chrysotile asbestos fibres (125). In parallel, there was a scientific drive to establish *in vitro* cell line models derived from different tissues. Therefore, key efforts to optimise culture methodologies for PMCs began in the late 1970s (26,125,126).

Initial mesothelial cell culture attempts using scrapings of rat parietal pleura resulted in epithelial-like, short-term cell cultures which survived for 7-14 days (125,127). Subsequently, digested rat parietal pleura was cultured up to passage 20 by Aronson and Cristofalo under feeder-free conditions in F12 medium (128). Using human clinical material, Lechner *et al*. was one of the first to successfully culture PMCs from pleural fluid (26). A seminal study followed, in which the widely used benign mesothelial cell line Met-5A was established by SV40 virus transformation of PMC cultures derived from pleural fluid (129). Notably, Met-5A remains one of the only benign mesothelial cell lines used to this day (19,129). Rheinwald and colleagues were the first to identify that long-term proliferation of up to 52 population doublings of mesothelial cells required the presence of the mitogen Epidermal Growth Factor (EGF) and hydrocortisone, with withdrawal of EGF reported to induce slowing of proliferation in

mesothelial cell cultures (130–132). During optimisation of mesothelial cell culture, they also reported that PMCs expressed lower levels of keratin proteins in culture and that addition of a feeder layer of irradiated mouse fibroblasts did not confer benefit to mesothelial cell expansion (131).

In the field of human PMC research, isolation methods remain reliant on pleural fluid which is sought from patients who have developed pleural effusion. Pleural fluid is frequently available due to the common clinical presentation of pleural effusion in patients with breast and lung cancers, liver cirrhosis and respiratory infections to name a few (53,133–135). In animal models, alternative approaches have been implemented to isolate PMCs. A lavage method is commonly described, in which the pleural cavity of mice, rats or rabbits is filled with trypsin for collection of mesothelial cells (136,137). In addition, scrapings using a blade to extract PMCs from visceral and parietal surfaces have been used in rats and sheep (54,128). As these methods potentially damage cell integrity, collected mesothelial cells are typically assessed for viability and expression of a mesothelial marker such as calretinin. However, although these two approaches are effective in animal models neither is suitable for application in humans.

Validation methods for mesothelial cultures rely on some of the shared properties between mesothelial and epithelial cells. Although these cell types have different developmental origins, they share expression of some markers and characteristics (135). Expression of CK5 and integrins as well as the expression of surface markers including Intercellular Adhesion Molecule-1 (ICAM-1) have been documented in both mesothelial and epithelial cells (134,138,139). Examples of shared characteristics are their flat morphology, tight cell-cell junctions (28), tethering to a basement membrane and surface modifications such as microvilli (2,3,18,27).

Three main approaches are used to support and validate the successful establishment of PMC cultures, two of which rely on presence of epithelial characteristics and expression of markers.

Firstly, the morphology of cultured cells which is often described as spindle-shaped or epithelial-like (131). Many studies feature brightfield images of confluent cell cultures which are reported as mesothelial due to their cobblestone morphology at confluency, as illustrated in pleural rat cultures in Figure 1.11. In addition, cell surface protrusions described as microvilli are assessed by SEM or TEM (Figure 1.11C). There are differences in microvilli location in the literature, as some studies found mesothelial cells covered in microvilli and others showed dense microvilli only at cell-cell boundaries of cultured mesothelial cells (27,128).

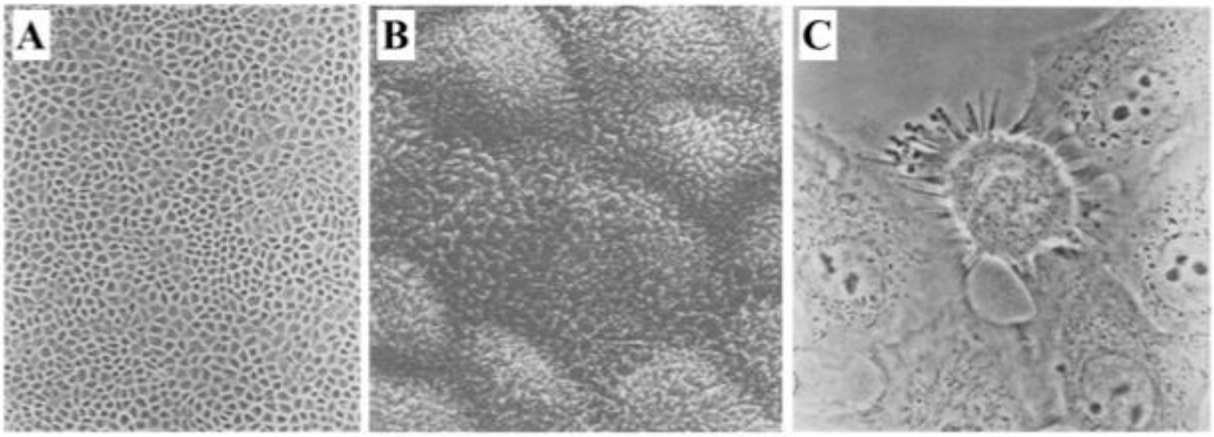

Figure 1.11 Morphology of rat parietal pleural cells. A) Brightfield image of confluent rat parietal pleural cells in culture. B) Scanning electron microscope image of 12 microvilli-covered mesothelial cells in fixed rat parietal pleura tissue, x2200 objective. C) Electron microscopy image of cultured rat parietal pleural cell with surface protrusions. Adapted from (128).

Secondly, expression of certain epithelial and mesenchymal markers is assessed. The lack of a definitive mesothelial cell marker hinders the validation of established cultures and thus a panel of markers is necessary. Human PMC validation is conducted by assessment of expressed markers, which include those used for differentiation of MPM. These include CK5, WT1, calretinin, podoplanin and MSLN (140). Some reports support WT1 as an embryonic mesothelial marker which is lost as development advances, whilst others show adult tissue and cells express WT1, further adding to the disparity of PMC marker expression in the literature.

Finally, in some studies cultured PMCs were verified by their relative sensitivity to carcinogenic asbestos fibres compared to other cultured cell types such as bronchial airway epithelial cells (26). Sensitivity measurements included the amount of cytotoxicity and necrosis present after asbestos incubation as well as levels of secreted cytokines (141).

1.3.2 Peritoneal mesothelial cell culture

The peritoneum is the serous membrane of the abdominal cavity. In humans, there are two predominant methods for isolating peritoneal mesothelial cells. Omentum is obtained during abdominal surgery and mesothelial cells are liberated using enzymes such as trypsin, dispase, liberase and collagenase I and II (142–147). Peritoneal mesothelial cell cultures from animals are similarly established by mincing of omentum and enzymatic digest.

Mesothelial cells are also collected from peritoneal ascitic fluid or dialysate (146). The establishment of the mesothelial cell line LP-9 from peritoneal fluid followed a similar approach to the establishment of the pleural cell line Met-5A (129). Comparison of LP-9 to Met-5A showed differences in their morphology and sensitivity to asbestos which indicates

differences in the nature of mesothelial cells in different cavities (148). However, it is apparent that a similar approach to establishment of pleural cultures is followed for peritoneal mesothelial cultures.

Similarly to pleural cell culture, peritoneal cell cultures derived from murine omentum have been reported to result in cultures with cobblestone morphology (147). In one study murine omentum cultured cells were assessed by immunofluorescence and found to express both mesenchymal and epithelial markers such as WT1, MSLN and CK5. Notably, the expression of these markers changed after serial passages, a phenomenon noted by others during culture of human PMCs (131). Thus, the tools with which peritoneal mesothelial cell cultures are verified rely on the same approaches as those implemented for PMC verification.

1.3.3 Mesothelial cell culture limitations

There are two key limitations in the approach of mesothelial cell culture studies. These limit the ability of established benign mesothelial cell lines still used today, to accurately recapitulate human mesothelial cells (26,125,128,129).

The first limitation entails the insufficient validation methods of mesothelial cell cultures. Current published methods are incomplete in their approach of validating the purity, both short-term and long-term, of mesothelial cell cultures. Due to the developmental origin of mesothelial cells, they share expression of epithelial cytokeratins as well as fibroblast markers vimentin and calretinin. Therefore, this constitutes a significant challenge in demonstrating that primary cells are identified correctly as mesothelial cells. In addition, there is no consensus on a definitive panel which should be used for the identification of normal mesothelial cells in different body cavities.

Scientific interest is predominantly focused on identification and differentiation of MPM cells and thus little is known about the expression levels of markers in normal human PMCs. This leads to disparity in published studies and a lack of knowledge regarding the expression status of primary PMCs in embryonic and adult pleura. Furthermore, PMCs are known to drastically change their morphology in response to environmental cues. This has also been noted in cell culture conditions, with some studies supporting that PMCs resemble spindle-like fibroblasts and others describing a more epithelial-like morphology. In addition, PMCs show different protein expression in culture. Notably the synthesis of cytokeratins has been reported to decrease over time in cultured PMCs (131). Finally, a characteristic of published primary PMC studies is to reference the cobblestone morphology observed when cells reach confluence.

However, this could be easily achieved when culturing other cell types and should not be used as an indication of PMC growth. Collectively, these issues present a persistent challenge for the correct identification of primary PMCs in culture.

The second limitation entails inadequate mesothelial cell isolation methods for human tissues. The two routine approaches for human mesothelial cell isolation are pleural fluid or peritoneal fluid centrifugation and less commonly, pleural or peritoneal tissue digestion. Both methods of isolating human mesothelial cells are intrinsically flawed as they result in heterogeneous populations of mesothelial cells.

Pleural fluid, which is the source of PMCs which the field relies on, is likely to contain viable PMCs from both pleural layers. Thus, all cell lines derived from pleural fluid are a mixed population of free-floating visceral and parietal mesothelial cells. Although this may not be a problem for basic functional comparisons of normal to malignant PMCs, it is a limitation which has hampered the investigation of visceral and parietal mesothelial cells as distinct cell types. However, this limitation of producing mixed populations of PMCs is rarely investigated or acknowledged in studies (37,128).

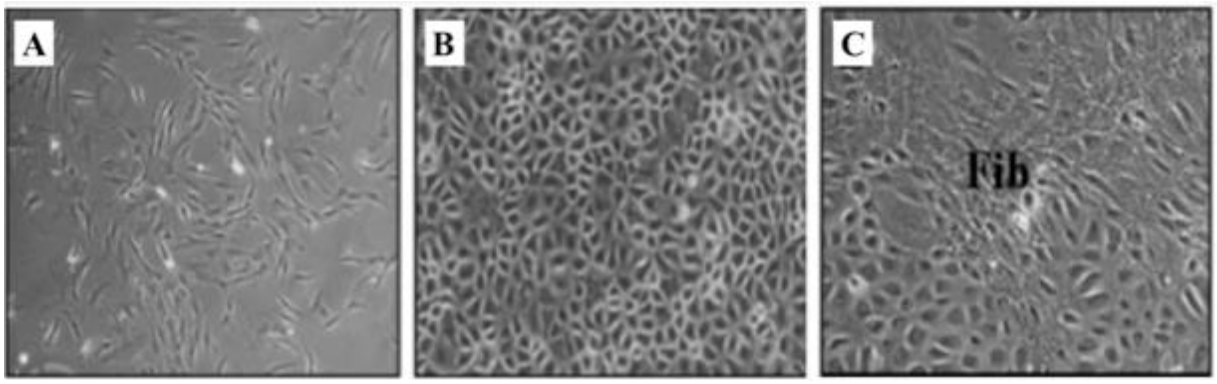

Figure 1.12 Heterogeneous peritoneal mesothelial cultures derived from human omentum. A) Cells adopt a fibroblast-like spindle shape after initial seeding. B) At 5 to 7 days cultures become confluent and adopt polygonal shape and epithelial morphology. C) Fibroblasts are often present in cultures derived from trypsin digestion of the omentum. Fibroblasts have different morphology to peritoneal mesothelial cells and can form multi-layers. Adapted from Yung *et al*. (146).

Pleural and peritoneal digestion approaches have been predominantly used in animal studies and are infrequently used in humans. Notably, one study noted that digest of human omentum resulted in cultures of polygonal cells which reached confluence at 7 days. However, at later passages senescence was observed and cultures became contaminated with fibroblasts and endothelial cells which grew in different patterns (Figure 1.12C). This heterogeneous culture provides evidence of the intrinsic limitations of digesting peritoneal and pleural tissues, which

are tethered to sub-mesothelial connective tissue that contains stromal cell types (Figure 1.12C). Unfortunately, despite over 40 years of mesothelial cell research, a more suitable method for PMC isolation in humans has not yet been developed.

1.4 Hedgehog signalling

1.4.1 Molecular signalling cascade

Hedgehog signalling is an important embryonic pathway and has multifunctional roles throughout development. One of the key functions of embryonic mesothelial cells of the intestine, heart and lung is to migrate and generate sub-mesothelial cell populations (4,7,12). In mouse embryonic pleura, Dixit *et al*. was the first to show that Hedgehog signalling plays a vital part in the migration and differentiation process of embryonic VMCs (7).

The Hedgehog signalling ligand Sonic Hedgehog (SHH) was first discovered due to its role as a mitogen in development (149,150). The family of Hedgehog proteins are long-range extracellular signalling molecules which are produced in the cell and trafficked to the cell membrane in vesicles (151). SHH plays an important role in tissue patterning, cell growth and differentiation, which contribute to a number of processes that include neural tube and cerebellar development, organogenesis of the lung, oesophagus and pancreas (149). In mammalian organisms an additional two ligands have been reported; Desert Hedgehog (DHH) and Indian hedgehog (IHH). In humans, SHH is thought to be the most highly expressed and remains the most well studied to date (150). There are several activation routes that the three Hedgehog ligands can adopt (152). As long-range signalling proteins, once secreted from a cell, they can act locally by binding to the receptor on the cell membrane of the cell which secreted them, therefore causing autocrine signalling activation (152). However, Hedgehog ligands can also exert an effect on adjacent cells and tissues in a paracrine activation model, as they are capable of signalling across distances estimated to range from 50 - 300 μm.

The primary cilium facilitates the SHH signal and subsequent Hedgehog pathway activation. Primary cilia are cell protrusions which emanate from the surface of quiescent cells and act as chemosensors (153,154). Primary cilia have been established as vital organelles for Hedgehog signalling in vertebrates (155–157). Evidence suggests that primary cilia are necessary for transduction of the Hedgehog signal across a spectrum of tissue types, from embryonic tissue to malignancy (157,158). Primary cilia form a compartment in which Hedgehog signalling components are post-translationally modified by kinases in response to the binding of one of the Hedgehog ligands to the Hedgehog receptor. Intraflagellar transport proteins and kinesins

regulate the formation of primary cilia, with Kinesin factor 7 (Kif7) reported to form a Hedgehog signalling compartment in the tip of the primary cilium (159). Importantly, primary cilia have been highlighted as crucial signal transducers during both autocrine and paracrine Hedgehog pathway activation (152,160,161).

In Hedgehog signalling, the pathway receptors function as the signal repressors (162). In a cell with inactive Hedgehog signalling, the Hedgehog receptor Patched1 (PTCH1) or homologue Patched2 (PTCH2) indirectly repress the signal mediator Smoothened (SMO), which in turn represses the zinc-fingered Glioma-associated (GLI) transcription factors GLI1 and GLI2 (Figure 1.13A). The exact mechanism by which PTCH1 inhibits SMO is yet unclear although several studies have indicated that this mechanism could involve pro-vitamin D3 and oxysterols including cholesterol. The expression of these is regulated by the PTCH1 protein functioning as a pump which pushes the oxysterols away from SMO and therefore prevents its activation. To test this hypothesis, Tang *et al*. used Vitamin D3 on *in vitro* models of basal cell carcinoma which have constitutively active Hedgehog signalling and found that Vitamin D3 was able to reduce cell proliferation and the mRNA level of *GLI1* at a comparative level to the SMO inhibitor Cyclopamine (163). This supports Vitamin D3 as a natural Hedgehog pathway inhibitor *in vivo* and combined with previous evidence suggests that PTCH1 regulation of Vitamin D3 is one of the indirect repression methods used to maintain the Hedgehog pathway in an inactive state (163–165).

The transcription factor GLI3 is a transcriptional repressor of the Hedgehog pathway and is active in the nucleus of the cell when the Hedgehog pathway is inactive (150). Hedgehog pathway components such as the receptor PTCH1 and GLI transcription factors, are targets of GLI3 transcriptional regulation, revealing a feedback loop (Figure 1.13).

In a Hedgehog active cell, one of the three Hedgehog ligands binds to the PTCH1 receptor, hence alleviating the repression of SMO (Figure 1.13B). (162). The signal mediator SMO is normally found in intracellular vesicles in the cytoplasm (Figure 1.13A). Upon the termination of its inhibition by the receptor, SMO is able to migrate to the primary cilium and undergo a conformational change mediated by phosphorylation of its C-tail, which allows the protein to become active (Figure 1.13B) (160). GLI2 expression increases in the primary cilia relative to SMO activation (160,161). Antithetically, PTCH1 becomes internalised and expression of ciliary PTCH1 declines. Active ciliary SMO releases the repression of GLI1 and GLI2 and allows them to enter the nucleus, hence enabling their function as transcription factors. GLI1

and GLI2 recognise the consensus binding site ‘GACCACCCA’ which they use to regulate a large number of genes including positive regulation Hedgehog pathway genes.

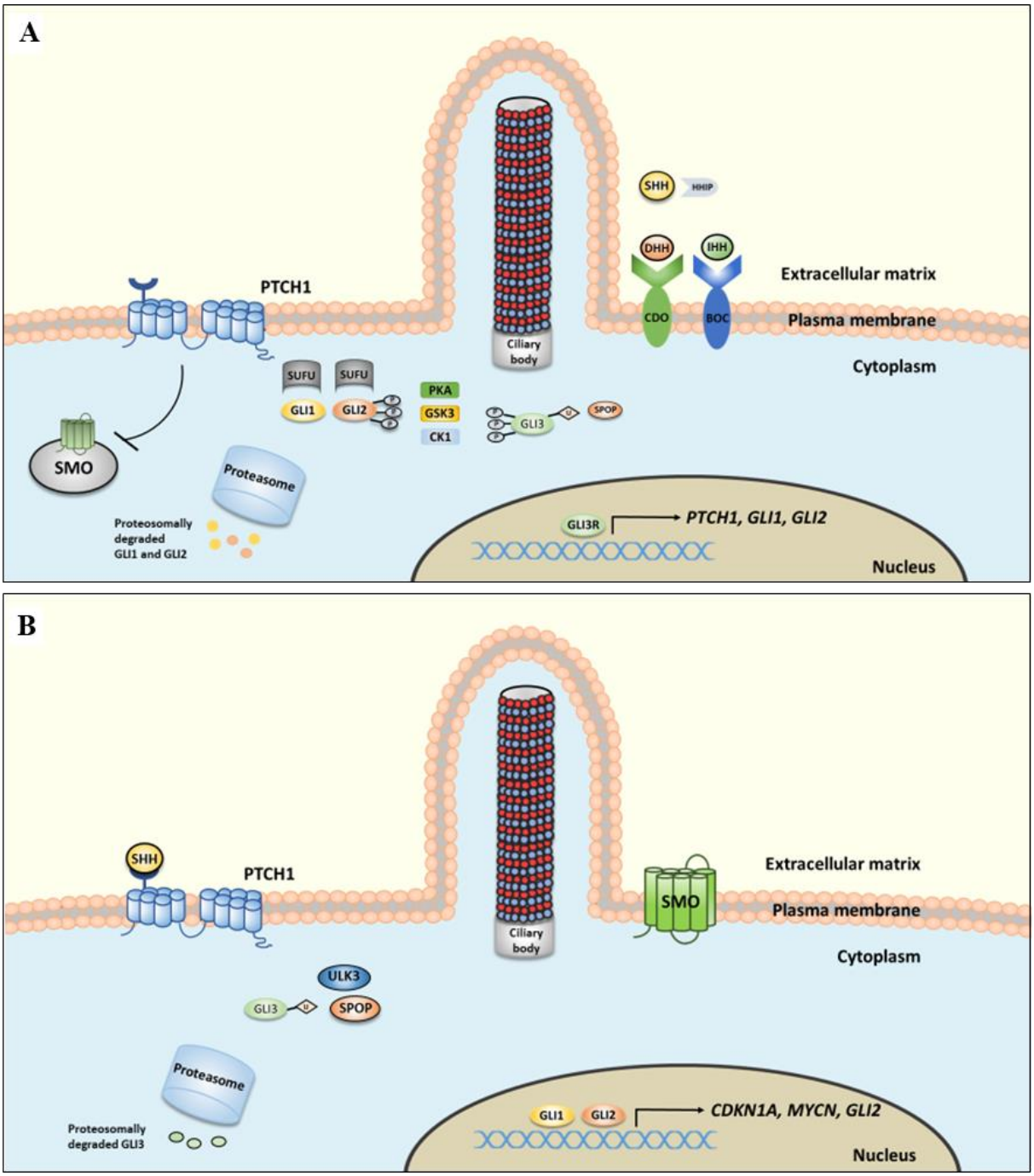

Figure 1.13 Schematic of canonical Hedgehog signalling. A) In an inactive cell, the receptor PTCH1 indirectly inhibits SMO. Hedgehog Interacting protein (HHIP), CDO and BOC sequester free Hedgehog ligands in the extracellular matrix. GLI1 and GLI2 proteins are phosphorylated by protein kinase A (PKA), glycogen synthase kinase 3 (GSK3) and casein kinase 1 (CK1) before proteosomal degradation. The cytoplasmic Hedgehog signalling regulator Suppressor of Fused (SUFU) tethers remaining GLI1 and GLI2 proteins to the cytoplasm. Nuclear GLI3 exerts negative regulation of PTCH1, GLI1 and GLI2. B) In an active cell, one of the three ligands (SHH, DHH or IHH) binds to PTCH1 and releases repression of SMO. Active ciliary SMO indirectly releases the repression of cytoplasmic GLI1 and GLI2 and allows nuclear migration where they bind to DNA. Cytoplasmic GLI3 is modified by kinases, ubiquitinated by SPOP and degraded by the proteasome. Based on descriptions (149–152,160,162,166).

An experiment in which GLI1 and GLI2 were knocked down via siRNA in pancreatic cells, revealed that *PTCH1* mRNA levels were only reduced in the GLI2 knockdown cells, indicating

that *PTCH1* transcription is regulated mainly by *GLI2* (167). A second receptor, *PTCH2*, has been reported to have high homology to *PTCH1*. A recent study utilising *PTCH1* negative cells showed that they had similar SHH chemotaxis to Wild-Type cells (168). Since *PTCH1* mutant cells remained sensitive to SHH ligand stimulation, it was hypothesised that the PTCH2 protein is able to fulfil the role of Hedgehog receptor and thus may serve as a PTCH1 substitute (168).

1.4.2 Non-canonical Hedgehog signalling activation routes

There is reported crosstalk between Hedgehog signalling and the Wnt and Notch pathways during development and in neural cells (169,170). In addition, interaction of the Hedgehog pathway with PI3K/AKT signalling has been shown to regulate stemness and cell proliferation in cancer (171). Common intermediates such as GSK3, PKA and CK1 kinases regulate the activation of GLI proteins in the Hedgehog pathway (Figure 1.13), facilitate β-catenin proteolysis in the Wnt pathway and exert regulation of TGFβ cascade components (Figure 1.14) (172,173). In addition, the cytokine $TGF\beta_1$ has been reported to have mitogenic effects on mesothelial cells and has been shown to interact with the Hedgehog pathway by transcriptionally regulating GLI2 through the SMAD proteins (Figure 1.14) (42,173,174). A study focusing on the regulation of GLI2 by TGFβ signalling showed that SMAD3 and β-catenin interact at a specific 91 base pair region to promote *GLI2* transcription (175). In HaCaT keratinocytes and HepG2 hepatocarcinoma cells, incubation with $TGF\beta_1$ for time periods up to 8 hours resulted in a significant spike in *GLI2* mRNA, with additional evidence of the interaction between these two pathways provided by a similar study in melanoma cells (176). Thus, Hedgehog signalling and these pathways may converge and regulate important cancer cell processes including chemoresistance, invasion and metastasis (171,177).

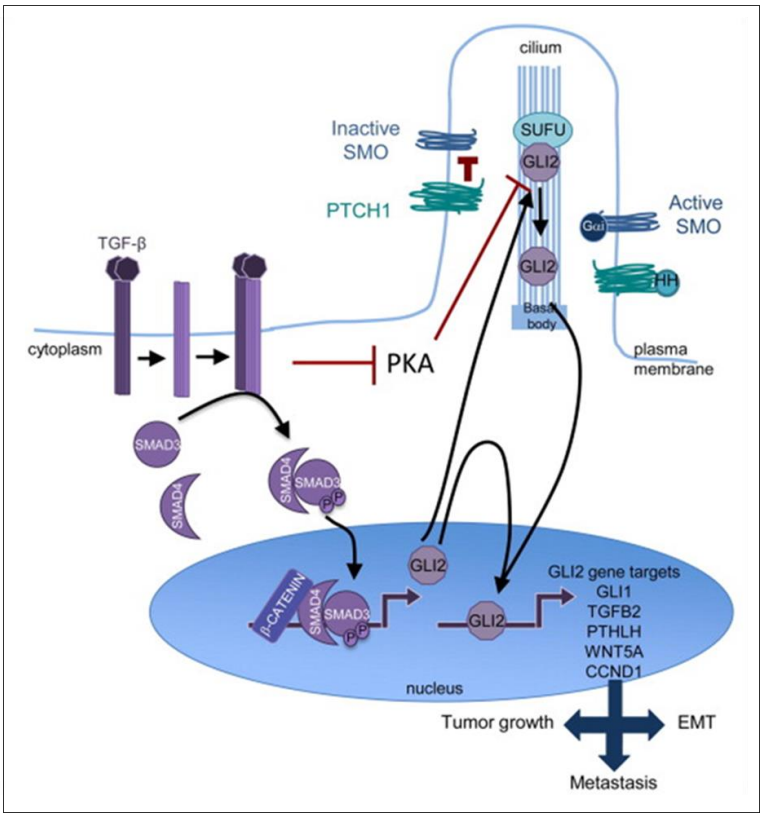

Figure 1.14 Schematic of non-canonical Hedgehog pathway activation by TGFβ signalling (174).

1.4.3 Hedgehog signalling in embryonic pleura

In the study by Dixit *et al.*, migration of VMCs into the parenchyma of embryonic mouse lung was linked to Hedgehog signalling by demonstrating expression of Ptch1 and Gli1 in the visceral mesothelium and migrating sub-mesothelial cells (7). Interestingly, the expression of the Hedgehog ligand Shh was not detected in embryonic pleural mesothelium although Shh was expressed in the lung epithelium. It was hypothesised that Shh may act as a mitogen or chemoattractant in a paracrine activation loop in developing visceral mesothelium (7). Importantly, treatment of embryonic mouse lung in air liquid interphase for 48 hours with the Hedgehog pathway inhibitor Cyclopamine, blocked VMC migration. In the same study, a floxed *Smo* mouse model was used to determine if Hedgehog signalling is essential for migration of both PMCs and mesothelial cells of the heart. Subsequent comparison of pleura and heart tissue in this model, showed that migration of pleural VMCs ceased in the absence of Smo, whereas mesothelial heart cells continued to migrate (7). This suggests that the signalling pathways which PMCs rely on are different from those of heart mesothelial cells (7,12).

1.4.4 Hedgehog dysregulation in developmental syndromes

The Hedgehog pathway is conserved between species and has been reported to play a vital role in cell differentiation and organ development in a number of animal and human organs.

Hedgehog signalling contributes to bud formation and branching of the lung (149). Mouse null *Shh* mutants exhibit holoprosencephaly, a cephalic disorder in which the developing embryo does not correctly form the two hemispheres of the brain. Homozygous null *Gli2* -/- mutant mice do not survive past birth, whereas in contrast, *Gli1* -/- mice are able to develop without any apparent phenotypic abnormalities (178). In addition, *Gli2* -/- mice have dysfunctional lungs, consistent with the role of *Gli2* in lung organogenesis.

In humans, mutations in the Hedgehog receptors cause the autosomal dominant disease termed Gorlin syndrome (179). This syndrome is commonly characterised by skeletal and developmental defects as well as predisposition to malignancies such as medulloblastoma and basal cell carcinoma (BCC) in adulthood (179). Rarer developmental disorders caused by Hedgehog pathway mutations include Greig cephalopolysyndactyly, brachydactyly and minifascicular neuropathy (150,180). These severe diseases illustrate the importance of Hedgehog signalling in human development.

1.4.5 Hedgehog signalling in tissue homeostasis

In adult tissues, the Hedgehog pathway is activated at a baseline level with increased flux through the pathway in response to a stimulus such as tissue damage (181,182). Hedgehog signalling functions include maintaining cell homeostasis, whilst also being able to communicate with a small population of stem or progenitor cells to facilitate organ maintenance and cell renewal (183). However, due to the complexity of the signalling pathway, aspects of the canonical Hedgehog signalling mechanism and importantly the cell and context specific mechanisms by which activation of Hedgehog signalling occurs in adult tissues, still elude us.

Hedgehog signalling has been reported to regulate EMT in colon cancer by regulation of the EMT-associated genes *TWIST1* and *SNAI1* as well as to co-operate with the Wnt pathway to control myofibroblast differentiation in lung fibrosis (184). Interestingly, a contrasting function of Hedgehog signalling in adult cells is that it regulates both homeostasis and tissue regeneration (182,185). The literature presents antithetical evidence regarding Hedgehog pathway expression models in response to a tissue regeneration stimulus such as injury (181,186). Notably, Watkins *et al.* first presented evidence of Shh and Gli1 increase in response to naphthalene injury in the airway epithelium of mice, data which is in accordance with a large amount of literature supporting the mitogenic role of Hedgehog transcription factors (186). In contrast, a subsequent study by Peng *et al.* provided evidence that baseline Hedgehog signalling decreases in response to injury (181). Peng *et al.* hypothesised that Hedgehog signalling

actively regulates quiescence in the murine lung and illustrated, by using multiple *in vivo* models, that decrease of Hedgehog signalling caused proliferation of the adjacent mesenchyme (181). Authors reported that this phenomenon ceased upon the restoration of Hedgehog signalling to baseline levels (181,187). The model of Hedgehog signalling in which secretion of Hedgehog ligand from an adjacent tissue activates neighbouring tissue pathways has been described in other contexts such as in pancreatic ductal adenocarcinoma (188). Collectively, these contradictory studies highlight our lack of knowledge regarding the complex molecular cues which activate Hedgehog signalling in adult tissues and the diverse phenotypic effects this signalling cascade can exert.

1.4.6 Aberrant Hedgehog signalling in cancer

Increased expression of Hedgehog signalling components has been demonstrated in multiple cancers including medulloblastoma, small cell lung cancer, breast cancer, colorectal cancer, pancreatic ductal adenocarcinoma and MPM (177,188–192).

There are three proposed mechanisms for aberrant Hedgehog signalling in cancers. Firstly, the initiators of the Hedgehog pathway, the three mammalian ligands (SHH, IHH and DHH) may be overexpressed in the target tissue or be secreted in dysregulated amounts from adjacent cells (187). Secondly, a somatic mutation may occur in one of the negative regulators of Hedgehog signalling components such as the pathway receptor *PTCH1* or the cytoplasmic regulator *SUFU*. However, the most frequent and clinically relevant Hedgehog mutation occurs in the signal mediator *SMO*, which causes constitutive pathway activation. A recent genomic analysis reported that 85% of 283 BCCs examined, harboured a mutation in *PTCH1*, *SMO* or *SUFU*, a finding which constitutes the highest published mutation rate per Mb in cancer (65 mutations/Mb) (193). Hedgehog signalling can be upregulated through a third route which converges directly on the GLI transcription factors; non-canonical GLI activation signals mediated by other pathways (166,194). Although it is known that Hedgehog components such as SMO can exert non-canonical effects which are not a result of GLI transcription factor activation (166), in this thesis non-canonical Hedgehog signal refers to stimulation of the GLI proteins which bypasses the classical PTCH1-SMO signalling axis.

Upregulation of the GLI proteins which are pleiotropic transcription factors can induce cell proliferation and contribute to processes including carcinogenesis and chemotherapy resistance (166,177,183,192,195). Interestingly, although the literature initially highlighted GLI1 as the most active Hedgehog transcription factor (186), recent studies have revealed that GLI2 is a

pleiotropic protein with similar transcriptional targets to GLI1 (196). Stably integrated expression of a mutant *GLI2* lacking the N-terminal repressor domain (GLI2ΔN) in keratinocytes, provided evidence of the ability of GLI2 to inhibit apoptosis (197). GLI2ΔN cells were reported to have an upregulation of the anti-apoptotic factor BCL-2 and became insensitive to UV light induced apoptosis compared to Wild-Type cells, suggesting a role for GLI2 in chemotherapy resistance (197). Overexpression studies of GLI2 have also reported its ability to cause genomic instability and progression to aneuploidy in keratinocytes as well as the emergence of BCC characteristics in Gli2 overexpressing murine models (196–198).

1.4.7 Upregulation of Hedgehog signalling in MPM

Several studies have provided partial evidence of Hedgehog upregulation in MPM. Notably, the Hedgehog pathway receptor *PTCH1* places in the top ten most frequently mutated genes in the TCGA MPM cohort (Figure 1.7).

Interrogation of MPM models has shown low to moderate efficacy of SMO inhibitors (Cyclopamine and Vismodegib) and a patented GLI inhibitor (GLI-I), although notably the efficacy reported would not warrant consideration for clinical use (191,199,200). However, these studies failed to implement appropriate GLI inhibition controls and Li *et al.* did not employ a significant number of MPM cell lines (n=3) to deduce if Hedgehog signalling inhibition is a feasible therapeutic strategy in MPM. To date, there is no definitive conclusion regarding the ability of GLI inhibitors to cause significant MPM cell growth reduction.

Although the canonical Hedgehog pathway has been mapped, there is no evidence regarding the route of Hedgehog activation in MPM or the phenotype of MPM cells which show increased activation of Hedgehog signalling. Shi *et al.* were the first to provide evidence of increased Hedgehog signalling in MPM (199). They assessed MPM samples by *in situ* hybridisation and qPCR analysis of primary MPM cells grown in hypoxic conditions (199). Primary cell cultures were established using digestion of malignant and non-malignant pleural tissue and were grown in low oxygen at 3%. However, a limitation of the study was the incomplete characterisation of the mesothelial cultures. An increase in *GLI1* and *SHH* was identified in both tumour samples and primary cells. In contrast, Li *et al.* showed an upregulation of GLI2 protein by immunohistochemistry in 24/27 MPM samples but did not find a significant increase in GLI1 and furthermore, detected very little protein expression of SHH (191). These strikingly different findings may be a result of contaminated cultures used by Shi *et al.*, as digestion is known to cause fibroblast and endothelial cell contamination of mesothelial cultures (146). Alternatively,

this could indicate that *GLI1* mRNA levels differ from the resulting protein, an aspect highlighted in the literature as these proteins undergo extensive post-translational modification such as phosphorylation, acetylation as well as alternative splicing into several isoforms; processes which dictate the resulting protein and their activity as transcription factors (201).

Upregulation of Hedgehog signalling in BCC is known to be caused by mutations. However, exome sequencing studies of MPM cell lines and patient samples showed few mutations in Hedgehog components (202). Hence, there are likely molecular events which drive increase of Hedgehog signalling in MPM which have not yet been determined.

1.4.8 Pharmacological agents for Hedgehog signalling inhibition

The first compound found to be capable of Hedgehog pathway inhibition was the natural alkaloid Cyclopamine, which caused cyclopia in sheep herds in the Western United States of America (USA) during the 1950s (203). Investigation into this phenomenon revealed that sheep were ingesting a plant containing the natural steroid alkaloid Cyclopamine, which was causing birth defects in lambs (203). A subsequent X-ray crystallography study revealed that Cyclopamine binds to the extra-terminal transmembrane domain of SMO and blocks its activation (204).

The Hedgehog signal mediator SMO is of clinical interest due to its key function in the Hedgehog signalling cascade and its frequent mutation in multiple disease settings. SMO mutations are considered the predominant early driver of BCC (193). Pharmaceutical drugs were successfully based on the structure of Cyclopamine, in an attempt to develop clinically applicable SMO inhibitors (192,205). The potent SMO inhibitors Vismodegib and Sonidegib were approved for use in locally advanced and metastatic BCC in 2012 and 2015 respectively, by the Food and Drug administration (FDA) in the USA.

The interest in developing GLI antagonists is partially due to the disappointing result of BCC patient *a priori* resistance during treatment with SMO inhibitors, Vismodegib and Sonidegib (206). Patient acquired resistance to these inhibitors within six months is thought to be primarily due to further mutations arising in *SMO*, which quench SMO inhibitor binding (206). Furthermore, SMO inhibitor resistance has also been attributed to non-canonical activation of the *GLI* transcription factors (207). This non-canonical signalling, bypasses SMO-GLI activation and renders SMO inhibitors ineffective (208). Therefore, targeting Hedgehog signalling downstream by direct inhibition of the GLI proteins is of significant clinical interest.

The cell-based screen conducted by Lauth *et al.* employed transduction of recombinant GLI1 and GLI2 in a cell-based model. GLI inhibitor identification was conducted by screening a library of small-molecule compounds and assessing their capacity to induce GLI luciferase inhibition (207). Two structurally different compounds were identified and named GANT-58 and GANT-61 due to their nature as GLI antagonists (207,209). The mechanism of action of GANT-61, has been studied using computational approaches and surface plasmon resonance (209). GANT-61 has an affinity for the DNA-binding zinc fingers 2 and 5 which are conserved between GLI1 and GLI2 (209,210). The identification and verification of GANT-61 as a GLI inhibitor, led to its widespread use. GANT-61 has been reported to have moderate anti-cancer effects in multiple cancer types, including *in vitro* and in *in vivo* models (208,211–213). However, a study by Lim *et al.* showed that GANT-61 kills MPM cells by production of Reactive Oxygen Species (ROS) which calls into question the efficacy of this drug as an inhibitor of GLI proteins (214).

Due to the multiple reports of aberrant Hedgehog signalling in cancer, a significant amount of interest has been shown in designing inhibitors of the GLI proteins. Although multiple studies have reported GLI inhibition with novel and patented compounds, most of these have very high IC_{50} values in cell-based models.

Recently, several publications highlighted the ability of Bromodomain and Extra-terminal motif (BET) protein inhibitors to block Hedgehog-mediated transcription. BET proteins consist of BRD2, BRD3 and BRD4 which are ubiquitously expressed in somatic cells and the germ cell specific BRDt. These proteins are epigenetic ‘readers’ and possess two bromodomains which are able to recognise and bind to acetylated lysine residues on open chromatin, such as the N-terminal tails of histone proteins and acetylated promoter and enhancer regions. One study showed that BRD4 binds to GLI1 and GLI2 promoter regions in medulloblastoma cells and thus act as a necessary regulator of their transcription (108). The prototypical BET Bromodomain inhibitor (BBI) drug JQ1 was first reported in 2010 and closely followed by a similar class of inhibitor, i-BET151 (215). Both drugs have been reported to reduce mRNA levels of *GLI* transcription factors by inhibiting BET proteins and thus preventing them from binding to *GLI* promoter regions (216). Studies have reported the use of JQ1 in MPM cell lines with moderate success and evidenced synergy with the platinum compound cisplatin, which is a first-line agent for patients with MPM (217). However, its ability to cause MPM cell death through GLI inhibition has not yet been investigated.

1.5 Summary

Relatively little is known about pleural VMCs in humans, as animal models have been widely used for the characterisation of PMC morphology and function (7,12,16,24). Although SEM has been successfully employed to characterise VMCs in rabbit and murine tissues, human imaging studies are few and offer a narrow imaging scope (45,46). To date, published images of human visceral mesothelium depict an area spanning 50 – 100 μm which offers a limited view of the dynamic cellular membrane which constitutes the visceral mesothelium (45,46). Thus, the macroscopic visualisation of human visceral mesothelium and assessment of the heterogeneity of human VMCs has not yet been achieved. Furthermore, the model of human VMC spatial distribution has been assumed to be a continuous single cell layer based on animal studies and reports of mesothelium in other organs, but this research question has not been conclusively addressed using human visceral pleura.

In addition, the current methods for isolation and culture of non-malignant mesothelial cells from human tissue are flawed (129). Establishment of normal primary human PMC cultures are infrequent and mainly derived from pleural fluid, which results in a heterogeneous population of PMCs. Thus, the research field would benefit from the development of more suitable methods to isolate human mesothelial cell populations which could progress our understanding of this cell type.

Despite extensive genomic and transcriptomic characterisation of MPM tumours, the gene expression of PMCs in homeostasis has not been investigated in animals or humans. Progress in PMC isolation methods would enable the transcriptomic analysis of both visceral and parietal mesothelial cells for the first time. Transcriptomic analysis of these cells during homeostasis would improve our limited understanding of their diverse functions and could provide valuable insight into upregulated signalling pathways in pleural malignancy and thus highlight yet unexplored therapeutic strategies for the lethal disease of MPM.

In summary, an integrated approach combining macroscopic morphological description, isolation of pure mesothelial cell populations and their transcriptomic analysis. This will improve our understanding of normal human pleural homeostasis and generate actionable insights into upregulated signalling pathways in MPM, which could improve treatment strategies.

1.6 Hypothesis

I hypothesise that distal lung from lung resection surgery and post-mortem tissue harvests can be used as a source of viable VMCs for research purposes and that an improved isolation protocol can be developed to extract a pure population of VMCs from these tissues. I hypothesise that transcriptomic characterisation of a pure population of VMCs during homeostasis will enable the identification of gene expression changes which characterise MPM and highlight potential therapeutic pathways for this disease.

1.7 Aims

- To investigate and validate lung resection surgery and post-mortem sample collection as sources of viable human VMCs.
- To determine the macroscopic morphology of adult human visceral pleura and to explore the intra-sample and inter-sample heterogeneity of VMCs.
- To optimise and implement a method for isolation, purification and transcriptomic characterisation of VMCs with the aim to determine gene expression changes between VMCs in homeostasis and malignancy.
- To examine the upregulation of Hedgehog signalling in MPM.

2 Materials and methods

2.1 Pleural tissue pipelines

2.1.1 ASCENT trial

Non-malignant human distal lung was acquired from ASCENT patients who participated in the SUMMIT trial (NCT03934866). Patients who were diagnosed with lung tumours during CT screening were scheduled for lung resection surgery. ASCENT patients were consented prior to scheduled surgery. All samples used from ASCENT patients (n=8) are shown in Table 2.1. Distal lung tissue was obtained from additional patients undergoing lung resection at University College Hospital on Westmoreland Street. All routine distal lung collections from patients undergoing lung resections (n=7), are referred to as shown in Table 2.2. Collections of distal lung samples from both sources, were approved by the Research Ethics Committee of University College London Hospital (REC ID 18/SC/0514, IRAS ID 245471).

Table 2.1 ASCENT patient IDs and clinical information.

Patient ID	Pathology	Age	Gender	Smoking status	Surgery
ASC004	Invasive adenocarcinoma	61	F	Current	Lobectomy
ASC006	Neuroendocrine	59	M	Current	Bilobectomy
ASC008	Invasive adenocarcinoma	58	F	Current	Lobectomy
ASC010	Invasive adenocarcinoma	73	M	Current	Lobectomy
ASC011	Invasive adenocarcinoma	73	M	Former	n/k
ASC012	Invasive adenocarcinoma	69	M	Former	n/k
ASC013	Squamous cell carcinoma	70	M	Current	n/k
ASC014	Invasive adenocarcinoma	55	F	Former	n/k

Table 2.2 Patient IDs and clinical information from routine distal lung collections.

Patient ID	Pathology	Age	Gender	Smoking status	Surgery
P362	Lung cancer – no histology	83	M	Ex-smoker	Lobectomy
P363	Non-small cell lung cancer	76	M	Smoker	Lobectomy
P364	Adenocarcinoma	83	F	Never smoker	Lobectomy
P366	Adenocarcinoma	68	M	Never smoker	Lobectomy
P367	Adenocarcinoma	74	F	Never smoker	Lobectomy
P369	Adenocarcinoma	66	F	Smoker	Lobectomy
P370	Adenocarcinoma	61	F	Ex-smoker	Lobectomy
P371	Nodal mass – no histology	59	M	Ex-smoker	Lobectomy

2.1.2 PEACE trial

A collaboration with the Posthumous Evaluation of Advanced Cancer Environment (PEACE) trial (NCT03004755) enabled access to post-mortem pleural tissues. Posthumous non-malignant distal lung and/or strips of parietal pleura from the chest wall, were obtained from PEACE patients. Posthumous tissue collections were covered by research ethics granted by the Research Ethics Committee of University College London Hospital (REC ID 13/LO/0972). Clinical details for all PEACE samples (n=12) are shown in Table 2.3.

Table 2.3 PEACE Patient IDs and clinical information. Where fresh tissue is stated as not collect, samples entailed formalin fixed lung tissue.

Patient ID	Pathology	Smoking status	Ischemic time
PEA118	Skin Cancer - Melanoma	Never Smoker	Fresh tissue not collected
PEA124	Skin Cancer - Melanoma	n/k	Fresh tissue not collected
PEA126	Skin Cancer - Melanoma	Never Smoker	Fresh tissue not collected
PEA139	Kidney Cancer - Carcinoma	Never Smoker	1 day
PEA172	Prostate Cancer	Ex-smoker	4 days
PEA173	Renal Cell Cancer	n/k	Fresh tissue not collected

PEA176	Non-Small Cell Lung Cancer	Ex-Smoker	Fresh tissue not collected
PEA203	Skin Cancer - Melanoma	n/k	Fresh tissue not collected

2.1.3 MS01 Trial

MPM FFPE blocks from the MS01 trial (NCT00075699) were obtained by collaboration and used for histological comparison of normal pleura to malignant tissue. All blocks used have been confirmed by a pathologist to contain MPM.

2.2 Isolation of human mesothelial cells

2.2.1 Liberase digestion

The enzyme liberase (Sigma-Aldrich) was used to create a suspension of cells from 1 cm^2 sections of fresh distal lung. Lyophilised liberase was re-constituted in sterile water according to manufacturer instructions and added to serum-free DMEM media. A small section of distal lung with visible pleura was minced and added to this. Liberase incubation was conducted for 25 minutes at 37 °C in a water bath with agitation. Subsequently, a 70 µm strainer was used to break up any residual clumps. Cells were then washed with PBS and either cultured in conditions outlined in 2.4 or analysed by flow cytometry as explained in 2.3.4.

2.2.2 Pleural brushing

The entire distal lung tissue collected (approximately 5 x 5 cm) was placed in a 10 cm sterile petri dish in PBS. A cytology brush was used to lightly brush the surface of the lung with care taken not to damage the visible translucent basal lamina of the visceral pleura. The cytology brush was then washed in a 50 mL falcon tube containing PBS. PBS from the dish was also collected. The collected liquid was centrifuged at 300 RCF for 5 minutes and the cell pellet was used for cell culture studies outlined in 2.4 or analysis outlined in 2.3.4.

2.3 Lung tissue processing

2.3.1 Histology

2.3.1.1 Formalin fixation and paraffin-embedding

Human tissues were fixed in 10% neutral buffered formalin (NBF) solution, at 4 °C for 24 hours. Following this, tissues were moved to 70% ethanol, placed in an automated tissue processor overnight (Leica TP 1050) and embedded in wax moulds. 5 µm sections were mounted on polylysine slides and left to dry overnight. Haematoxylin and eosin (H&E) staining to determine tissue architecture, was conducted by an automated tissue stainer (TissueTek). A pleural tissue microarray was obtained from US Biomax (T932A) and H&E stained in the same way as FFPE sections. All slides were converted into digital images by NanoZoomer 2.0 (Hamamatsu) and analysed using NDP.view2 (Hamamatsu). The H&E stains of normal lung shown in Figure 3.2 were obtained from The Genotype-Tissue Expression (GTEx) Project Histology viewer. Images from GTEX-11ZTT-0626 and GTEX-146FQ-0926 were used as reference to normal lung (Figure 3.2).

2.3.1.2 Cryopreservation in OCT blocks

A plastic box containing isopentane was placed on dry ice for 30 minutes prior to embedding. Fresh sections of distal lung including lung parenchyma were sectioned using a disposable scalpel and placed vertically in cryomolds (E6032, Sigma-Aldrich) using sterile tweezers. CellPath OCT embedding matrix (15212776, ThermoFisher) was used to cover the tissue. The cryomolds were incubated in the cold isopentane until opaque. Blocks were stored at -80 °C.

2.3.2 Scanning electron microscopy

Human tissues were fixed in 10% neutral buffered formalin solution, at 4 °C for 24 hours. Following this, tissues were moved to 70% ethanol and were either kept at 4 °C for long-term storage or processed further by incubation in increasing concentrations of ethanol, up to 100%. Dehydrated tissues, approximately 1 – 2 cm^2, were critical-point dried from 100% ethanol using carbon dioxide (CPD300 Auto, Leica). Once dried, tissues were transferred to a sputter coater (Q150R, Quorum) for gold coating. Following electron microscopy preparation, the tissues were mounted on carbon tape and imaged by a Scanning Electron Microscope (Hitachi, S3400N), operated at 5 kV. Quantification of SEM images was done using ImageJ v2.

2.3.3 Whole-mount confocal imaging

Whole-mount distal lung was sectioned into pieces of approximately 1 x 2 cm and placed in a 24-well plate. All incubations took place on a rocker with gentle rotation. Incubations were at

room temperature unless otherwise specified. Tissue was permeabilised in PBS containing 5% Triton X for 2 hours followed by blocking for 2-3 hours in PBS containing 5% foetal bovine serum (FBS), 4% DMSO, 2.5% BSA, 0.5% Triton X and 0.05% ProClin™ 300. Primary antibodies were incubated for 24 hours at 4 °C. The following day, tissues were washed three times for one hour in PBS containing 0.05% Tween 20 (PBS-T). Tissues were incubated with species appropriate secondary AlexaFluor-conjugated antibodies AlexaFluor-488 (A21131, ThermoFisher) and AlexaFluor-AF555 (A31572 and A21127, ThermoFisher). All AlexaFluor-conjugated antibodies were used at a concentration of 1:200 and were incubated for 24 hours at 4 °C. The following day, washing steps were repeated before nuclear staining with 0.1 μg/mL DAPI in PBS-T for 30 minutes. Tissue was then washed with PBS containing 0.05% ProClin™ for 1 hour and was optically cleared using RapiClear 1.52 (SunJin Labs) for 30 minutes. Tissues were mounted with RapiClear on polylysine slides, using appropriate 0.5 – 1 mm spacers (iSpacer, SunJin Labs). A coverslip was adhered onto the spacer and sealed in place with nail polish. Immunofluorescent images were acquired by a Leica SP8 confocal microscope using either a 20x or 40x objective. Images were viewed in Fiji software and z-stacks were reconstructed into 3D projections using Imaris version 9.5.

2.3.4 Flow cytometry

Prior to flow cytometry, cell populations isolated from liberase digestion and pleural brushing were lysed for 5 minutes at room temperature with 10ml red blood cell lysis buffer (BioVision). Samples were analysed by flow cytometry on a BD LSR Fortessa I machine. All flow cytometry data was analysed using FlowJo software (Tree Star Inc., Oregon, USA).

2.3.4.1 Cell viability dyes

To measure cell viability in digested pleura and pleural brushings, the fluorescent cell viability dyes Zombie Red™ and Zombie Green™ (BioLegend) were used. The lyophilised dyes were reconstituted in 100 μLs of 100% DMSO. Cells were washed with PBS prior to incubation. The dye was diluted 1:1000 in PBS and added to the cells for 15-20 minutes at room temperature, protected from light.

2.3.4.2 Extracellular and intracellular staining

Antibodies were added to cells according to Table 2.4. For intracellular markers, CellFix™ buffer (340181, BD Biosciences) was diluted 1:100 with RNAse free tissue grade water (W3500, Sigma-Aldrich) and added to cells at 4 °C for 5-15 minutes. Cells were then washed

in FACS sort-buffer and were permeabilised using a 1:100 dilution of PermWash (BD) to which FACS antibodies were added at 1:100.

Table 2.4. Antibodies used for flow cytometry and fluorescence-activated cell sorting.

Antibody	Fluorochrome	Catalogue ID	Supplier	Concentration
ALCAM	PE	343903	BioLegend	1:100
Annexin V	AF647	A23204	ThermoFisher	1:50
CD235α	Pacific Blue	349107	BioLegend	1:100
CD31	PerCP-Cy5.5	102419	BioLegend	1:100
CD45	BV421	304032	BioLegend	1:100
CD90	Pe/Cy7	328124	BioLegend	1:100
Cytokeratin 5	AF488	ab193894	Abcam	1:100
Cytokeratin 5	FITC	FCMAB291F	Millipore	1:100
E-cadherin	APC	324107	BioLegend	1:100
EpCAM	APC	324207	BioLegend	1:100
ITGA6	APC	313615	BioLegend	1:100
PDGFRα	PE	135909	BioLegend	1:100
PDGFRβ	AF700	323605	BioLegend	1:100
Podoplanin	Pe/Cy7	127411	BioLegend	1:100

2.3.4.3 Fluorescence-activated cell sorting

BD FACS Aria II was used for FAC-sorting. Gates were set based on fluorescence minus one (FMO) stains. Where an FMO was not used due to low cell numbers this has been stated. OneComp eBeads (ThermoFisher) were used to create a fluorochrome compensation matrix.

2.3.5 Primary cell RNA Extraction

All surfaces and equipment were decontaminated with RNAse AWAY (7002, ThermoFisher). For RNA extraction of FACS-sorted mesothelial cells the Arcturus PicoPure RNA Isolation kit (ThermoFisher, 12204-01) was used. Cells were first incubated in 10% BSA in PBS before centrifugation at 3000 RCF for 10 minutes and re-suspension in RNA extraction buffer according to the kit instructions. RNA quality was assessed by Qubit and all samples with a RIN ≥ 2 were prepared with NEBNext® Low Input RNA Library Prep Kit for RNA Sequencing on an Illumina platform at UCL Genomics.

2.4 Primary mesothelial cell culture

Cell culture conditions were based on published methods (131). The cell media referred to as complete medium is a 1:1 mixture of medium 199 (M199, Sigma-Aldrich) and medium MCDB 105 (Sigma-Aldrich), 10% FBS, 10 ng/mL EGF, 0.4 µg/ml hydrocortisone, 10 µg/mL gentamycin, 0.25 µg/mL Amphotericin B and 1% Penicillin/Streptomycin.

To assess the purity of the cell population as well as monitor morphology and confluence, primary cells were imaged with a brightfield microscope (AXIO, A159).

2.5 Pleural mesothelioma cell lines

2.5.1 MPM cell culture

MPM cell lines were obtained from the Sanger Institute in Cambridge and MesobanK. Sanger cells were cultured in RPMI-1640 with 10% FBS, 1% Penicillin/Streptomycin and 5 mM sodium pyruvate in 5% CO2 at 37 °C. MesobanK and HEK293T cells were grown in DMEM with 10% FBS, L-glutamine and 1% Penicillin/Streptomycin under the same conditions. Primary fibroblasts (patient ID: P0001) were acquired from the TRACERx trial.

2.5.2 Cell viability assay

Cells were seeded at 4 x 10^3 cells/well in 96-well tissue culture plates (Greiner). Three days after treatment, 10% MTT (M-2128, Sigma-Aldrich) was added to the cells and incubated for three hours at 37 °C. Wells were replaced with 100 µLs of 100% DMSO (VWR) and fluorescence was measured at 560 nm wavelength by spectrophotometer. Values were normalized to untreated cells. For proliferation analysis cells were seeded at 4 x 10^3 cells/well in 96-well tissue culture plates. BrdU incorporation kit (ROCHE) was used according to manufacturer instructions.

2.5.3 Stimulation assay

The cytokines TGFβ_1 (PHP143B, Bio-Rad) and TGFβ_2 (PHG9114, ThermoFisher) were used at final concentrations ranging from 1 – 10 ng/mL. The N-terminus of Sonic hedgehog (C24II, BioTechne) was used at a final concentration of 100 – 200 ng/mL. All cell stimulations were for 48 hours unless otherwise stated. RNA was extracted from cells using an RNAeasy mini kit (QIAGEN).

2.5.4 Colony forming assay

For colony forming assays 1000 cells/well were seeded in 6-well tissue culture plates. Media was replenished every three days. At 12 days, cells were washed with PBS, fixed with 4% paraformaldehyde for 10 minutes, stained with 300 μLs crystal violet for 20 minutes, washed with diH2O and left to dry overnight. Plate imaging was conducted with ImageQuant Las 4000 (GE Healthcare). Colonies were quantified using ImageJ according to methods published by Moestrup *et al*. (218).

2.5.5 RNA interference

Cells were seeded at 4 x 10^3 cells/well in 96-well tissue culture plates for MTT assay or at 2 x 10^6 in 6-well plates for protein and RNA extraction. GLI2 siRNA was re-suspended in siRNA diluent to 20 μM according to manufacturer instructions (Dharmacon). Cells were subjected to small interfering RNA (siRNA) treatments at 50 nM and 100 nM. Lipofectamine 2000 (ThermoFisher) was added to OptiMem (Gibco) culture media and allowed to form complexes with siRNA before treating cells for six hours. Values for qPCR and MTT assays were normalized to control wells which were transfected with scrambled siRNA (Dharmacon). Cells were replenished with RPMI media after a 6-hour incubation with siRNA and were harvested at 48 and 72 hour time points.

2.5.6 Lentiviral transduction

The lentiviral pGIPZ GLI2 shRNA plasmid (V3LHS_321208, GE Healthcare) containing the *GLI2* targeting sequence 'TGATGTAGGCCACTAGCGA', was obtained from UCL shRNA library. Bacteria were cultured in the presence of Ampicillin (100 μg/mL) and grown at 37 °C overnight. Plasmid extraction was conducted with MaxiPrep kit (QIAGEN). Sanger sequencing using a WPRE primer (5' - GCATTAAAGCAGCGTATC - 3') to confirm presence of the correct insert.

HEK293T cells were seeded in T175 flasks to 80 – 90% confluence and transfected with second generation lentiviral plasmids. Transfection was done with jetPEI (Source Bioscience UK Ltd), 20 μg pGIPZ-GLI2 shRNA, 7 μg packaging plasmid pCMV-dR8.74 and 13 μg envelope plasmid pMD2.G. The lentiviral packaging plasmids were kind gifts from Dr Adrian Thrasher (Addgene plasmids #22036 and #12259 respectively). The pGIPZ virus was concentrated by PEG-it™ (System biosciences) and lentiviral titration was conducted in HEK293T cells in the presence of 8 μg/mL Polybrene (Sigma-Aldrich). GFP incorporation was measured by flow cytometry 48 hours after viral transduction. Viral titer was calculated according to the formula:

TU/mL = number of cells seeded x % of GFP / virus volume in 1 mL

H2803 cells were transduced with estimated multiplicity of infection (MOI) 1 and 3 of pGIPZ GLI2 virus and empty pGIPZ backbone respectively.

2.5.7 CRISPR/Cas9 transfection

All CRISPR/Cas9 reagents were purchased from Integrated DNA Technologies (IDT). Alt-R® CRISPR-Cas9 crRNA, Alt-R® CRISPR-Cas9 tracrRNA ATTO™ 550 and Alt-R® S.p. Cas9 Nuclease V3 were used with RNAiMAX (ThermoFisher) for transfection of CRL2081 mesothelioma cells, according to manufacturer instructions. Two BAP1 crRNAs were used, targeting *BAP1* Exon 4 (TCAAATGGATCGAAGAGCGC) and Exon 5 (GGCATGAGTTGCACAAGAGT). A non-targeting crRNA was purchased from IDT and was used at the same concentration as a negative control crRNA. Briefly, the crRNA and tracrRNA were mixed in equimolar concentrations to form 1 µM of gRNA duplex. The Cas9 V3 nuclease was diluted to 1 µM. For a 24-well plate 200 µLs of RNP complex (10 nM) per well were formed using Optimem. The RNP complex was reverse transfected using 5 µLs of RNAiMAX for each well of a 24-well plate containing 200,000 cells/well. Cells were checked under a fluorescent microscope at 24 hours to check for incorporation of tracrRNA ATTO-550. Subsequently, cells were collected by trypsinisation and single cells positive for ATTO-550 were FACS sorted into a 96-well plate.

2.5.8 Screening and validation of CRISPR/Cas9 BAP1 Knockout

Once clones grew into colonies, they were moved to a 12-well plate for further expansion and DNA was extracted using the PureLink Genomic DNA mini kit (K182001, Invitrogen). DNA was quantified using a NanoDrop 2000. A RedTaq polymerase (Sigma-Aldrich) was used to amplify the crRNA targeted *BAP1* exonic regions. Polymerase Chain Reaction (PCR) primers for *BAP1* are shown in Table 2.5. PCR products were validated qualitatively using gel electrophoresis, cleaned up with a Wizard® PCR Clean-Up Kit (Promega) and Sanger Sequenced at Source Biosciences. Sanger Sequencing data was assessed for InDels using SnapGene version 4.0.

Table 2.5 PCR and Sanger Sequencing primers for *BAP1* exons 4 and 5.

***BAP1* exon**	**Direction**	**Primer sequence**
Exon 4	Forward	CTTCATAAGGAGACTGGGTG
Exon 4	Reverse	GCCCCAAGCCCATATAC
Exon 5	Forward	TTGTTTGGAGGGTGGGATGC

Exon 5	Reverse	AAGCAACATGGCCTGAGAGG

2.5.9 Cell lysis and immunoblot

Cells were lysed in radioimmunoprecipitation assay (RIPA) buffer (Sigma-Aldrich) supplemented with protease inhibitor (Roche) at 4 °C for 30 minutes. Cells were pelleted at 1500 RCF and supernatant was quantified by Pierce protein BCA assay (ThermoFisher). 25 μg of protein was separated on a 4 – 12 % Bis-Tris gel and transferred to nitrocellulose membrane. Primary antibodies were used according to Table 2.6. ECL substrate (Luminata Forte, Millipore) was used for chemiluminescence detection by ImageQuant Las 4000.

Table 2.6 Antibodies used for immunoblot.

Immunoblot antibodies				
Antibody	**Species**	**Catalogue ID**	**Supplier**	**Concentration**
BAP1	Mouse	28383	Santa Cruz	1:1000
BCL-XL	Rabbit	2764	Cell Signalling	1:1000
α-tubulin	Rabbit	2125	Cell Signalling	1:1000
CDC2	Rabbit	28439	Cell Signalling	1:1000
CD45	Mouse	M0701	DAKO	1:1000
GLI1	Mouse	2643	Cell Signalling	1:1000
GLI2	Mouse	271786	Santa Cruz	1:500
GLI3	Goat	AF3690	R&D Systems	1:1000
Histone H2A	Rabbit	12349	Cell Signalling	1:1000
Ubiquityl-histone H2A	Rabbit	8240P	Cell Signalling	1:1000
p21	Rabbit	12D1	Cell Signalling	1:1000
PARP	Mouse	ab32064	Abcam	1:2000
SHH	Rabbit	ab53281	Abcam	1:1000
SMO	Rabbit	NBP2-24543	BioTechne	1:2000
Snail	Mouse	3895s	Cell Signalling	1:1000
SUFU	Rabbit	2522	Cell Signalling	1:1000
Vinculin	Rabbit	13901	Cell Signalling	1:1000

2.5.10 Immunofluorescence and immunohistochemistry

FFPE sections were cut at 5 μm, dewaxed and rehydrated using a TissueTek autostainer protocol which entailed immersion in xylene followed by subsequent incubation in decreasing concentrations of alcohol. Antigen retrieval was conducted in citrate buffer (pH = 6) boiled at 95 °C for 15 minutes. VECTASTAIN Elite ABC kit and DAB Peroxidase HRP substrate kit were obtained from Vector Laboratories and used according to manufacturer instructions.

Table 2.7. Antibodies used for immunofluorescence and immunohistochemistry.

Immunofluorescence and immunohistochemistry antibodies				
Antibody	**Species**	**Catalogue ID**	**Supplier**	**Concentration**
Calretinin	Mouse	NCL-L-CALRET-566	Leica	1:200
Cytokeratin 5	Chicken	3475	Sigma-Aldrich	1:500
Podoplanin	Mouse	ab10288	Abcam	1:200
Smooth muscle actin	Mouse	M0851	DAKO	1:1500

2.5.11 Statistical analysis

All cell-based experimental data was analysed in GraphPad Prism version 8.0. ANOVA and t-tests were reported as significant if $p \leq 0.05$ (* =$p < 0.05$, ** =$p < 0.01$, *** =$p < 0.001$). All MPM RNA sequencing data was accessed through the TCGA and analysed in R 3.2.1. Linear regression models were used to determine the association between rank normalized GLI1 or GLI2 expression as the independent variable and rank-normalized expression of the remaining 36725 genes in the RNA sequencing dataset as the dependent variable. Bonferroni adjustment for multiple testing was used by dividing the p-value by the number of tests (0.05/36725). A significance cut-off of $\alpha = 0.05$ was used for false discovery rate (fdr) adjusted p value of differentially expressed genes in the H2803 U133 plus 2.0 human genome array dataset.

KEGG enrichment analysis was performed using DAVID version 6.8 with the background set to all human genes and the Bonferroni significant genes from the GLI1 (n=198) and GLI2 (n=357) association analysis. Ingenuity Pathways analysis software was used for the differentially expressed genes (DEGS) (n=141) from the parental cells and shRNA-mediated GLI2 knockdown microarrays in H2803 cells. All normal lung and normal tissue data were accessed through the Genotype-Tissue Expression (GTEx) project. The scRNA-seq data shown as UMAP analyses were accessed through the IPF atlas (www.ipfcellatlas.com).

3 Characterisation of normal human adult pleura

3.1 Background

In 2015 a total of 2,542 MPM fatalities were recorded in the UK (67,219). MPM has a relevantly low incidence rate in the population both in the UK and globally. Therefore, few laboratories have access to normal and malignant pleural tissue, as MPM cases are consolidated at a limited number of specialised centres. Previously, murine models have been relied on for insights into MPM morphology and function (23,32,147), as there are limited and infrequent opportunities to study human pleural tissue. However, it is increasingly recognised that understanding of human cells in tissue homeostasis is necessary to progress cancer research. Therefore, it is vital to validate sources and establish tools for study of normal human PMCs and to increase our limited knowledge of mesothelial cells during pleural homeostasis.

To address the unmet scientific demand for validation of suitable pleural tissue sources, I aimed to investigate the feasibility of using two different human distal lung pipelines as sources of normal VMCs; an external collaboration for acquisition of non-malignant post-mortem distal lung from advanced cancer patients and an internal tissue source for acquisition of non-malignant distal lung from patients undergoing routine lung resection surgery. Due to the nature of these tissue sources, it was not possible to obtain parietal pleura from lung resection surgery and parietal pleura was infrequently available through post-mortem. Thus, the work outlined in this thesis focuses on the study of VMCs. The criteria I aimed to assess included demonstration of intact and discernible pleural histology, VMC expression of mesothelial markers and the morphology of VMCs detected by SEM imaging.

A new finding in the MPM field is the MPM pre-malignant stage, named MMIS (220). This study highlighted the importance of assessing reactive and suspect pleural tissues for signs of pre-malignancy and to improve understanding of early cases of pleural change. Assessment constitutes histological assessment for cytological changes in mesothelial cells as well as investigation of BAP1 expression in mesothelial cells by IHC. As many of the samples obtained in this study were derived from patients with lung pathologies or metastatic lung malignancy, I hypothesised that some cases would not exhibit normal mesothelium. I aimed to utilise this and assess the expression of BAP1 in cases with reactive mesothelium.

3.2 Aims

- To validate the utility of two human tissue pipelines as sources of normal VMCs.

- To determine the characteristics of VMCs and investigate heterogeneity in VMC size in human pleural samples.
- To ascertain the global spatial distribution of VMCs in normal human adult pleura by whole-mount confocal imaging and SEM.
- To delineate the expression of BAP1 in reactive mesothelium.

3.3 Results

3.3.1 Tissue architecture of normal and malignant reference tissues

Initially, normal human pleura was required as a baseline reference to determine the histology of pleural tissue. As normal human pleura was not routinely availably in our laboratory, external sources were sought.

A pleural tissue microarray was obtained from US Biomax and was interpreted after consultation with a pathologist. The parietal pleura is the mesothelial layer attached to the chest wall. Therefore, its histology is largely composed of chest wall musculature, including a layer of fibrous material, adipose tissue and skeletal muscle (Figure 3.1).

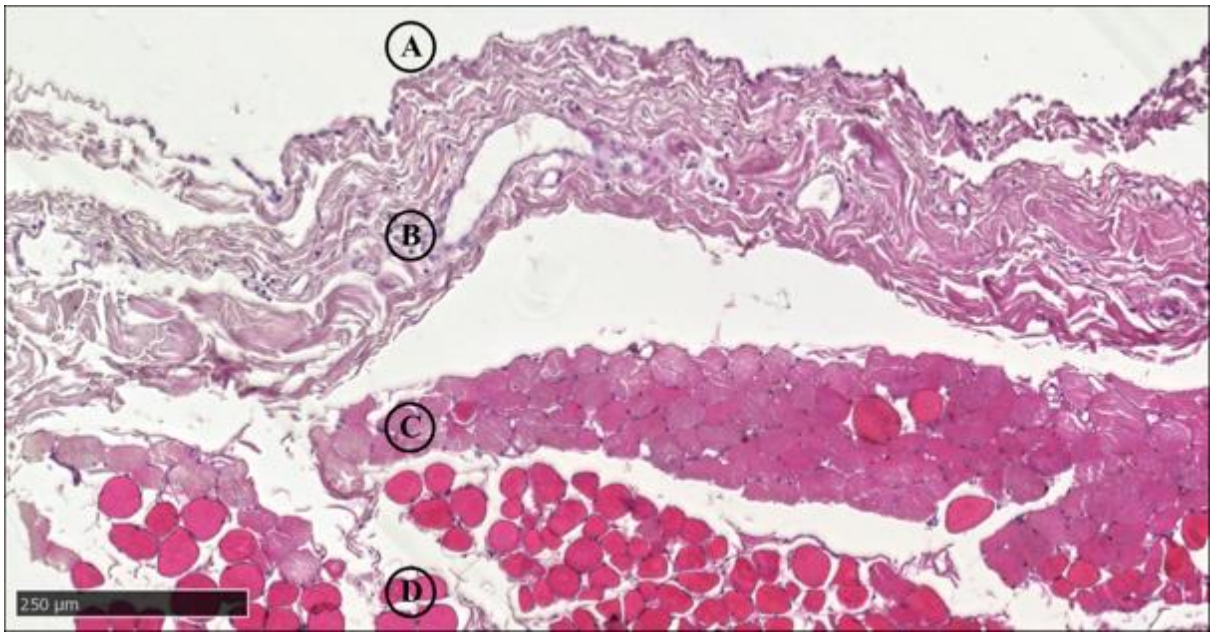

Figure 3.1 Histology of normal human parietal pleura. Representative H&E stain of normal human parietal pleura from tissue microarray (n=4). A) A single layer of parietal mesothelial cells attached to a basement membrane. B) The pleura is composed of fibrous connective tissue and contains multiple veins and lymphatic vessels. C) A layer of adipose tissue separates the pleura from the underlying musculature. D) A section of skeletal muscle.

An online resource was used for histological assessment of normal human visceral pleura. The GTEx portal contains RNA Sequencing and histology of post-mortem non-malignant lung

samples. All GTEx histology images are evaluated and graded by a panel of pathologists and are publicly available through GTEx Histology Viewer. The visceral pleura accessed through GTEx is benign, although patients have some underlying pathologies (Figure 3.2). Thus, these H&E stains are not an ideal reference control for visceral pleura but provide some insight into the structure of the tissue (Figure 3.2). Based on literature descriptions, it is possible to discern the thin layer of visceral mesothelial cells (VMCs) attached to a basement membrane and the underlying lung parenchyma, featuring a large population of immune cells (Figure 3.2).

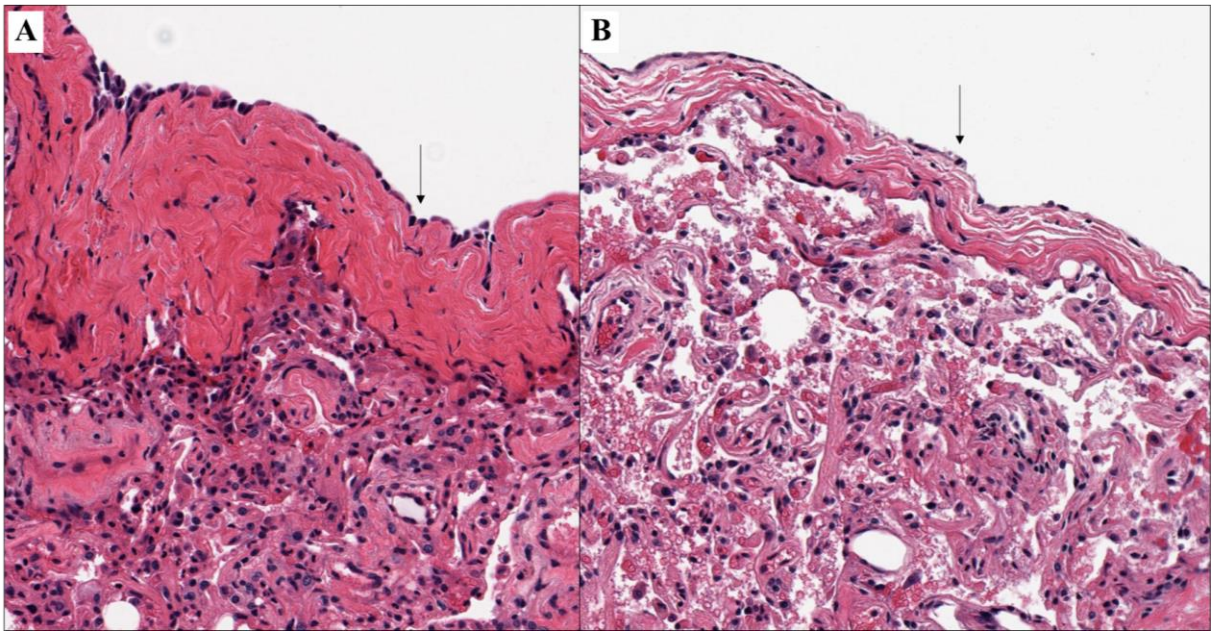

Figure 3.2 Histology of normal visceral pleura acquired from post-mortem. Images and tissue descriptions acquired through GTEx Histology viewer as described in 2.3.1.1. A) 1cm of thickened visceral pleura with some fibrosis, atelectasis, and emphysematous change. Scattered neutrophils are present. B) Pleura is visible in 1/3 of the section, atelectasis and emphysema. Arrows point to surface mesothelial cells.

To compare normal and malignant reference tissues, histological analysis of MPM blocks from the MS01 trial was performed. The malignant pleural sections were characterised by proliferation and invasion of malignant mesothelial cells (Figure 3.3). The single cell layer of the mesothelium appears to have proliferated to form cell clusters which migrate away from the basal lamina to which the cells are tethered. Furthermore, there are sections of necrosis (Figure 3.3A) as well as diffuse fibrin aggregates (Figure 3.3B). Although both samples shown in Figure 3.3 are epithelioid subtypes of MPM, they are structurally and morphologically dissimilar. This demonstrates the heterogeneity of MPM tissues and the striking change in tissue architecture between normal (Figure 3.1, Figure 3.2) and malignant pleural tissues (Figure 3.3).

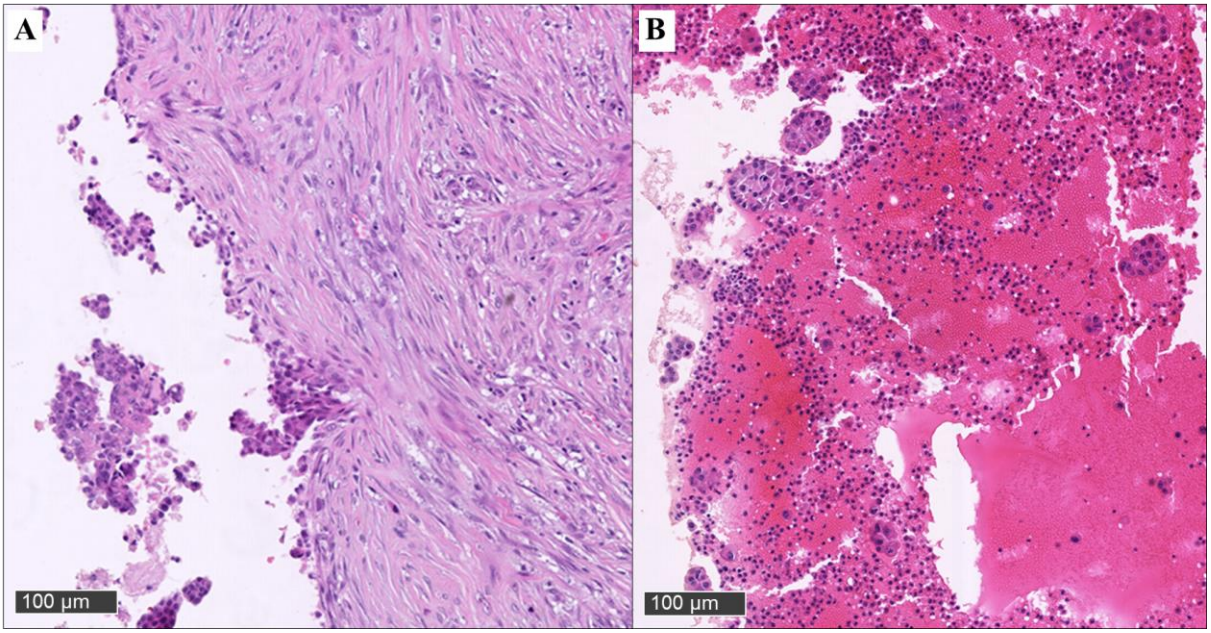

Figure 3.3 Histology of epithelioid malignant pleural mesothelioma. Representative H&E stains of two MPM samples from the MS01 trial. A) Thickened and fibrotic malignant pleura. B) Fibrin aggregates containing mesothelioma cells and immune cells.

3.3.2 Validation of lung resection tissue as a source of visceral mesothelial cells

Initial biopsies of distal lung acquired from lung resection surgery did not contain VMCs when assessed histologically (n=3, data not shown). Sampling modifications and vertical embedding of tissue were implemented to include VMCs in histology blocks.

After optimisation, histological assessment of 6 distal lung samples acquired from lung resection surgery showed similar tissue architecture to visceral pleura in published literature. Furthermore, a pathologist was consulted to verify the correct identification of VMCs in the sections of visceral pleura.

Notably, samples of visceral pleura differed in the thickness of underlying connective tissue and density of attached VMCs (Figure 3.4). The number of attached cells ranged from no detectable VMCs to sparse patches of continuous visceral mesothelium (Figure 3.4). In most sections with detectable VMCs, these resembled flat endothelial-like cells with a thin, uniform nucleus (Figure 3.4C).

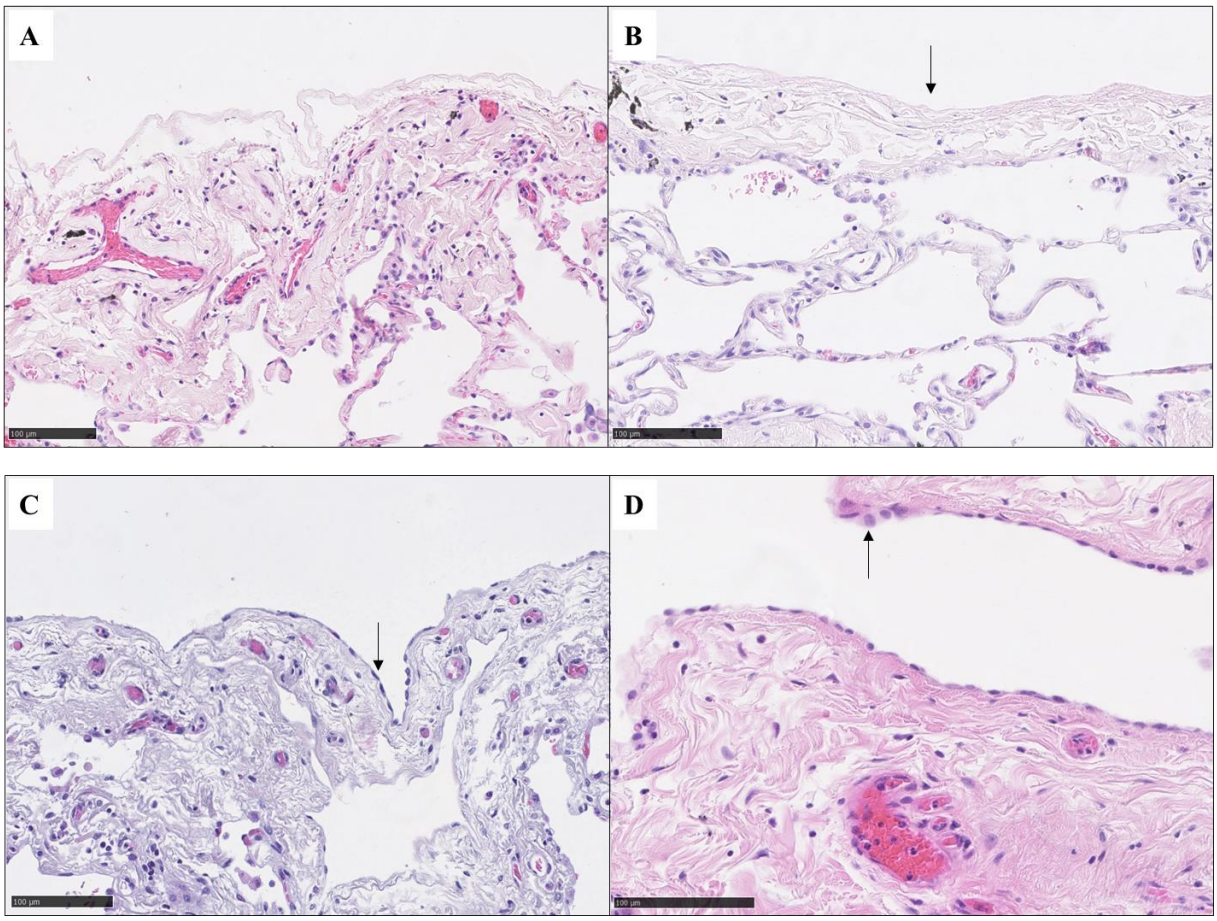

Figure 3.4 Histological validation of distal lung samples acquired from lung resection surgery. Representative H&E stains from four patient samples. A and B) The basal lamina is bare, with no visible attached VMCs. Arrow points to intact basal lamina. Representative images from samples P360 and P367 respectively. C) Flat VMCs with small, thin nuclei are sparsely present in lung undulations of sample P363. Arrow points to VMCs in lung undulation. D) Cuboidal VMCs with larger, circular nuclei are tethered to the basal lamina and form a segment of continuous mesothelium on sample P364. Arrow points to continuous layer of VMCs attached to the basal lamina.

Interestingly, sample P364 contained the largest number of VMCs compared to the other 5 lung resection samples assessed histologically. Sample P364 was from an 83-year old female, with no smoking history who underwent lobectomy for lepidic adenocarcinoma. A macroscopic histological view of the visceral pleura of sample P364 showed heterogeneity in VMC presence and distribution (Figure 3.5A). This ranged from no VMCs to small, localised reactive patches of round, proliferative VMCs with large nuclei (Figure 3.5C and Figure 3.5D).

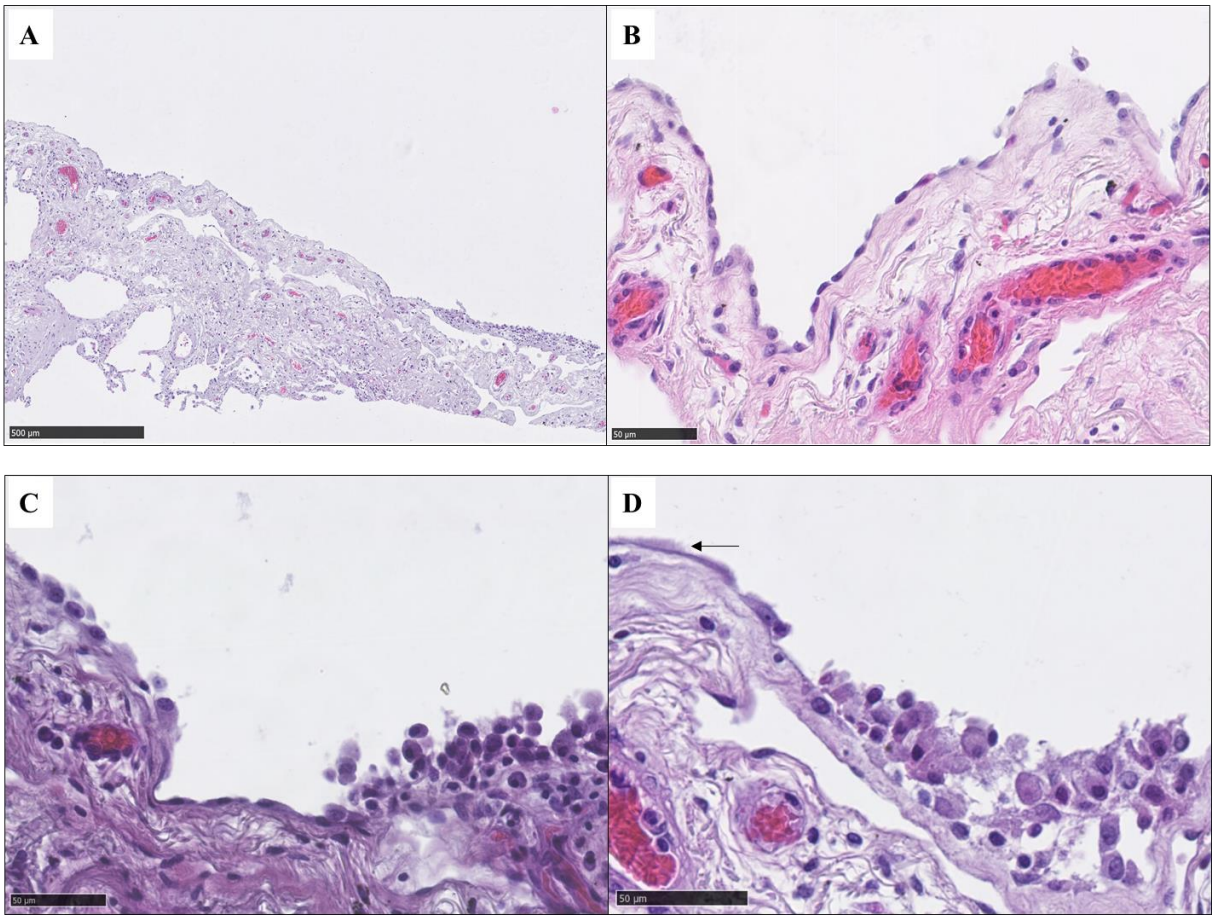

Figure 3.5 Heterogeneity of visceral mesothelial cells in lung resection sample P364. A) Macroscopic view revealed heterogeneity in VMC numbers across sample P364. B) A segment of continuous, simple VMCs. C and D) Locally reactive patches of cells containing VMCs and immune cells. Arrow points to abundant vertical microvilli visible on the surface of a VMC in the H&E section. Multiple blocks were assessed and were found to contain locally reactive patches of VMCs (n=3).

Due to the large number of VMCs in sample P364, this sample was used to investigate VMC expression of mesothelial markers. Sections of normal pleura were outsourced to a clinical diagnostics laboratory for staining with commonly used mesothelial markers CK5, MSLN and WT1 (7,16). All staining was conducted in parallel to a positive control for comparison (Figure 3.6).

VMCs were found to strongly express CK5 (Figure 3.6A). MSLN was strongly expressed by surface VMCs but was also expressed by some underlying alveolar epithelial cells (Figure 3.6C). In sample P364, alveolar epithelial cells were located at approximately 200 – 300 µm under the visceral mesothelium (Figure 3.6C). This demonstrates the lack of specificity of MSLN in differentiating normal VMCs from neighbouring cell types. Assessment of WT1 showed nuclear staining of VMCs although not all VMCs appeared to uniformly express this marker (Figure 3.6E).

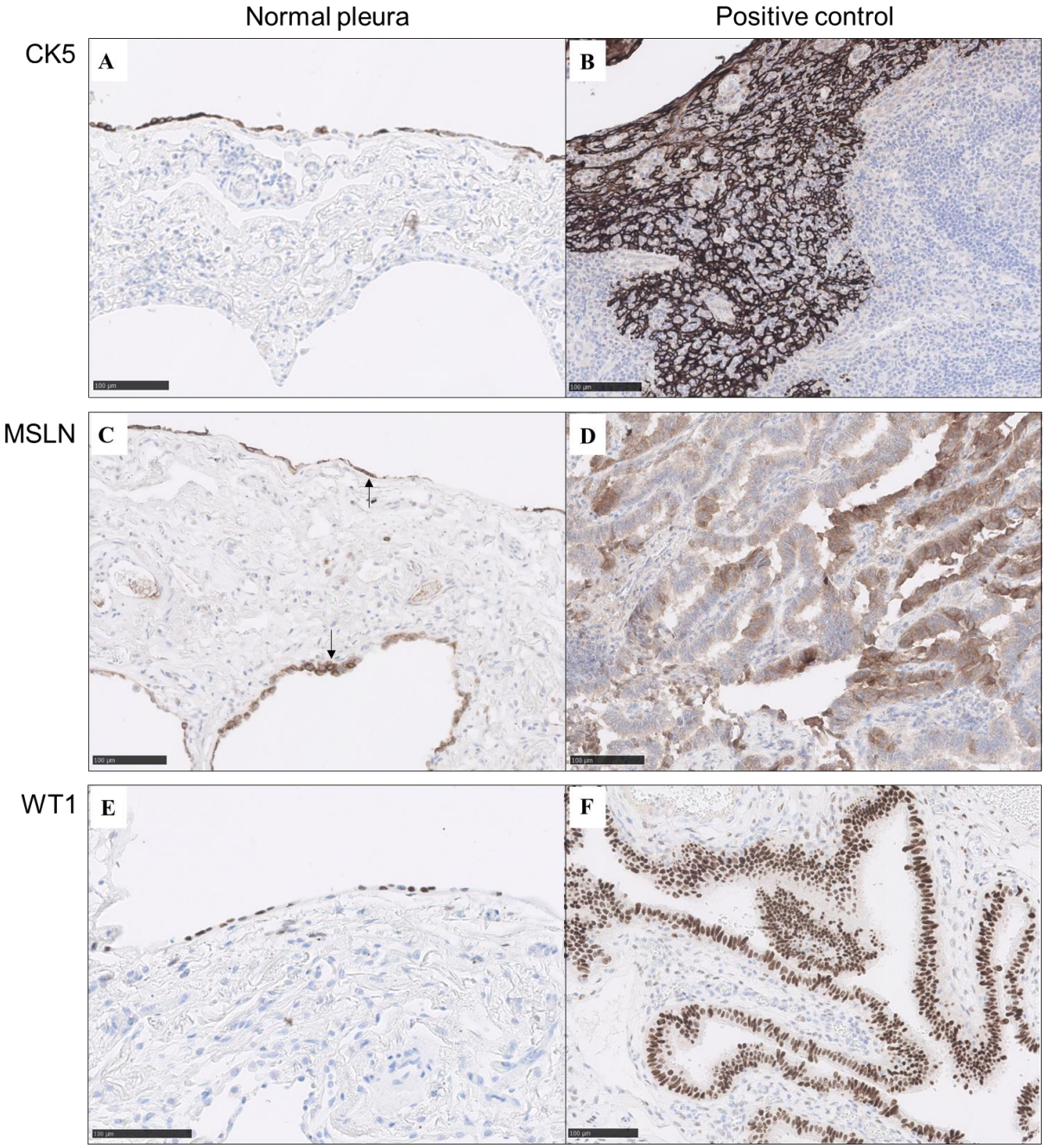

Figure 3.6 Expression of mesothelial markers in normal pleura. Representative IHC images of CK5, Mesothelin (MSLN) and WT1 in normal pleural sections from patient sample P364 are shown. A and B) CK5 expression in normal pleura and positive control tissue. C and D) MSLN expression in normal pleura and positive control tissue. Upward facing arrow points to VMCs and downward facing arrow points to alveolar epithelial cells. E and F) WT1 expression in normal pleura and positive control tissue.

Sections of visceral pleura from sample P364 were stained by immunofluorescence for CK5 and calretinin (Figure 3.7). VMCs on the pleural surface strongly expressed both markers, with staining observed in some cells of the underlying lung parenchyma (Figure 3.7). Notably, CK5 expression was seen in both normal and reactive VMCs (Figure 3.7B).

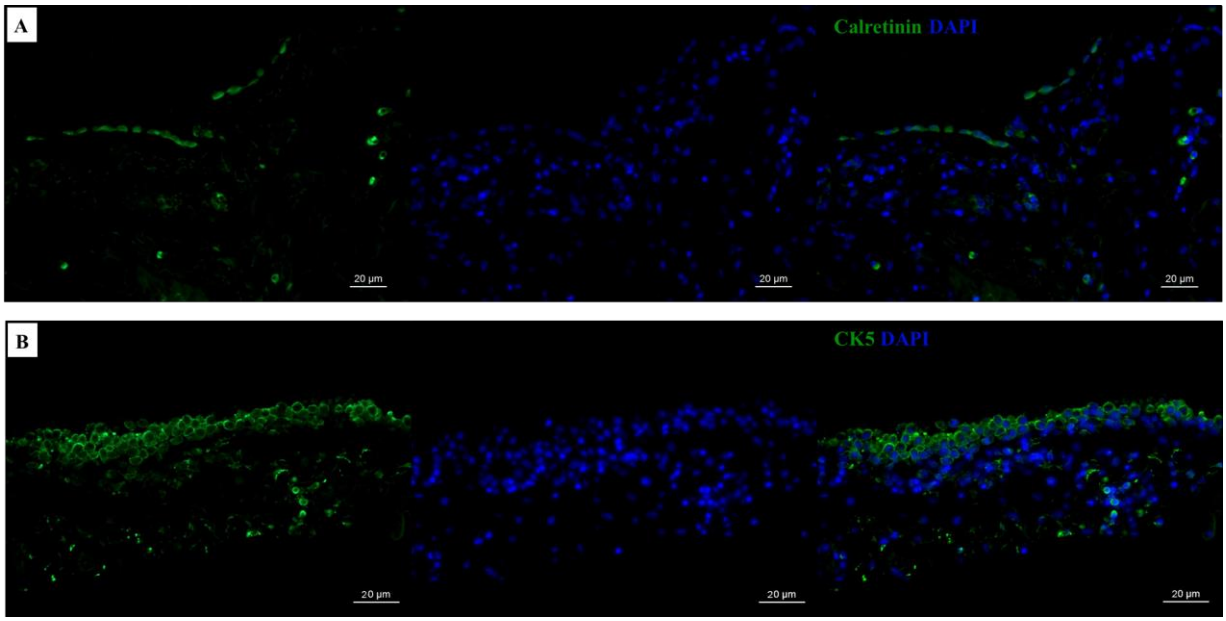

Figure 3.7 Expression of mesothelial markers in visceral pleura of lung resection sample. A) Immunofluorescence image of calretinin expression in normal visceral pleura. B) Immunofluorescence image of CK5 expression in locally reactive visceral mesothelial cell patch. Representative images are shown of immunofluorescence staining from sample P364.

In summary, this staining approach confirmed the presence of VMCs which expressed known mesothelial markers and thus confirmed that lung resection samples acquired from surgery are a useful source of VMCs for research purposes.

3.3.3 Assessment of visceral mesothelial cell spatial distribution in homeostasis

As the histology of visceral pleura only showed sparse continuous mesothelium, to determine if this was a consistent feature of human visceral mesothelium, the continuity of VMCs was examined by whole-mount confocal imaging.

Initially, assessment of whole-mount distal lung was performed using DAPI stain. The presence of known lung structures such as the aerated alveolar space, were used to determine that distal lung tissue remained intact (Figure 3.8).

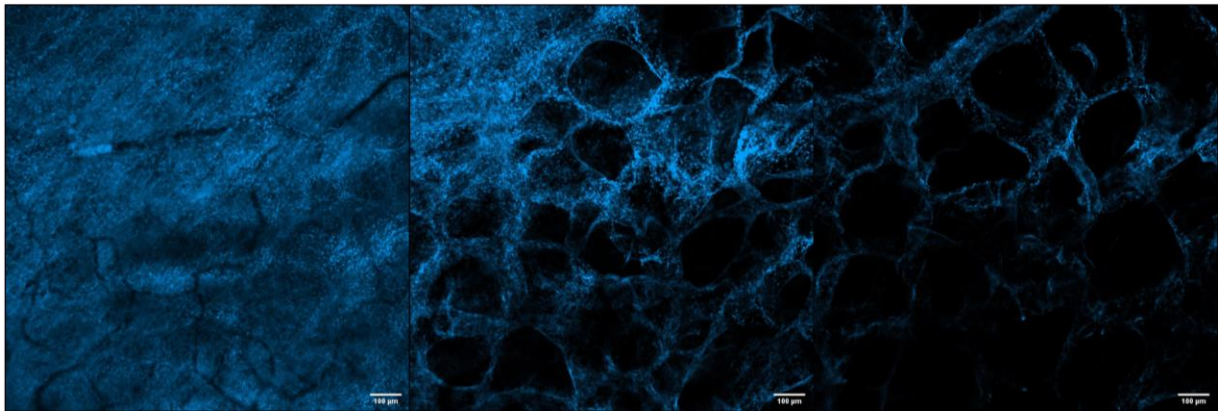

Figure 3.8 Alveoli in sub-pleural space imaged by whole-mount confocal microscopy of human distal lung acquired from lung resection surgery. Aerated space beneath the pleural surface is easily discernible.

Visualisation of the dense pleural ECM of the sub-pleural connective tissue was possible in part due to the auto-fluorescent nature of fibrous and collagenous bundles (Figure 3.9A). Podoplanin was assessed as a marker of mesothelial cells but in sample P362 podoplanin only labelled cells in the alveolar space (Figure 3.9A) and endothelial cells lining lymphatic vessels (data not shown). In addition, large vessels lined with αSMA expressing cells were visualised in the sub-pleural connective tissue (Figure 3.9B).

A

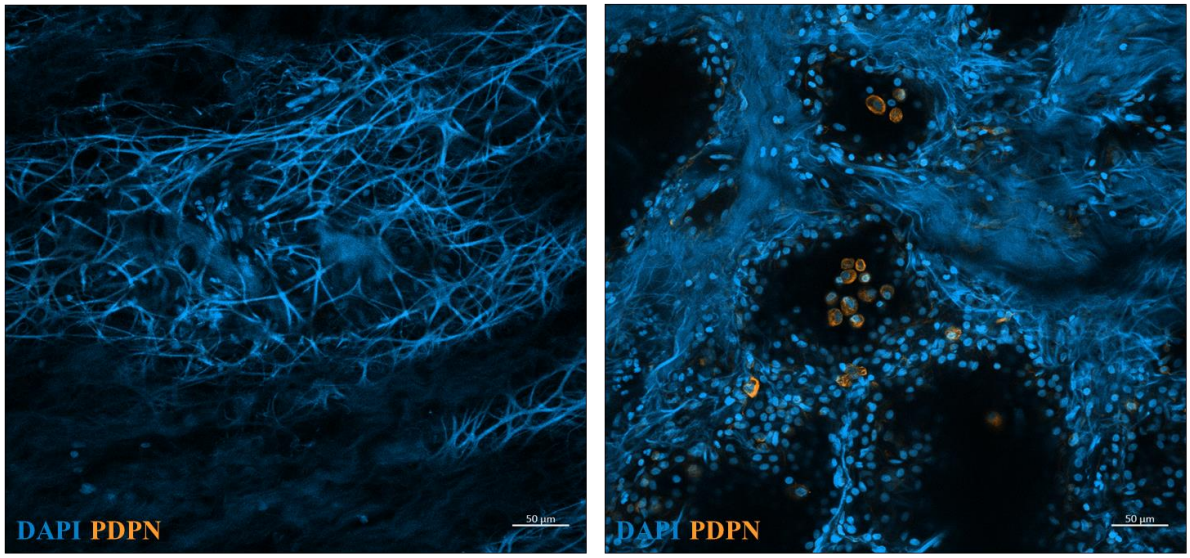

B

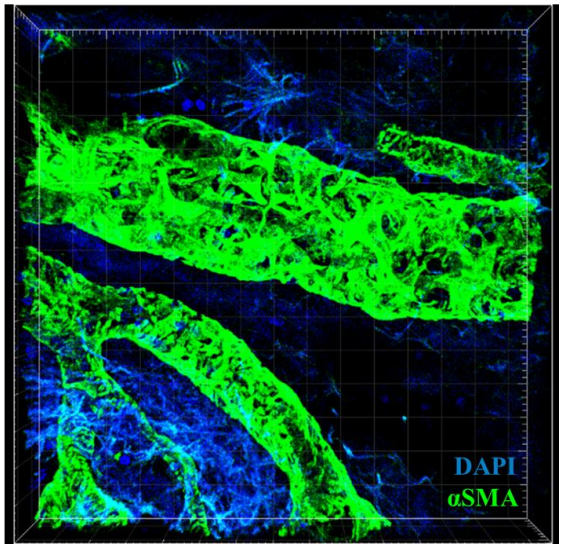

Figure 3.9 Whole-mount confocal imaging of distal lung. A) Immunofluorescence images of DAPI and podoplanin (PDPN) expression in whole-mount distal lung from sample P362. A dense meshwork of auto-fluorescent fibres was visible on the lung surface. Cells in the alveolar space expressed PDPN. B) Immunofluorescent staining showed that αSMA-expressing cells lined the vessels in sub-pleural connective tissue. 3D z-stack reconstruction was conducted with Imaris software.

To assess the distribution of surface mesothelial cells and determine if they form a continuous mesothelium, CK5 expression was investigated in whole-mount distal lung samples (Figure 3.10). Visualisation of CK5 expression by whole-mount confocal imaging confirmed the presence of VMC patches on the lung surface (Figure 3.10A). Continued use of the same sample revealed a declining number of detectable VMCs on the lung surface at each imaging attempt (n=3), indicating post-fixation VMC detachment (Figure 3.10B).

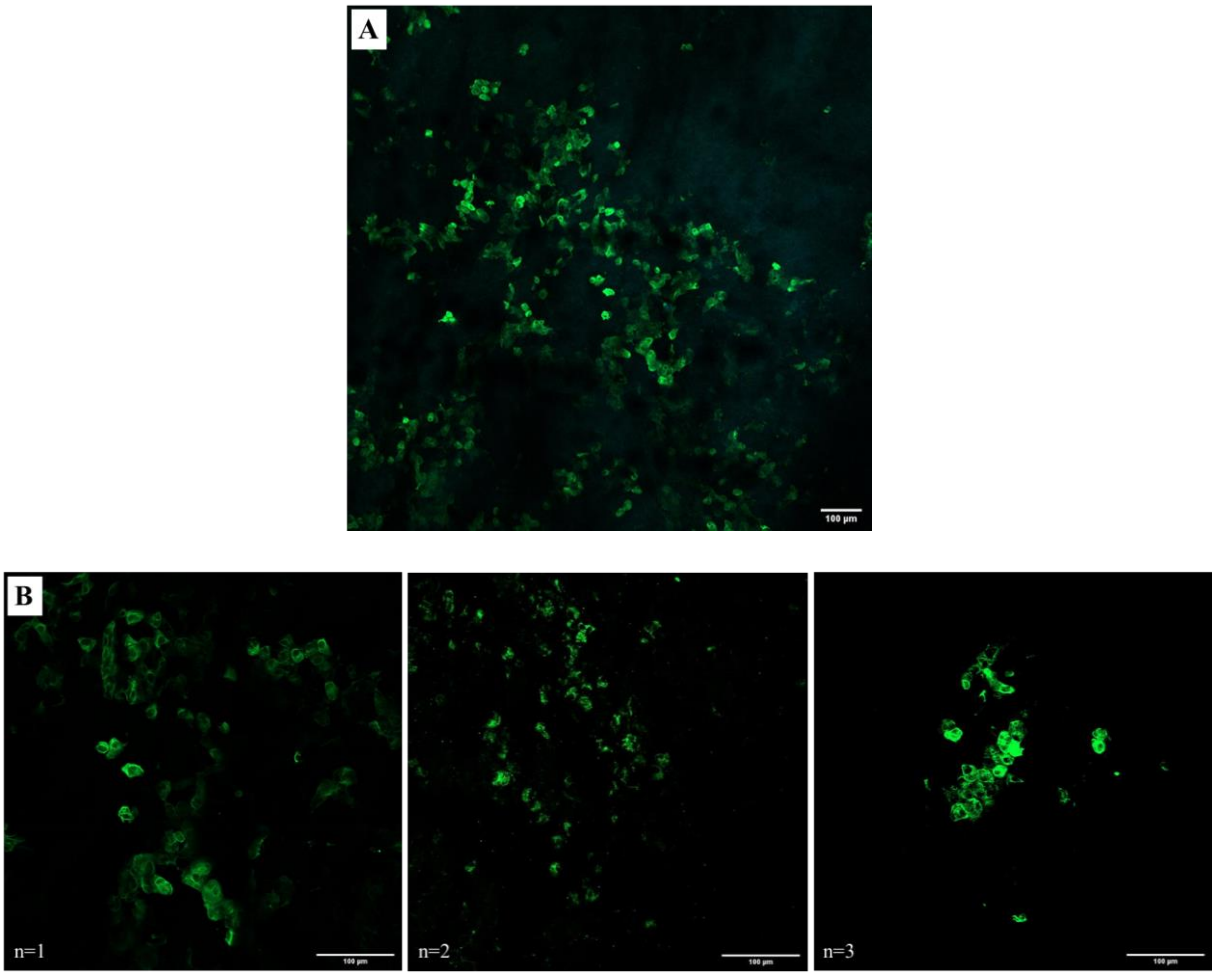

Figure 3.10 Visualisation of CK5-expressing visceral mesothelial cells by confocal imaging of whole-mount distal lung. A) Immunofluorescence revealed sparse CK5-expressing visceral mesothelial cells on the surface of lung resection sample P362. B) Panel of images represents consecutive immunofluorescence experiments using lung resection sample P362. This showed that visceral mesothelial cells detach from the lung surface with continuous sample use, despite tissue fixation (n=3).

There is currently no established pleural mesothelial marker. Thus, immunofluorescence imaging of VMCs by single markers has intrinsic limitations, as a subset of the mesothelial cell population may not be detected. Therefore, to complement the histology and whole-mount confocal imaging approaches and to investigate pleural morphology, I used SEM imaging as an additional tool to investigate VMC distribution.

To achieve efficient imaging of visceral mesothelium by SEM, the optimal fixative for human distal lung tissue was first investigated. Three common tissue fixatives were compared; 10% neutral-buffered formalin (NBF), 4% paraformaldehyde and a mixture of 1.5% glutaraldehyde with 2% paraformaldehyde in 0.1M cacodylate buffer. Comparison of imaging quality with these three fixation methods indicated that NBF and glutaraldehyde had similar capability in preserving morphology of human visceral pleura. It is notable that paraformaldehyde was the

least effective of the three fixation approaches, as surface tension cracked the basal lamina after critical-point drying and there was discernible artefact (n=2) (Figure 3.11). In contrast, fixation with NBF allowed visualisation of an intact basal lamina and a mesothelial cell population which retained surface characteristics and distinctive microstructures (Figure 3.11). Based on this imaging evaluation, NBF was selected as the fixative for subsequent SEM imaging (Figure 3.11).

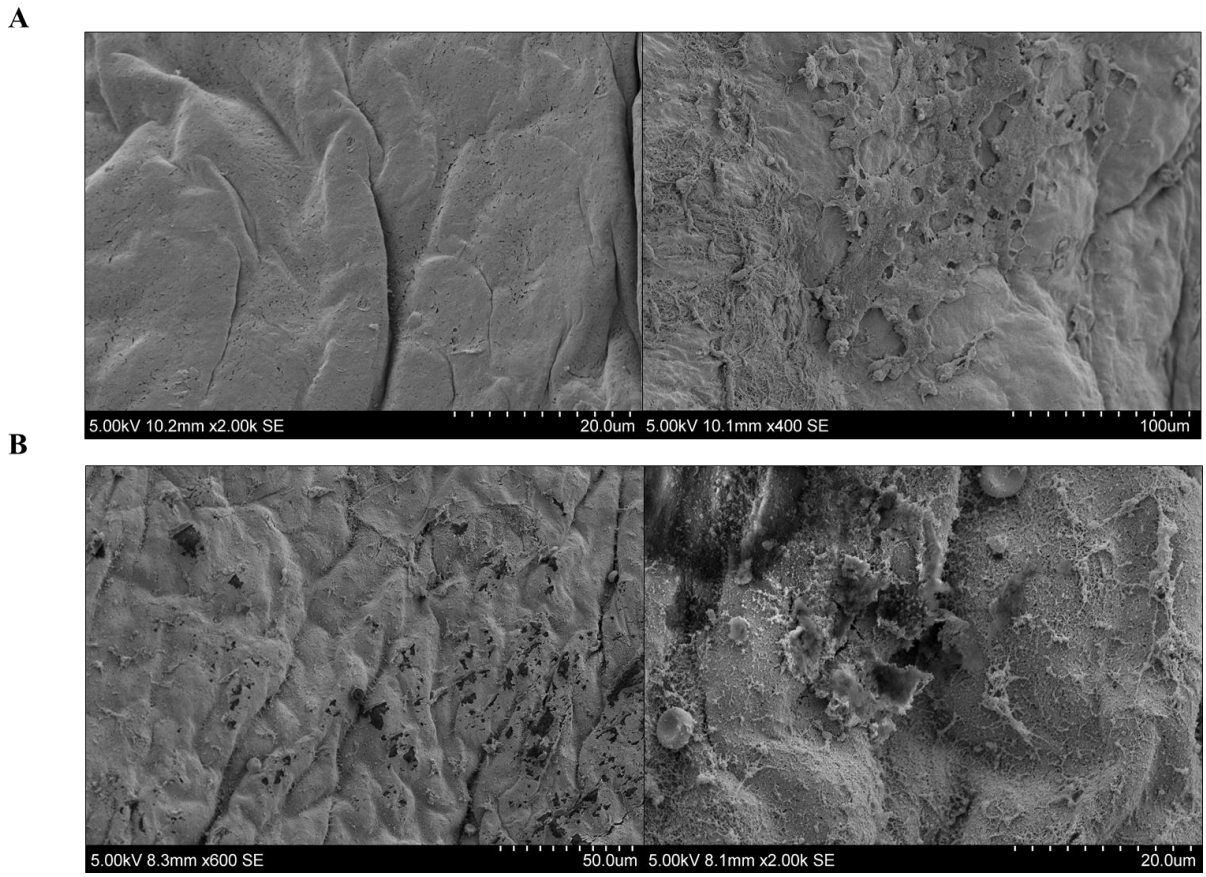

Figure 3.11 SEM imaging with two fixation methods. A) Representative SEM images of visceral pleura fixed in 10% neutral-buffered formalin which allowed clear visualisation of intact basal lamina and discernible patch of VMCs. B) Representative SEM images of visceral pleura fixed in 4% paraformaldehyde. Surface degradation and artefact are visible in both images. SEM imaging findings from lung resection sample P371 are shown in both panels.

SEM imaging of visceral mesothelium on lung resection samples was technically challenging due to partial or complete denudation of the mesothelium and in some cases the dissolution or stripping of the basal lamina (4/6). One sample completely lacked a basal lamina revealing the dense network of ECM components and immune cells in the sub-mesothelial tissue (Figure 3.12A). The basal lamina remained intact, but no mesothelial cells were detected on a further 3 lung resection samples (Figure 3.12B).

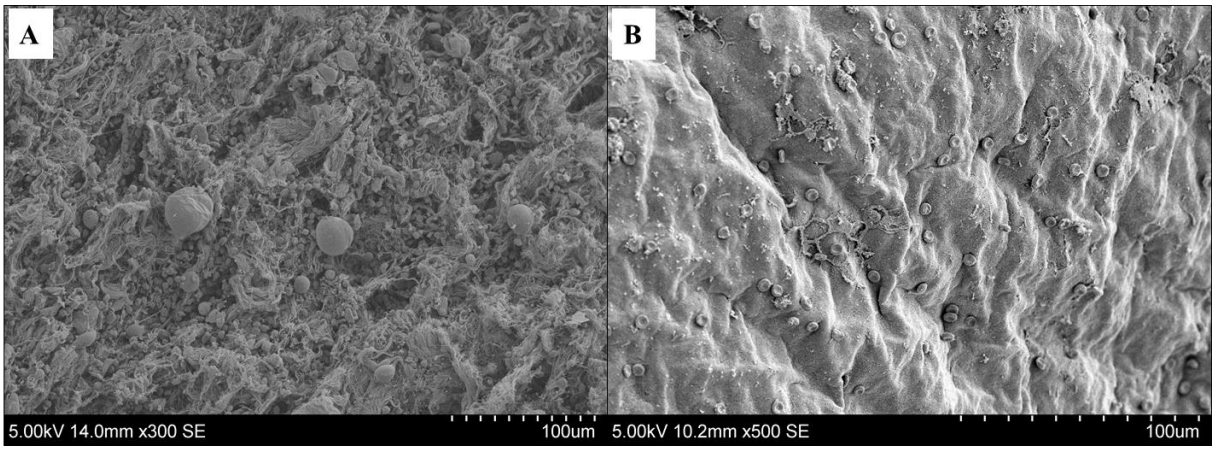

Figure 3.12 SEM imaging of lung resection samples demonstrates lack of intact visceral mesothelium. A) The dense immune cell population and ECM of the sub-pleural space is visible due to the degradation of the basal lamina on sample P362. B) Representative image of the basal lamina on distal lung sections. The basal lamina is coated with sparse red blood cells on sample P369.

Patches of VMCs were identified on 2/6 lung resection tissues assessed by SEM (Figure 3.13). On sample P364, a total of four VMC patches consisting of 18 – 133 cells, were identified (Figure 3.13A-D). In one of the VMC patches, part of the apical visceral mesothelium appeared loosely tethered to the underlying basal lamina (Figure 3.13A). VMCs on sample P364 were round and plump with sparse microvilli uniformly distributed on their surface (Figure 3.13A-D).

Mesothelial cells on sample P370 contained characteristic microvilli which completely covered their luminal surface. The VMC patches seen in samples P364 and P370 were morphologically different. Whereas VMCs on sample P364 were round with sparse microvilli, the one patch identified on sample P370 contained flat VMCs with bushy microvilli. In addition, it was not possible to discern the shape of individual cells or their cell-to-cell boundaries on sample P370, due to the density of microvilli. Interestingly, there was no continuous, intact visceral mesothelium present on any of the lung resection samples assessed (n=6).

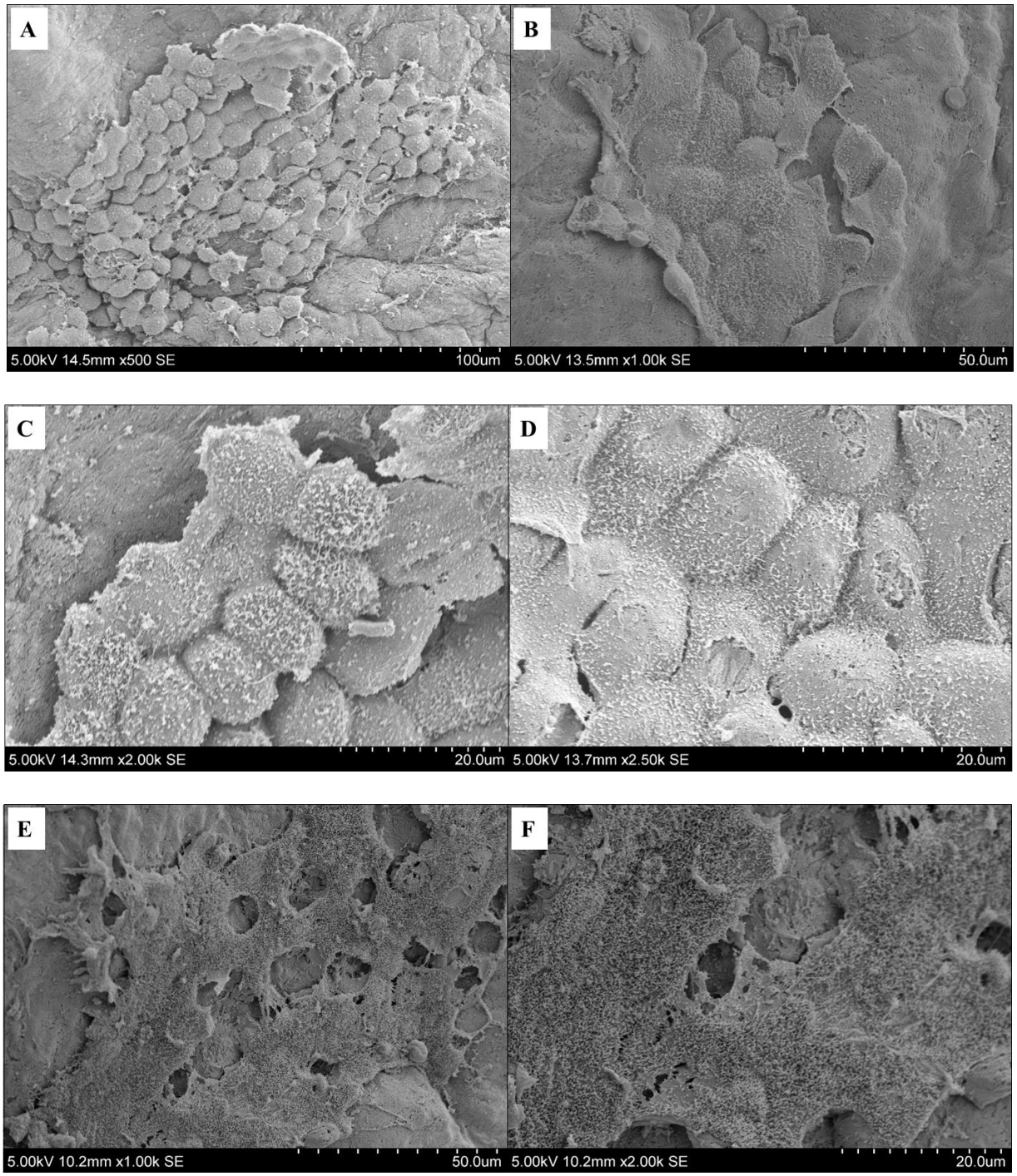

Figure 3.13 Patches of visceral mesothelial cells on lung resections samples. SEM imaging of visceral pleura from sample P364 (A-D) and P370 (E-F). A) A large cluster of plump VMCs attached to an undulating segment of lung. B) A small cluster of round VMCs with abundant microvilli, tethered to the basal lamina. C) Patch of VMCs shown in Panel A, under higher magnification shows loose attachment to the underlying basal lamina. D) VMCs are uniformly covered in microvilli and have visible individual cell boundaries. E) Patch of VMCs with bushy microvilli. F) Individual cell boundaries are not visible due to complete cell coverage with dense microvilli.

Next, I aimed to determine if there was intra-sample variation in VMC size, using quantification of the three VMC patches detected on sample P364 (Figure 3.13A-D). Due to the limitation of dense microvilli, quantification of VMC size was not possible for patches of VMCs detected

on sample P370 (Figure 3.13E-F). VMCs on lung resection sample P364 were found to measure on average 110 μm^2 (±9.13) in cell surface area and 12.81 μm (±0.47) in cell length (longest axis) (Figure 3.14). Statistical analysis of mesothelial cell measurements suggested that there was no significant heterogeneity in VMC size across sample P364 (Figure 3.14).

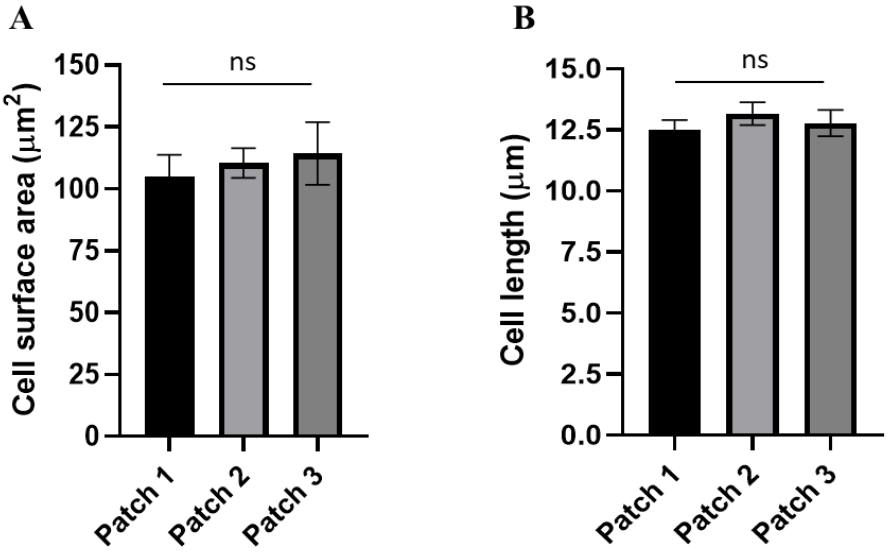

Figure 3.14 Quantification of visceral mesothelial cell size on lung resection sample. ImageJ was used for quantification of SEM images from three separate visceral mesothelial cell patches on the lung surface of P364. Ten mesothelial cells from each cell patch were quantified. No significant heterogeneity in mesothelial cell size was detected across cell patches. A) Quantification of individual mesothelial cell surface area (μm^2) was determined by ImageJ analysis (n=30). The surface area did not differ significantly across mesothelial cell patches (one-way ANOVA, p=0.26). B) Quantification of individual mesothelial cell length (μm) was determined by ImageJ analysis (n=30). Cell length did not differ significantly across mesothelial cell patches (one-way ANOVA, p=0.068). Error bars depict standard error of the mean (SEM).

Analysis of visceral pleura by histology, SEM and confocal imaging, did not reveal a continuous mesothelial cell layer in lung resection samples acquired from surgery. Subsequently, I sought to determine if this lack of continuous visceral mesothelium was due to surgical tissue limitations and processing artefact or a characteristic of active human mesothelium in homeostasis.

3.3.4 Comparison of visceral mesothelial cells in post-mortem and lung resection samples

To further explore visceral pleura in homeostasis and to assess if the visceral mesothelium consists of a continuous monolayer in homeostasis, histological assessment and SEM imaging of post-mortem pleural tissues were employed. Histology of 8 post-mortem visceral pleura samples demonstrated that post-mortem tissue with up to 5-day ischemic time maintained an intact structure when assessed histologically (Figure 3.15). The histology of post-mortem tissue

(Figure 3.15) was similar to the tissue architecture of lung resection samples (Figure 3.5). There was some variability in the presence of VMCs with sections completely devoid of VMCs (7/8) and others entirely encased by a single mesothelial cell layer (1/8) (Figure 3.15).

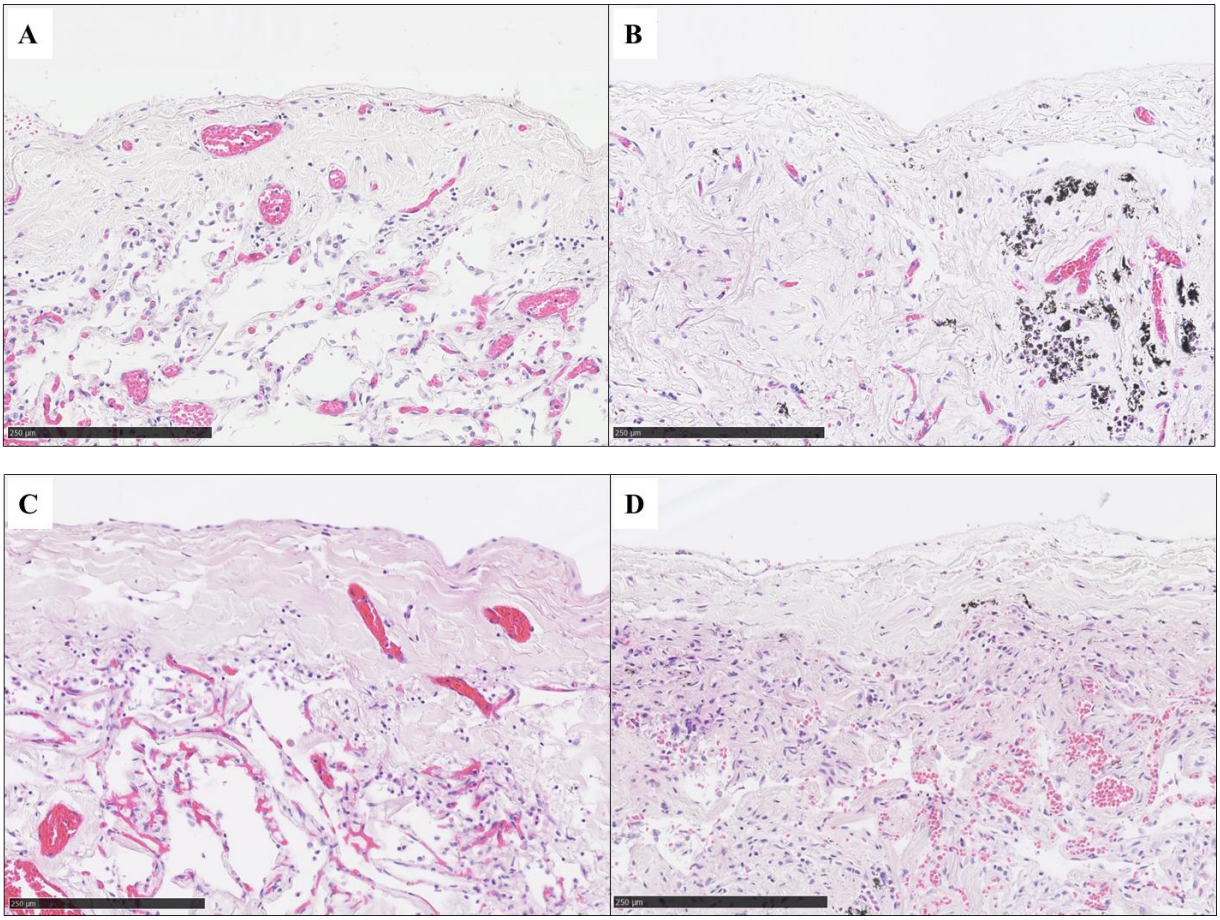

Figure 3.15 Histology of visceral pleural acquired from post-mortem. Representative H&E stains of four patient samples. A and B) No mesothelial cells were found attached to the basal lamina of samples PEA126 and PEA124 respectively. C) Mesothelial cells form a continuous layer of flat cells with thin nuclei on the surface of sample PEA172. D) Small, sparse cells are present on the visceral pleura of sample PEA139, which are likely immune cells.

Despite the presence of the antifungal Amphotericin B in transport medium, fungal contamination of post-mortem samples significantly hindered the visualisation of VMCs by SEM imaging (Figure 3.16). Imaging of three post-mortem samples revealed spores covering the lung which obscured the surface structures (Figure 3.16). Furthermore, one post-mortem sample showed signs of malignancy and one uninfected sample had an intact basal lamina but no VMCs were detected by SEM imaging.

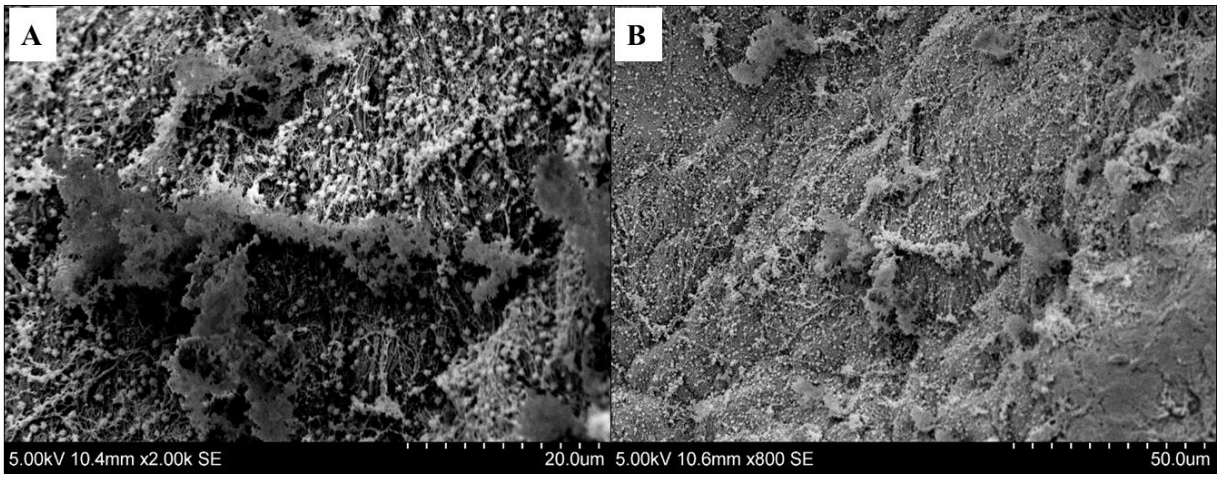

Figure 3.16 Surface contamination of post-mortem lung tissue. Representative SEM images of post-mortem visceral pleura contamination (sample PEA213). A) Dense clumps of spores are identified on the lung surface. B) Individual spores can be seen diffusely on the lung surface.

Of the six post-mortem tissues imaged by SEM, only one post-mortem sample showed an intact, continuous visceral mesothelium which visibly encased the lung (Figure 3.17). Sample PEA172 was from a male, ex-smoker, diagnosed with head and neck cancer and multiple metastases. In this sample, flat VMCs formed an uninterrupted cellular sheet which covered the basal lamina of the lung. Notably, these VMCs lacked surface protrusions and microvilli, in contrast to the VMC appearance of lung resection samples (Figure 3.13).

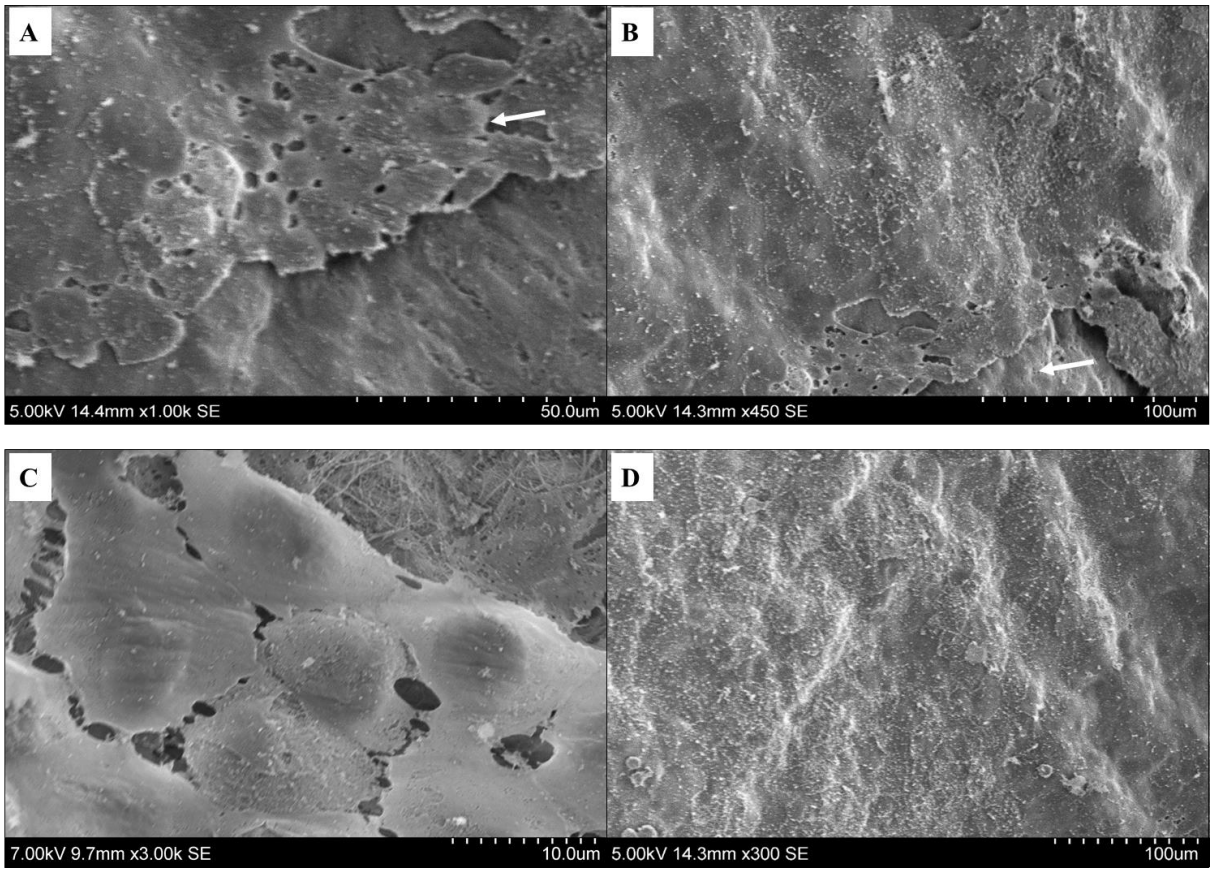

Figure 3.17 Intact visceral mesothelium of post-mortem sample PEA172. A) VMCs are flat and uniform in shape. Area of denudation reveals the edge of visceral mesothelium. Arrow points to single mesothelial cell. B) Cell-to-cell boundaries are visible in the visceral mesothelium. Arrow points to exposed basal lamina. C) An area with partial denudation and minimal degradation of the basal lamina. VMCs have a stretched cytoplasm, with prominent, ovoid nuclei. D) Extensive covering of lung with intact visceral mesothelium.

To investigate the consistency of VMC size in sample PEA172, three distinct cell patches were quantified and compared. Statistical analysis indicated that there was significant intra-sample variation between VMC patches for both cell size metrics used (Figure 3.18). Notably, due to the clear visualisation of mesothelium across sample PEA172, the VMC patches selected were spatially further apart than the patches sampled for P364 (Figure 3.14).

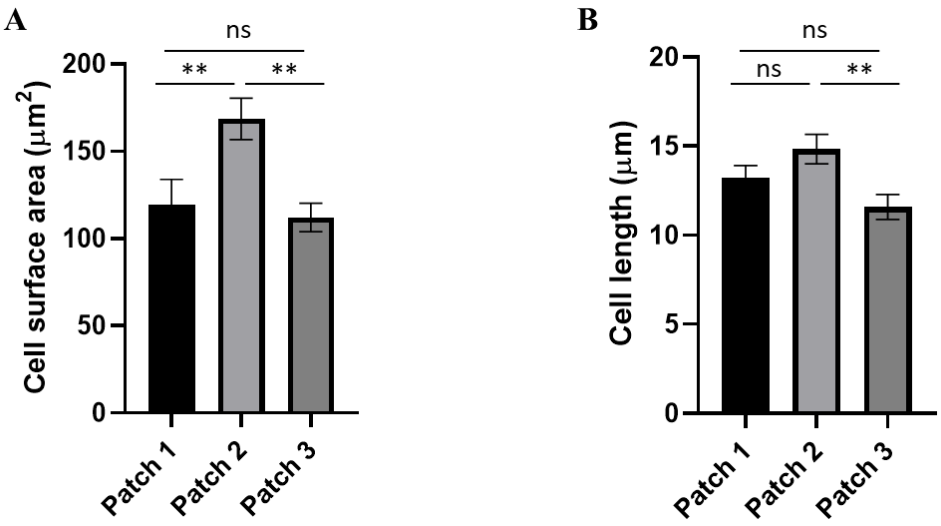

Figure 3.18 Quantification of visceral mesothelial cell size on post-mortem sample. ImageJ was used for quantification of SEM images from three separate visceral mesothelial cell patches on the lung surface of PEA172. Ten mesothelial cells from each cell patch were quantified. Significant heterogeneity in both cell size metrics was detected across cell patches. A) Quantification of individual mesothelial cell surface area (μm^2) was determined by ImageJ analysis (n=30). Cell surface area differed significantly between cell patches (one-way ANOVA, **p=0.002). B) Quantification of individual mesothelial cell length (μm) was determined by ImageJ analysis (n=30). Cell length differed significantly between cell patches (one-way ANOVA, **p=0.005). Error bars depict SEM.

As VMC patches were detected on both fresh lung resection tissues and post-mortem samples, inter-sample variation of VMC size was assessed next (n=2). Quantification of the cell surface area and cell length of VMC patches on sample P364 demonstrated an average cell surface area of 110 μm^2 (±9.13) and cell length of 12.81 μm (±0.47), whilst VMC patches on sample PEA172 exhibited an average surface area of 127.9 μm^2 (±7.23) and cell length of 12.82 μm (±0.48). Comparison of cell measurements from samples P364 and PEA172 did not suggest significant heterogeneity in VMC size between the two samples (Figure 3.19).

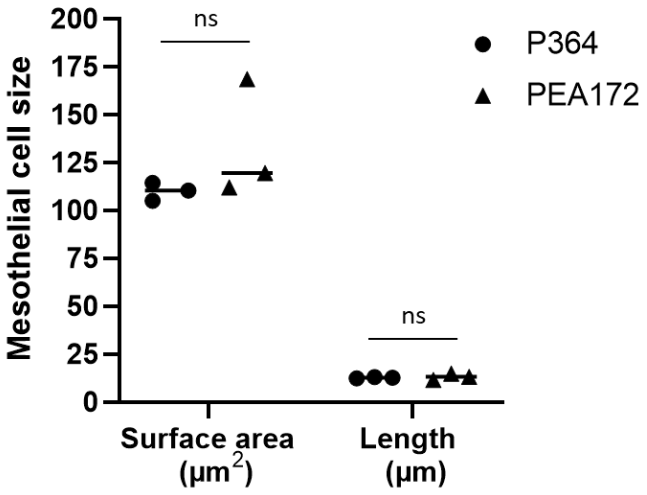

Figure 3.19 Visceral mesothelial cells have similar size in fresh and post-mortem visceral pleura. Statistical analysis of cell surface area and cell length measurements showed no difference between the two samples assessed (t-test, p=0.26 and p=0.69 respectively).

Macroscopic imaging of sample PEA172 showed intact visceral mesothelium on the entire visceral pleura, which spanned an area of 5.63 cm^2 (±0.02).

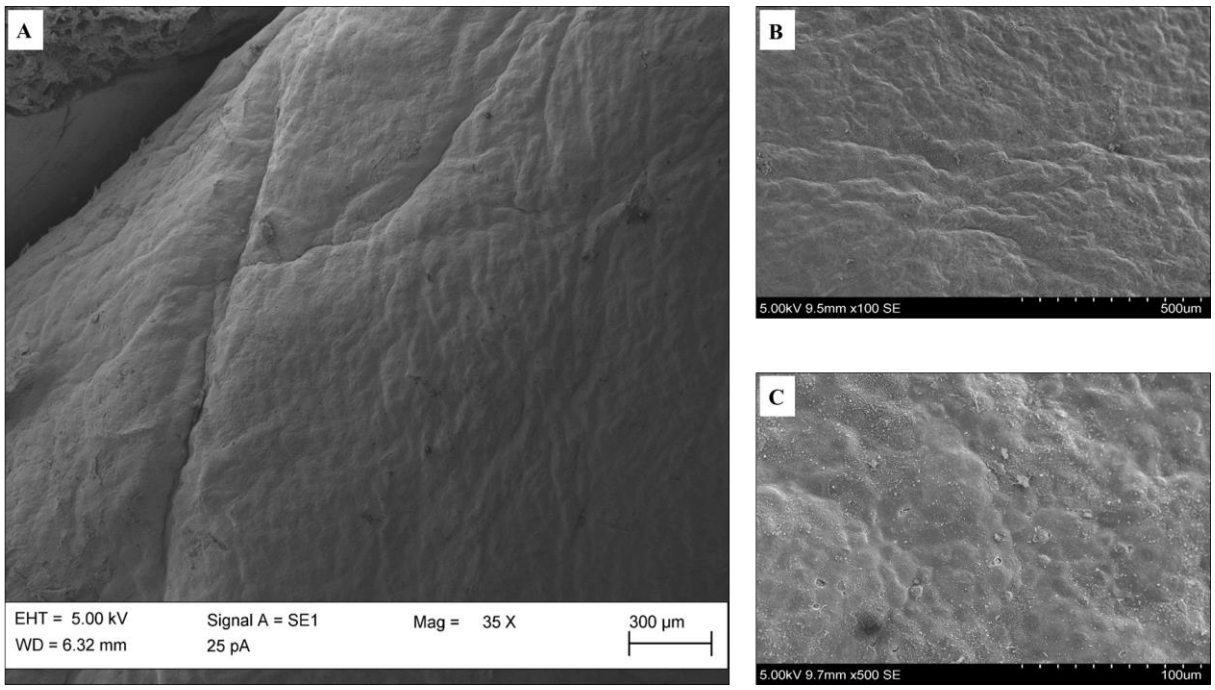

Figure 3.20 Macroscopic SEM imaging of intact visceral mesothelium of post-mortem visceral pleura. Representative SEM images from post-mortem sample PEA172 are shown. A) Macroscopic SEM image of visceral mesothelium spanning 5.63 cm^2. B) SEM image of section of continuous visceral mesothelium. Scale bar = 500 µm. C) Mesothelial cell barriers are faintly visible in SEM image of visceral mesothelium. Scale bar = 100 µm.

Sample PEA172 was notable for its intact continuous visceral mesothelium. The presence of VMCs on sample PEA172 was confirmed by histology and CK5 staining (Figure 3.21).

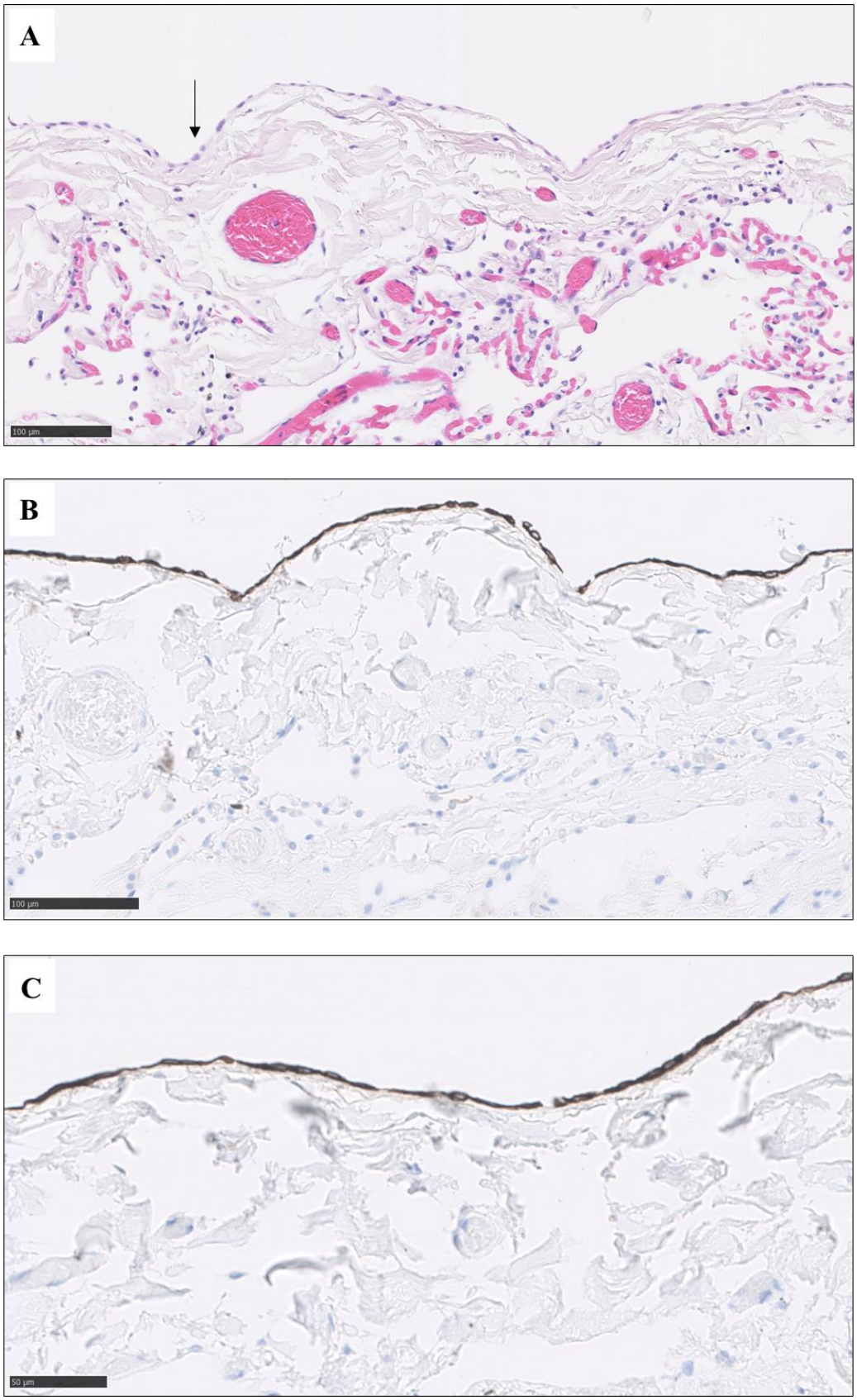

Figure 3.21 CK5 expression in intact visceral mesothelium of post-mortem sample PEA172. A) Representative H&E stain of sample PEA172. Arrow points to visceral mesothelial cells. B) Immunohistochemistry image of CK5-expressing visceral mesothelium. Scale bar = 100 µm. C) Immunohistochemistry image of CK5-expressing visceral mesothelium. Scale bar = 50 µm.

Matched parietal pleura from sample PEA172 showed shrunken histology, which could be attributed in part to the emaciated state of the patient at the time of death (Figure 3.22A). The patient's poor physical condition contributed to sample acquisition difficulty at post-mortem, as the parietal pleura was challenging to detach from the chest wall. The histological structure of the parietal pleura was not easy to ascertain (Figure 3.22A).

IHC analysis determined parietal mesothelial cells which expressed CK5, adjacent to adipose tissue (Figure 3.22B). Parietal mesothelial cells of sample PEA172 weakly expressed calretinin (Figure 3.22C) and were positive for BAP1 (Figure 3.22D).

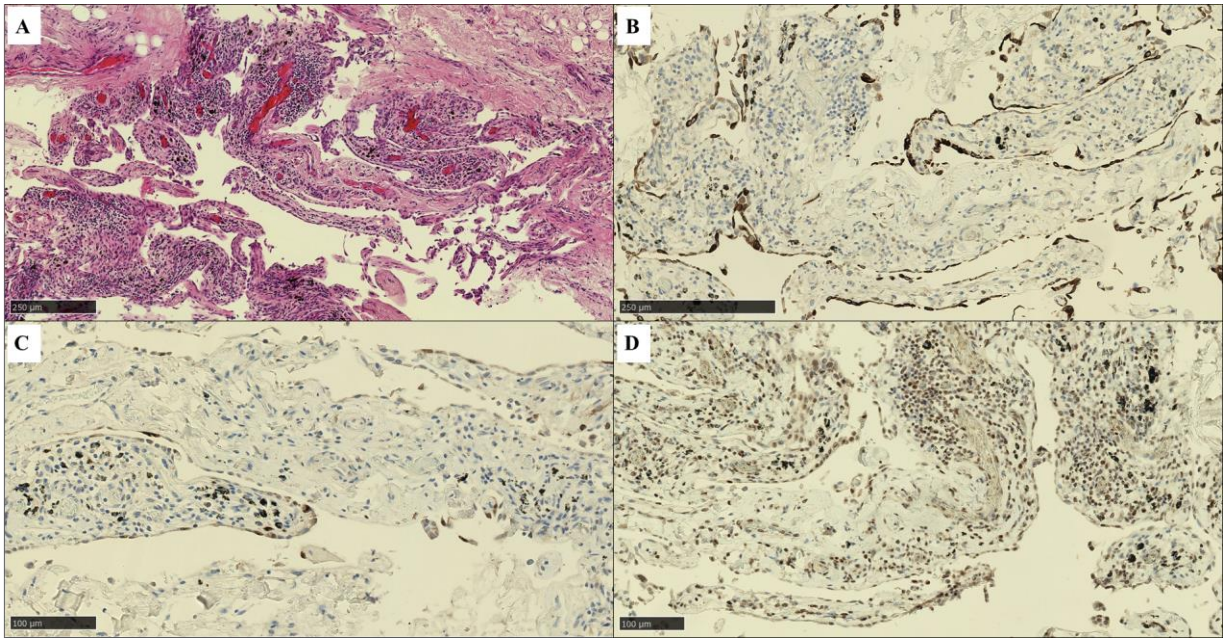

Figure 3.22 Expression of mesothelial markers in parietal pleura of sample PEA172. A) H&E stain of parietal pleura. B) CK5 IHC stain shows that parietal mesothelial cells strongly express CK5. C) IHC stain of calretinin expression in parietal pleura. D) IHC stain of BAP1 expression in parietal pleura.

3.3.5 Examination of cell viability in post-mortem pleural tissue

To determine the viability of cells from post-mortem tissue, flow cytometry was employed. Following digestion of visceral pleura, flow cytometry analysis of the heterogeneous cell population containing immune cells, VMCs and other cell types, showed that 92.3 and 95.4% of cells remained alive, when assessed with Zombie Red viability dye (Figure 3.23). The pleural tissue digested and assessed for cell viability by flow cytometry had an ischemic time of 2 and 5 days respectively.

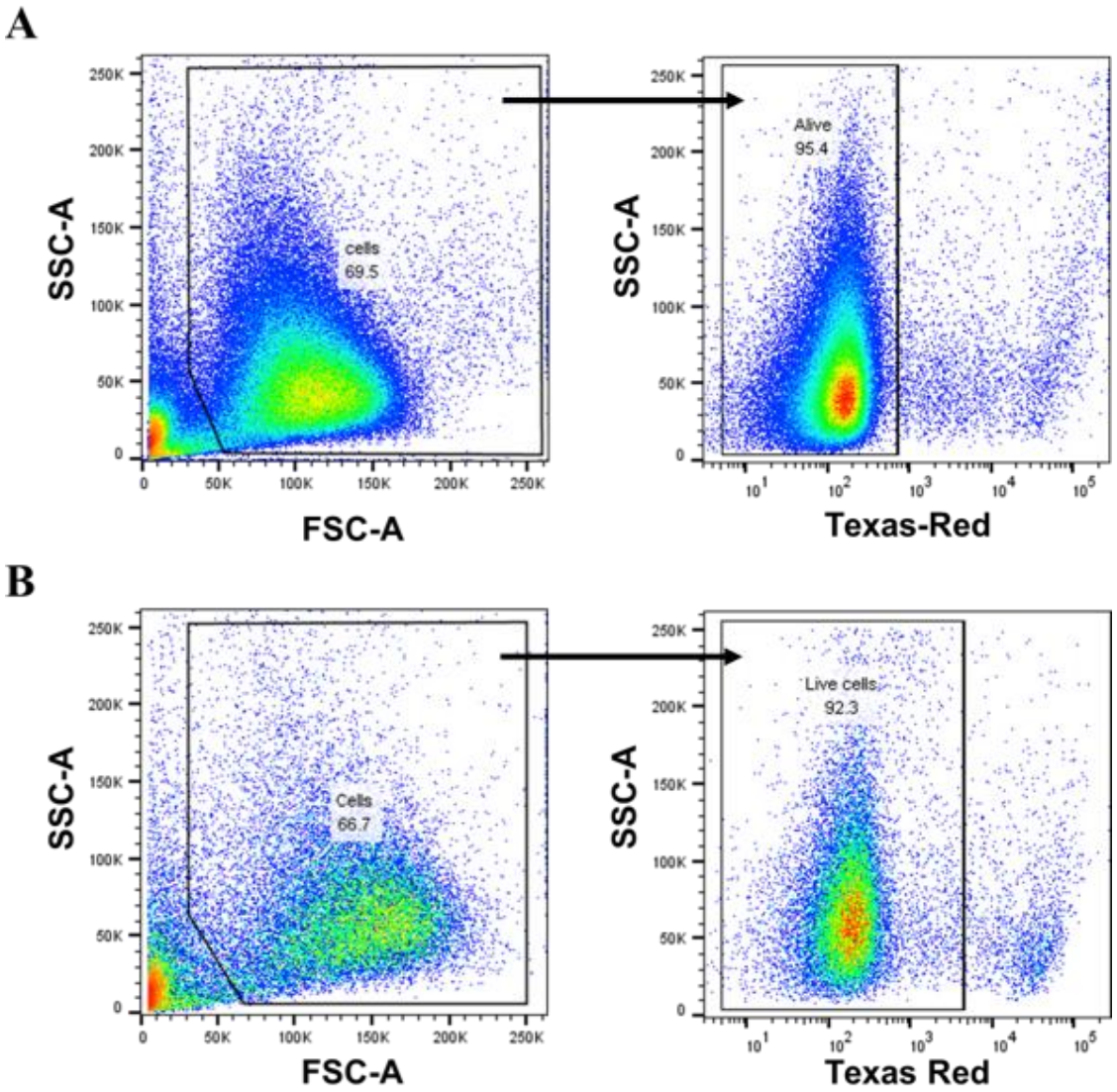

Figure 3.23 Flow cytometry plots demonstrate the cell viability of digested visceral pleura from post-mortem samples. A) There was 95.4% positive cell viability in digested visceral pleura of sample PEA213. B) 92.3% of the cell population was still alive in digested visceral pleura of sample PEA216. Zombie Red was used for viability analysis and Texas Red gates were drawn based on unstained control cells. Ischemic time was 5 days for PEA213 and 2 days for PEA216.

Since flow cytometric analysis of post-mortem tissue showed a viable cell population, I investigated the capacity of visceral pleural cells to grow in tissue culture conditions. Digested visceral pleura from PEA172, PEA213, PEA216 and a visceral pleural brushing from PEA224 were cultured with mixed success. PEA216 and PEA213 cell cultures succumbed to infection immediately. PEA172 and PEA224 cells attached to tissue culture dishes but colonies became contaminated with fungal growth after 1 – 3 days. Thus, it was not possible to culture isolated pleural cells from post-mortem lung samples (n=5).

Interestingly, further flow cytometric analysis revealed that 92.4% of the viable cell population in digested visceral pleura from post-mortem distal lung tissue, was composed of CD45-expressing immune cells (Figure 3.24). Confirmation of this finding was sought by SEM imaging of the lung surface in post-mortem samples.

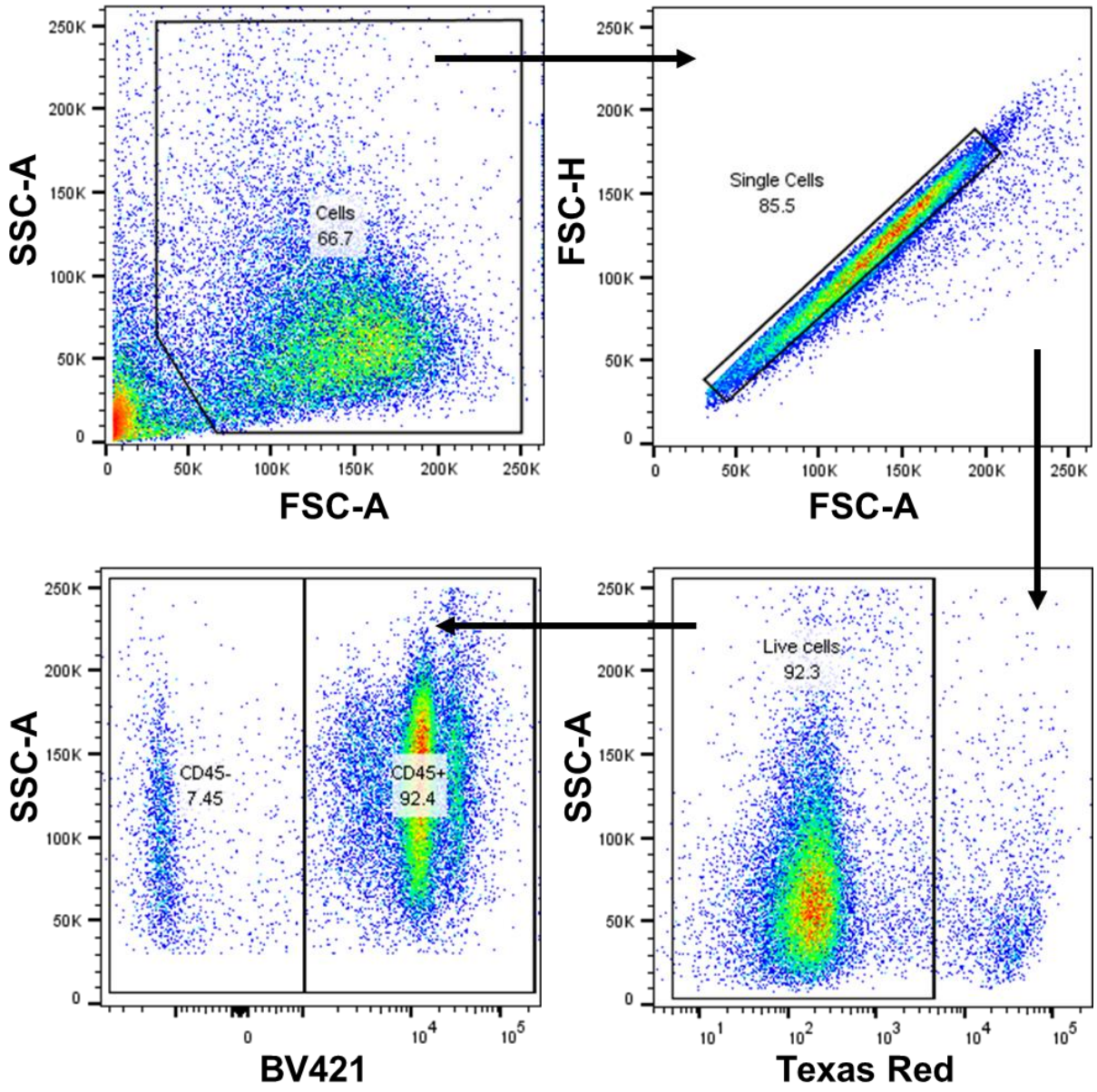

Figure 3.24 Flow cytometric analysis of digested visceral pleura from post-mortem tissue. Ischemic time of 2 days in patient sample PEA216. 92.3% of the single cell population was alive and 92.4% of this viable cell population consisted of CD45+ cells.

Large immune cell clusters containing red blood cells, which are discernible due to their characteristic morphology, were identified on the surface of post-mortem lung tissue (Figure 3.25). Interpretation of flow cytometric analysis of the cell population (Figure 3.24) and SEM

imaging of the lung surface (Figure 3.25), indicate a large number of viable and active immune cells after patient death.

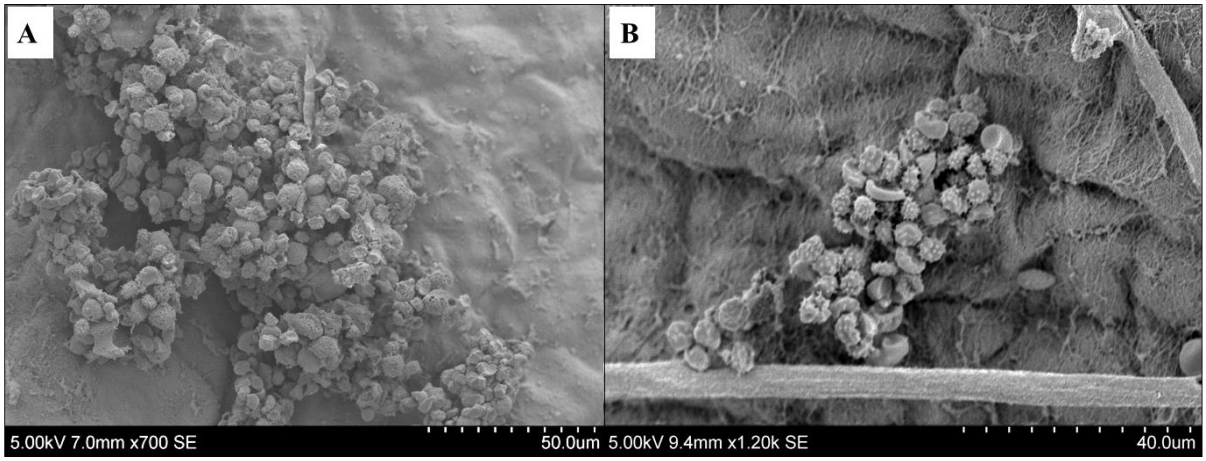

Figure 3.25 Activated immune cells form clusters on lung surface in post-mortem tissue. A) A large aggregation of cells, including immune cells, on the lung surface of PEA224. B) A cluster of immune cells and red blood cells appear to be attacking a surface object which could be fungal hyphae, on the lung surface of PEA216.

3.3.6 Identification of reactive mesothelium in post-mortem parietal pleura

One post-mortem sample revealed diffusely reactive parietal mesothelium. These cellular changes were not visible in CT scans prior to patient death. This case was a male, metastatic melanoma patient, with no known smoking history or asbestos exposure. The patient had lung metastases in the right lower and left upper lobes. At post-mortem it was evident that the parietal pleura had been infiltrated by the secondary tumour as there were multiple milky spots on the pleura observed by the pathologist. Histology and SEM imaging of parietal pleura revealed a continuous sheet of cells, with immune cells entangled in malignant cells of unknown origin (Figure 3.26).

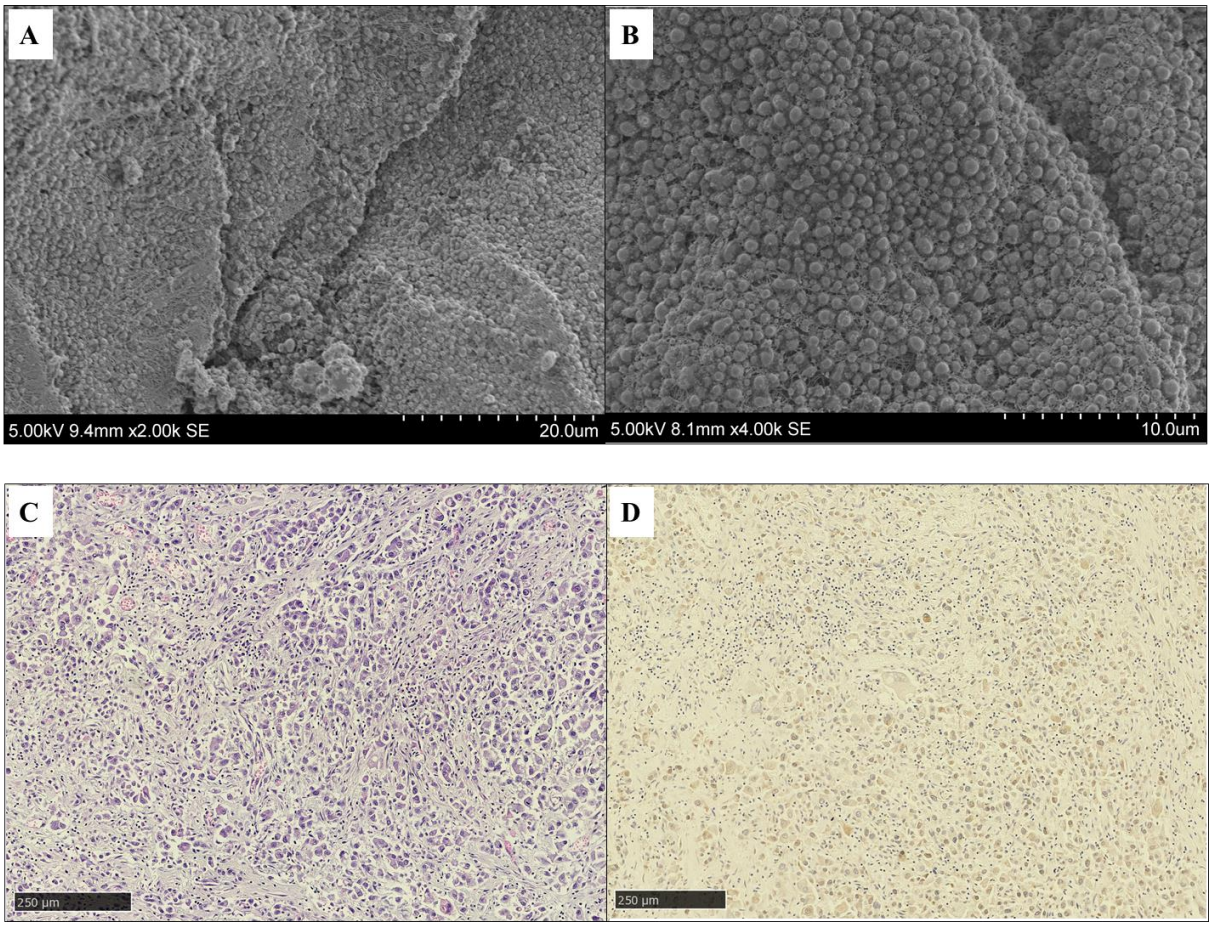

Figure 3.26 Parietal pleura containing malignant cells from lung metastasis in post-mortem sample PEA118. A and B) SEM imaging of parietal pleura. C) H&E stain of parietal pleura shows an aggregation of immune cells and malignant cells of unknown origin. D) Immunohistochemistry image of BAP1 expression in malignant parietal pleura.

In a separate post-mortem case, histological assessment identified diffuse reactive parietal mesothelium (Figure 3.27). This case was a 75-year old male, metastatic kidney cancer patient with no known prior asbestos exposure, smoking history or pleural disease. This post-mortem sample is referred to as PEA139 and had an ischemic time of less than 24-hours.

The cellular perturbations of the pleural mesothelium seen in some areas by histology did not correlate to clinical evidence of pleural disease, as thoracic imaging data prior to death showed that only mediastinal lymph nodes were involved (Figure 3.27). In normal mesothelium and benign reactive mesothelium, the cells have small, uniform nuclei and nucleoli. In contrast, reactive areas of parietal pleura in sample PEA139 showed visible increase in cell proliferation and parietal mesothelial cells had atypical features including enlarged nuclei and prominent nucleoli (Figure 3.27).

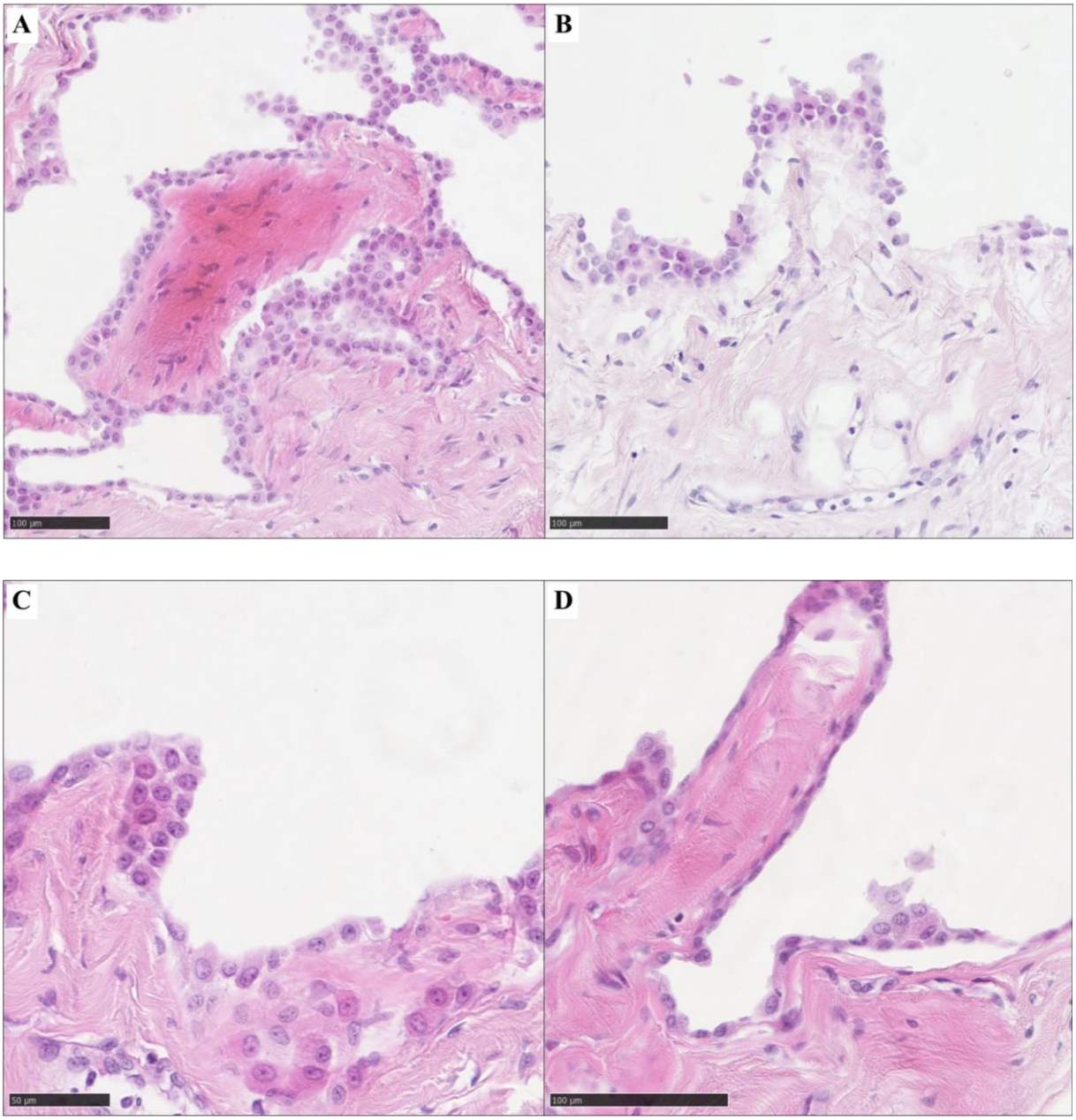

Figure 3.27 Reactive mesothelium in the parietal pleura of a kidney cancer patient with no known pleural disease. A and B) Representative H&E stains of parietal mesothelial cell clusters. Multiple sections of pleural tissue from PEA139 were sampled and all FFPE blocks contained patches of reactive mesothelium when assessed histologically (n=6). C and D) Representative H&E stains of atypical reactive parietal mesothelial cells.

IHC staining of parietal pleura showed that parietal mesothelial cells expressed CK5 (Figure 3.28). The strong expression of CK5, combined with previous flow cytometry viability data from post-mortem samples at 2 and 5 days after patient death and the fast collection of sample PEA139 24 hours after patient death, suggest that parietal mesothelial cells in sample PEA139 were still alive at the time of collection (Figure 3.23, Figure 3.28).

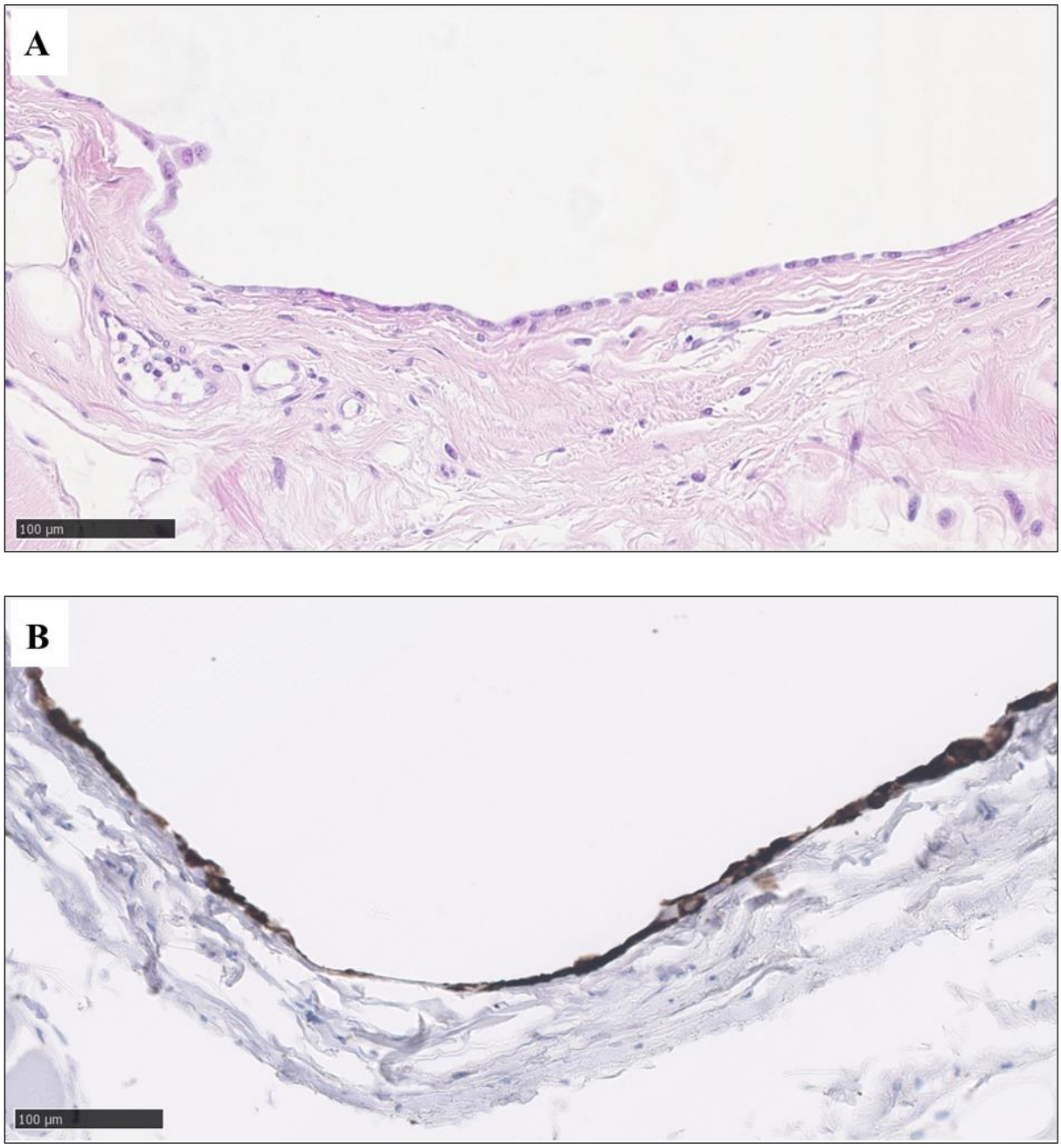

Figure 3.28 CK5 expression in parietal mesothelial cells of post-mortem sample PEA139. A) Representative H&E stain of post-mortem sample PEA139 showing atypical parietal mesothelial cells forming a simple monolayer. B) Parietal mesothelial cells strongly expressed CK5 when assessed by IHC.

3.3.7 Investigation of BAP1 expression in reactive parietal mesothelium

Interestingly, when sections of reactive parietal pleura from sample PEA139 were stained by IHC for BAP1 in-house, BAP1-loss was detected in reactive mesothelial patches (Figure 3.29).

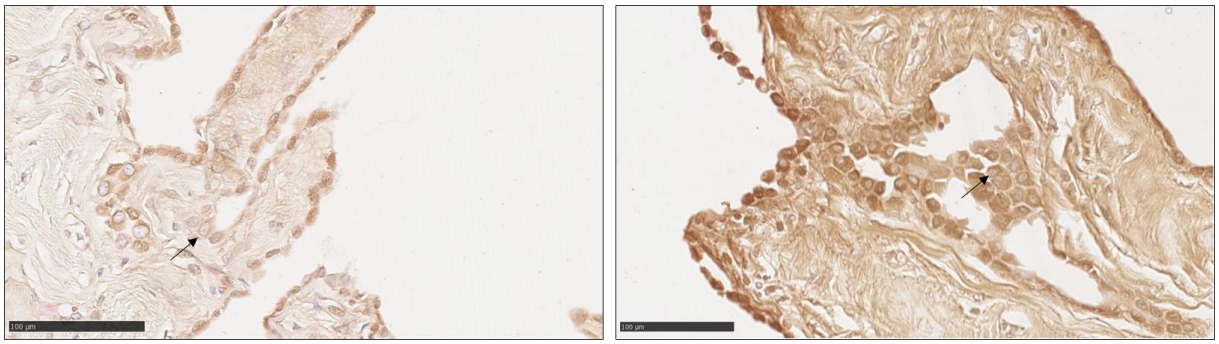

Figure 3.29 In-house BAP1 IHC staining in reactive parietal pleura. Representative IHC images from post-mortem patient sample PEA139. BAP1-negative nuclei of parietal mesothelial cells were visible within reactive cell clusters. Arrows point to BAP1-negative nuclei of reactive parietal mesothelial cells.

The BAP1 staining pattern observed in-house was verified by outsourcing sections of parietal pleura from sample PEA139 to a clinical diagnostics lab, which conducted BAP1 IHC staining on sample PEA139 in parallel to positive control tissues (Figure 3.30).

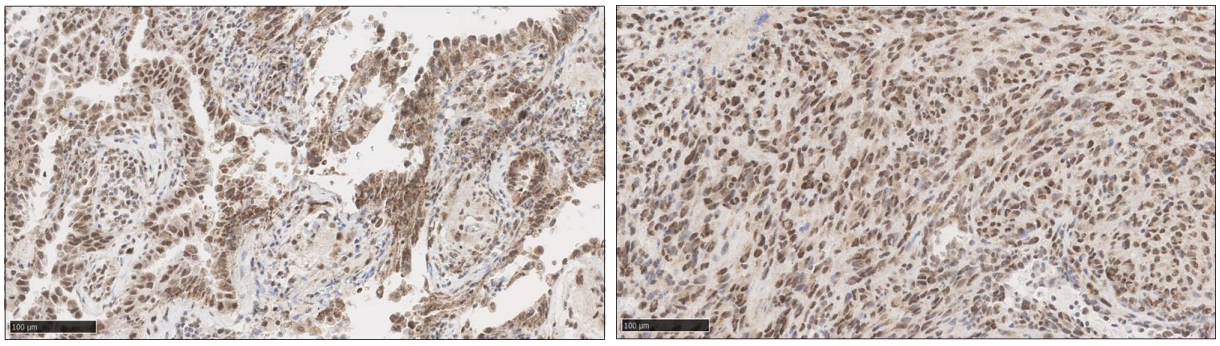

Figure 3.30 Positive control tissue stained for BAP1. Tissue stained in parallel to sample PEA139 for BAP1 by IHC. BAP1 nuclear staining is visible throughout the positive control sections (n=3).

Externally conducted IHC staining verified BAP1 expression pattern in reactive mesothelial patches (Figure 3.31). Reactive mesothelial cells formed proliferative clusters in which the majority of cells had no detectable nuclear expression of BAP1 as determined by IHC (Figure 3.31).

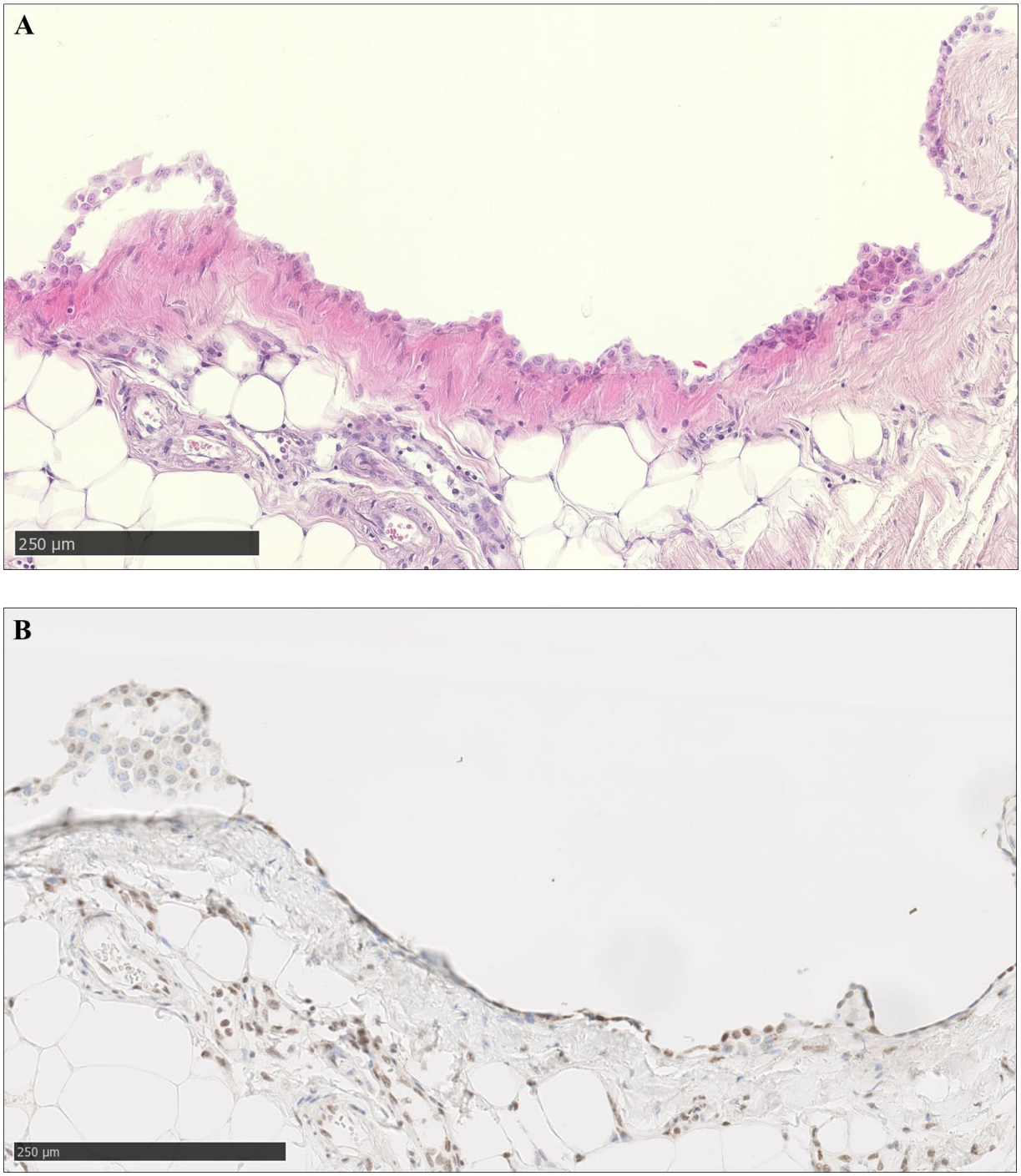

Figure 3.31 Nuclear BAP1 loss-of-expression in a subset of reactive parietal mesothelial cells. A) Representative H&E stain of reactive parietal mesothelium. Connective tissue and sub-pleural adipose tissue are present. B) Representative IHC image of BAP1 expression (n=5). BAP1 staining is visible in immune cells and in single layer of mesothelium. BAP1 loss is seen in the nucleus of reactive parietal mesothelial cell clusters.

There was no visible mesothelial cell penetration of the basement membrane or sub-pleural tissue invasion by reactive mesothelial cells, which is in agreement with the criteria for MMIS (Figure 3.31, Figure 3.32) (220). However, there were identical cells directly below the basement membrane, interspersed in the adipose tissue (Figure 3.31A). Although possibly a sign of early invasion, this section of cells would need verification with CK5 staining for this to be deduced conclusively.

A closer view of the BAP1-negative cells in the reactive mesothelium revealed atypical mesothelial cell morphology (Figure 3.32A). The majority of cells (94/154) in this reactive cluster showed complete loss of nuclear BAP1 (Figure 3.32B). However, nuclear BAP1 expression was uniformly expressed across the surface of the mesothelium and BAP1-loss was not identified in areas other than the proliferative mesothelial cell clusters (Figure 3.31). Therefore, as BAP1-loss was not seen uniformly across the surface mesothelium, sample PEA139 did not fit the current molecular criteria for diagnosis with MMIS. However, nuclear BAP1 loss-of-expression is clearly a predominant trait of reactive parietal mesothelium in sample PEA139, as only a small number of cells (23/154) in the reactive cluster retained BAP1 expression (Figure 3.32). Thus, this constitutes an interesting finding and warrants the investigation of BAP1 expression a larger number of parietal pleural tissues to ascertain if this is indeed an indication or trend of pre-invasive pleural malignancy.

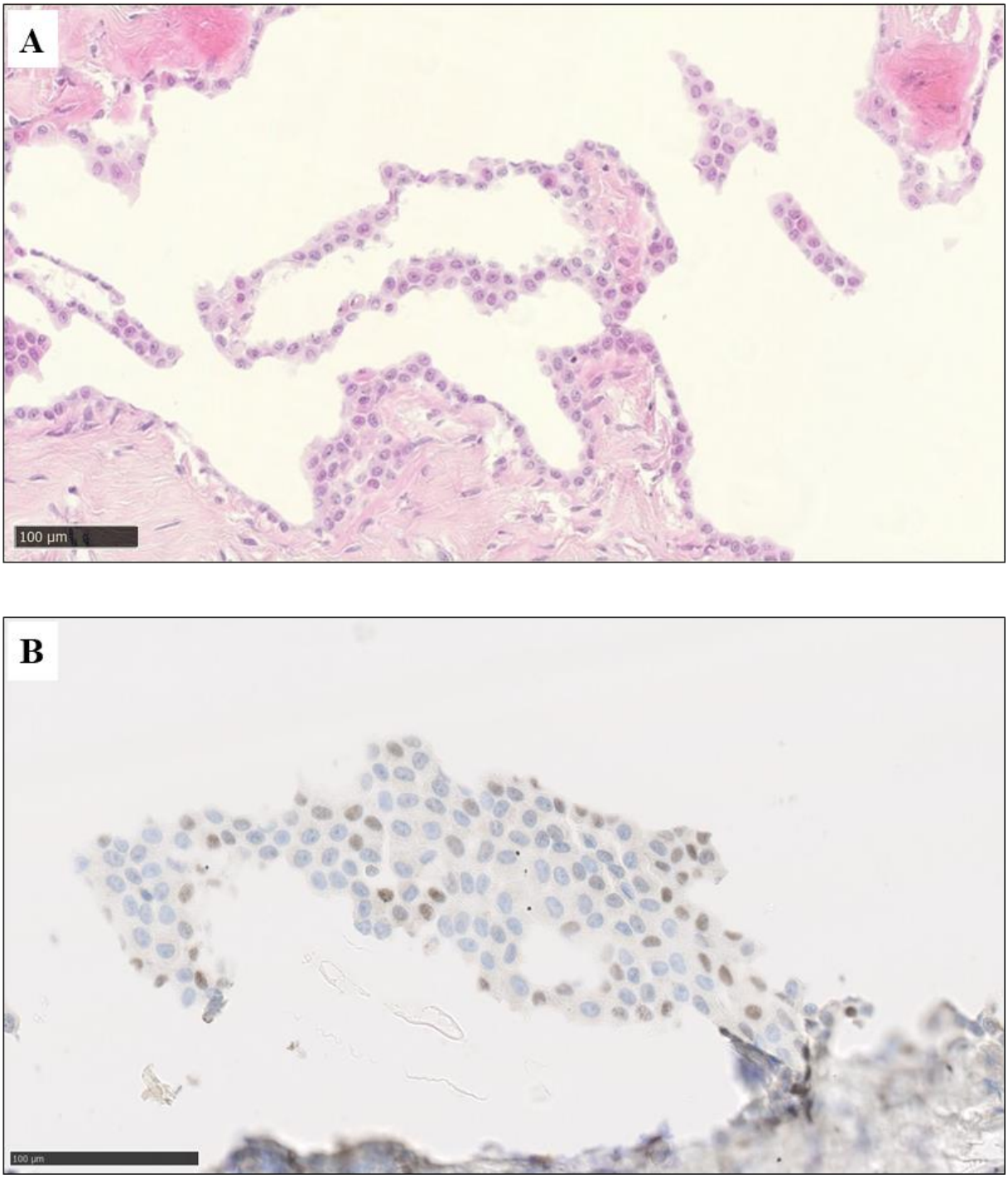

Figure 3.32 Loss of BAP1 expression in proliferative mesothelial cells of sample PEA139. A) H&E stain of reactive parietal mesothelium. B) IHC image of BAP1 expression in reactive mesothelial cluster. There was complete loss of BAP1 nuclear expression in 94/154 cells, 37/154 cells showed weak nuclear expression and only 23/154 cells retained BAP1 nuclear expression.

3.3.8 Proof of concept for CRISPR/Cas9 BAP1 knockout

Developing a genetic method for introducing BAP1 loss-of-function into MPM cell lines is of significant interest to the MPM research field. As indicated in 3.3.7, BAP1 loss-of-function may also be important in pre-malignant mesothelial tissues.

To provide a proof of concept for successful BAP1 knockout *in vitro*, I utilised CRISPR/Cas9 to knockout BAP1 in an established MPM cell line. First, I assessed the Wild-Type status of BAP1 in the MPM cell line CRL2081 by PCR amplification and Sanger Sequencing of exonic regions of interest (data not shown). Once I confirmed that no Single Nucleotide Polymorphisms (SNPs) were present in the two exons of interest, I used a Cas9 Ribonucleoprotein (RNP) complex for *BAP1* gene editing.

I transfected gene editing RNP molecules into CRL2081 cells. I used a crRNA targeting exon 4, as this exonic region encodes the BAP1 protein catalytic site which is important for DUB function (Figure 3.33A). After positive selection by FACS for fluorescent tracr-ATTO™ 550 incorporation, I expanded clones and screened for *BAP1* knockout cells by western blot (Figure 3.33B). Although two exons were targeted using this method, exon 4 targeting resulted in a higher rate of successful *BAP1* knockout clones compared to exon 5 targeting (Figure 3.33B). Successful gene editing was validated by Sanger Sequencing of PCR-amplified DNA from suspect knockout clones. Chromatogram analysis enabled probing at the crRNA site and comparison to the negative (non-targeting) crRNA control clone to confirm a mutation had occurred at the targeted exonic region (Figure 3.33C). For exon 4 clone #1, western blot indicated a loss of BAP1 protein after gene editing and Sanger Sequencing confirmed this by revealing multiple substitution mutations. Notably, there was a substitution of Guanine with Adenine at the crRNA targeting site in exon 4 (Figure 3.33C).

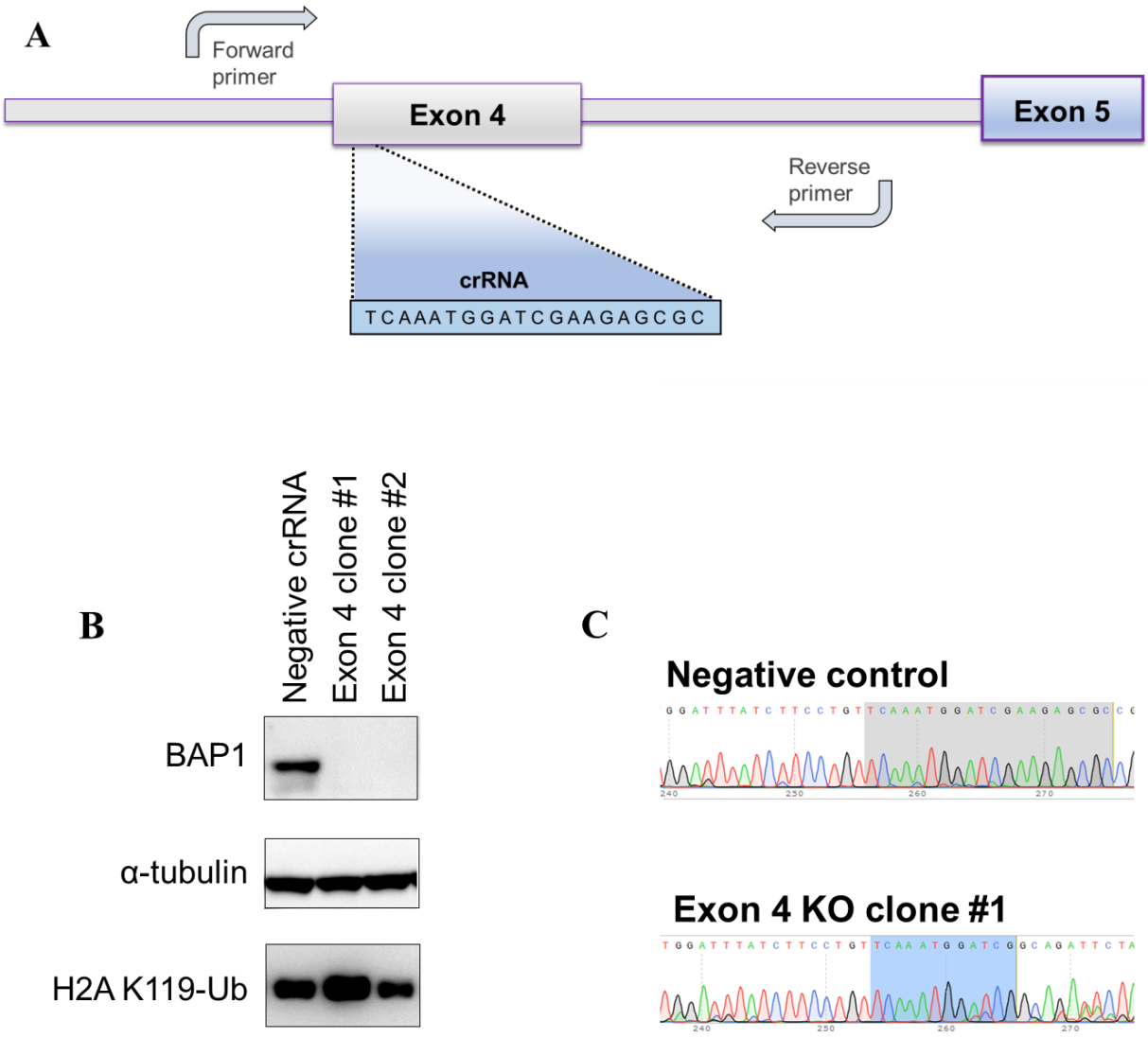

Figure 3.33 BAP1 CRISPR/Cas9 Knockout strategy in CRL2081 cells. A) Illustration of BAP1 exon 4 targeting. B) Immunoblot of gene edited clones revealed two potential *BAP1* knockout clones. The protein level of known BAP1 substrate Histone 2A increased in clone #1, which suggests loss of BAP1 DUB function. C) Sanger Sequencing analysis showed that multiple substitutions were present in the *BAP1* targeting site of clone #1.

This provides proof of concept for a *BAP1* gene editing approach and could offer a valid strategy for targeted knockout of *BAP1* in mesothelial cell models with Wild-Type expression of *BAP1*.

3.4 Discussion

3.4.1 Morphology and spatial distribution of human visceral mesothelial cells

The aim of this study was to determine if two distinct human tissue pipelines offered a robust source of intact visceral pleura. I used histology to investigate sample structure and found an intact basal lamina in 6 lung resection samples as well as discernible intact sub-pleural elements but the visceral mesothelium was not continuous (Figure 3.4). In addition, I demonstrated a sparse layer of CK5-expressing VMCs on the lung surface by whole-mount confocal imaging of distal lung (Figure 3.10). To determine if the attenuated visceral mesothelium identified by histology was due to tissue processing artefact or if this was the natural spatial distribution of human VMCs in homeostasis, I sought to image the surface of pleural samples by SEM.

SEM imaging is considered the 'gold-standard' for determining the morphology of visceral pleura and has been used extensively in morphological studies of animal pleura (56,221). Using SEM imaging I detected small patches of VMCs on 2/6 lung resection samples (Figure 3.13). Notably, long-term sample storage hampered imaging quality, as the basal lamina became susceptible to damage and sub-mesothelial ECM matrix was often partially exposed in these samples (Figure 3.12). Consistent with previous studies, the morphology of VMCs showed heterogeneity with some appearing plump and round and others resembling flat cells, although microvilli were a ubiquitous feature (Figure 3.13) (45–47). Here, I quantified SEM images of VMCs and found an average cell surface area of 119 μm^2 (±8.8) and cell length of 12.8 µm (±0.02). The human VMC length reported here is slightly lower than the 16 – 42 µm described as the mesothelial cell diameter in animal studies. Importantly, as the original morphometric studies of visceral pleura in animals are now significantly dated, the mesothelial cell surface area has not been measured previously. Thus, these quantifications constitute valuable measurements which could be used to aid recognition and validation of human VMCs in future imaging and cell culture studies.

Collectively, three experimental approaches demonstrated that lung resection samples lacked a continuous visceral mesothelium, instead providing evidence for a sparse, attenuated mesothelial monolayer, as illustrated in Figure 3.34. Fresh surgical samples are likely to be subject to greater mechanical stress than post-mortem samples, with greater loss of the fragile visceral mesothelial layer. However, fresh lung resection samples from surgery offer unparalleled insight into VMC morphology and function.

Surprisingly, post-mortem tissue allowed the most comprehensive morphological characterisation of visceral mesothelium, although the tissue's ischemic time renders it an imitation of VMC morphology and VMC spatial distribution in homeostasis. I successfully imaged intact visceral mesothelium on 1/8 post-mortem samples, sample PEA172. SEM imaging revealed a flat, continuous cellular mesothelium which encased the basal lamina across sample PEA172 (Figure 3.20) and expressed CK5 (Figure 3.21). SEM imaging demonstrated that the detection of a continuous, uninterrupted visceral monolayer is possible in human lung samples. However, this finding raises questions as to why intact visceral mesothelium was not identified on any fresh distal lung samples, assessed by histology and imaging (n=10). It is possible that due to the long ischemic time of post-mortem sample PEA172, VMCs underwent apoptosis during the patient's refrigeration prior to post-mortem. This could also explain the change in VMC morphology on sample PEA172, as VMCs were flat, shrunken and lacked microvilli (Figure 3.17).

Importantly, the presence of a continuous visceral mesothelium on post-mortem sample PEA172, indicated that the mechanical forces applied to VMCs during surgery and transport contribute to processing artefact due to VMC detachment. However, mechanical forces were not likely the only reason for VMC detachment in lung resection samples, as the post-mortem samples were transported in an identical manner but did not demonstrate the same extent of VMC detachment that lung resection samples showed. This observation led to the hypothesis that VMCs may have an innate ability to detach and circulate in pleural fluid *in vivo* during disruption of homeostasis, which may be emulated when the pleural tissue is placed in a high volume of transport medium. Combined with knowledge of peritoneal mesothelial shedding *in vivo*, I hypothesised that pleural VMCs can actively shed from the visceral pleura to complete yet undetermined functional roles, leaving sparse patches of VMCs on the surface of the visceral pleura which are visible by SEM and confocal imaging (Figure 3.34). This proposed phenomenon may explain the rare populations or even complete lack of detection of mesothelial cells represented in scRNA-seq studies of digested human lung (81–84). The viability and function of detached, circulating PMCs remains to be explored, although studies of free-floating peritoneal mesothelial cells have suggested that circulating mesothelial cells are involved in wound healing (31,32).

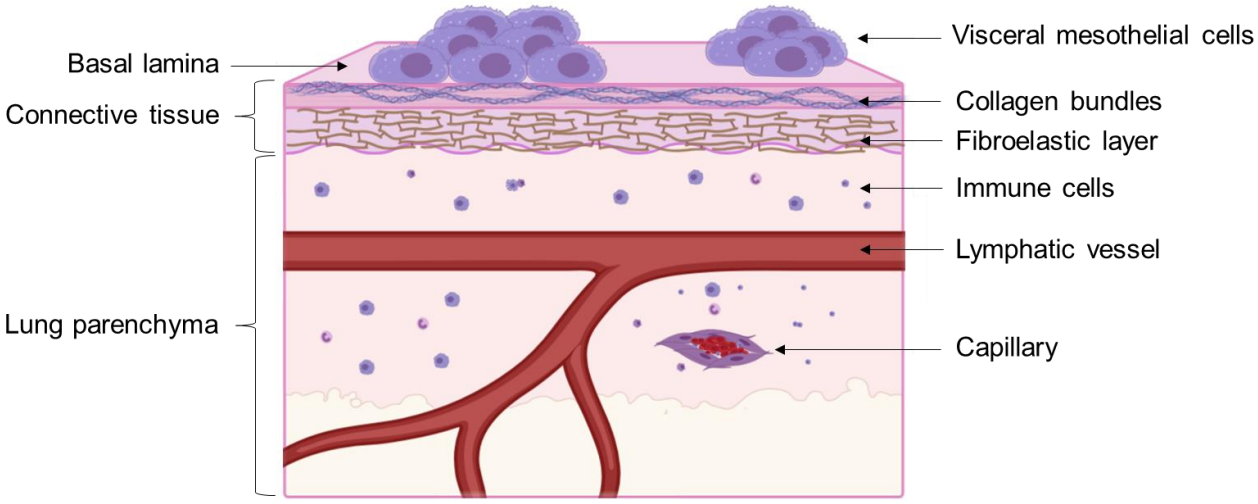

Figure 3.34 Proposed spatial distribution model of visceral mesothelial cells in lung resection samples. The schematic represents the structure of visceral pleura and underlying lung parenchyma as seen in lung resection histology and imaging (n=6). Sparse VMCs are identified in patches on the lung surface. Remaining VMCs are tethered to the basal lamina which is exposed in some areas. Underneath the VMCs is a connective ECM layer composed of a dense network of elastin, bundles of fibrin and collagen. The lung parenchyma contains immune cells and stromal cells, lymphatic vessels and veins. Schematic created using BioRender.

Another key aim of the human pleural sample work was to determine if there is significant heterogeneity in human VMCs. Although the sample size presented here is too small to deduce firm conclusions regarding VMC variability, the two cell size metrics used for VMCs were similar between samples (n=2). However, there was significant intra-sample heterogeneity in both VMC size metrics for sample PEA172 (Figure 3.18). This significant variation may reflect the distance between quantified patches, as a large pleural area of 5.63 cm^2 was imaged by SEM for sample PEA172 (Figure 3.20). To my knowledge, imaging of human pleura at this scale has not been previously conducted and is valuable to the research field as it constitutes a baseline to which to compare perturbations of visceral pleura.

The MPM research field is hindered by infrequent availability of non-malignant pleural control tissues with which to objectively compare pleural malignancy, relying instead on animal models. Thus, there is an unmet scientific need to identify alternative human tissue sources. Utilising two distinct human tissue pipelines I showed that both sources offer visceral pleura with normal structure when processed by histology and assessed by a pathologist (n=14). However, despite structural uniformity observed in pleural histology sections, characteristics of mesothelial cells including cell number, size and morphology differed significantly across samples from the two tissue sources.

Intriguingly, the viability of cells digested from post-mortem tissue remains very high, with an estimated 92.3% cell viability observed (Figure 3.23). This significant positive viability of this heterogeneous population of cells could be partially due to fast refrigeration time of the deceased patient. Immediate tissue processing after tissue harvest could also contribute to sustaining high cell viability. Attempts to culture post-mortem cells from digested tissue resulted in fungal infections (n=5). However, based on flow cytometric analysis, isolation and further characterisation of the VMC population should be feasible if fungal contamination can be eliminated in cell culture with use of an appropriate level of antifungal agent. Despite the difficulties in mesothelial cell culture, post-mortem tissues offer an invaluable resource for morphological and histological analysis.

Collectively, I determined that both sources of distal lung could provide samples with viable VMCs. The findings presented here support the use of both tissue sources for research purposes. These observations are relevant to the wider MPM research field as they provide evidence that these pipelines can offer a human tissue resource with which to better characterise normal pleural mesothelium in homeostasis.

3.4.2 Sub-clinical alterations in post-mortem parietal mesothelium

I have shown frequent sub-clinical changes in parietal mesothelium (2/4) of post-mortem samples (Figure 3.26, Figure 3.27). In two cases, I observed reactive areas of proliferative mesothelial cells in parietal pleura which was not seen in clinical imaging prior to patient death. Atypical reactive mesothelial cells have been described as enlarged, with prominent nuclei which contain visible nucleoli (123,220). The parietal mesothelium of sample PEA139 displayed increased cellularity and moderate atypical features (Figure 3.32A). Verification of parietal mesothelial cells was performed by CK5 stain (Figure 3.28).

It has been extensively shown that loss of BAP1 staining determined by IHC correlates with BAP1 loss-of-function due to mutation (116). BAP1 loss-of-function results in loss of the DUB regulation exerted by this key tumour suppressor protein which may allow BAP1-negative mesothelial cells to gain enhanced cell growth or cell competition advantages. In post-mortem sample PEA139 I identified clusters of reactive mesothelial cells with loss of nuclear BAP1 expression, determined by IHC (Figure 3.32). In a large reactive mesothelial cell cluster, which protruded from the basal lamina, 94/154 mesothelial cells demonstrated complete loss of nuclear BAP1 (Figure 3.32). As loss of BAP1 in mesothelium has been shown to signal pre-invasive MPM, partial BAP1 loss in the mesothelium may be indicative of a phenotypic change

in *BAP1* mutant cells which could result in a growth advantage. Therefore, it is notable that sample PEA139 presented prominent BAP1-loss as it supports this gene as a key driver and molecular step towards malignant cellular behaviour, such as increased proliferation. A vital experiment to determine if BAP1 loss-of-function is sufficient to drive mesothelial cells towards malignancy, would be to implement the BAP1 CRISPR/Cas9 gene editing strategy described here, in the mesothelial cell line Met-5A or in primary human mesothelial cells (Figure 3.33). This would emulate the BAP1-negative status of mesothelial cells seen in sample PEA139 and allow the identification of any potential clonal advantages of BAP1-negative cells.

It is important to note that BAP1 loss-of-expression in this case is almost certainly due to a somatic mutation and not a germline mutation, as the latter would result in uniform BAP1-loss in mesothelial cells (90,92). However, in the post-mortem case study of sample PEA139 it was not possible to verify the mutational status of *BAP1* due to tissue fixation limitations.

In the study by Churg *et al.,* MMIS status was confirmed by complete lack of BAP1 expression in surface mesothelium. Ubiquitous loss of BAP1 was not demonstrated in the case of sample PEA139. However, as this was a post-mortem case it is not possible to know if over time the BAP1-negative mesothelial cells would have evolved into a reactive mesothelium with complete loss of BAP1, which constitutes the current molecular criterion for diagnosis with MMIS (123,222).

In summary, *BAP1* is a frequently mutated gene in MPM and is significant in the pre-malignant stage of MMIS. The observations presented here support the use of post-mortem pleural samples for MMIS research as they may offer a valuable resource with which to study the early stages and evolution of pleural malignancy.

3.5 Summary

- Lung resection samples contained VMCs which expressed CK5, MSLN, WT1 and calretinin.
- The visceral mesothelium in lung resection samples consisted of a sparse, attenuated mesothelial cell layer.
- Human VMCs identified by SEM imaging had an average surface area of 119 μm^2 and cell length of 12.8 µm.
- Significant heterogeneity in VMC size was demonstrated in one post-mortem sample.

- Lung resection and post-mortem samples offer a viable source of VMCs, with distinct advantages and limitations for different experimental approaches.
- BAP1-negative cells were discovered in a subset of atypical reactive parietal mesothelial cells of a patient with no known pleural disease, which supports the importance of *BAP1* in early pleural malignancy.

4 Isolation, purification and transcriptomic analysis of VMCs

4.1 Background

Human mesothelial biology research lacks selective VMC isolation methods. The 'gold-standard' for deriving mesothelial and mesothelioma cell cultures is to collect cells by centrifugation of pleural effusions (148). However, pleural fluid centrifugation does not allow the study of a pure population of VMCs, as it produces a heterogeneous PMC population and thus our limited understanding of visceral and parietal pleural cells remains restricted to functional differences deduced from *in vivo* experiments in animal models (24,37). In addition, the widespread availability of pleural effusions and the ease of cell isolation from pleural fluid has resulted in underutilisation of human distal lung tissue, which is available through routine lung-related surgery and offers a valuable source of visceral pleura for research purposes (129,133,134).

Although cell models are the backbone of cancer research, it is known that karyotypic changes and genomic instability associated with prolonged culture conditions depletes their ability to accurately recapitulate human tissue and disease (223,224). Met-5A is a transformed cell line derived from pleural fluid, which poorly mimics PMCs after decades in culture (148). Thus, methods for the efficient isolation and establishment of primary human VMC cultures is desirable, as these models do not currently exist in the research field.

In contrast to the pleural fluid isolation approach, I sought to isolate a pure population of VMCs from distal lung with the intention to characterise the transcriptome of human VMCs in homeostasis. I sought to test and identify a suitable method to isolate human VMCs and to use cell cultures of extracted populations as a guide to assess VMC culture purity.

Despite recent advances in the genomic characterisation of MPM, there is limited understanding of the transcriptome of normal VMCs which is restricted to microarray analysis of bulk RNA extracted from normal pleura. Furthermore, the gene expression changes between normal and malignant pleural cells remain largely unexplored. To better assess the current information of the publicly available TCGA gene expression MPM dataset (n=86), generation of a transcriptomic datasets for normal human pleura is required. To address this, RNA Sequencing was performed on purified populations of human VMCs to gain an understanding of this cell type in homeostasis.

4.2 Aims

- To develop a more suitable and selective method for isolation of a pure population of VMCs from human visceral pleura.
- To explore a method for VMC cell culture.
- To delineate the gene expression of VMCs in tissue homeostasis.
- To compare the gene expression of non-malignant VMCs to MPM and identify upregulated pathways in MPM which may have therapeutic potential.

4.3 Results

4.3.1 The expression of epithelial markers in mesothelial cell models

To assess which epithelial markers could be used for identification of primary mesothelial cells by flow cytometry, a panel of 5 epithelial markers was tested in a range of normal and malignant mesothelial cell lines (Table 4.1). The cell lines assessed included the established MPM cell line CRL2081, primary MPM cells derived from pleural effusion referred to as PK061219 and the transformed non-malignant mesothelial cell line Met-5A.

Table 4.1 Summary of flow cytometric expression of epithelial cell markers in benign and malignant mesothelial cell lines. Positive expression (+) and negative expression (-) are shown. Where primary MPM cells were not enough to investigate expression of markers not known (n/k) is used.

Expression	ALCAM	CK5	E-cadherin	EpCAM	ITGA6	PDPN
CRL2081	+	+	+	-	+	-
PK061219	-	+	n/k	n/k	n/k	+
MeT-5A	+	+	+	+	+	-

All three cell lines expressed CK5 (Table 4.1). During the flow cytometric antibody selection stage, two CK5 antibodies were tested, of which CK5-FITC (clone D5/16B4, Millipore) showed stronger staining and was selected for subsequent flow cytometry experiments (data not shown). ALCAM, which is found on antigen presenting cells, as well as Integrin Alpha 6 (ITGA6), were the second most expressed markers. Interestingly podoplanin expression was only detected in the primary MPM cells and was not detected in either of the established cell models (Table 4.1).

The mesothelial cell line Met-5A showed very low expression of EpCAM (Figure 4.1) but stained strongly for ALCAM and CK5. Met-5A cells were also assessed for expression of the endothelial marker CD31 (PECAM-1) but no expression was detected (data not shown).

Flow cytometric investigation of these cell models indicated that mesothelial and mesothelioma cells *in vitro* often express epithelial markers such as CK5 and overall were found to express 4/5 common epithelial markers when assessed by flow cytometry.

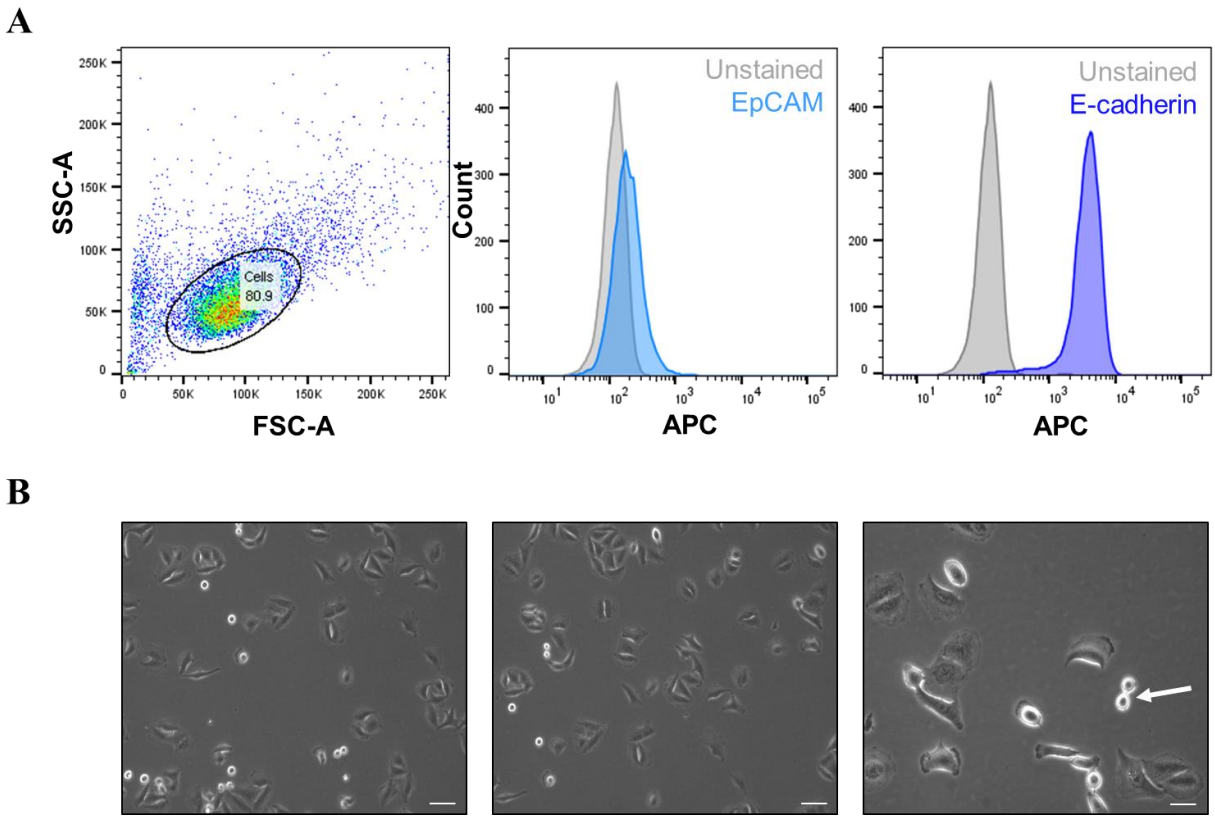

Figure 4.1 Characterisation of transformed benign mesothelial cell line Met-5A. A) Flow cytometry plots depict Met-5A expression of EpCAM and E-cadherin compared to unstained control cells. B) Morphology of cultured Met-5A cells, used for flow cytometric analysis (scale bar = 20 µM). Arrow points to dividing circular cell (scale bar = 10 µM).

Brightfield images of Met-5A cells showed that two distinct cell morphologies are present in Met-5A cultures (Figure 4.1B). The first type has spindle-like morphology and the second type consists of bright cells with round morphology, both of which were attached to plastic and divided (Figure 4.1B). Therefore, this widely used cell model of benign mesothelial cells can only provide an indication of what VMC morphology may resemble.

4.3.2 Visceral mesothelial cell isolation strategies and culture

Initially, enzymatic digestion of visceral pleura with liberase was used for the isolation of VMCs from distal lung. This yielded low cell numbers, although scale up of liberase digestions

marginally improved cell yields. Brightfield images of cells from pleural digests revealed presence of fibroblasts in early cultures (Figure 4.2).

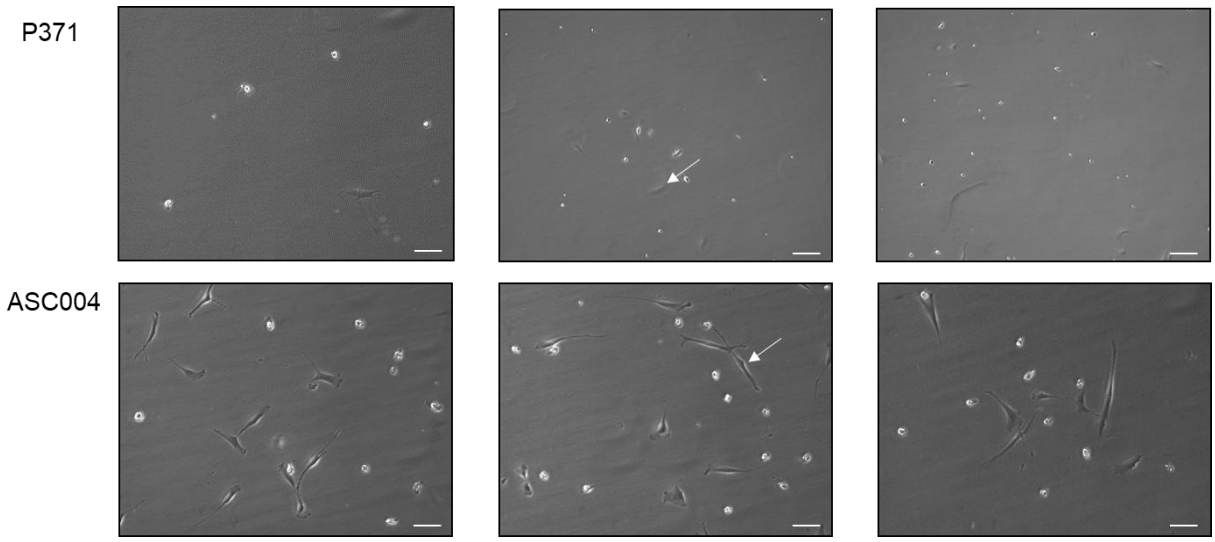

Figure 4.2 Brightfield images of digested pleural cells in early culture. Digested cells from samples P371 and ASC004 were cultured in complete medium and imaged at 4 days. Difference in cell numbers between the two samples is due to increased number of liberase digestions for sample ASC004. Scale bar = 20 µm.

After liberase digestion and before the heterogeneous population was cultured, referred to as Passage 0 (P0), up to 64.5% of cells from digested visceral pleura expressed CK5 when assessed by flow cytometry (Figure 4.3). However, at Passage 1 (P1) the detectable CK5 population had drastically declined to 14.1 – 25.1% (Figure 4.3, Figure 4.4).

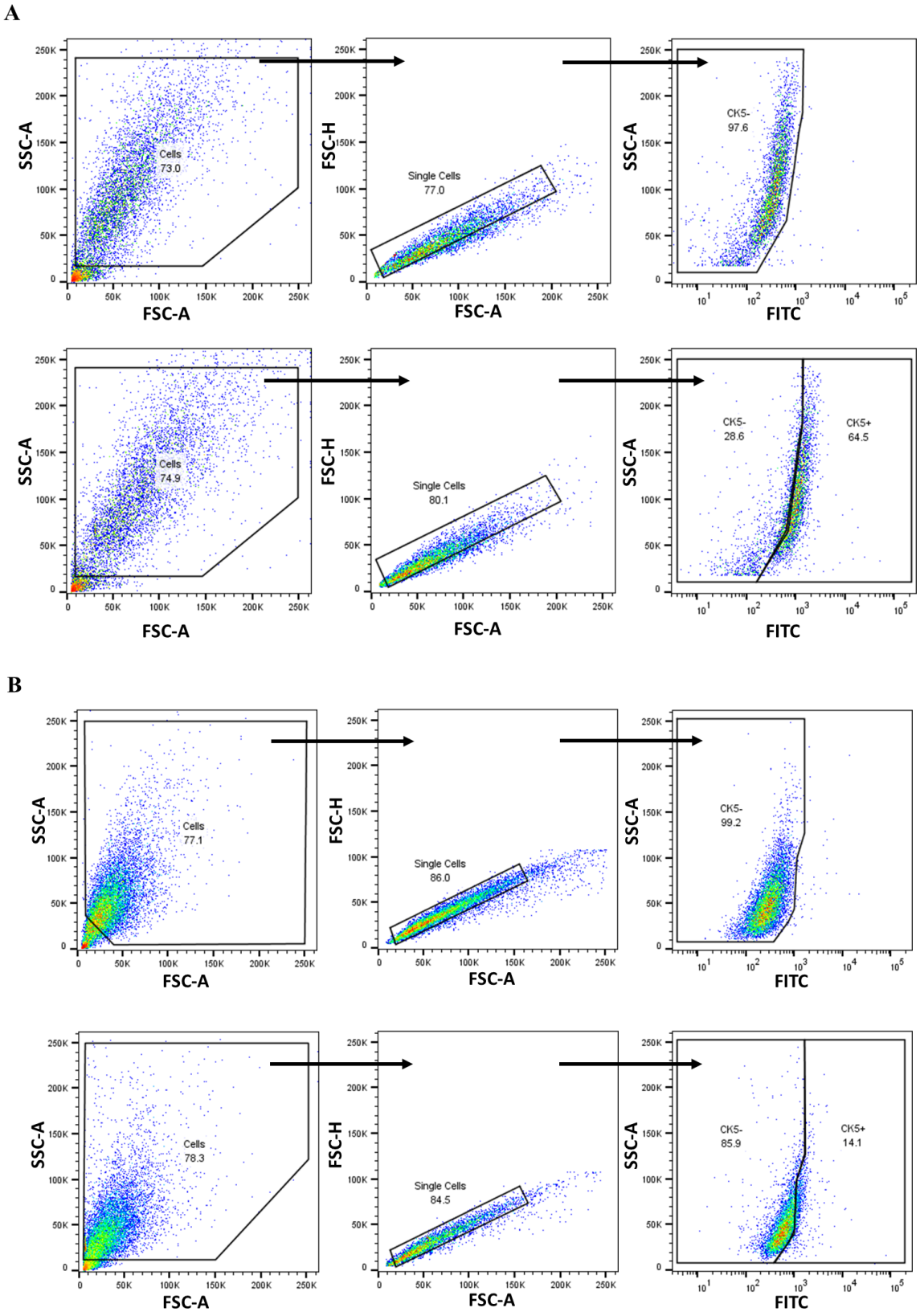

Figure 4.3 Culture of pleural cells resulted in reduction of CK5 expression. Flow cytometric comparison of digested pleural cells at P0 and P1, from sample P370. Gates for single CK5-FITC stains were implemented based on unstained control cells, which are shown in the top panel of A and B. A) Flow cytometry plot shows 64.5% CK5 expression in a mixed cell population following pleural digest with liberase. B) Flow cytometry plot shows 14.1% CK5 expression in cultured cells from digest at P1.

The digested cells were further investigated at P1 to ascertain expression of epithelial markers highlighted in 4.3.1 as potential markers of mesothelial cells *in vitro*. In this flow cytometric analysis, up to 25.1% of cultured cells expressed CK5, a slightly larger subset of 52.9% expressed podoplanin, a small subset of 15.1% expressed E-cadherin and up to 96.3% of the cell population expressed ALCAM (Figure 4.4). As the combination of markers did not label a distinct cell population, this analysis suggests that the panel of epithelial markers reviewed here is not selective enough to detect primary mesothelial cells in a heterogeneous cell population. Furthermore, brightfield images of the cultured cells prior to P1 revealed a heterogeneous population which appeared to be composed of an increasing number of fibroblasts and thus contamination of these primary cultures with unwanted cell types was evident (Figure 4.4B).

A

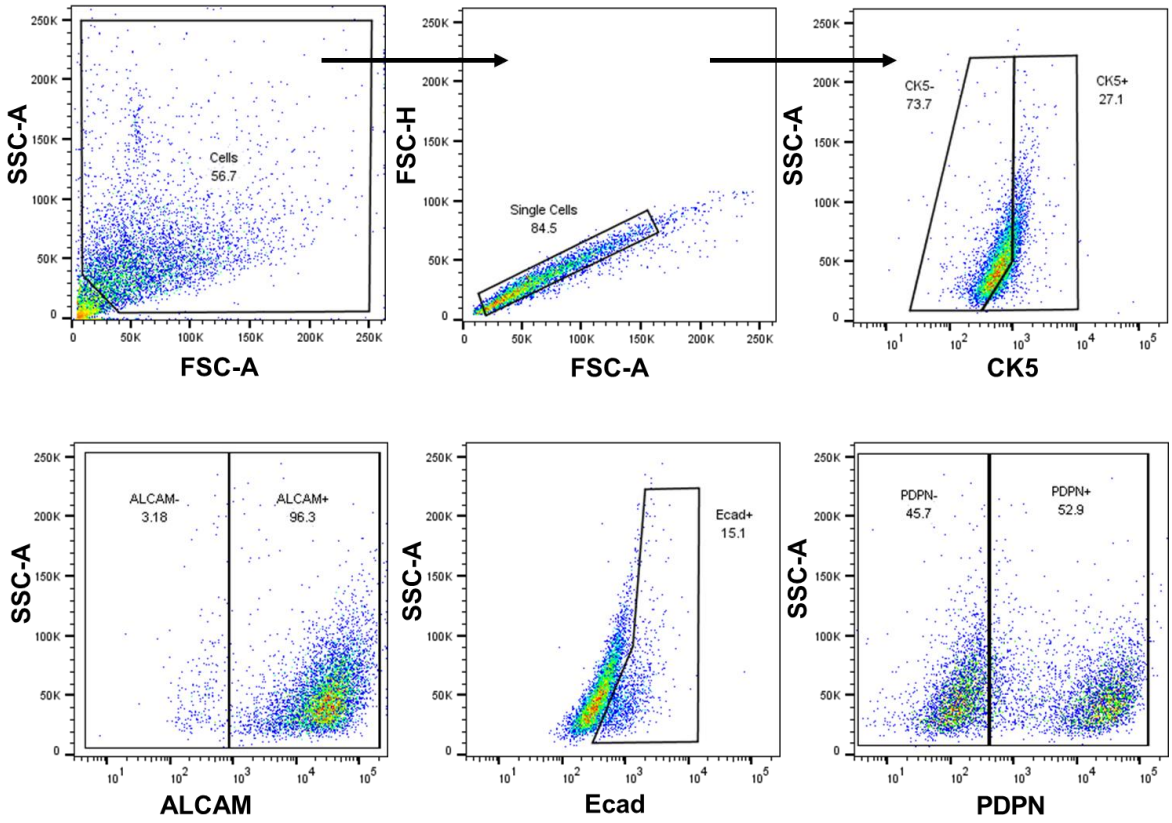

B

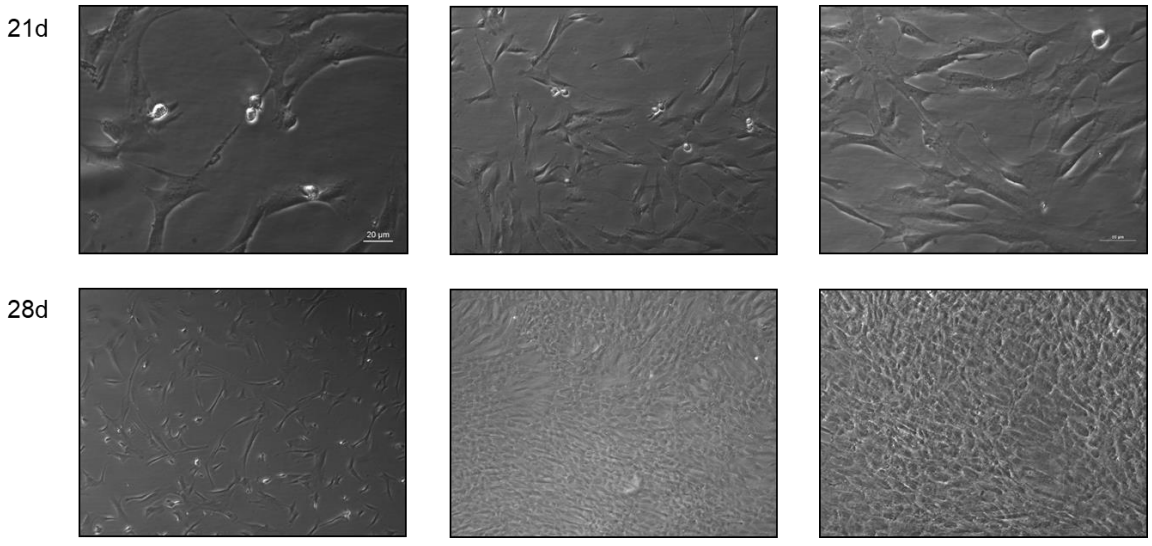

Figure 4.4 Assessment of digested pleural cells from sample P370. Cells were assessed at P1. A) Flow cytometric characterisation of cells stained with antibodies against: CK5-FITC, PDPN-PeCy7, E-cadherin-APC and ALCAM-PE. Gates were drawn based on FMO stains. B) Brightfield images of cultured cells prior to flow cytometry analysis revealed fibroblasts as the predominant cell type in culture.

To confirm the presence of fibroblasts in digested pleural cultures established from sample P370 (Figure 4.4B), the expression of three fibroblast markers was assessed by flow cytometry

(Figure 4.5). Cultured cells from sample P370 were stained with the fibroblast markers PDGFRβ, PDGFRα and CD90 at Passage 2 (P2) (Figure 4.5). Strikingly, CD90 showed the highest expression of the three fibroblast markers, as 90.6% of the cell population was CD90+ when compared to unstained control cells. However, approximately 9% of the population did not express CD90, indicating that a second cell type remained present in this heterogeneous culture at P2 (Figure 4.4 and Figure 4.5A).

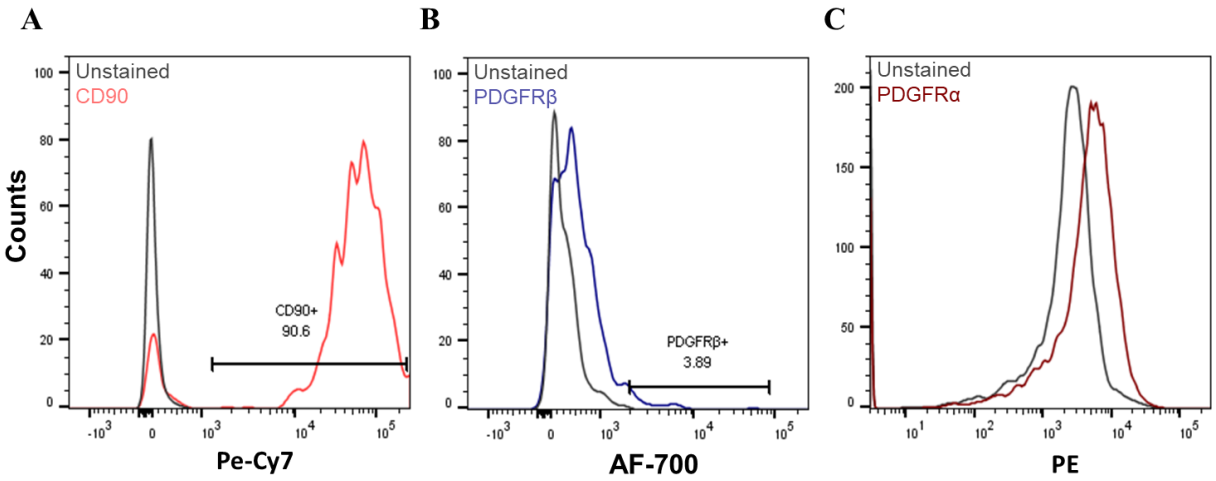

Figure 4.5 Flow cytometric analysis of three fibroblast markers in digested pleural cells derived from sample P370. Cells were assessed at P2. A) Flow cytometry plot demonstrates that CD90 was expressed by 90.6% of the cell population. B) Flow cytometry revealed that PDGFRβ was weakly expressed by 3.89% of the cell population. C) PDGFRα expression was not detected in the cell population. Gates were drawn based on unstained control cells.

In a separate pleural cell culture derived from digest of sample ASC004, brightfield images suggested that fibroblasts expanded faster than other cells as culture time progressed (Figure 4.2). In addition, high expression of fibroblast markers was demonstrated in flow cytometric analysis of cells from sample ASC004 at P1 (Figure 4.6). CD90 was expressed in up to 98.2% of the P1 cell population and PDGFRα was expressed by 21.8% of CD90-positive cells (Figure 4.6).

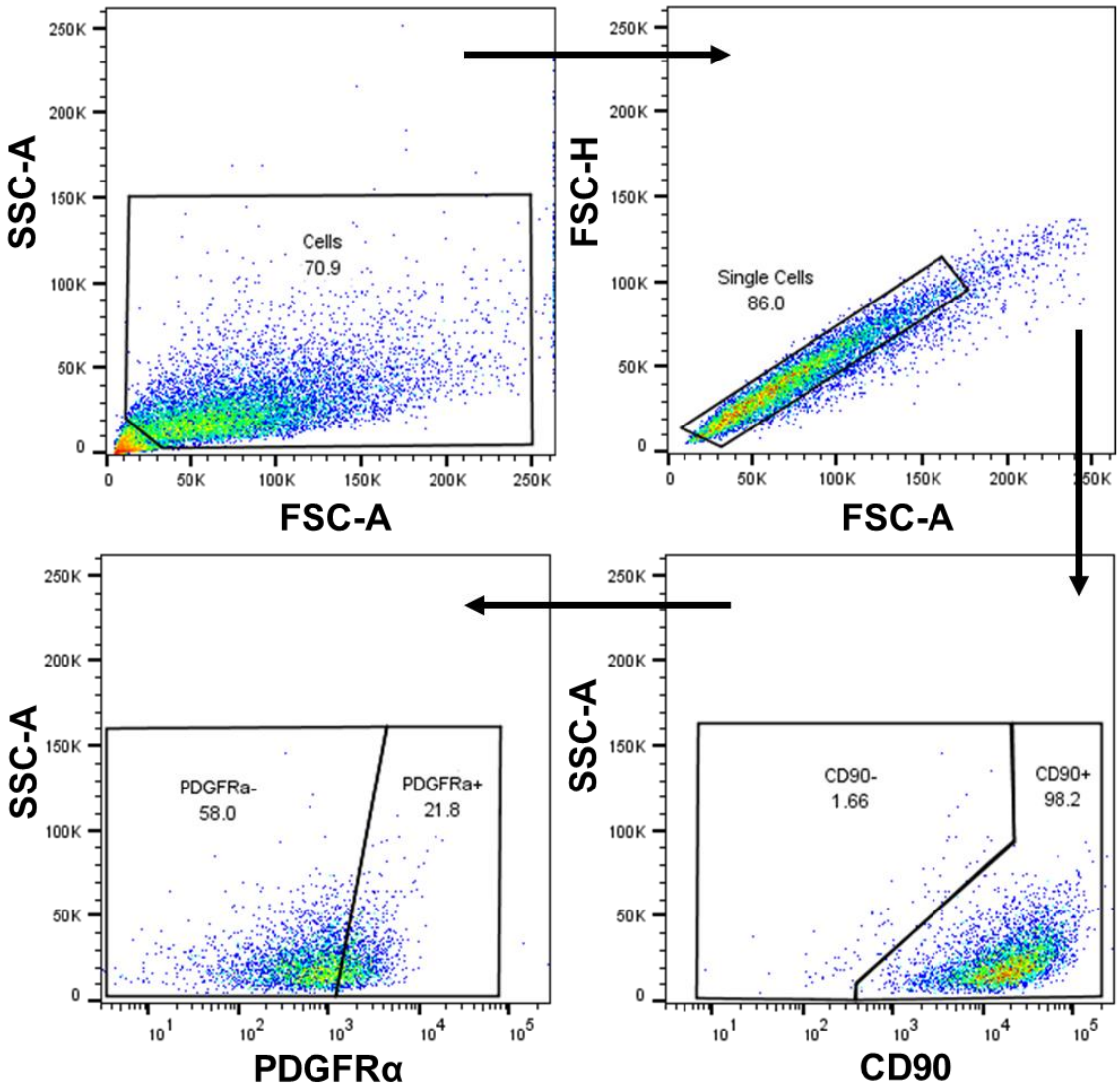

Figure 4.6 Flow cytometric analysis of fibroblasts marker expression in P1 cells derived from pleural digest. Lung resection sample ASC004 was used for digestion. Antibodies used were CD90-PeCy7 and PDGFRα-PE. Gates were drawn based on FMO stains.

Due to the limitations of the pleural digestion approach which included low cell yield and confirmed contamination of subsequent mesothelial cultures with CD90+ fibroblasts, a second isolation method was explored. This entailed use of a cytology brush to extract VMCs by brushing the visceral pleura. A schematic of isolation techniques and the phenotype or resulting early cultures is summarised in Figure 4.7.

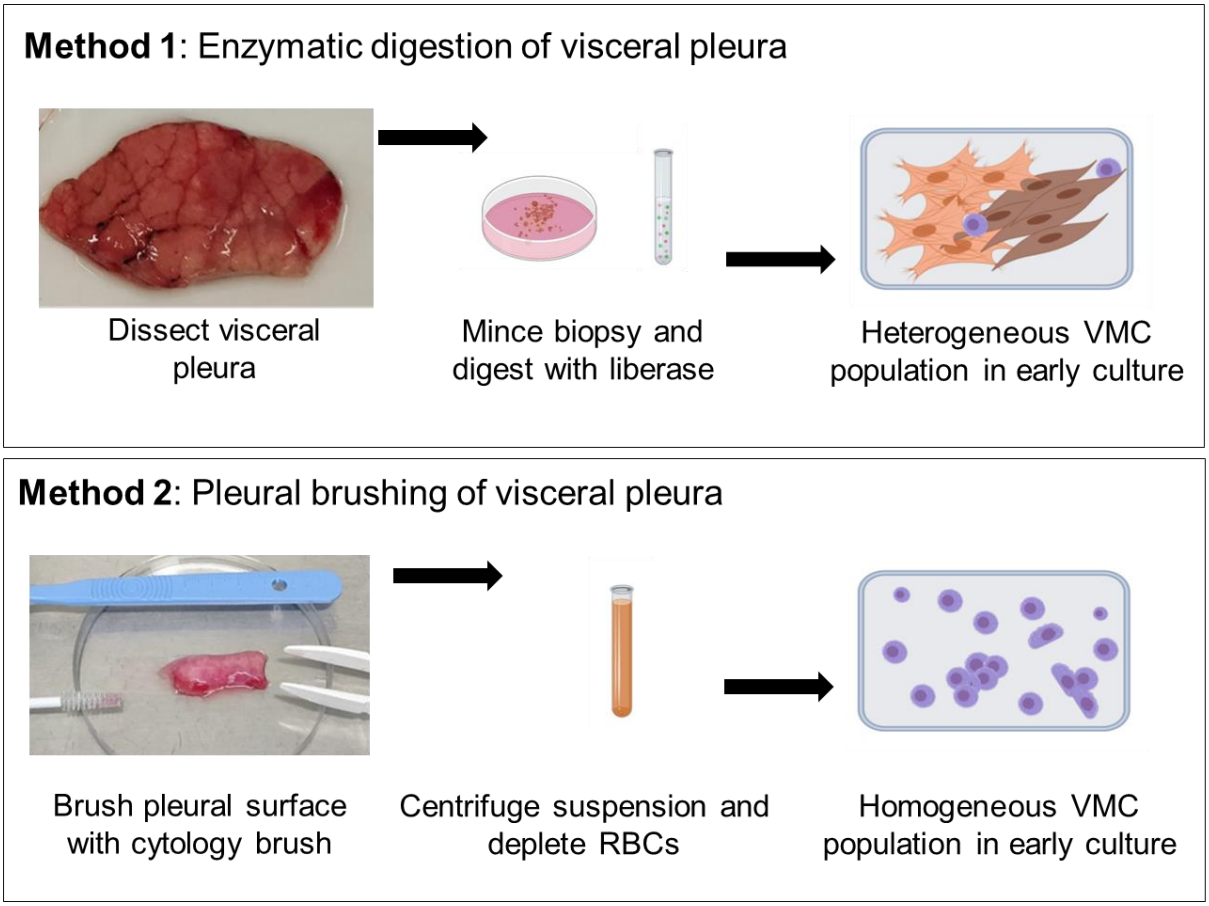

Figure 4.7 Schematic representation of the two VMC isolation methods used and the morphology of early cultures. Schematic created using BioRender.

Cell yields from the second VMC isolation method, which consisted of pleural brushing, were much higher than cell yields produced by pleural digests. Strikingly, flow cytometric characterisation of cells from pleural brushings at P0 showed a positive population of CK5 cells of up to 92.1% (Figure 4.8), which indicated a purer population of mesothelial cells than the 65.1% CK5+ population previously demonstrated in cells from pleural digest (Figure 4.3).

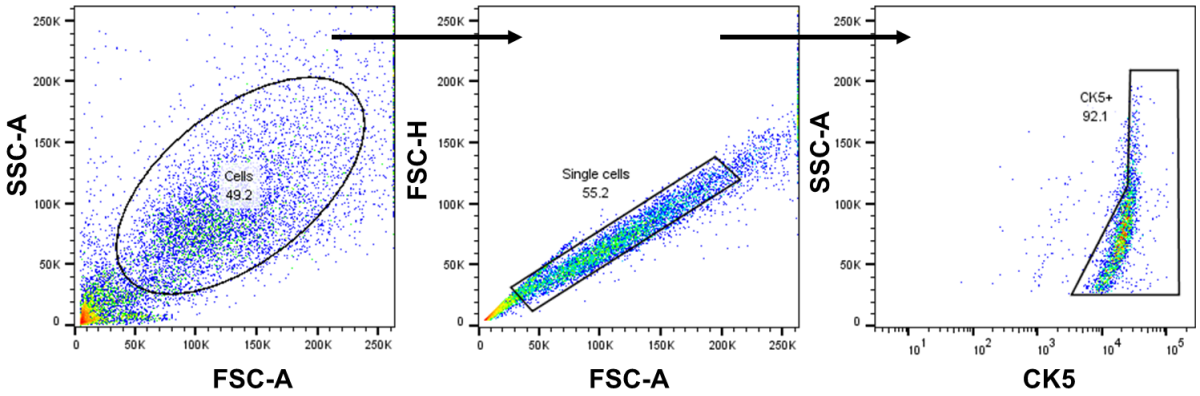

Figure 4.8 Flow cytometry plot demonstrates high CK5 expression in mesothelial cells derived from pleural brushing. Pleural brushing was from lung resection sample ASC009. CK5 expression was detected in 92.1% of the cell population. Gates were drawn based on unstained control.

A striking difference to the cultures established from digested cells, was that early cultures derived from pleural brushings showed a uniform population of round cells with visible surface protrusions (Figure 4.9). Quantification of imaged cells at 4 days revealed that cells measured 11.2 µM (±0.47) in length (Figure 4.9), which is comparable to the VMCs measured as 12.8 µM previously (Figure 3.14). These observations support the establishment of mesothelial cell cultures from pleural brushings. However, at 7 days fibroblast-like cells were clearly visible and by 12 days it was evident that fibroblasts had begun to expand underneath the round mesothelial cells (Figure 4.9).

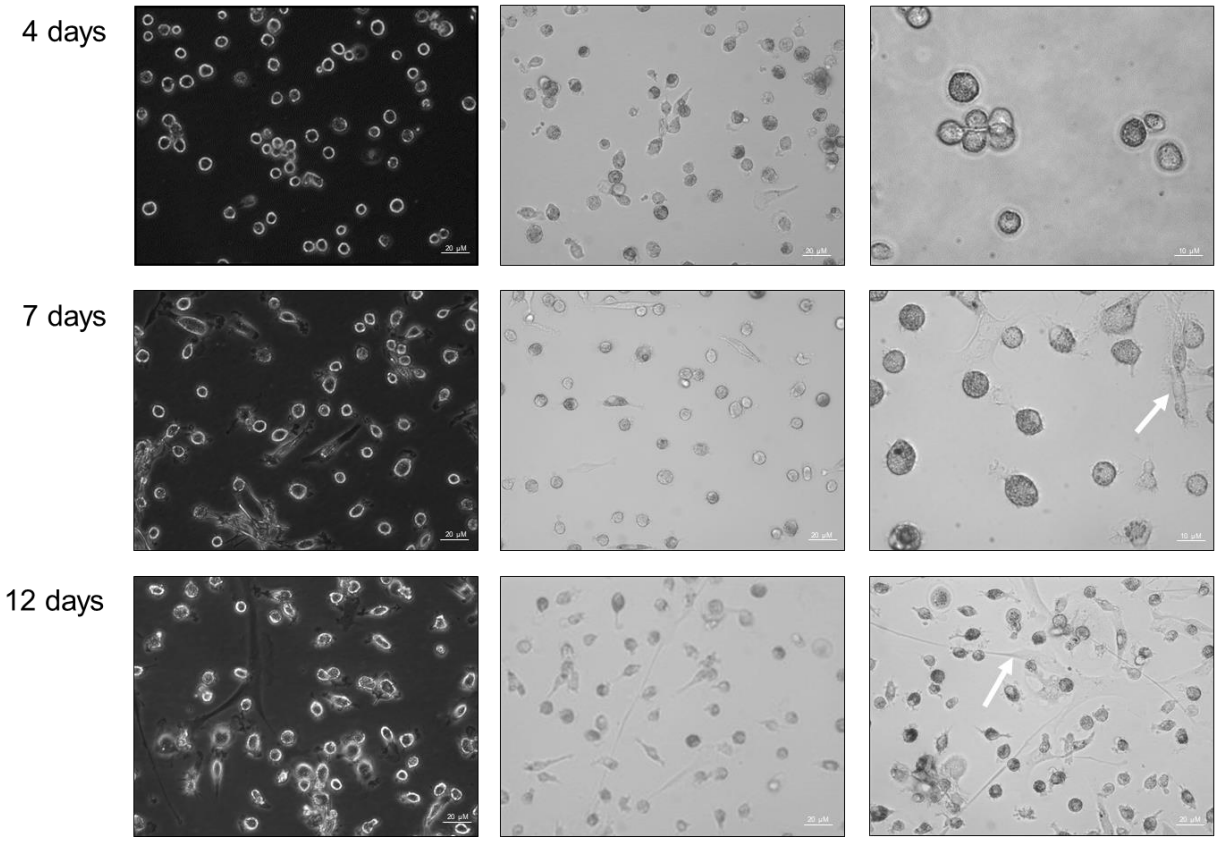

Figure 4.9 Brightfield images show mesothelial cell morphology in early culture derived from pleural brushing. Pleural brushing was from sample ASC008. Representative images are shown from 4, 7 and 12 days of culture respectively (n=3). Arrows point to fibroblast-like cells in the cell population.

Mesothelial cultures slowly proliferated and took 37 days to reach confluence in a T25 flask. At this stage they were trypsinised and analysed by flow cytometry for expression of the fibroblast marker CD90 and mesothelial marker CK5 (Figure 4.10). This analysis revealed that only 35.3% of the cell population was CD90-negative and out of these, a small subset of 5.45% expressed CK5 (Figure 4.10).

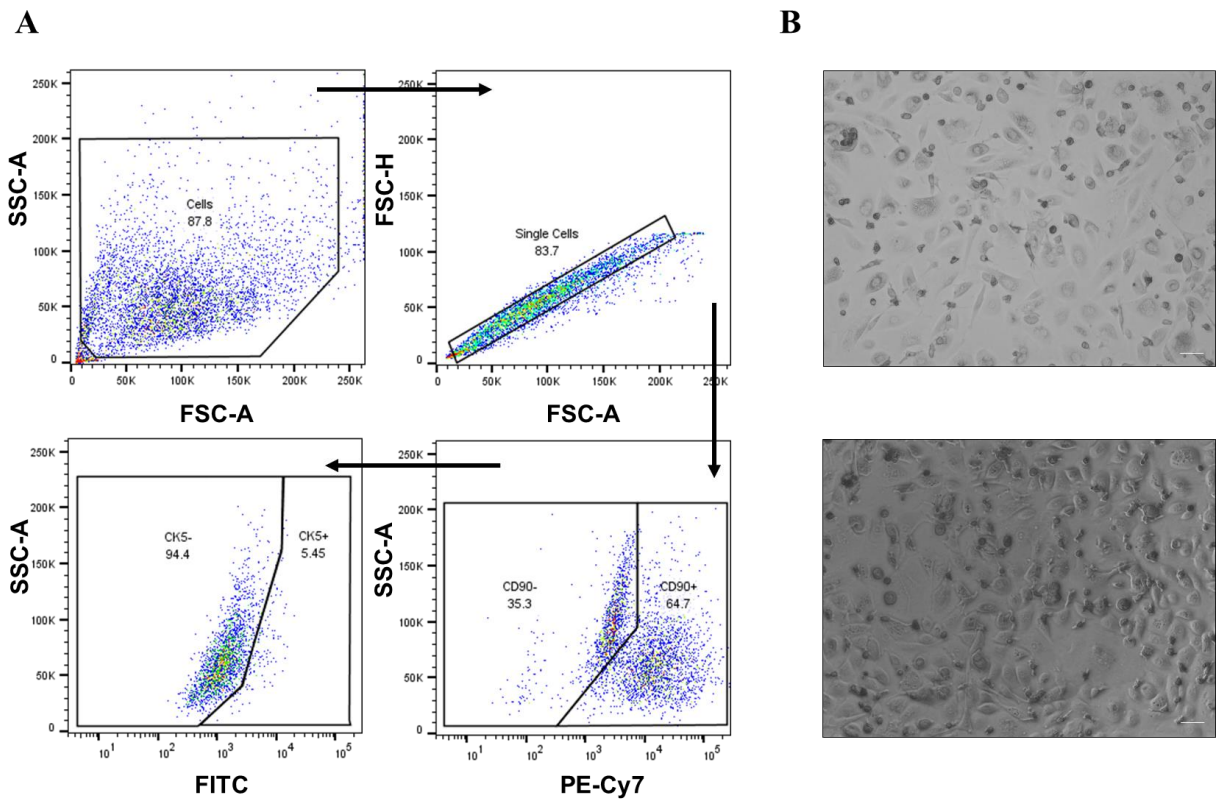

Figure 4.10 Flow cytometric characterisation of primary mesothelial cells from pleural brushing. A) Flow cytometry demonstrates that the cell population contains fibroblasts which express CD90. A small number of cells expressed CK5. Assessment was carried out on primary cells at Passage 1. Antibodies used were CD90-PeCy7 and CK5-FITC. B) Representative brightfield images of confluent primary cells prior to Passage 1. Scale bar = 20 µm.

Collectively, flow cytometric analysis and quantification for the marker CK5 suggests that pleural brushing allows isolation of a greater number of VMCs compared to digestion methods. However, as culture time progressed, fibroblast contamination persisted and therefore the purity of the pleural brushing cultures long-term, although superior to the digested cultures, require further improvement.

4.3.3 Identification of free-floating viable mesothelial cells

Distal lung sections were transferred to the laboratory on ice, in 50 mL of transport medium containing FBS and antibiotics. Due to the low cell numbers seen in pleural digests, the transport medium was investigated as a reservoir of detached mesothelial cells. Comparative flow cytometric analysis of transport medium and digested cells from visceral pleura, revealed a striking population of free-floating cells which was 97.5% CK5+ (Figure 4.11). A similar population of CK5+ cells in transport medium was identified in a further three samples.

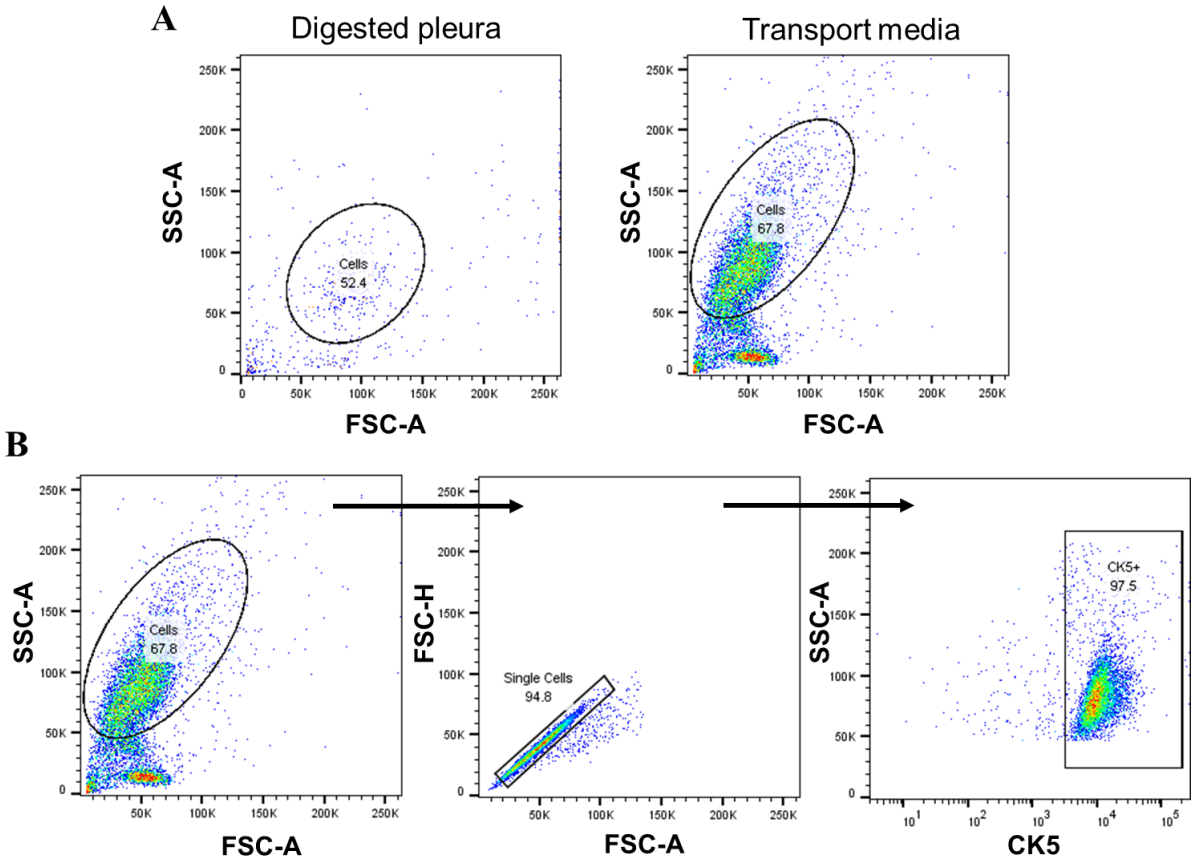

Figure 4.11 Flow cytometric comparison of cells from digested visceral pleura and transport medium of sample P371. A) Representative SSC-FSC plots depict low cell yields in pleural digests at approximately 2,000 cells and a large proportion of cells in pleural transport medium at 10,000 cells (n=4). B) Analysis of free-floating cells in transport medium showed that 97.5% of the distinctive cell cluster was CK5 positive.

Next, I sought to determine if the free-floating cells were apoptotic cells which had detached from the tissue during transport. Comparison between transport medium and VMCs from pleural brushing was performed. The 50 mL of transport medium used for sample ASC014 was centrifuged and stained in parallel to cells isolated by pleural brushing of sample ASC014. Subsequent flow cytometric viability assessment demonstrated that free-floating cells in transport medium had higher viability than tissue-resident cells from pleural brushing, as alive populations constituted 60.2% and 45.7% respectively (Figure 4.12).

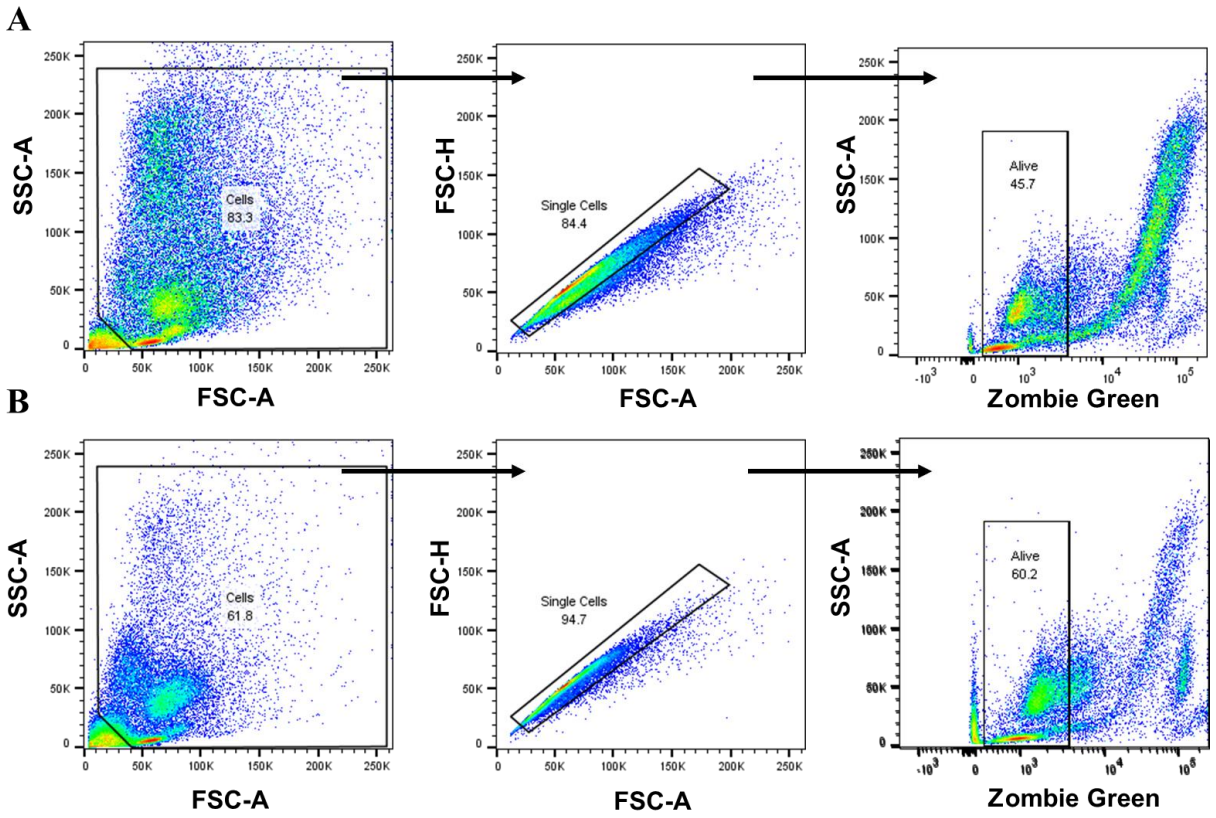

Figure 4.12 Flow cytometric cell viability comparison of pleural brushing and transport medium. A) Pleural brushing of sample ASC014. B) Transport medium of sample ASC014. Gates were drawn based on unstained control cells. Cells with negative staining for Zombie Green are viable and are shown in gated plots as the alive population.

This analysis revealed several differences between the pleural brushing and transport medium populations. Pleural brushing resulted in clumps of cells which were located higher up in the SSC-FSC plot. This had been previously observed by brightfield images of cultured cells from pleural brushings and can be decreased by passing the cell suspension through a 70 µm cell strainer (Figure 4.13).

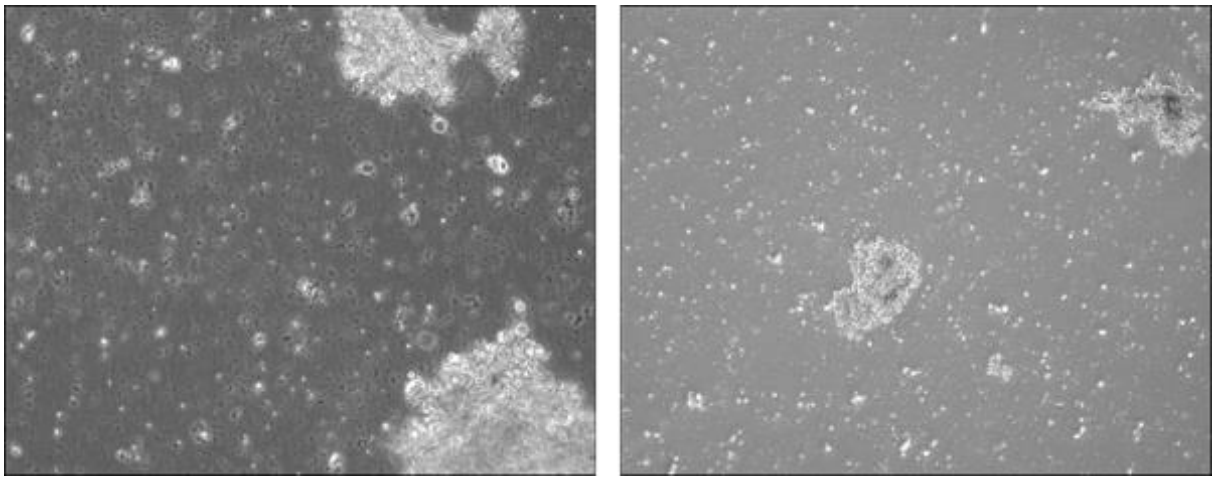

Figure 4.13 Cell culture revealed clumps of visceral mesothelial cells derived from pleural brushing. Brightfield images were taken before attachment of cells to plastic, at 0 days of culture. Large cellular aggregates of VMCs are visible in the culture dish. Images were from pleural brushing of post-mortem sample PEA224. After attachment of cells to the culture dish they developed a fungal infection.

Secondly, the debris captured by flow cytometry was significantly increased in the transport medium compared to the cell population from pleural brushing, as would be expected. To provide an accurate representation of viability, the Zombie Green gates were drawn to exclude debris from both flow cytometry plots.

4.3.4 FACS-purification of visceral mesothelial cells acquired by pleural brushing

Results suggested that although pleural brushing provided an improved VMC isolation method, a small population of contaminating stromal cells was still present at P0 (Figure 4.8, Figure 4.9). To mitigate this, a panel of negative markers was used to exclude contaminating cell types with the aim of purifying the VMC population acquired from pleural brushing.

Based on findings from fibroblast marker expression of *in vitro* fibroblasts (Figure 4.5, Figure 4.6), CD90 was selected as a fibroblast marker for the FACS-purification panel (Figure 4.14). CD31 was selected as an endothelial marker (Figure 4.14). Although red blood cell (RBC) lysis was conducted on cells acquired from pleural brushings, the RBC marker CD235α was included to mitigate autofluorescence of RBCs by negative selection of this population. CD235α was used in conjunction with the marker CD45 in the BV421 channel to mark and exclude any remaining RBCs and immune cells respectively (Figure 4.14). A Zombie viability dye was utilised to ascertain and select live cells for sorting (Figure 4.14).

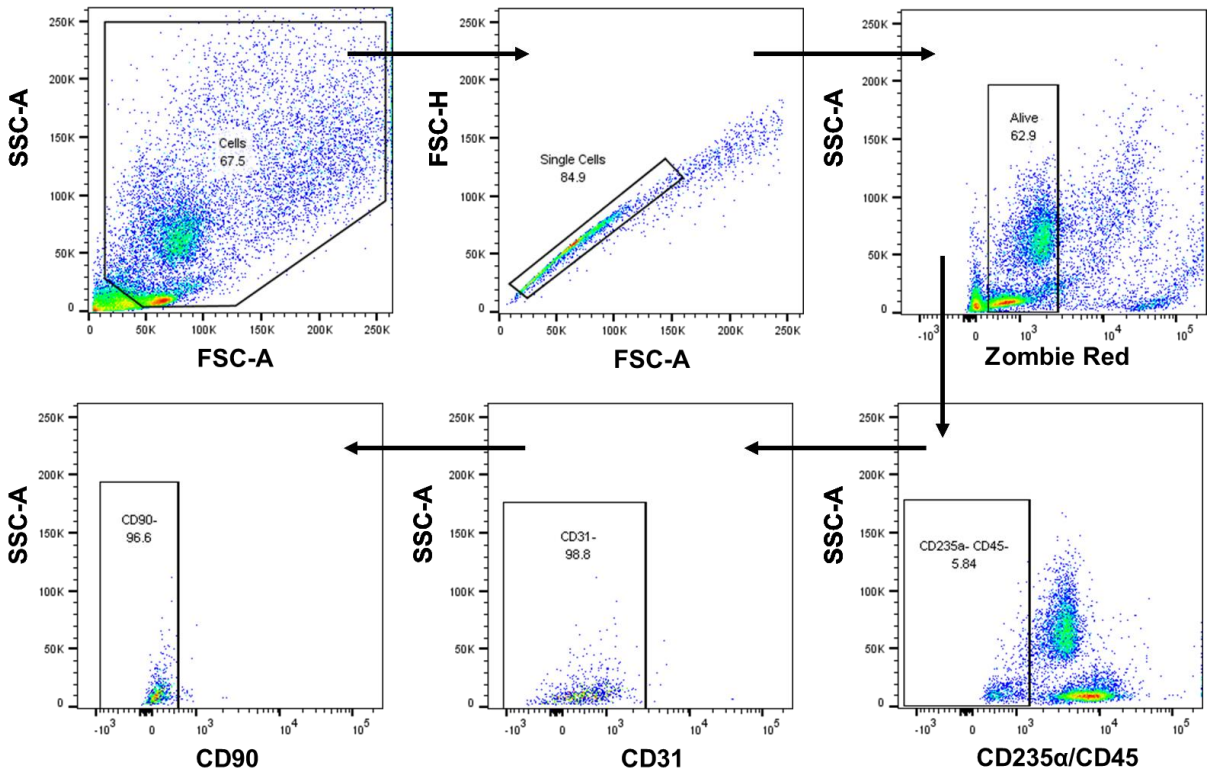

Figure 4.14 FACS strategy for purification of visceral mesothelial cells from pleural brushings. Antibodies were used in the following colours: CD235a-Pacific Blue, CD45-BV421, CD31-PerCPCy5.5, CD90-PeCy7. Gates were drawn based on FMO stains.

A total of four purified VMC populations were sorted by FACS, for subsequent RNA sequencing. FACS analysis revealed that the average live population of CD235α- CD45- cells was 21.1% (±11.22). Of the live population across the four samples, contaminating endothelial cells which were CD235α- CD45- CD31+ constituted 4.3% (±1.78) and of the remaining CD235α- CD45- CD31- population CD90+ fibroblasts represented a further 4% (±1.75) of cells.

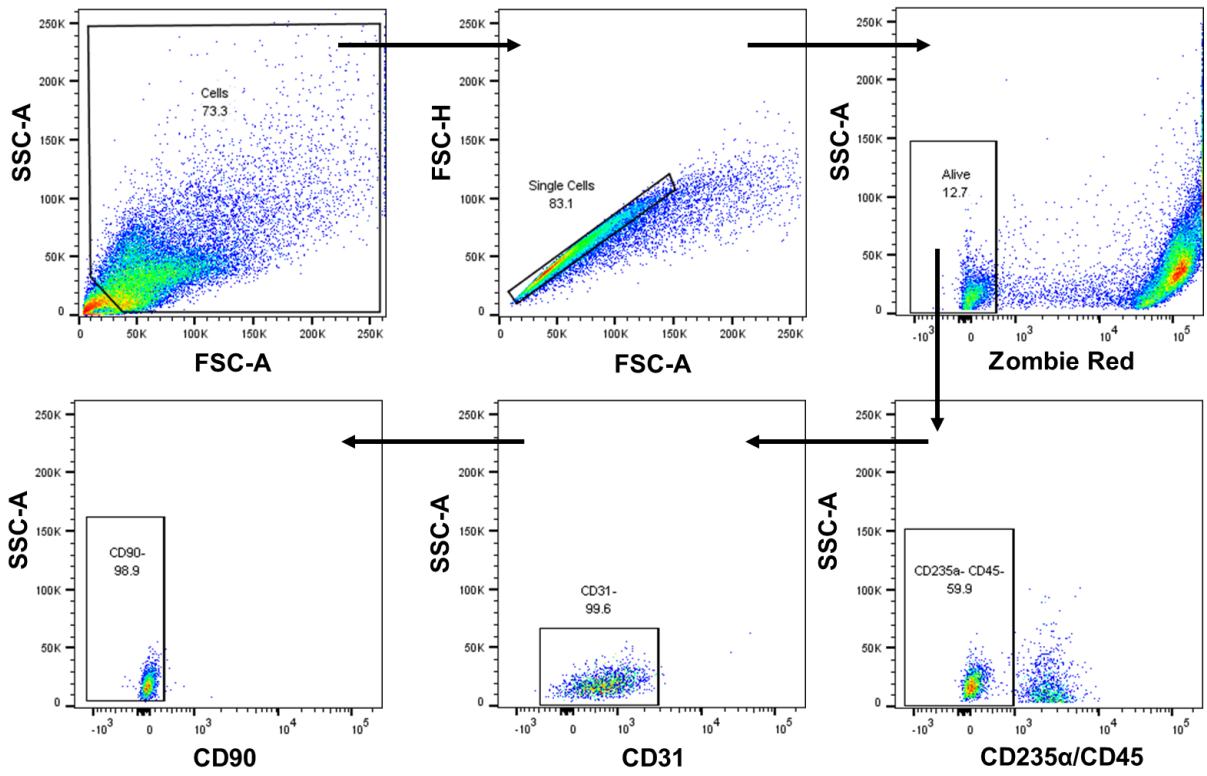

Figure 4.15 FACS strategy for purification of visceral mesothelial cells from post-mortem sample PEA254. Antibodies were used in the following colours: CD235a-Pacific Blue, CD45-BV421, CD31-PerCPCy5.5, CD90-PeCy7. Gates were drawn based on FMO stains.

Due to sample acquisition restrictions, samples were stored overnight before FACS-sorting the following day. This caused significant reduction in cell viability. In lung resection samples from surgery, the percentage of living cells ranged from 54 – 77.2% of the single cell population (n=3). In the post-mortem sample a drastic decrease of viability to 12.7% was observed (n=1) (Figure 4.15). However, the post-mortem sample yielded a high VMC count when assessed and purified by FACS.VMC counts from FACS-purified VMC populations ranged from 17 x 10^2 – 25 x 10^3 (Table 4.2). The direct comparison of isolated VMCs from pleural brushing and transport medium represented in Figure 4.12, provided VMC counts of 95 x 10^2 and 14 x 10^2 respectively, suggesting that transport medium which distal lung has been transferred in can be used as a source of viable VMCs (Table 4.2).

RNA sequencing of these purified VMC populations from four patients was conducted to gain insight into the gene expression of VMCs in homeostasis. The tissue-resident and free-floating VMC populations acquired from ASC014 were isolated but not RNA sequenced due to time constraints.

Table 4.2 Summary of isolated VMC population from distal lung samples. Cell count represents number of cells acquired after FACS-purification of VMC populations.

Sample	Tissue source	Isolation method	Cell count	RNA sequencing status
PEA254	Post-mortem	Pleural brushing	10,000	Yes
ASC011	Lung resection	Pleural brushing	6,100	Yes
ASC012	Lung resection	Pleural brushing	25,000	Yes
ASC013	Lung resection	Pleural brushing	1,700	Yes
ASC014	Lung resection	Pleural brushing	9,500	No
ASC014	Lung resection	Transport medium	14,200	No

4.3.5 Assessment of MPM markers in RNA Sequencing datasets

Before analysis of the gene expression of VMC populations, an assessment of IHC-derived MPM markers was conducted, to gain insight into the utility of these markers in RNA sequencing datasets. The panel of iMig recommended markers for MPM differentiation was used for this analysis (Table 1.1). Using the RNA sequencing datasets available through cBioportal, the expression of 4 negative and 4 positive MPM markers was compared between lung adenocarcinoma (n=317) and MPM (n=87) cohorts (Figure 4.16).

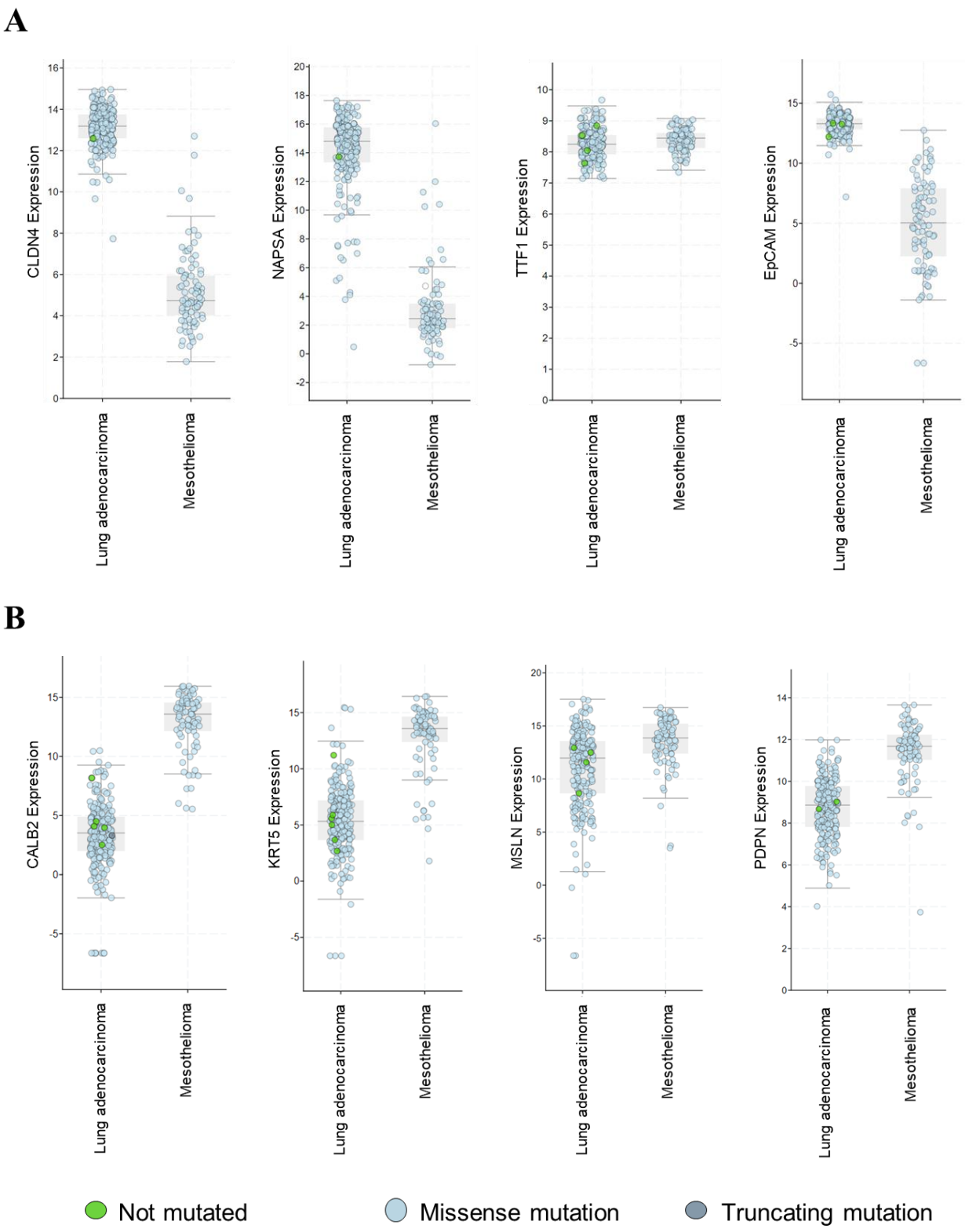

Figure 4.16 Expression of iMig recommended MPM markers in exome and RNA sequencing datasets of lung adenocarcinoma and MPM. RNA sequencing analysis generated from cBioportal. Plots depict RNA sequencing counts (log2) from TCGA lung adenocarcinoma and MPM datasets. A) Expression of negative markers of MPM are compared between lung adenocarcinoma and MPM datasets. B) Expression of positive markers of MPM are compared between lung adenocarcinoma and MPM datasets.

The expression of negative IHC markers in MPM agree with the findings in RNA sequencing data, for CLDN4 and NAPSA (2/4) (Figure 4.16A). However, TTF1 expression which should be limited to lung adenocarcinoma cells, showed nearly identical expression to MPM (Figure 4.16A). In addition, expression of EpCAM in the RNA sequencing data of MPM tumours is variable, with evident RNA sequencing count heterogeneity (Figure 4.16A). The assessment of positive markers for MPM revealed higher calretinin and CK5 expression in MPM compared to lung adenocarcinoma, which was the expected trend (Figure 4.16B). However, for MSLN and PDPN it was not possible to discern a significant difference between the median expression level of these markers between the two tumour types (Figure 4.16B).

Collectively, assessment of iMig MPM markers in RNA sequencing datasets indicated that 2/4 negative (TTF1 and EpCAM) as well as 2/4 positive (MSLN and PDPN) markers could be of use to validate the presence of MPM cells, with the negative markers performing slightly better than the positive markers (Figure 4.16). However, this data suggests that markers known for differentiation of MPM by IHC should be used with caution in RNA sequencing datasets.

4.3.6 Quality control and validation of normal pleura RNA sequencing dataset

All RNA sequencing experiments were outsourced to UCL genomics and subsequent bioinformatic interrogation of the dataset was achieved in collaboration with Dr Adam Pennycuick.

Initially, quality control of the four populations which comprise the VMC dataset (samples S, T, U and W) was conducted (Table 4.3). For ease of analysis this dataset is referred to as normal pleura henceforth.

Table 4.3 Summary of FACS-sorted VMC populations which make up the pleural dataset.

Sample	Tissue source	Isolation method	Cell count	Sample name
PEA254	Post-mortem	Pleural brushing	10,000	S
ASC011	Lung resection	Pleural brushing	6,100	T
ASC012	Lung resection	Pleural brushing	25,000	U
ASC013	Lung resection	Pleural brushing	1,700	W

We found similar library size across the four samples although a low RNA sequencing depth was identified in the normal pleura dataset (Figure 4.17A). Analysis by PCA plot revealed no obvious outliers (Figure 4.17B), although the sample size is too small to deduce this

conclusively (n=4). Sample S was the only post-mortem sample and was located slightly apart from the remaining three lung resection samples in the PCA plot (Figure 4.17B). GTEx samples were used as a reference, to compare the library size between bulk sequenced normal tissues and the normal pleura (Figure 4.17C). This showed that the GTEx bulk sequenced tissues had a much larger library size compared to the pleural samples (Figure 4.17C).

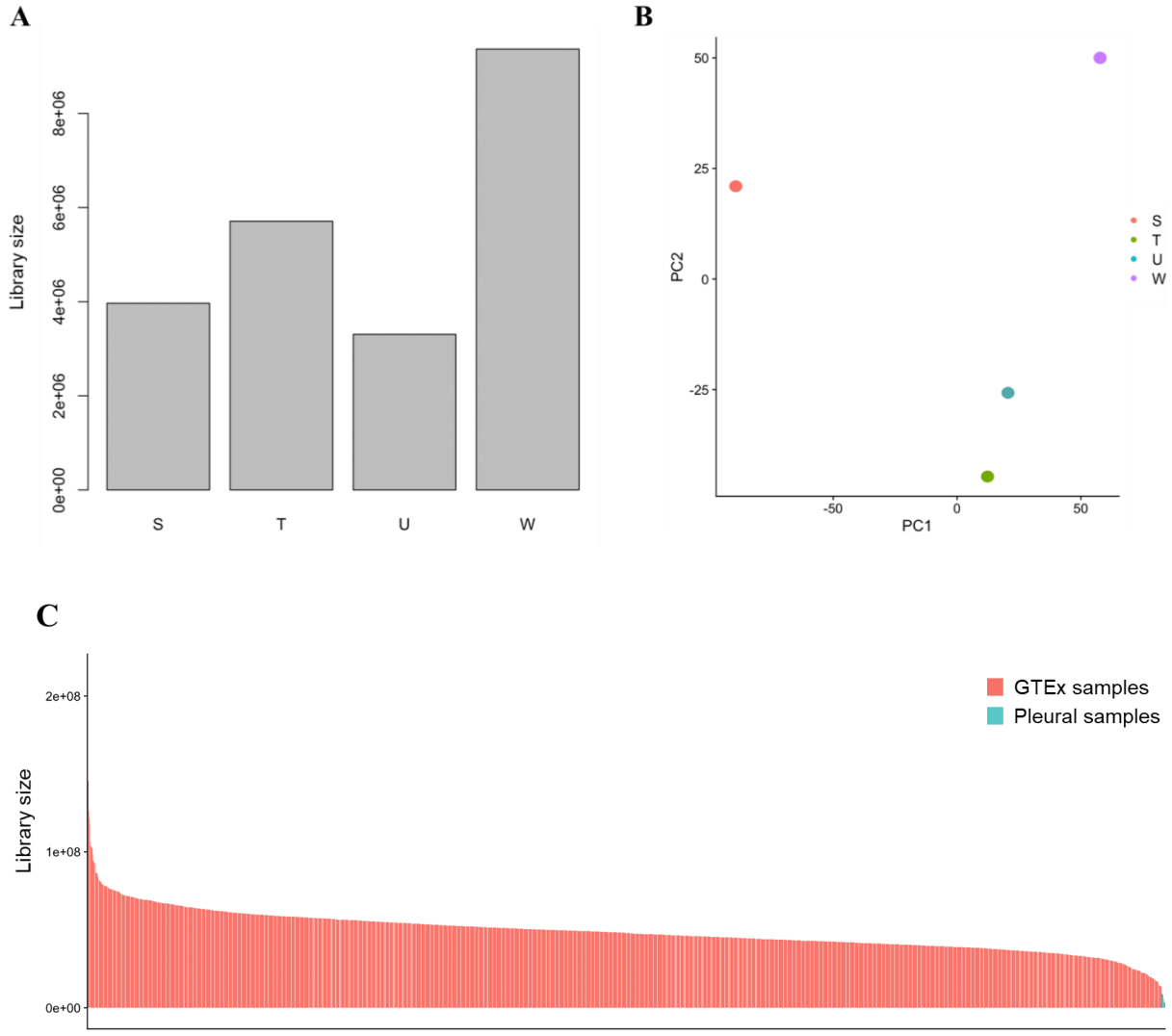

Figure 4.17 Quality control of the pleural dataset. A) Plot shows library size across the pleural samples, named S, T, U and W. B) PCA plot analysis of the pleural samples. C) Comparison of library size between GTEx bulk sequenced tissues and the four pleural samples showed the library size of pleural samples to be much lower.

Next, the GTEx bulk RNA sequenced repository of normal tissues was used to determine the similarity of the pleural samples to all other available normal tissue types (Figure 4.18A). UMAP analysis revealed that the pleural samples most closely resembled lung tissue, although these formed an adjacent and distinct group compared to the lung samples (Figure 4.18B).

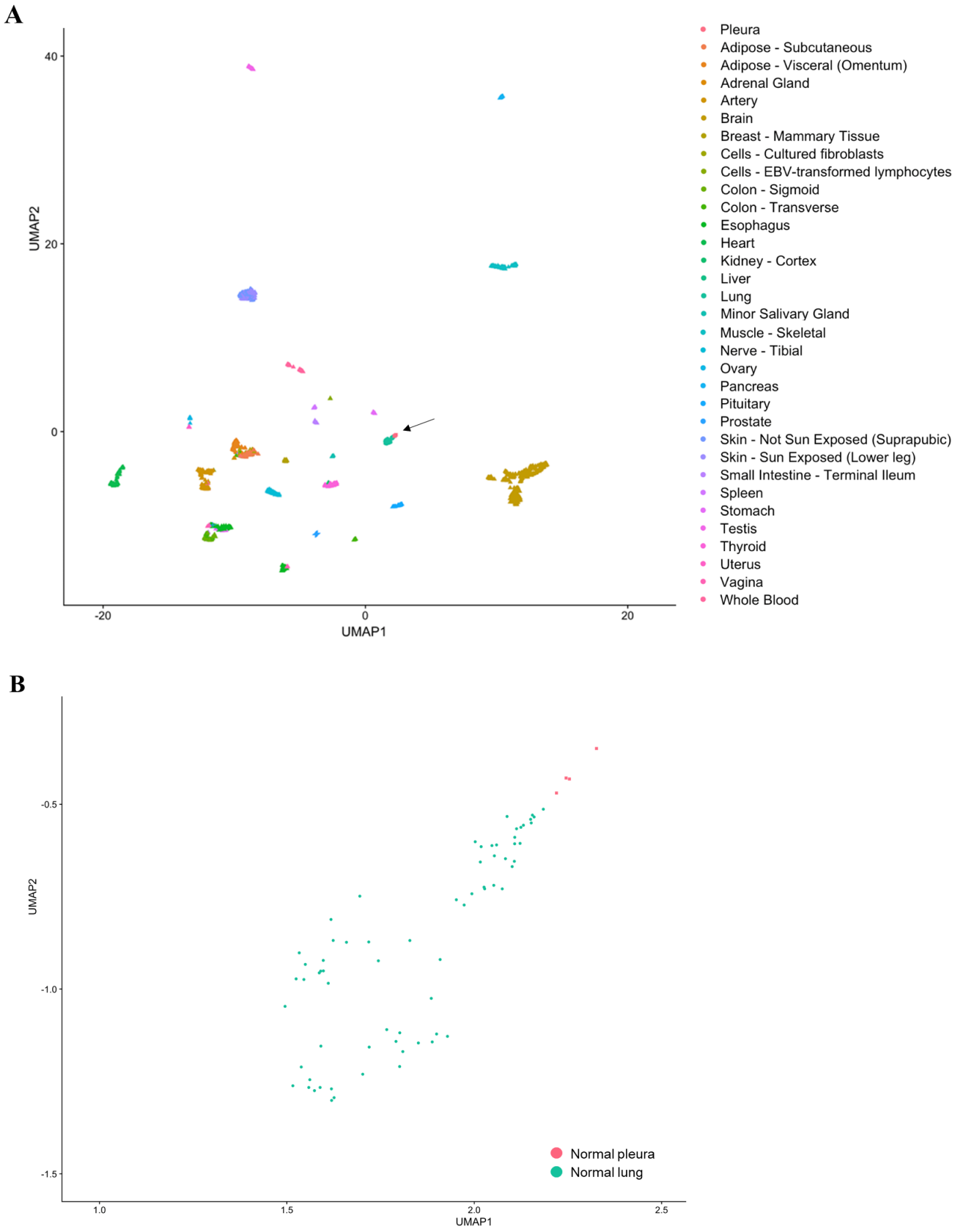

Figure 4.18 UMAP analysis of pleural samples compared to normal tissues. All data accessed through the GTEx portal. A) Arrow points to pleural samples which cluster close to normal lung tissue. B) Closer view of normal pleura (n=4) and normal lung populations (n=68).

4.3.7 Transcriptomic comparison of normal pleura and normal lung tissue

Normal pleura and GTEx normal lung tissue datasets were compared, to identify differentially expressed genes (DEGs) and to use these to perform pathway analysis. We identified 11,037 DEGs which were subsequently used for pathway analysis. Pathway analysis revealed 27 significantly downregulated and 3 significantly upregulated pathways in normal pleura compared to normal lung (Figure 4.19). Our pathway analysis suggested that normal pleura has upregulated oxidative phosphorylation and thus mitochondrial activity, protein production and DNA repair compared to normal lung tissue. Interestingly, TGFβ signalling and Hedgehog signalling were found to be downregulated in the normal pleura compared to normal lung.

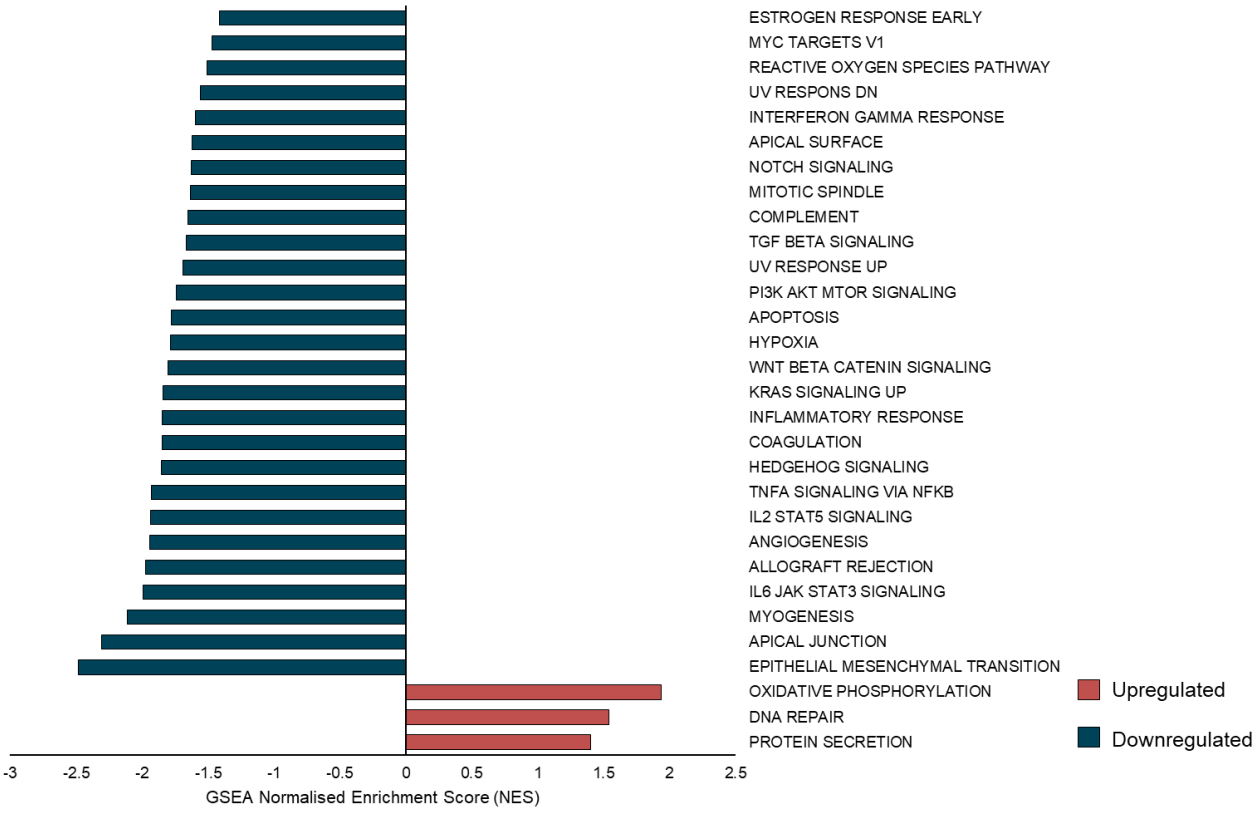

Figure 4.19 Pathways analysis using normal pleura and normal lung RNA sequencing datasets.

Finally, we used the iMig panel of IHC markers recommended for MPM differentiation, to investigate expression of specific genes in the normal pleura compared to normal lung tissue. We did not expect the trends shown previously to be reproduced (Figure 4.16) as these markers are used for MPM and not normal mesothelial cells but we wanted to use these as an indicator to validate the normal pleural samples. Importantly, none of the gene expression comparisons between normal pleura and normal lung for the 8 MPM markers reached statistical significance and therefore it was not possible to biologically interpret these trends (Figure 4.20).

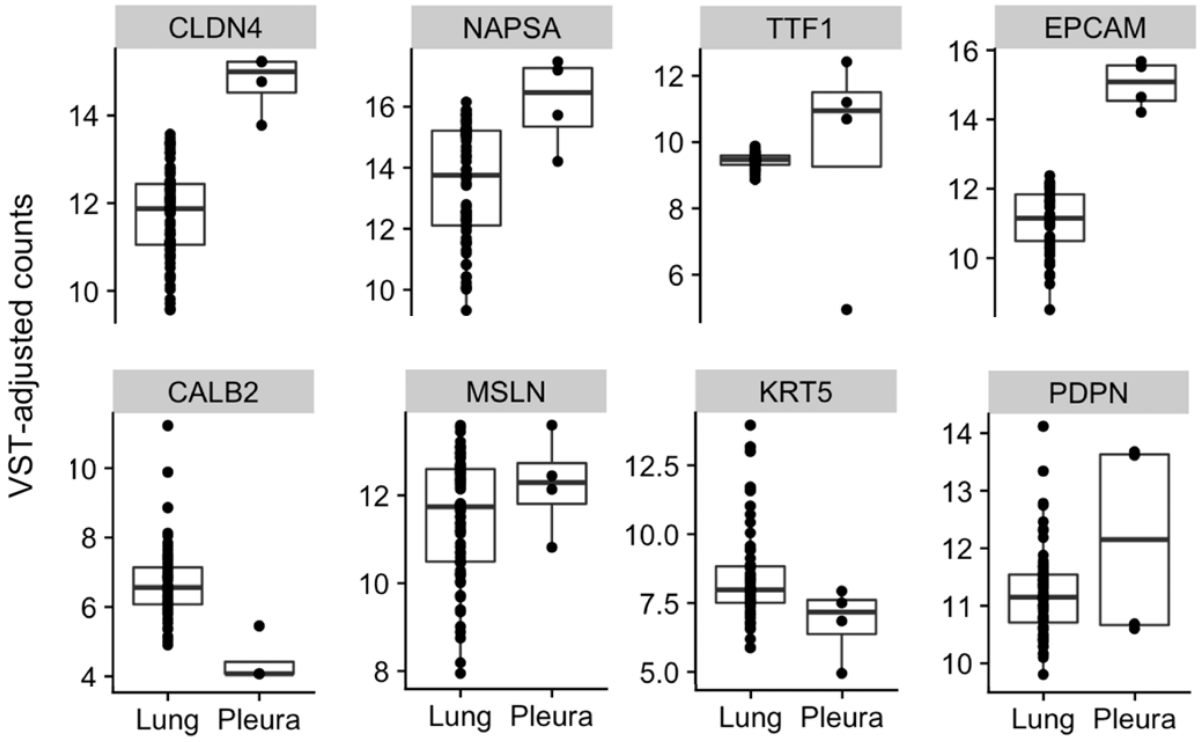

Figure 4.20 Comparison of RNA sequencing counts for iMig recommended MPM markers, between bulk RNA sequenced lung tissue and normal pleura. Lung samples (n=68) from GTEx were compared to normal pleural samples (n=4). The top panel represents the gene expression of 4 negative MPM markers and the top panel represents 4 positive MPM markers. A statistically significant threshold ($p < 0.05$) was not reached for any of the comparisons.

4.3.8 Comparative gene expression between normal pleura and MPM

Using the normal pleura dataset, we aimed to identify and highlight changes in gene expression between normal pleura and MPM. To assess the gene expression signature of normal pleura, we conducted UMAP analysis of normal pleura, normal lung and MPM. UMAP analysis revealed that pleural samples are situated closer to lung tissue than MPM tissue (Figure 4.21). MPM samples formed a separate and distinct group with only one clear outlier visible.

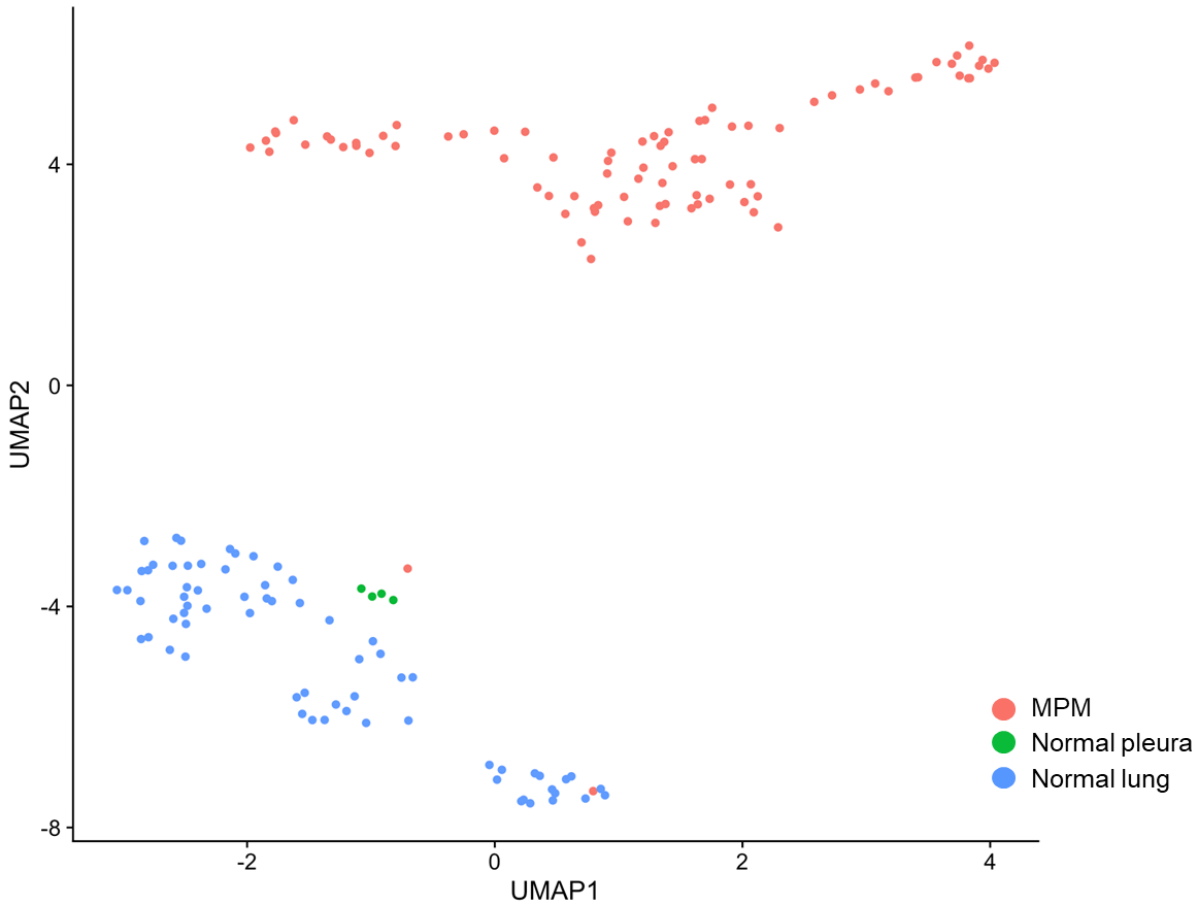

Figure 4.21 UMAP analysis of normal pleura and lung compared to MPM. GTEx bulk RNA Sequenced lung tissue (n=68) and TCGA bulk RNA Sequenced MPM tissue (n=86) were used for this analysis.

Differentially expressed genes (DEGs) between the normal pleura and MPM datasets were identified. Implementing cut-off criteria of larger than two-fold change (log2FC > 2 and log2FC < -2) and adjusted p-value lower than 0.05, we identified 6,683 DEGs between the two datasets. The top ten DEGs based on ascending adjusted p-value are shown in Table 4.4.

Table 4.4 List of most significantly altered genes in normal pleura compared to MPM. Genes are ranked by lowest adjusted p-value. Positive fold change indicated upregulation in normal pleura while negative fold change indicates downregulation in normal pleura.

Gene	Gene name	Fold change (log2)	Adjusted p-value
PDXDC2P	pyridoxal dependent decarboxylase domain containing 2, pseudogene	8.20	2.9E-163
LINC00674	long intergenic non-protein coding RNA 674	6.15	2.1E-111
ZBTB20	zinc finger and BTB domain containing 20	8.69	3.9E-101
HNRNPL	heterogeneous nuclear ribonucleoprotein L	-3.16	6.7E-101
SARNP	SAP domain containing ribonucleoprotein	5.06	1.19E-98

RBM34	RNA binding motif protein 34	5.48	1.06E-96
CHMP4B	charged multivesicular body protein 4B	-5.51	8.74E-93
PRPF19	pre-mRNA processing factor 19	-5.86	8.44E-92
HNRNPH2	heterogeneous nuclear ribonucleoprotein H2	-4.46	1.5E-86
SPSB3	splA/ryanodine receptor domain and SOCS box containing 3	4.91	1.53E-79

Using the list of 6,683 DEGs, we carried out KEGG Pathway analysis to ascertain which pathways are downregulated in normal pleura compared to MPM (Figure 4.22). Thirty significantly upregulated pathways were identified as downregulated in normal pleura.

This analysis suggested that MPM is characterised by oncogenic pathway activation, EMT, hypoxia, apoptosis and metabolic changes (Figure 4.22). Key findings included, TGFβ signalling and Hedgehog signalling downregulation in normal pleura compared to MPM. Notably, *TGFB1* and Hedgehog transcription factor *GLI2* were in the top 500 and top 1250 DEGs respectively.

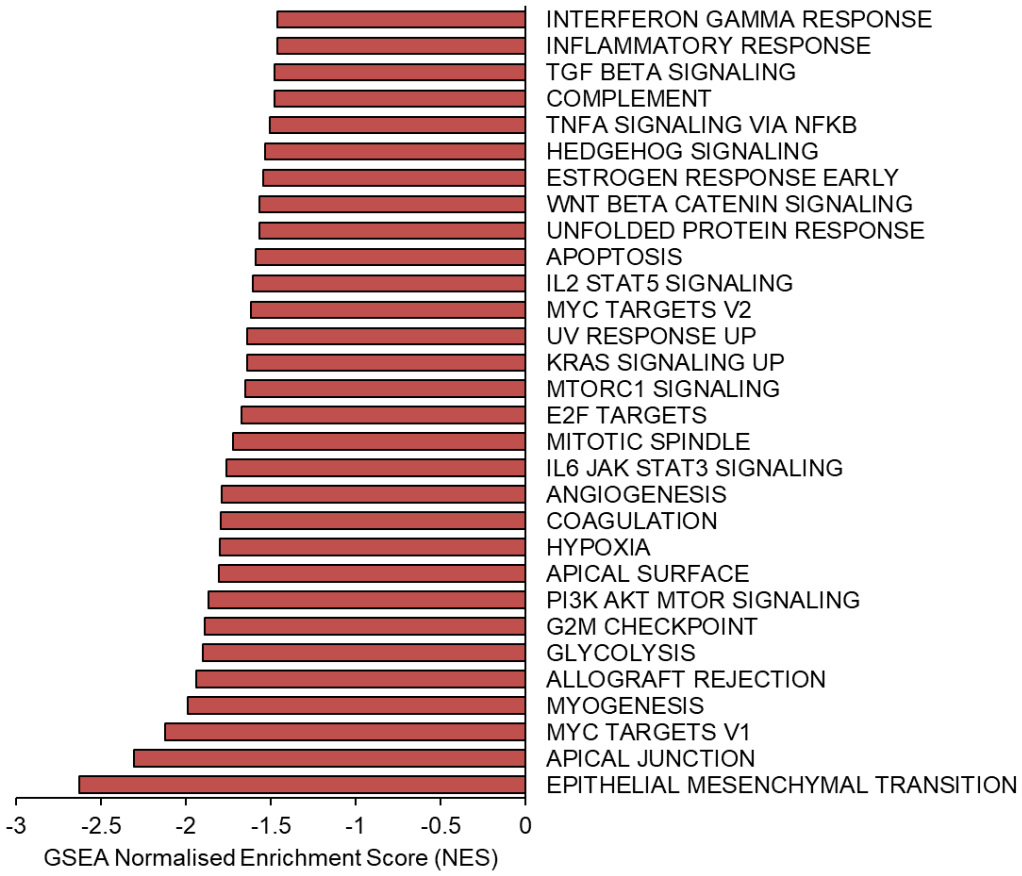

Figure 4.22 Summary of significantly downregulated pathways in normal pleura compared to MPM. TCGA cohort of MPM (n=86) was compared to normal pleura (n=4).

4.4 Discussion

The aim of this research was to isolate and analyse the transcriptome of normal human VMCs from distal lung tissue. An early finding when I implemented enzymatic digestion of human visceral pleura was the inefficiency of this method for isolation of a homogeneous population of human VMCs, as there was extensive fibroblast growth in early cultures. As culture time progressed, spindle-like fibroblasts took over the cultures and became the predominant cell type by P1 (Figure 4.4). Flow cytometry demonstrated that in cultures from digests at P1, CD90+ fibroblasts constituted up to 98.2% of the cell population (Figure 4.5). Thus, a key limitation of enzymatic digestion for isolation of VMCs is that lung parenchyma cannot be completely removed from the pleural layer and thus the underlying connective tissue which consists of ECM matrix and stromal fibroblasts contaminate the resulting digested cell population. Therefore, an alternative approach to isolate VMCs was sought.

Brushings of human airways have been used successfully in our laboratory, to culture primary bronchial airway epithelial cells. I extrapolated this method to distal lung and used a cytology

brush to collect surface VMCs without damaging the surface of the pleural basal lamina (Figure 4.7). Flow cytometric analysis of cells derived from pleural brushing showed a CK5+ population of 92.1%, whilst the CK5+ population obtained from pleural digest was 65.2% (Figure 4.8, Figure 4.3A). Furthermore, brightfield images of early VMC pleural brushing cultures indicated that the predominant cell type consisted of round cells which measured 11.2 µm and had surface protrusions (Figure 4.5). This size is comparable to the 12.8 µm VMCs identified by SEM imaging and quantified by ImageJ previously (Figure 3.14). Collectively, pleural brushing is a much more efficient VMC isolation method when compared to pleural digestion due to the speed, ease and inexpensive nature of the technique and its ability to provide populations of VMCs at P0 with minimal fibroblast contamination (Figure 4.7).

However, the flow cytometric analysis of P1 cells from pleural brushing indicated a key issue; that mesothelial cells are still gradually outcompeted by fibroblasts as culture time progressed (Figure 4.10). There are several options which could aid VMC growth for the establishment of long-term cultures. It is possible that primary VMCs require a feeder layer to grow *in vitro* which may emulate the connective tissue layer which underpins the visceral mesothelium (128). In addition, there is some evidence to suggest that mesothelial cells grow under hypoxic conditions (199). Thus, to optimise primary VMC cultures conditions, multiple approaches should be attempted, including seeding of VMCs onto a feeder layer of mitotically inactivated mouse fibroblasts and reduction in oxygen concentration (225).

A surprising finding was the large cell population identified in the sample transport medium. This cell population was postulated to be mesothelial cells rather than epithelial cells, due to epithelial cells requiring enzymatic digestion of lung tissue to be released. Furthermore, the previous SEM imaging of lung resection samples (n=6) provided evidence that VMCs detach from the pleural surface (Figure 3.13). Finally, this hypothesis was supported by the finding that the population of cells in the transport medium highly expressed CK5 up to an estimated 97% of the population (n=4).

The cells found in transport medium are referred to as free-floating VMCs, to distinguish them from the tissue-resident VMCs acquired through pleural brushing. Importantly, in the one patient sample for which the free-floating cells and tissue-resident VMCs were quantified in parallel, the viability of free-floating VMCs was measured at 60.2% compared to a viability of 40.7% identified in tissue-resident cells (Figure 4.12). Thus, free-floating VMCs in the medium appear to remain viable despite detachment. Therefore, it is unlikely that these VMCs detached

from the pleural surface due to induction of apoptosis. In future, to avoid unnecessary loss of viable mesothelial cells, lung resection samples could be transported in air from theatre to the laboratory rather than submerged in transport medium.

Importantly, the positive free-floating VMC viability can be used to interpret the SEM images of visceral mesothelium depicted in the previous Chapter (Figure 3.34). Two hypotheses can be formed based on this result. The first hypothesis is that VMCs detach due to unavoidable mechanical forces imposed on the visceral pleura during transport. However, due to frequent denudation of the visceral mesothelium observed on fixed distal lung tissue (Figure 3.13), it is possible to hypothesise that VMC detachment can only be partially attributed to transportation artefact. The second hypothesis is that free-floating VMCs respond to the increase in transport liquid and this causes their passive detachment. This could be due to an innate mesothelial response to the increase of pleural fluid, which *in vivo* could be a sign of infection, inflammation or malignancy. Thus, free-floating VMCs could mimic the role of VMCs *in vivo*. It is possible that a VMC shedding model is necessary for intrinsic functions of the mesothelium, such as wound healing or tissue regeneration, as proposed previously (Figure 3.34). To determine if detached, free-floating VMCs have a functional role, comparative characterisation of the gene expression differences between the two cell populations is required.

A key objective of this research was to determine the transcriptomic expression of VMCs in homeostasis. As long-term cultures of pleural brushings indicated that a population of fibroblasts remained present, I developed a FACS-purification method to exclude contaminating cell types directly after pleural brushing, at P0 (Figure 4.14). This approach was similar to the negative panel of markers used by Rinkevich *et al.* to isolate mouse mesothelial cells from mesothelium of visceral organs (16). In the approach used by Rinkevich *et al.*, the endothelial markers CD31 and Tie1 as well as the immune cell marker CD45 and Ter119 for RBCs, were used as negative markers whilst MSLN was used as a positive marker for mesothelial cell sorting. Their FACS-purification strategy from mouse mesothelia resulted in mesothelial cell yields of 5×10^3 cells per tissue sample.

In the FACS-purification outlined here, no positive mesothelial cell marker was used because a ubiquitous positive marker does not exist in the literature and was not identified in flow cytometry assessment of *in vitro* mesothelial models (Table 4.1) (17). Furthermore, MSLN which was used by Rinkevich *et al*. as a positive mesothelial marker, was shown to stain sub-pleural cells including alveolar epithelial cells (Figure 3.6C). Therefore, to avoid selection bias,

an elimination strategy for contaminating cell types was employed to purify VMC population and enable a 'cleaner' view of VMCs by RNA sequencing. The endothelial cell surface marker CD31 (PECAM-1) was used to differentiate and negatively sort contaminating endothelial cells (143,226). From the *in vitro* investigations, CD90-positive fibroblasts appeared to contaminate the primary VMC cultures (Figure 4.5, Figure 4.6). There is no universal fibroblast marker *in vivo* although CD90 has been reported to identify *in vitro* fibroblasts and endothelial cells (227). Thus, CD90 was incorporated in the negative marker panel to label fibroblasts and endothelial cells. Finally, CD235α was used as a marker of RBCs and CD45 was used to mark immune cells. This FACS-purification strategy revealed that populations of endothelial cells and fibroblasts constituted approximately 4.3% and 4% of the live CD235α- CD45- pleural brushing-derived cell population respectively (n=4). This agrees with the earlier finding that pleural brushing cells were 92.1% positive for CK5 (Figure 4.8) and adds confidence that the pleural brushing method allows the isolation of a purer VMC population than other human PMC isolation methods.

Using the pleural brushing isolation method, four VMC populations were FACS-purified, which resulted in VMC counts of up to 25 x 10^3 cells per sample (Table 4.1). Purified VMC populations were subsequently RNA extracted and RNA sequenced. Although this approach will not be able to provide information of subpopulations or intra-population heterogeneity, which are advantages of scRNA-seq, it provides a fast, easily accessible and location-specific isolation method which can be applied in a large number of research laboratories for the study of VMCs in homeostasis and various pleural disease settings. A limitation of my approach is that a completely homogeneous VMC population is unlikely due to marker limitations. However, the CK5 expression and homogeneous nature of early cultures suggest that remaining contamination with other cell types is minimal, estimated at ~5% based on flow cytometry results.

The availability of normal human pleura is limited, with no previous attempts to isolate a pure population of human VMCs to my knowledge. Transcriptomic analysis of VMCs in homeostasis and their comparison to MPM offered insight into the gene expression changes which underpin pleural malignancy and generated 30 pathways which are downregulated in normal pleura compared to MPM (Figure 4.22). Therefore, as the identified pathways are upregulated in MPM, they present an unexplored area of significant therapeutic interest.

In summary, this research constitutes a significant progress in the capture and transcriptomic characterisation of this mesothelial cell type about which little is known. Importantly, my method provides VMC yields far superior to those reported in mouse isolation methods and several scRNA-seq mesothelial datasets from IPF studies (16,81–83). Finally, the methodology for acquisition and gene expression information from this non-malignant pleural VMC dataset will allow the research field to fully utilise the MPM cohorts which have been culminated by research consortiums and are publicly available.

4.5 Summary

- Enzymatic digestion of human visceral pleura is not suitable for isolation of a pure VMC population.
- Pleural brushing of human visceral pleura is a new, fast and more effective VMC isolation method compared to currently used approaches of pleural digestion and pleural fluid centrifugation.
- Viable free-floating mesothelial cells indicate that VMCs easily and frequently detach from the basal lamina during transport.
- A FACS strategy utilising negative sorting allows the isolation of a purified VMC population from human pleural brushings with cell yields of up to 25×10^3 and estimated mesothelial cell population purity of ~95%.
- Gene expression analysis of four FACS-purified VMC populations revealed their transcriptomic expression to be similar yet distinct from normal lung tissue by UMAP analysis.
- Pathways analysis resulted in 30 upregulated pathways in MPM compared to normal pleura, including upregulation of TGFβ and Hedgehog signalling.

5 Investigation of Hedgehog signalling in MPM

5.1 Background

Hedgehog signalling is critical for the embryonic development of the lung and pleura but is thought to be expressed at low levels in adult tissues during homeostasis (186). In embryonic studies of murine visceral pleura, VMCs have been shown to express Hedgehog signalling proteins Smo and Gli1 (7). A small number of previous studies suggest that the Hedgehog pathway may be reactivated in a subset of MPM cell models and tumours, with increased expression of the Hedgehog transcription factors GLI1 and GLI2 previously reported (191,199,200). However, there is disparity in the literature regarding which transcription factor, between GLI1 and GLI2, is responsible for upregulated Hedgehog signalling in MPM (191,199). In addition, their function in MPM has not been explored.

After bioinformatic comparison between our normal pleura dataset and the publicly available TCGA MPM cohort, we sought to examine Hedgehog signalling as it was identified as 1 of 30 upregulated pathways in MPM. Furthermore, by using the normal lung tissue dataset from GTEx we were able to identify that Hedgehog signalling is downregulated in normal pleura compared to normal lung tissue, which indicates that the Hedgehog pathway is only expressed at a low or baseline level in normal pleura and may be aberrantly activated in a subset of MPM tumours. I sought to examine this hypothesis and to identify which components of the Hedgehog pathway are upregulated in MPM.

GLI proteins are transcription factors which are activated by post-translational modifications regulated either by the Hedgehog signal mediator SMO or by non-canonical activation through pathways such as Notch, Wnt, PI3K/AKT and TGFβ (169,171,173). The upregulation of GLI transcription factors in MPM has been noted in the literature but the activation route of upregulated GLI proteins in MPM has not previously been investigated (191). Furthermore, the investigation of the therapeutic potential of the Hedgehog pathway has been incomplete due to a low number (n=3) of *in vitro* models used to test GLI inhibitors (200). I aim to address both these unexplored areas of Hedgehog signalling in MPM using a panel of 6 MPM cell models.

5.2 Aims

- To determine which Hedgehog transcription factors are upregulated in MPM.
- To examine the expression of Hedgehog signalling components in MPM cell models.
- To explore the route of activation of Hedgehog transcription factors in MPM.

- To investigate the function of upregulated Hedgehog transcription factors.
- To investigate the therapeutic efficacy of Hedgehog pathway inhibition in MPM cell models.

5.3 Results

5.3.1 Investigation of Hedgehog transcription factor expression in MPM

Based on pathway analysis findings from the comparison between normal pleura and MPM (Figure 4.22), we sought to use the TCGA MPM cohort to investigate the gene expression of Hedgehog transcription factors. All bioinformatic analyses of the TCGA dataset were done in collaboration with Dr Adam Pennycuick and Dr Ryan Arathimos.

To establish which, if any, of the Hedgehog transcription factors were significantly upregulated, the RNA sequencing counts of *GLI1*, *GLI2* and *GLI3* were compared between MPM and other cancers. The transcription factor *GLI2* was significantly upregulated in MPM (n=86) when compared to 20 other cancer types (Figure 5.1A). In addition, the distribution in *GLI2* RNA sequencing counts suggested a distinct subset of MPM tumours with high expression of *GLI2* (Figure 5.1A). We did not identify a significant upregulation in *GLI1* RNA sequencing counts when conducting the same comparative gene expression analysis (Figure 5.1B). Similarly, *GLI3* was not found to be significantly upregulated in MPM (data not shown).

A

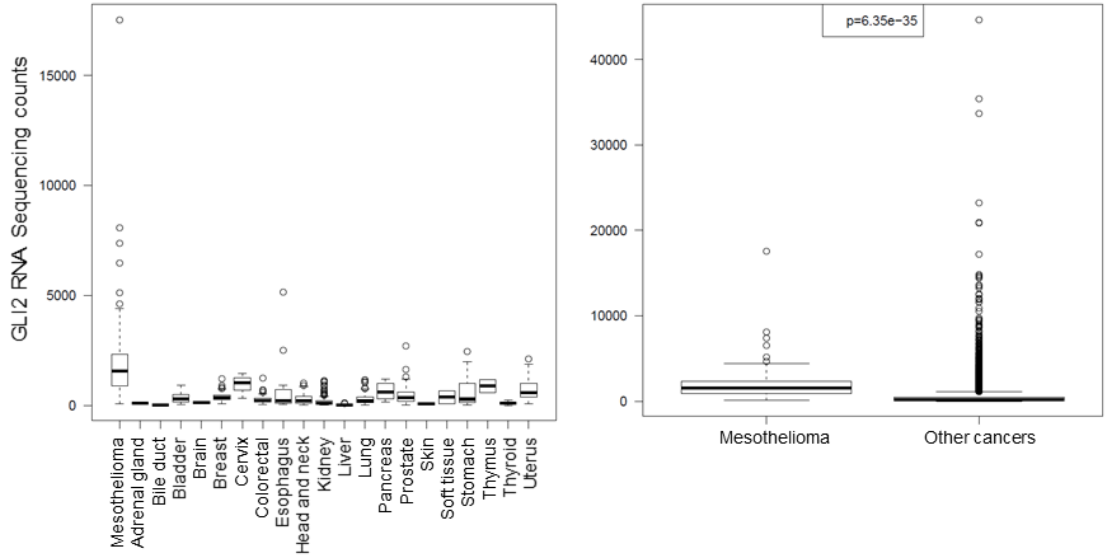

B

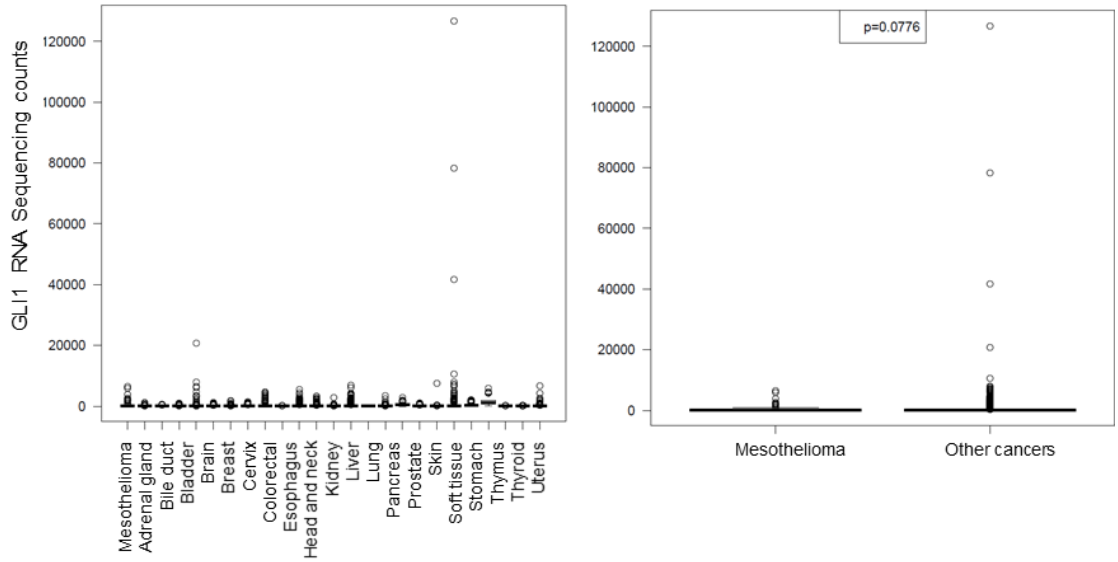

Figure 5.1 Gene expression of Hedgehog signalling transcription factors in MPM compared to other cancer types. A) *GLI2* is upregulated in MPM (n=86) compared to 20 other cancer types ($p=6.35 \times 10^{-35}$). B) *GLI1* is not significantly upregulated in MPM (n=86) compared to other cancer types (p=0.0776). All RNA sequencing data was accessed through the TCGA. This analysis was performed with the help of Dr Adam Pennycuick.

To investigate the gene expression of GLI transcription factors in MPM compared to normal pleura we used the normal VMC dataset. *GLI1* and *GLI2* RNA sequencing counts were higher in MPM than in normal pleura (Figure 5.2). Statistical comparison was not significant, due to low statistical power.

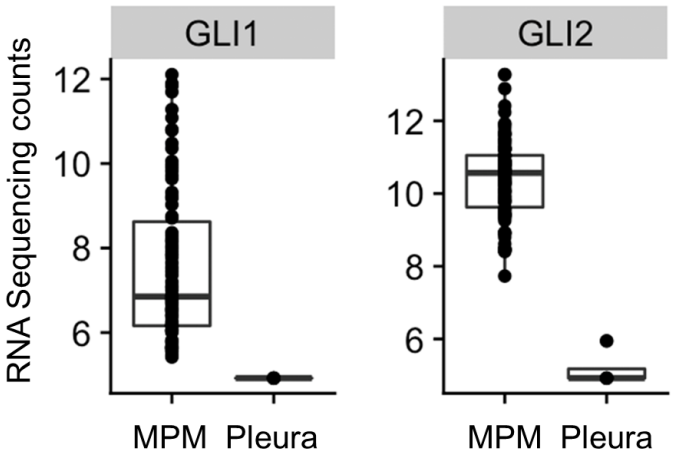

Figure 5.2 Gene expression of Hedgehog signalling transcription factors in MPM compared to normal pleura. Difference in gene expression of GLI1 and GLI2 between MPM (n=86) and normal pleura (n=4) is shown. Statistical comparison was performed by t-test. All MPM RNA sequencing data was accessed through the TCGA. This analysis was performed with the help of Dr Adam Pennycuick.

To validate the Hedgehog upregulation trend seen in our comparison of normal pleura to MPM and to explore the *GLI2* upregulation identified in the TCGA dataset, we sought to measure GLI2 expression in normal pleura by IHC. We utilised a tissue microarray containing normal pleura. Human airway was stained in parallel as a positive control. This assessment revealed minimal or no GLI2 staining in all microarray cores of normal pleura (n=4) (Figure 5.3).

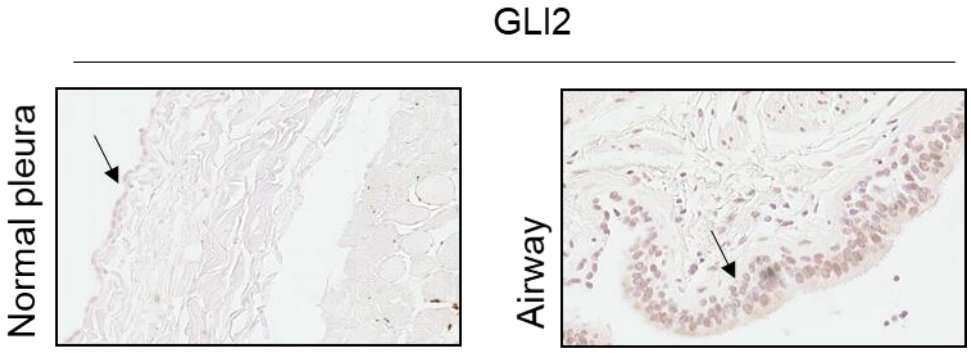

Figure 5.3 GLI2 expression detected by immunohistochemistry in normal pleural tissues. Representative GLI2 IHC images are shown from normal pleura (n=4). Human airway was used as a positive control tissue.

To identify whether the Hedgehog pathway harboured mutations which could cause the upregulation of *GLI2*, we next interrogated the status of all major Hedgehog pathway components in the MPM dataset through cBioportal. This genetic analysis depicted by OncoPrint plot, indicated that a subset of tumours constituting 8.4% showed an upregulation in Hedgehog ligands, *SHH*, *DHH* or *IHH* (Figure 5.4). Genomic alterations were present in two Hedgehog pathway components which are known tumour suppressor genes; truncating and

missense mutations in the receptor *PTCH1* as well as missense and deep deletions in *SUFU* (Figure 5.4). The activator transcription factors *GLI1* and *GLI2* showed a combined estimate of 12% genetic perturbation in this tumour cohort and were characterised by mRNA upregulation. Interestingly, *GLI2* analysis revealed mRNA upregulation with no detectable Hedgehog pathway mutations in this MPM cohort. Furthermore, cases which had *GLI2* mRNA upregulation did not exhibit mutations in other Hedgehog pathway components. Therefore, based on this investigation there is no clear Hedgehog pathway mutation which could explain the identified *GLI2* upregulation in MPM.

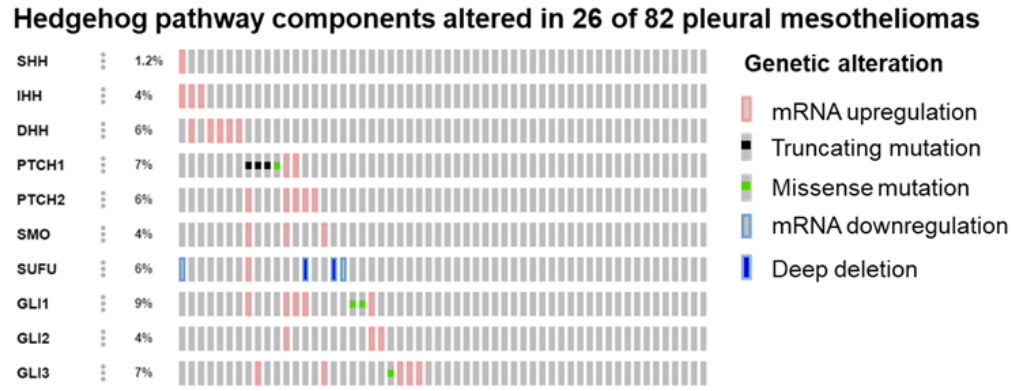

Figure 5.4 Summary of genomic alterations in Hedgehog pathway genes from the TCGA cohort of MPM tumours. OncoPrint analysis generated in cBioPortal is based on DNA and RNA sequencing data from MPM PanCancer Atlas dataset (n=82). An mRNA expression z-score threshold of 2.0 relative to diploid samples was implemented.

5.3.2 Investigation of the Hedgehog pathway in MPM cell models

To investigate the expression of Hedgehog signalling components at protein level, I utilised a panel of 8 MPM cells lines; 5 early passage cell cultures were purchased from MesobanK and 3 MPM cell lines were obtained from the Sanger Institute (Figure 5.5). MesobanK cells are thought to have been cultured less extensively than the established Sanger cell lines and thus may constitute better MPM models as they more closely resemble patient tumours. The ovarian cancer cell line TOV112D and adenosquamous lung carcinoma cell line H513 were used as positive controls for the immunoblot, as these are known GLI and SHH expressing cell lines respectively (Figure 5.5). Primary non-immortalised lung fibroblasts were also included in the analysis as a model of stromal cells (Figure 5.5).

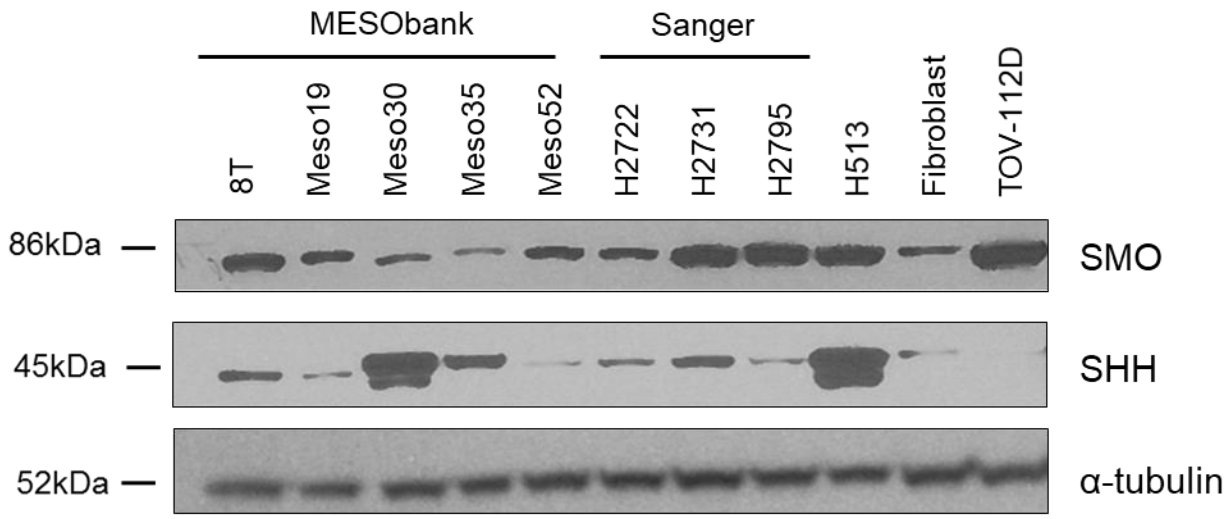

Figure 5.5 Immunoblot showing expression of Hedgehog ligand SHH and signal mediator SMO.

Expression of the ligand SHH was detected in all MesobanK cell lines although Meso52 only showed weak expression (Figure 5.5). All Sanger cell lines (3/3) expressed the ligand SHH (Figure 5.5). All MPM cell lines (8/8) expressed the signal mediator SMO, with the three Sanger cell lines showing the strongest expression (Figure 5.5). As the Sanger cell lines strongly expressed Hedgehog pathway proteins by immunoblot, I expanded the number of Sanger cell lines used for Hedgehog signalling investigation.

Next, to determine the expression of key Hedgehog pathway components I examined the protein expression of all three GLI proteins, SMO, SHH and the negative cytoplasmic regulator SUFU in a panel of 6 Sanger MPM cell lines and the transformed mesothelial cell line Met5A (Figure 5.6).

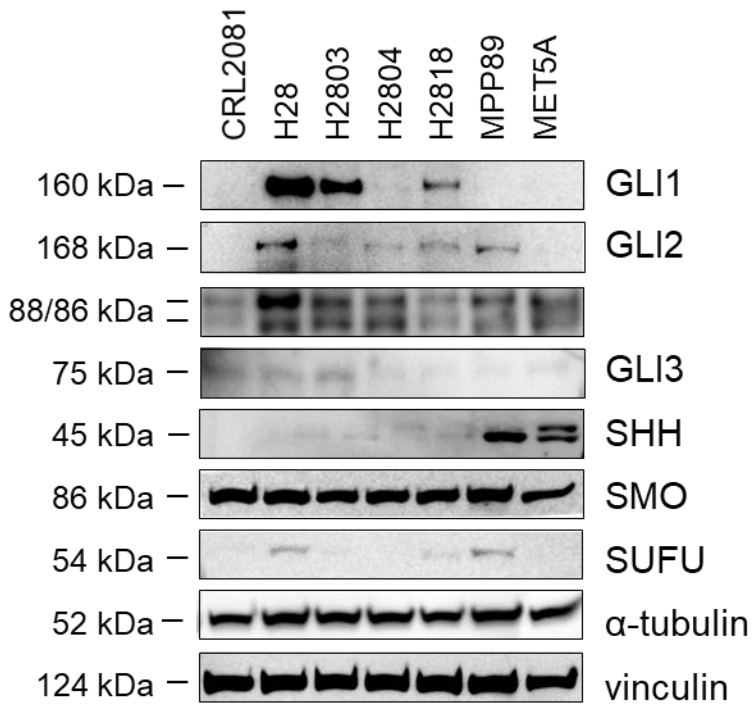

Figure 5.6 Immunoblot showing the expression of Hedgehog pathway components. Six MPM Sanger cell lines and the transformed mesothelial cell line Met5A were probed for expression of Hedgehog signalling proteins. GLI2 has 4 isoforms of which 3 are detectable by immunoblot in these cell lines (168, 88 and 86 kDa). Antibodies against α-tubulin (52 kDa) and vinculin (124 kDa) were used as loading controls.

5.3.3 Association of TGFβ with Hedgehog transcription factors

To explore the possible route of GLI protein upregulation, their association with other genes was investigated using the MPM RNA sequencing dataset from the TCGA. Linear regression analysis of *GLI1* revealed 198 genes which satisfied Bonferroni adjustment (Appendix Table 7.1). The volcano plot in Figure 5.7 depicts *GLI1* association with other genes in the RNA sequencing dataset. The ten genes with lowest Bonferroni adjusted p-value are shown in the table (Figure 5.7). This analysis revealed that GLI1 expression is associated with the Hedgehog receptor homologue *PTCH2*, followed by the classical receptor *PTCH1* while the negative Hedgehog pathway regulator *HHIP* is also strongly associated with *GLI1* gene expression. The third and fourth most strongly associated genes are Inhibin beta subunit E (*INHBE*) and transforming growth factor beta-2 (*TGFB2*). This suggests TGFβ pathway interaction with the Hedgehog transcription factor in this MPM cohort.

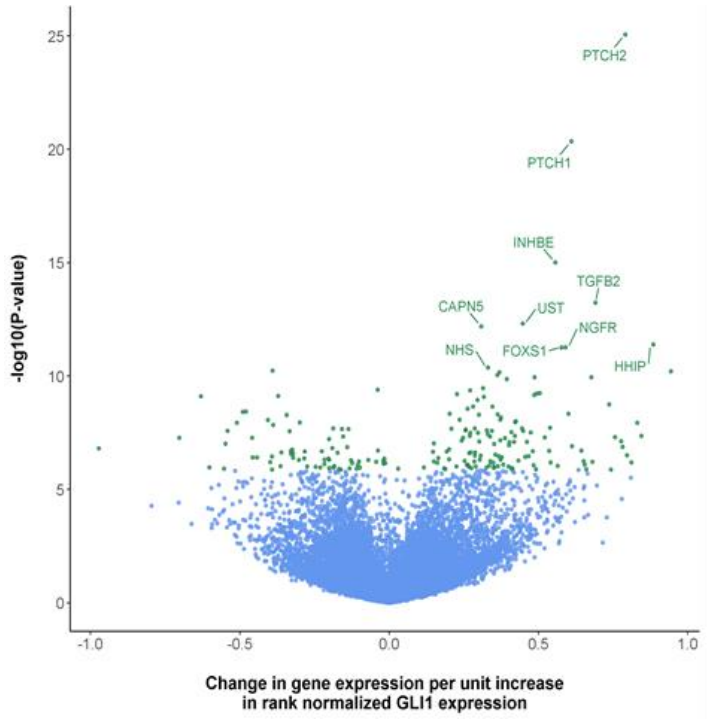

Gene	Bonferroni adjusted p-value
PTCH2	3.23626E-21
PTCH1	1.62393E-16
INHBE	3.60651E-11
TGFB2	2.11217E-09
UST	1.76282E-08
CAPN5	2.37361E-08
HHIP	1.51037E-07
NGFR	1.97753E-07
FOXS1	2.04586E-07
NHS	1.57796E-06

Figure 5.7 Association of GLI1 with genes in the MPM TCGA dataset. Volcano plot depicts association of GLI1 gene expression with expression of 36,725 genes in MPM RNA sequencing dataset, available through the TCGA (n=86). Genes which satisfy Bonferroni adjustment ($p \leq 0.05$) are represented in green (n=198). The top 10 *GLI1* associated genes are shown in the table. Genes on the right side of the volcano plot are positively associated with *GLI1* while genes on the left side are negatively associated with *GLI1*. This analysis was provided as part of a collaboration with Dr Ryan Arathimos.

To examine the association of *GLI2* we conducted the same linear regression analysis. Interestingly, *GLI2* was found to be associated with 357 genes, compared to 198 genes associated with *GLI1*. In the *GLI2* linear regression analysis *PTCH1* appeared in the top 20 associated genes and was positively associated with *GLI2*. The gene *STK36* that encodes a serine/threonine kinase and is known as a positive regulator of GLI proteins was positively associated with *GLI2* gene expression.

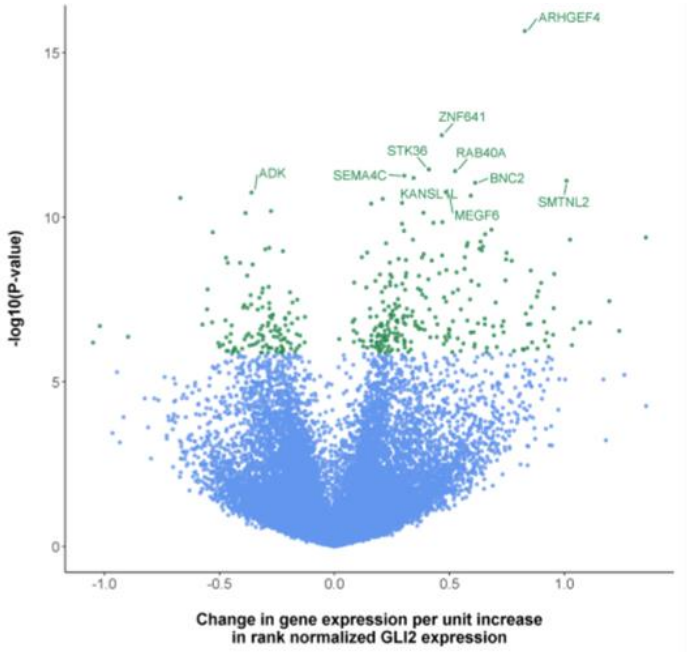

Gene	Bonferroni adjusted p-value
ARHGEF4	8.03E-12
ZNF641	1.17E-08
STK36	1.30E-07
RAB40A	1.46E-07
SEMA4C	2.00E-07
KANSL1L	2.31E-07
SMTNL2	2.83E-07
BNC2	3.24E-07
MEGF6	6.24E-07
ADK	6.49E-07

Figure 5.8 Association of GLI2 with genes in MPM TCGA dataset. Volcano plot depicts association of *GLI2* gene expression with expression of 36,725 genes in MPM RNA sequencing dataset, available through the TCGA (n=86). Genes which satisfy Bonferroni adjustment ($p \leq 0.05$) are represented in green (n=357). The top 10 *GLI2* associated genes are shown in the table. Genes on the right side of the volcano plot are positively associated with *GLI2* while genes on the left side are negatively associated with *GLI2*. This analysis was provided as part of a collaboration.

To assess the expression of *TGFB* in the same MPM cohort, we compared the RNA sequencing counts for *TGFB1*, *TGFB2* and *TGFB3* between MPM and normal tissues as well as other cancers. Only *TGFB1* was found to be significantly upregulated in MPM (Figure 5.9).

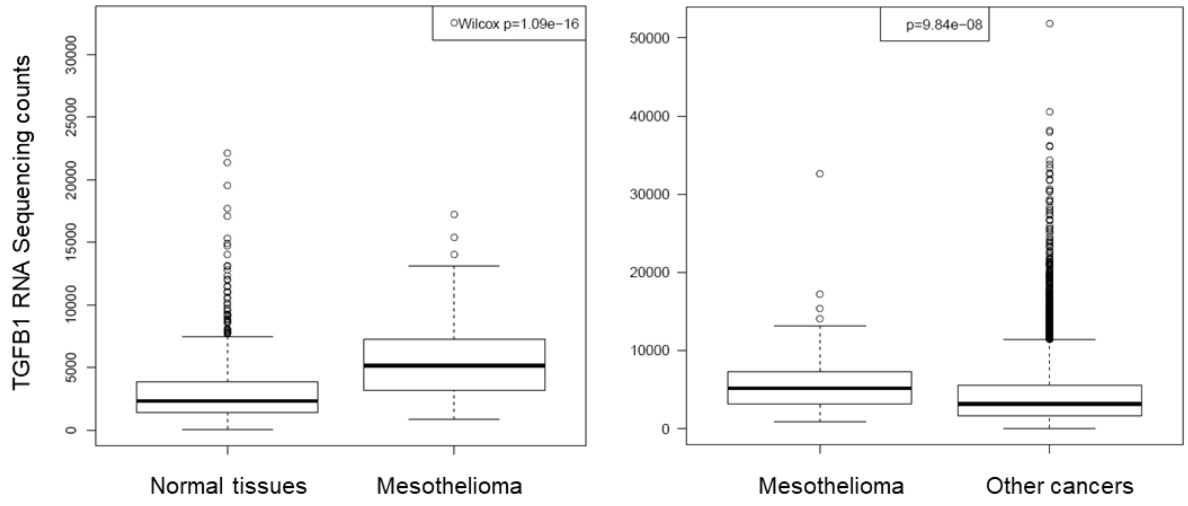

Figure 5.9 *TGFB1* gene expression in MPM compared to normal tissues and other cancers. Plots depict the upregulation of *TGFB1* in MPM compared to normal tissues ($p=1.09 \times 10^{-16}$) and other cancers ($p=9.84 \times 10^{-8}$). All RNA sequencing data was accessed through TCGA. This analysis was provided by Dr Adam Pennycuick.

5.3.4 The effects of TGFβ stimulation in MPM cell models

Based on the GLI1 linear regression and the upregulation of *TGFB1* in MPM findings, I next sought to determine if there is an interaction between the TGFβ cytokines and the Hedgehog transcription factors in MPM cell models. To investigate the non-canonical activation route of Hedgehog signalling *in vitro*, the cytokines $TGF\beta_1$ and $TGF\beta_2$ were used to stimulate MPM cells. Subsequent qPCR analysis showed that $TGF\beta_1$ significantly increased *GLI1* and to a lesser extent *GLI2* mRNA levels in H2803 cells. Treatment with both $TGF\beta_1$ and $TGF\beta_2$ caused a significant increase in *GLI2* mRNA levels in CRL2081 cells.

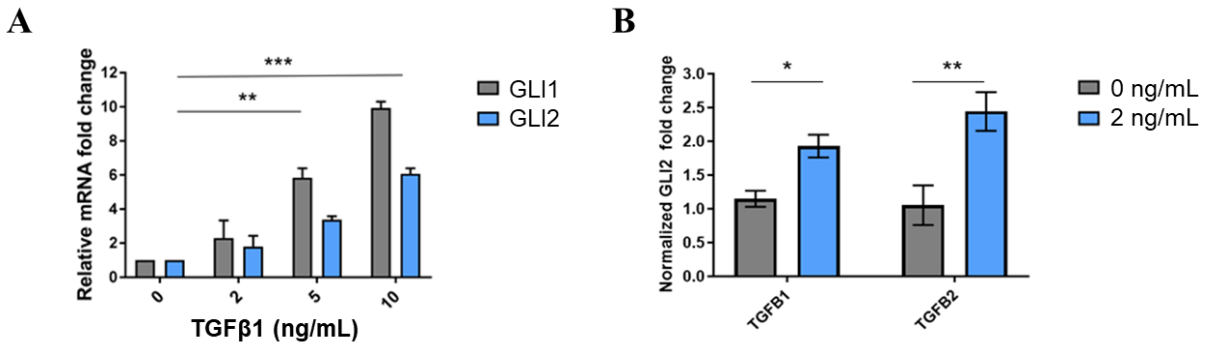

Figure 5.10 The cytokines TGFβ1 and TGFβ2 caused an increase in GLI1 and GLI2 mRNA.. A) Treatment with 2, 5 and 10 ng/mL of the cytokine $TGF\beta_1$ for 48 hours in H2803 cells. Treatments with $TGF\beta_1$ caused statistically significant increase of *GLI1* and *GLI2* mRNA compared to untreated H2803 cells (ANOVA, **p<0.01, ***=p<0.001). B) Treatment with 2 ng/mL of the cytokines $TGF\beta_1$ and $TGF\beta_2$ for 48 hours in CRL2081 cells caused a statistically significant increase of *GLI2* mRNA compared to untreated cells (t-test, *p<0.05, **p<0.01).

To examine classical Hedgehog pathway activation, *GLI* mRNA level was examined after stimulation with the Hedgehog ligand SHH. Interestingly, stimulation of H2803 cells with the canonical Hedgehog signalling ligand SHH did not elicit a significant increase in either *GLI1* or *GLI2* mRNA levels (Figure 5.11).

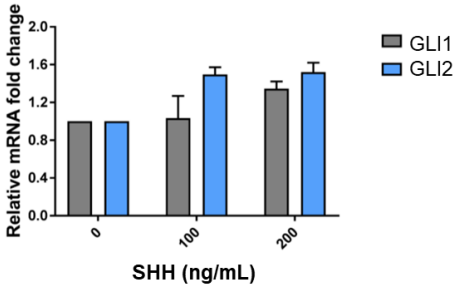

Figure 5.11 Stimulation of MPM cells with Hedgehog ligand SHH. Treatment with 100 ng/mL and 200ng/mL of N-terminal Sonic Hedgehog ligand (N-Shh) for 48 hours did not cause a significant induction of *GLI1* or *GLI2* mRNA in H2803 cells (ANOVA, p>0.05).

The cytokine TGFβ has been shown to promote differentiation of mesothelial cells into myofibroblasts through EMT and to increase cell adhesion (228,229). To explore the phenotype of TGFβ-stimulated cells, I conducted colony forming assays in which MPM cells were stimulated with $TGF\beta_1$ and $TGF\beta_2$. Stimulation with both cytokines caused a drastic increase in colony forming size. There was a clear trend in the colony forming assays for H2803 and CRL2081 cell lines (Figure 5.12), which previously showed an increase in *GLI1* and *GLI2* mRNA when stimulated with $TGF\beta_1$ (Figure 5.10). Interestingly, both H28 and H2818 cell lines did not show a significant increase in colony size or an increase in *GLI* mRNA when stimulated with $TGF\beta_1$ (data not shown).

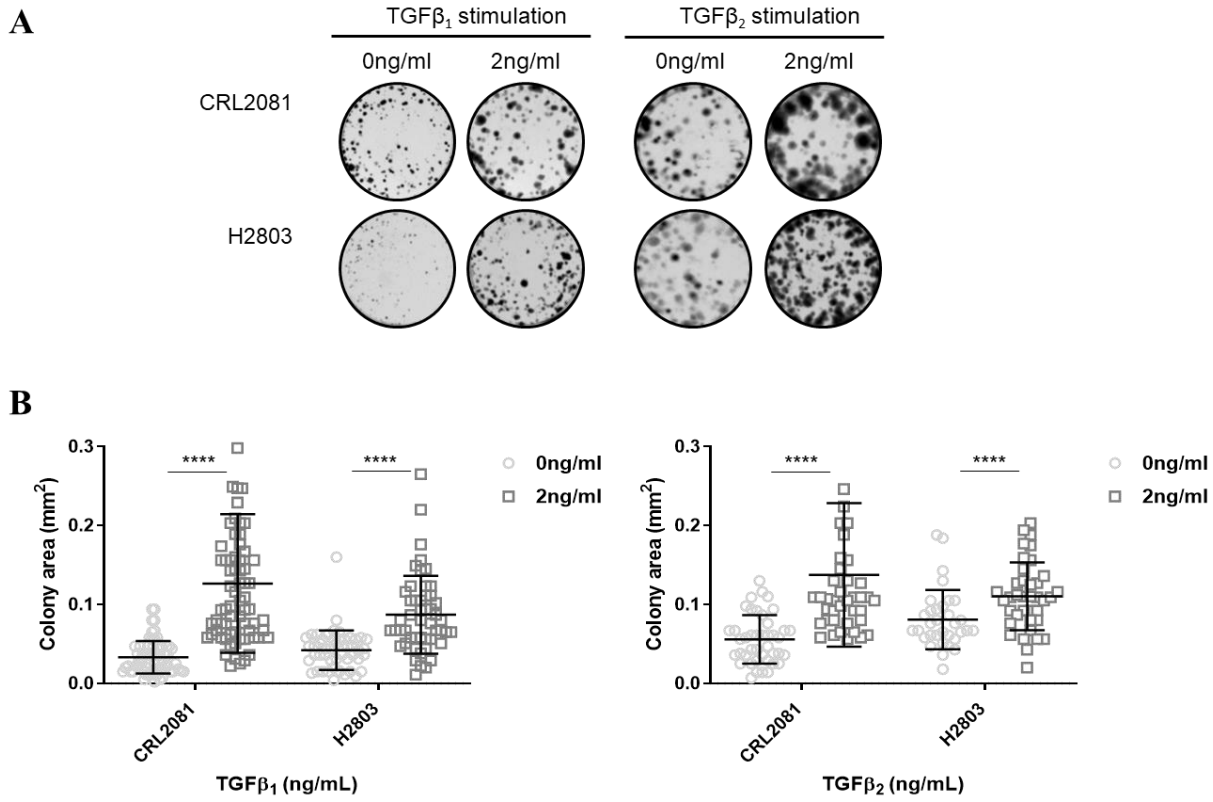

Figure 5.12 Stimulation of MPM cell lines with TGFβ1 and TGFβ2 causes increase in colony size. A) Representative images from colony forming assays for MPM cell lines H2803 and CRL2081 (n=3). B) Quantification of individual colony area in stimulated and untreated cells. Treatments with $TGF\beta_1$ and $TGF\beta_2$ induced statistically significant increase in colony size of H2803 and CRL2081 cells (t-test, ****=p<0.0001)

5.3.5 The effects of GLI2 knockdown by siRNA and shRNA in MPM cell models

To determine if siRNA-mediated GLI2 knockdown caused a reduction in cell viability, the apoptotic marker Annexin V was used in combination with the nuclear stain DAPI for flow cytometric quantification of apoptosis and cell death. Annexin V+/DAPI+ cells were classed as dead while Annexin V+/DAPI- were considered apoptotic. The amount of detectable dead cells

was higher in the GLI2 knockdown treatment group, as cell death was measured at 20.6% for GLI2 siRNA-treated cells and 10.6% in the non-targeting siRNA-treated cells (Figure 5.13A). There was no difference between the two treatment groups in the percentage of apoptotic cells, which was measured at 6%.

To further investigate the effect of siRNA-mediated GLI2 knockdown on cell viability, I expanded the use of siRNA to a panel of 6 MPM cell lines (Figure 5.13B). Analysis of cell response to GLI2 siRNA compared to non-targeting oligonucleotides by two-way analysis of variance revealed significant change between the treatment groups (p=0.049) (Figure 5.13B).

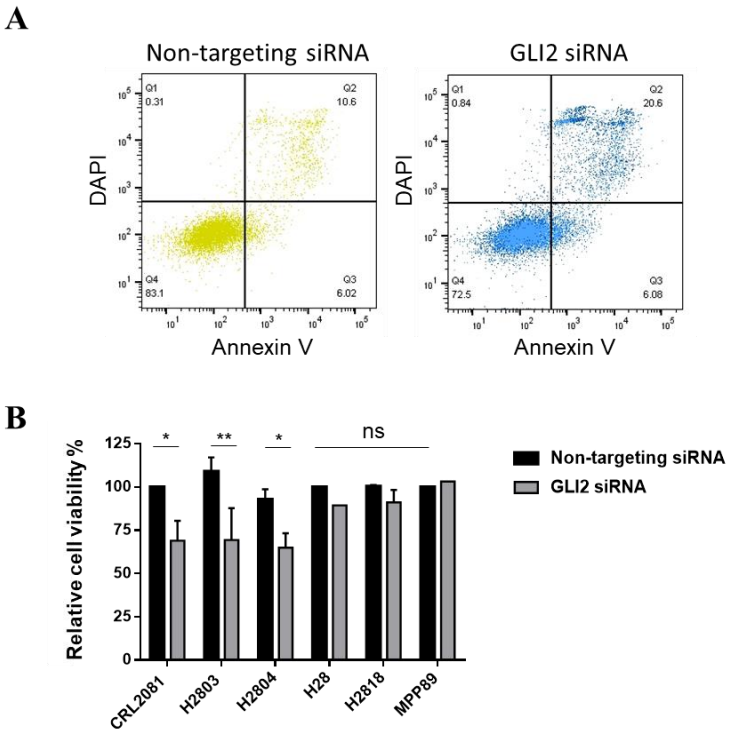

Figure 5.13 Transient GLI2 knockdown by siRNA causes a decrease in MPM cell viability. A) Flow cytometry plots demonstrate an increase in dead cells in siRNA GLI2 knockdown cells compared to non-targeting siRNA treated H2803 cells. Double staining with the apoptotic marker Annexin V and nuclear marker DAPI allowed the identification of dead cells in Q2 and apoptotic cells in Q3. The Annexin V antibody conjugated to AF647 was used. B) Treatment with GLI2 siRNA caused significant reduction in cell viability of 6 MPM cell lines compared to non-targeting siRNA control cells (two-way ANOVA, p=0.049). Error bars represent mean ±SD of six replicates, from at least two independent experiments.

Due to the transient nature of siRNA, I created a cell line with stable GLI2 knockdown by lentiviral shRNA transduction. I transduced H2803 cells with the pGIPZ system, containing a *GLI2* targeting insert which recognized all four GLI2 isoforms. ShRNA-mediated GLI2 knockdown (shGLI2) was validated at protein level by immunoblot (Figure 5.14). Known targets of GLI2 were investigated in the shGLI2 cells in comparison to control cells. The

expression of cell cycle proteins CDC2 and p21, EMT marker SNAI1 and anti-apoptosis protein BCL-XL increased in H2803 shGLI2 cells (Figure 5.14).

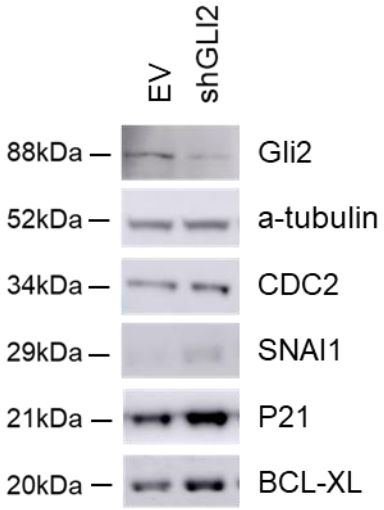

Figure 5.14 ShRNA-mediated knockdown of GLI2 in H2803 cells caused change in protein levels of known Hedgehog targets. Empty vector cells were used as a control. Protein level of CDC2 (34 kDa), SNAI1 (29 kDa), p21 (21 kDa) and BCL-XL (20kDa) increased in shGLI2 H2803 cells.

To further assess the effect of GLI2 knockdown in H2803 cells, I performed a colony-forming assay. ShRNA-mediated GLI2 knockdown in H2803 cells caused a statistically significant reduction in colony-forming capacity and colony size compared to control cells (Figure 5.15).

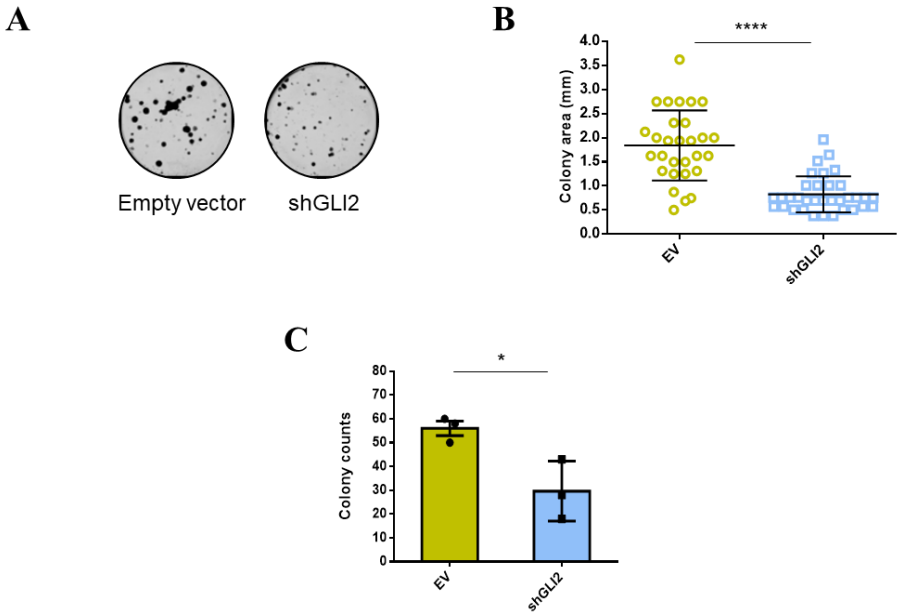

Figure 5.15 Stable knockdown of GLI2 by shRNA causes reduction of colony-forming capacity and colony size. A) Representative colony forming assay images (n=3). B) Colony size was quantified using ImageJ. ShGLI2 cells demonstrated a significantly smaller colony area compared to control cells transduced with empty vector. C) Colony number was quantified manually using a brightfield microscope. ShGLI2 cells formed a significantly lower number of colonies compared to control cells.

To further explore the phenotype that GLI2 knockdown causes, U133 plus 2.0 human genome microarrays were used to characterise the transcriptome of parental control H2803 cells transduced with the pGIPZ empty vector backbone and shGLI2 H2803 cells. Three replicates were used for each treatment group. The shGLI2 H2803 cells were transduced with virus at an estimated MOI of 3.

The top 10 most significant differentially expressed genes which were found based on gene expression comparison between the two treatment groups, are shown in Table 5.1.

Table 5.1 Summary of top ten differentially expressed genes identified by microarray analysis of shGLI2 H2803 cells compared to empty vector control cells. Fold change and false discovery rate (FDR) are shown for each gene. Genes are ranked by ascending FDR.

Gene	Gene name	Fold change	FDR
CALB1	calbindin 1	2.801979	0.000197
OASL	2'-5'-oligoadenylate synthetase like	2.738153	0.00075
KRT17	keratin 17	3.131546	0.003461
SMOC2	SPARC related modular calcium binding 2	2.161251	0.009463
NNMT	nicotinamide N-methyltransferase	1.648153	0.019024
CDKN1A	cyclin dependent kinase inhibitor 1A	1.695109	0.024362
PSG7	pregnancy specific beta-1-glycoprotein 7 (gene/pseudogene)	1.838149	0.024362
NIPSNAP1	nipsnap homolog 1	1.700162	0.024362
JUP	junction plakoglobin	1.619912	0.024362
GDF15	growth differentiation factor 15	1.662195	0.024362

Microarray analysis revealed significant changes in 141 genes; 38 downregulated genes and 103 upregulated genes in the shGLI2 H2803 cells compared to H2803 EV cells (Appendix Table 7.2). Ingenuity pathway analysis indicated that multiple cell processes including proliferation, movement and cell cycle were altered in shGLI2 H2803 cells (Figure 5.16). The cell cycle gene *CDKN1A* appeared as upregulated in our differentially expressed gene analysis of shGLI2 H2803 cells (Table 5.1). *CDKN1A*, which encodes the protein p21, was selected from the top upregulated genes for validation. Both qPCR and immunoblot analysis demonstrated a significant upregulation in the *CDKN1A* mRNA and p21 protein respectively in shGLI2 H2803 cells compared to H2803 EV cells (Figure 5.16C, Figure 5.14).

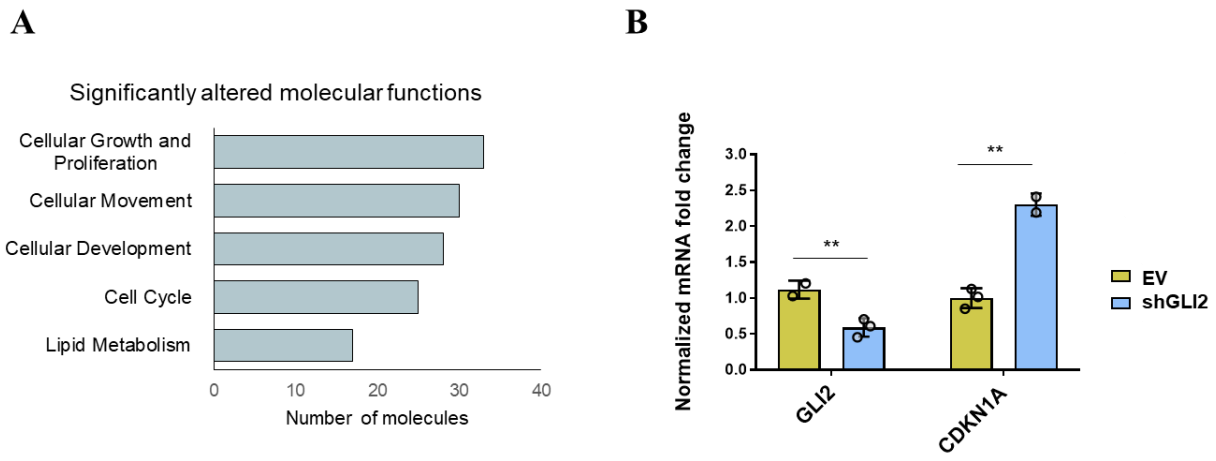

Figure 5.16 Transcriptomic analysis of shGli2 knockdown and empty vector H2803 cells shows change in cell cycle genes. A) Venn diagram of microarray results from shRNA-mediated GLI2 knockdown in H2803 cells. 141 differentially expressed genes were identified, of which 38 were downregulated and 103 were upregulated in shGLI2 cells. B) Ingenuity Pathway Analysis based on 141 differentially expressed genes. C) Validation of *GLI2* knockdown and *CDKN1A* increase in mRNA from shGLI2 and empty vector H2803 cells.

5.3.6 Pharmacological inhibition of Hedgehog signalling

To test the hypothesis that *GLI1* and *GLI2* have therapeutic potential as molecular targets, pharmacological agents were used to investigate MPM cell death. The direct GLI antagonist GANT-61 was used to treat 6 MPM Sanger cell lines (Figure 5.17A). Of these, 5/6 cell lines showed IC_{50} at above 10 μM of GANT-61 (Figure 5.17A). Next, to examine if MesobanK cell lines were more sensitive to pharmacological GLI inhibition, I conducted a dose response curve with GANT-61 (Figure 5.17B). The 4 MesobanK cell lines Meso35, Meso30, Meso19 and Meso52 showed a similar lack of sensitivity to the direct GLI antagonist, as they demonstrated an IC_{50} at above 20 μM (Figure 5.17B). Overall, all 10 MPM cell lines required high concentrations of GANT-61 to reach IC_{50} (Figure 5.17).

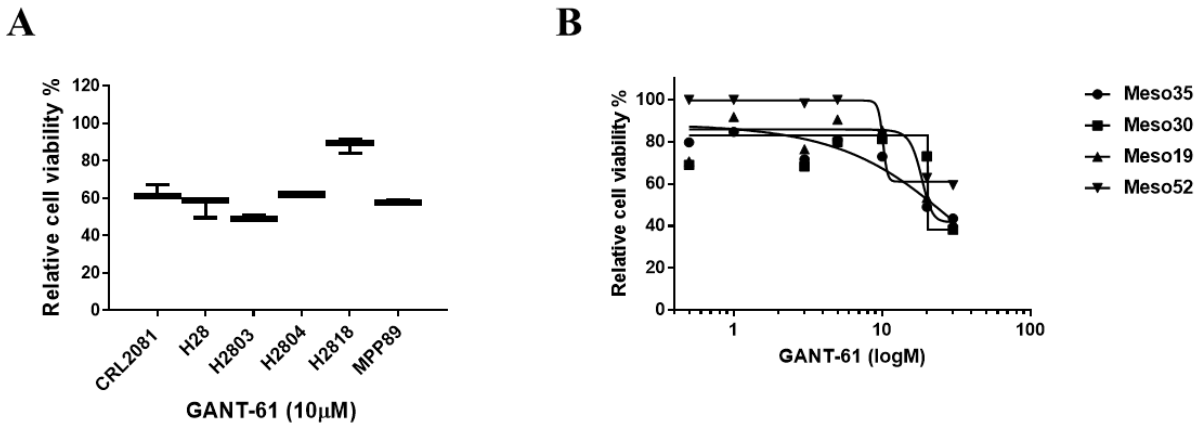

Figure 5.17 GLI antagonist GANT-61 reduces cell viability of MPM cells. A) Box and whisker plot represents reduction in cell viability of 6 MPM cell lines treated with 10 μM of GANT-61 for 72 hours. B) Dose response curve of 4 MesobanK cell lines dosed with GANT-61 up to 30 μM for 72 hours. Cell viability was measured by MTT assay. Data represent the mean ± SD of at least two independent experiments, each performed in six replicates.

I sought to further interrogate the sensitivity of MPM cell lines to GLI inhibition with additional GLI antagonists. Due to the ability of the epigenetic BET inhibitor JQ1 to reduce the mRNA level of *GLI1* and *GLI2* in cell-based models, JQ1 was used to treat the same panel of MPM cell lines as GANT-61 (216).

JQ1 at 1 μM was able to cause a 50% reduction in cell viability in 3/6 cell lines (Figure 5.18). In comparison to previous IC_{50} results which required a 10-fold higher concentration of GANT-61 to reach IC_{50}, the indirect GLI inhibitor JQ1 showed potential as an MPM inhibitor.

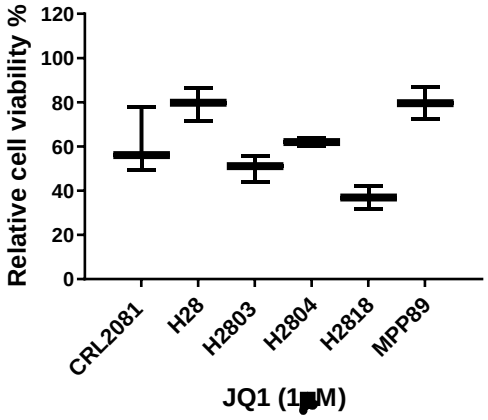

Figure 5.18 Indirect GLI inhibitor JQ1 reduces cell viability of MPM cells. Box and whisker plot represents relative cell viability of 6 MPM cell lines, treated with JQ1 (1μM) for 72 hours. Cell viability was measured by MTT assay. There is no significant difference between the cell lines (ANOVA, p=0.23). Data represent the mean ± SD of at least two independent experiments, each performed in six replicates.

5.4 Discussion

Collectively, the findings outlined here provide evidence that Hedgehog signalling is upregulated in MPM compared to normal pleura and that the Hedgehog transcription factor *GLI2* is aberrantly expressed in a subset of MPM tumours (Figure 4.22, Figure 5.1). In addition, *GLI2* RNA sequencing counts appeared to be elevated in a subset of MPM tumours and thus GLI2 may be the most interesting candidate out of the GLI transcription factor family to investigate further. Linear regression analysis, visually represented by GLI1 and GLI2 volcano plots, supported this, as the number of genes which satisfied significance criteria was lower in the *GLI1* analysis (n=198) compared to the *GLI2* analysis (n=357). This could be attributed to a broader regulatory role exerted by GLI2 as a transcription factor (Figure 5.7, Figure 5.8).

I detected Hedgehog signalling cascade components by immunoblot in MPM cell models (Figure 5.5, Figure 5.6). Notably, the *in vitro* characterisation revealed that 6/6 Sanger cell lines expressed Hedgehog components SMO and SHH (Figure 5.6). In addition, I detected GLI2 protein isoforms in all cell lines tested which indicates that the protein is active in the MPM cell lines assessed (Figure 5.6). Notably, others have not been able to detect protein levels or have found low protein expression of Hedgehog intermediates such as SHH, SMO and GLI1 in keratinocytes, pancreatic and squamous cell lung cancer cell models (230–232). In contrast, the *in vitro* characterisation I conducted in MPM cell lines revealed protein expression of key Hedgehog pathway components in all MPM cell lines, which indicates the functionality and activity of Hedgehog signalling in MPM.

Interestingly, gene expression levels of the *PTCH1* homologue *PTCH2* were significantly associated with *GLI1* in the TCGA linear regression analysis. A further Hedgehog gene, *HHIP*, also appeared in the *GLI1* associated genes. *PTCH2* has an uncertain role in Hedgehog signalling although its functionality has been suggested in some studies (168). The analysis in Figure 5.7 indicated that *PTCH2* expression correlates to high *GLI1* expression in MPM, which suggests functionality of the receptor *PTCH2* and potentially a positive transcriptional feedback loop by *GLI1* for both receptors (Figure 5.7). This suggests, for the first time, that the *PTCH2* receptor may be involved in Hedgehog signalling in MPM.

A key insight was generated from the TCGA gene expression dataset which showed that *GLI1* expression was associated with *TGFB2* expression. When we tested the hypothesis that $TGF\beta_1$ activates the transcription of GLI proteins, by stimulating MPM cell lines with the cytokine, I found that *GLI1* and *GLI2* mRNA levels increased in response to treatment. In addition, MPM

cells showed increased colony size when treated with the cytokines TGFβ_1 and TGFβ_2. This MPM *in vitro* data supports the MPM RNA sequencing association data. The Hedgehog ligand SHH was selected for investigation of canonical Hedgehog pathway activation due to its widespread use in the literature and reports of its ability to induce proliferation of various cell types including keratinocytes, mesenchymal stem cells and granule cell precursors (187,233,234). I found that *GLI* and *GLI2* mRNA levels increased to a lesser extent in response to the canonical ligand N-SHH compared to TGFβ stimulation (Figure 5.11, Figure 5.10). The poor response to canonical ligand SHH could be attributed to canonical pathway saturation *in vitro*, as most cell lines expressed endogenous SHH when unstimulated (Figure 5.6). However, the qPCR results from the canonical Hedgehog signalling agonist N-SHH support the specificity of increase of TGFβ-induced increase in *GLI1* and *GLI2* mRNA levels in response to these non-canonical agonists (Figure 5.10). Although non-canonical Hedgehog activation and the relationship between Hedgehog and TGFβ signalling pathways has been well characterised in other cancer types their interaction has not been reported to my knowledge (192,195,235).

A strength of the GLI inhibition work outlined in this report is the use of multiple MPM cell models to investigate the effects of inhibiting the Hedgehog pathway. Cell viability results from treatment of 10 MPM cell lines did not suggest any therapeutic efficacy in use of the direct GLI antagonist GANT-61. I attributed the ability of GANT-61 to cause cell death at high concentrations to the production of ROS, which has previously been reported in the literature (214). The IC_{50} generated from GANT-61 treatments are too high for *in vivo* use or clinical translation, which corroborates findings from other studies (208,236). In contrast, the BET protein inhibitor and indirect GLI antagonist JQ1 resulted in much more promising cell viability profiles due to lower IC_{50} values. Although the BBI class of drugs are indirect inhibitors of Hedgehog signalling, these results indicate that MPM cell lines may be sensitive to GLI inhibition to some extent and thus the further research into more selective GLI inhibitors could provide a useful tool for MPM research into blocking the Hedgehog pathways as a therapeutic strategy.

In summary, investigation of GLI2 function in MPM tumours and cell lines supports the pleiotropic regulation of a large number of targets by this Hedgehog transcription factor (Figure 5.8, Figure 5.14, Figure 5.16). Although Ingenuity Pathway analysis revealed that shRNA-mediated GLI2 knockdown caused changes in cell proliferation, movement and cell cycle

pathways (Figure 5.16), GLI2 may not be an ideal therapeutic target due to the number of contrasting targets and variety of regulation which it exerts in MPM.

In conclusion, the development of effective MPM treatments has been hindered by inadequate understanding of the signalling mechanisms which underpin the proliferative and chemotherapy resistant advantages of aggressive MPM cells. Hence, the preliminary work conducted thus far on Hedgehog signalling in MPM constitutes an important contribution to understanding the aberrant signalling patterns of MPM biology.

6 Conclusions and future directions

The work presented here identifies two distinct human tissue sources and validates their ability to provide viable and intact visceral pleura which can be utilised for the study of VMCs. In the future, the focus of the field may shift away from animal models due to the adoption of human tissue resources such as those outlined here, which will enable much needed progress in mesothelial and MPM biology research.

Interestingly, I have shown prominent nuclear BAP1-loss in reactive pleura of a patient with no known pleural disease. The predominant loss of BAP1-expression in proliferative mesothelial cells indicates that BAP1-loss may be a driver or marker of pre-malignant pleura. Although this post-mortem case does not align with the current criteria of MMIS it raises questions regarding if other BAP1-loss patterns could be used as a marker of pleural pre-malignancy. Overall this finding agrees with previous reports that pre-invasive stages of MPM are asymptomatic but it furthers this work by suggesting MMIS could be more heterogeneous in its features than our current understanding, To improve our knowledge and ability to diagnose MMIS, BAP1 staining by IHC should become a routine analysis in laboratories with access to human pleural biopsies, so that more cases can be identified and the pre-malignant stages of MPM can be better characterised.

The unique use of normal human pleura for integrative characterisation and VMC isolation emphasised the technical issues associated with previous human mesothelial cell isolation methods. Here, I have developed a new method to isolate VMCs which is superior to known approaches and allows collection and subsequent FACS-purification of a VMC population with an estimated purity of 95%. The validation of the pleural brushing method is valuable as it is applicable to the parietal pleura as well as the peritoneum. Isolation and sequencing characterisation of visceral and parietal mesothelial cell populations will enable the study of normal PMC function, the exploration of PMC subsets and the identification of a ubiquitous PMC marker. As PMCs have been shown to be pluripotent during development, VMC collection by pleural brushing and single-cell sequencing could conclusively elucidate the presence of progenitor or stem cell populations in the adult pleura.

Finally, I have characterised the transcriptome of human VMCs in homeostasis for the first time. Although the RNA sequencing dataset has several limitations including utilisation of a small patient cohort and low sequencing depth, the insights from the comparison to MPM are promising and valuable to the field. Previous studies of MPM cell lines and tumours have

suggested an increase in Hedgehog signalling in this cancer type. The bioinformatic results from our comparison of normal pleura to MPM highlighted Hedgehog signalling as an upregulated pathway in MPM and subsequent investigations indicated that Hedgehog signalling transcription factor *GLI2* was upregulated in a subset of MPM cases. *TGFB1* was also upregulated in the MPM RNA sequencing dataset and stimulation of MPM cells *in vitro* resulted in an increase of *GLI1* and *GLI2* mRNA. Although Hedgehog pathway inhibition may have therapeutic potential in MPM, blockade of the Hedgehog pathway in MPM cell models with chemical agents is currently not effective enough to warrant clinical progression of these candidate drugs. Further research into selective and more potent GLI inhibitors is necessary to efficiently explore the therapeutic potential of Hedgehog signalling inhibition in MPM.

7 Appendix

Appendix Table 7.1 List of genes identified by linear regression analysis of GLI1 in the MPM RNA sequencing dataset (n=86) available through the TCGA. A total of 198 genes were found to be significantly associated with GLI1 expression. Genes are ranked by ascending adjusted p-value.

Gene	Gene name	Adjusted p-value
PTCH2	patched 2	3.236E-21
PTCH1	patched 1	1.624E-16
INHBE	inhibin subunit beta E	3.607E-11
TGFB2	transforming growth factor beta 2	2.112E-09
UST	uronyl 2-sulfotransferase	1.763E-08
CAPN5	calpain 5	2.374E-08
HHIP	hedgehog interacting protein	1.510E-07
NGFR	nerve growth factor receptor	1.978E-07
FOXS1	forkhead box S1	2.046E-07
NHS	NHS actin remodeling regulator	1.578E-06
TTC22	tetratricopeptide repeat domain 22	2.142E-06
CFC1	cripto, FRL-1, cryptic family 1	2.246E-06
MYOZ3	myozenin 3	2.512E-06
TSHZ3	teashirt zinc finger homeobox 3	3.334E-06
FOXF1	forkhead box F1	4.123E-06
SFRP5	secreted frizzled related protein 5	4.125E-06
PKNOX2	PBX/knotted 1 homeobox 2	5.070E-06
LRP6	LDL receptor related protein 6	1.254E-05
TRAM1	translocation associated membrane protein 1	1.473E-05
SOBP	sine oculis binding protein homolog	1.590E-05
CPAMD8	C3 and PZP like alpha-2-macroglobulin domain containing 8	2.120E-05
NRXN2	neurexin 2	2.161E-05
FOXP4	forkhead box P4	2.285E-05
MDFI	MyoD family inhibitor	2.499E-05
ARAP2	ArfGAP with RhoGAP domain, ankyrin repeat and PH domain 2	2.784E-05

KIR3DX1	killer cell immunoglobulin like receptor, three Ig domains X1 (pseudogene)	2.879E-05
FOXD2	forkhead box D2	3.056E-05
ATP1B2	ATPase Na+/K+ transporting subunit beta 2	4.250E-05
PRR31	long intergenic non-protein coding RNA 2692	6.557E-05
TTLL5	tubulin tyrosine ligase like 5	8.158E-05
PCDH19	protocadherin 19	8.280E-05
MGAT5	alpha-1,6-mannosylglycoprotein 6-beta-N-acetylglucosaminyltransferase	1.028E-04
VGLL3	vestigial like family member 3	1.360E-04
KIR2DL4	killer cell immunoglobulin like receptor, two Ig domains and long cytoplasmic tail 4	1.422E-04
TGFB2-AS1	TGFB2 antisense RNA 1 (head to head)	1.672E-04
MICU3	mitochondrial calcium uptake family member 3	1.686E-04
RNF144A	ring finger protein 144A	1.829E-04
FOXD2-AS1	FOXD2 adjacent opposite strand RNA 1	1.856E-04
SLC9C1	solute carrier family 9 member C1	1.925E-04
FGD5	FYVE, RhoGEF and PH domain containing 5	2.516E-04
GLCE	glucuronic acid epimerase	3.058E-04
RCOR2	REST corepressor 2	3.090E-04
KLRC1	killer cell lectin like receptor C1	3.230E-04
HHIP-AS1	HHIP antisense RNA 1	3.652E-04
SEMA6A	semaphorin 6A	4.006E-04
LINC00884	long intergenic non-protein coding RNA 884	4.125E-04
KRT17	keratin 17	4.188E-04
LINC00605	long intergenic non-protein coding RNA 605	4.285E-04
RBM47	RNA binding motif protein 47	5.320E-04
SDK2	sidekick cell adhesion molecule 2	7.092E-04
MAP1A	microtubule associated protein 1A	7.533E-04
ADAMTS10	ADAM metallopeptidase with thrombospondin type 1 motif 10	7.538E-04
PLEKHM1	pleckstrin homology and RUN domain containing M1	7.589E-04

RCBTB2	RCC1 and BTB domain containing protein 2	7.784E-04
ATG3	autophagy related 3	7.924E-04
TEC	tec protein tyrosine kinase	8.103E-04
NR2F2	nuclear receptor subfamily 2 group F member 2	8.466E-04
GDF11	growth differentiation factor 11	9.003E-04
SETBP1	SET binding protein 1	9.221E-04
DLX5	distal-less homeobox 5	9.564E-04
LINC02015	long intergenic non-protein coding RNA 2015	9.692E-04
ENTPD2	ectonucleoside triphosphate diphosphohydrolase 2	9.730E-04
HLA-G	major histocompatibility complex, class I, G	1.007E-03
PDE5A	phosphodiesterase 5A	1.083E-03
FOXL1	forkhead box L1	1.144E-03
PCDH18	protocadherin 18	1.176E-03
SPATS2	spermatogenesis associated serine rich 2	1.186E-03
CAMK2N1	calcium/calmodulin dependent protein kinase II inhibitor 1	1.321E-03
AGXT	alanine--glyoxylate and serine--pyruvate aminotransferase	1.589E-03
BAHCC1	BAH domain and coiled-coil containing 1	1.590E-03
COL21A1	collagen type XXI alpha 1 chain	1.602E-03
NOTCH3	notch receptor 3	1.738E-03
NEU1	neuraminidase 1	1.739E-03
RBP2	retinol binding protein 2	1.815E-03
SAMD11	sterile alpha motif domain containing 11	1.859E-03
AP1M2	adaptor related protein complex 1 subunit mu 2	1.950E-03
SHF	Src homology 2 domain containing F	1.953E-03
LINC01822	long intergenic non-protein coding RNA 1822	1.958E-03
ADAMTSL2	ADAMTS like 2	1.986E-03
TMEM62	transmembrane protein 62	2.222E-03
ADGRA2	adhesion G protein-coupled receptor A2	2.507E-03
ADCY5	adenylate cyclase 5	2.602E-03
MPPED1	metallophosphoesterase domain containing 1	2.777E-03

DACT3	dishevelled binding antagonist of beta catenin 3	2.876E-03
THSD4	thrombospondin type 1 domain containing 4	2.921E-03
NCAM1	neural cell adhesion molecule 1	2.957E-03
TSPAN11	tetraspanin 11	3.024E-03
CENPJ	centromere protein J	3.412E-03
LILRP2	leukocyte immunoglobulin-like receptor pseudogene 2	3.536E-03
SNED1	sushi, nidogen and EGF like domains 1	3.673E-03
NFATC4	nuclear factor of activated T cells 4	4.136E-03
LINC01276	long intergenic non-protein coding RNA 1276	4.544E-03
RALYL	RALY RNA binding protein like	4.925E-03
SELENOS	selenoprotein S	5.059E-03
TTC7A	tetratricopeptide repeat domain 7A	5.579E-03
CPB1	carboxypeptidase B1	5.714E-03
SOX13	SRY-box transcription factor 13	6.332E-03
SECTM1	secreted and transmembrane 1	6.450E-03
RSPO2	R-spondin 2	7.179E-03
PRDX6	peroxiredoxin 6	7.239E-03
TACR3	tachykinin receptor 3	7.359E-03
KRT42P	keratin 42 pseudogene	7.484E-03
HCG4P11	HLA complex group 4 pseudogene 11	7.510E-03
ETV7	ETS variant transcription factor 7	7.706E-03
SQOR	sulfide quinone oxidoreductase	7.834E-03
PDS5B	PDS5 cohesin associated factor B	7.846E-03
PLCG1	phospholipase C gamma 1	8.059E-03
FKBP7	FKBP prolyl isomerase 7	8.593E-03
PGAP1	post-GPI attachment to proteins inositol deacylase 1	8.689E-03
HLA-H	major histocompatibility complex, class I, H (pseudogene)	8.692E-03
SLC50A1	solute carrier family 50 member 1	8.872E-03
SDC2	syndecan 2	9.078E-03

HLA-L	major histocompatibility complex, class I, L (pseudogene)	9.353E-03
NABP1	nucleic acid binding protein 1	1.016E-02
TBX2	T-box transcription factor 2	1.062E-02
OLFM4	olfactomedin 4	1.146E-02
TRIB2	tribbles pseudokinase 2	1.179E-02
DLG4	discs large MAGUK scaffold protein 4	1.186E-02
ADGRB1	adhesion G protein-coupled receptor B1	1.258E-02
EPHA3	EPH receptor A3	1.268E-02
SUSD3	sushi domain containing 3	1.290E-02
NKAIN4	sodium/potassium transporting ATPase interacting 4	1.355E-02
TRABD2B	TraB domain containing 2B	1.370E-02
FAM153C	family with sequence similarity 153 member C, pseudogene	1.422E-02
MST1R	macrophage stimulating 1 receptor	1.430E-02
HLA-U	major histocompatibility complex, class I, U (pseudogene)	1.499E-02
ATF7	activating transcription factor 7	1.549E-02
LACTB2	lactamase beta 2	1.574E-02
CTSD	cathepsin D	1.615E-02
HCG4	HLA complex group 4	1.618E-02
TMEM133	Rho GTPase activating protein 42	1.752E-02
LARGE1	LARGE xylosyl- and glucuronyltransferase 1	1.761E-02
UNC93B1	unc-93 homolog B1, TLR signaling regulator	1.770E-02
DACH1	dachshund family transcription factor 1	1.778E-02
VAMP8	vesicle associated membrane protein 8	1.790E-02
SOD2	superoxide dismutase 2	1.833E-02
ERN1	endoplasmic reticulum to nucleus signaling 1	1.852E-02
TAP1	transporter 1, ATP binding cassette subfamily B member	1.920E-02
RBP1	retinol binding protein 1	1.950E-02
AFAP1L2	actin filament associated protein 1 like 2	2.038E-02

OAZ1	ornithine decarboxylase antizyme 1	2.046E-02
HMGA2	high mobility group AT-hook 2	2.084E-02
DCHS1	dachsous cadherin-related 1	2.113E-02
NCBP3	nuclear cap binding subunit 3	2.131E-02
MEX3B	mex-3 RNA binding family member B	2.133E-02
CD47	CD47 molecule	2.135E-02
LINC01497	long intergenic non-protein coding RNA 1497	2.201E-02
SERP1	stress associated endoplasmic reticulum protein 1	2.232E-02
TBC1D2	TBC1 domain family member 2	2.269E-02
IRS4	insulin receptor substrate 4	2.363E-02
PHBP18	prohibitin pseudogene 18	2.398E-02
KCNIP1	potassium voltage-gated channel interacting protein 1	2.459E-02
GPR162	G protein-coupled receptor 162	2.479E-02
PPA1	inorganic pyrophosphatase 1	2.513E-02
HLA-B	major histocompatibility complex, class I, B	2.540E-02
S100A6	S100 calcium binding protein A6	2.711E-02
LBX2-AS1	LBX2 antisense RNA 1	2.828E-02
HR	HR lysine demethylase and nuclear receptor corepressor	3.001E-02
LINC02538	long intergenic non-protein coding RNA 2538	3.002E-02
FLOT2	flotillin 2	3.029E-02
TLN2	talin 2	3.096E-02
BPI	bactericidal permeability increasing protein	3.209E-02
ITGA10	integrin subunit alpha 10	3.302E-02
EDIL3	EGF like repeats and discoidin domains 3	3.391E-02
CFB	complement factor B	3.438E-02
NUDT5	nudix hydrolase 5	3.474E-02
HEYL	hes related family bHLH transcription factor with YRPW motif like	3.520E-02
SHANK2	SH3 and multiple ankyrin repeat domains 2	3.598E-02

CNIH3	cornichon family AMPA receptor auxiliary protein 3	3.598E-02
PPP1R13L	protein phosphatase 1 regulatory subunit 13 like	3.622E-02
NMNAT2	nicotinamide nucleotide adenylyltransferase 2	3.638E-02
STX3	syntaxin 3	3.691E-02
LINC00924	long intergenic non-protein coding RNA 924	3.715E-02
MFAP4	microfibril associated protein 4	3.815E-02
ACSL1	acyl-CoA synthetase long chain family member 1	3.929E-02
NRIP2	nuclear receptor interacting protein 2	3.929E-02
TMPRSS7	transmembrane serine protease 7	3.943E-02
BLVRA	biliverdin reductase A	3.943E-02
LRFN5	leucine rich repeat and fibronectin type III domain containing 5	3.996E-02
MYLK2	myosin light chain kinase 2	4.069E-02
LINS1	lines homolog 1	4.086E-02
RPS6KA1	ribosomal protein S6 kinase A1	4.150E-02
UNC13A	unc-13 homolog A	4.164E-02
NOVA1	NOVA alternative splicing regulator 1	4.174E-02
FAM86EP	family with sequence similarity 86 member E, pseudogene	4.394E-02
DDHD1	DDHD domain containing 1	4.398E-02
KHDRBS1	KH RNA binding domain containing, signal transduction associated 1	4.427E-02
PKDCC	protein kinase domain containing, cytoplasmic	4.451E-02
KRT39	keratin 39	4.469E-02
HERPUD1	homocysteine inducible ER protein with ubiquitin like domain 1	4.478E-02
ESRRA	estrogen related receptor alpha	4.553E-02
GPHN	gephyrin	4.612E-02
GSG1L	GSG1 like	4.792E-02
KRT17P3	keratin 17 pseudogene 3	4.831E-02
ABLIM2	actin binding LIM protein family member 2	4.854E-02

NR1H4	nuclear receptor subfamily 1 group H member 4	4.887E-02
EDEM2	ER degradation enhancing alpha-mannosidase like protein 2	4.928E-02

Appendix Table 7.2 List of differentially expressed genes identified by microarray in shGLI2 H2803 cells when compared to empty vector control cells. A total of 141 differentially expressed genes were identified. Genes are ranked by ascending false discovery rate (FDR).

Gene	Gene name	Fold change	FDR
CALB1	calbindin 1	2.80	1.967E-04
OASL	2'-5'-oligoadenylate synthetase like	2.74	7.497E-04
KRT17	keratin 17	3.13	3.461E-03
SMOC2	SPARC related modular calcium binding 2	2.16	9.463E-03
LOC101926967	uncharacterized LOC101926967	1.85	1.338E-02
NNMT	nicotinamide N-methyltransferase	1.65	1.902E-02
CDKN1A	cyclin dependent kinase inhibitor 1A	1.70	2.436E-02
PSG7	pregnancy specific beta-1-glycoprotein 7 (gene/pseudogene)	1.84	2.436E-02
NIPSNAP1	nipsnap homolog 1	1.70	2.436E-02
JUP	junction plakoglobin	1.62	2.436E-02
GDF15	growth differentiation factor 15	1.66	2.436E-02
C1orf116	chromosome 1 open reading frame 116	1.59	2.436E-02
BCO2	beta-carotene oxygenase 2	1.62	2.436E-02
CHMP2A	charged multivesicular body protein 2A	1.61	2.436E-02
PSMB9	proteasome subunit beta 9	1.54	2.436E-02
APBB3	amyloid beta precursor protein binding family B member 3	1.60	2.436E-02
TINF2	TERF1 interacting nuclear factor 2	1.65	2.436E-02
ANO2	anoctamin 2	1.58	2.436E-02
ZBED2	zinc finger BED-type containing 2	1.85	2.436E-02

NRIP1	nuclear receptor interacting protein 1	-1.67	2.436E-02
ORAI3	ORAI calcium release-activated calcium modulator 3	1.58	2.436E-02
ZFR	zinc finger RNA binding protein	-1.54	2.436E-02
IFIT1	interferon induced protein with tetratricopeptide repeats 1	1.69	2.436E-02
DCLK1	doublecortin like kinase 1	-1.81	2.436E-02
PINK1	PTEN induced putative kinase 1	1.62	2.436E-02
THBS3	thrombospondin 3	1.74	2.436E-02
MFSD3	major facilitator superfamily domain containing 3	1.83	2.436E-02
MIR503HG	MIR503 host gene	1.63	2.479E-02
DDX60	DExD/H-box helicase 60	1.90	2.479E-02
CYSRT1	cysteine rich tail 1	1.56	2.479E-02
CELSR3	cadherin EGF LAG seven-pass G-type receptor 3	1.50	2.502E-02
UTP20	UTP20, small subunit processome component	-1.55	2.502E-02
DDIT4	DNA damage inducible transcript 4	1.53	2.502E-02
TMEM92	transmembrane protein 92	1.81	2.502E-02
IGFBP3	insulin like growth factor binding protein 3	-1.47	2.502E-02
CYTL1	cytokine like 1	-1.48	2.598E-02
FLNB	filamin B	1.48	2.598E-02
JAK2	Janus kinase 2	-1.69	2.598E-02
LINC00520	long intergenic non-protein coding RNA 520	1.92	2.624E-02
FUT8	fucosyltransferase 8	-1.49	2.624E-02
ZFP36	ZFP36 ring finger protein	1.75	2.624E-02
GNAZ	G protein subunit alpha z	1.56	2.624E-02
ALS2CL	ALS2 C-terminal like	1.59	2.624E-02

NRBP2	nuclear receptor binding protein 2	1.54	2.624E-02
LINC01943	long intergenic non-protein coding RNA 1943	1.52	2.624E-02
RAPGEF6	Rap guanine nucleotide exchange factor 6	-1.53	3.046E-02
AADACP1	arylacetamide deacetylase pseudogene 1	-1.83	3.101E-02
CALCOCO1	calcium binding and coiled-coil domain 1	1.63	3.101E-02
RNF138	ring finger protein 138	-1.45	3.101E-02
ZNF436-AS1	ZNF436 antisense RNA 1	1.54	3.101E-02
VAT1	vesicle amine transport 1	1.49	3.101E-02
PLIN1	perilipin 1	-1.43	3.101E-02
BLVRB	biliverdin reductase B	1.45	3.101E-02
CAPG	capping actin protein, gelsolin like	1.46	3.101E-02
TRPM4	transient receptor potential cation channel subfamily M member 4	1.67	3.101E-02
PDLIM1	PDZ and LIM domain 1	1.50	3.101E-02
IDNK	IDNK, gluconokinase	1.48	3.101E-02
RCN2	reticulocalbin 2	-1.47	3.101E-02
HMGCL	3-hydroxymethyl-3-methylglutaryl-CoA lyase	1.67	3.101E-02
VMP1	vacuole membrane protein 1	1.57	3.101E-02
ARHGAP28	Rho GTPase activating protein 28	1.49	3.101E-02
C11orf68	chromosome 11 open reading frame 68	1.48	3.101E-02
MVP	major vault protein	1.49	3.101E-02
SLC37A4	solute carrier family 37 member 4	1.46	3.101E-02
RARRES3	retinoic acid receptor responder 3	2.24	3.101E-02
FZD6	frizzled class receptor 6	-1.58	3.101E-02
SLC35F2	solute carrier family 35 member F2	-1.51	3.101E-02

LMBR1L	limb development membrane protein 1 like	1.49	3.101E-02
C11orf71	chromosome 11 open reading frame 71	1.41	3.101E-02
PRAF2	PRA1 domain family member 2	1.47	3.101E-02
MYPN	myopalladin	1.43	3.101E-02
UBE2L6	ubiquitin conjugating enzyme E2 L6	1.44	3.101E-02
TRIML2	tripartite motif family like 2	1.42	3.101E-02
LINC02582	long intergenic non-protein coding RNA 2582	1.46	3.101E-02
HTATSF1	HIV-1 Tat specific factor 1	-1.49	3.111E-02
TUBA1A	tubulin alpha 1a	1.52	3.111E-02
TRIM22	tripartite motif containing 22	1.47	3.148E-02
TXNIP	thioredoxin interacting protein	1.61	3.208E-02
MIF4GD	MIF4G domain containing	1.49	3.208E-02
TNKS1BP1	tankyrase 1 binding protein 1	1.54	3.208E-02
CHCHD6	coiled-coil-helix-coiled-coil-helix domain containing 6	1.43	3.208E-02
INHBA	inhibin beta A subunit	1.49	3.208E-02
RXYLT1	ribitol xylosyltransferase 1	-1.41	3.208E-02
TMEM256	transmembrane protein 256	1.42	3.208E-02
ABHD14A	abhydrolase domain containing 14A	1.38	3.208E-02
G3BP2	G3BP stress granule assembly factor 2	-1.43	3.208E-02
ABHD14B	abhydrolase domain containing 14B	1.46	3.208E-02
NUP58	nucleoporin 58	-1.44	3.229E-02
ASL	argininosuccinate lyase	1.63	3.338E-02
TBC1D12	TBC1 domain family member 12	-1.48	3.338E-02
HOXA1	homeobox A1	1.58	3.419E-02

UGT2B28	UDP glucuronosyltransferase family 2 member B28	1.47	3.420E-02
CPZ	carboxypeptidase Z	1.49	3.618E-02
CCP110	centriolar coiled-coil protein 110	-1.46	3.662E-02
CADM2	cell adhesion molecule 2	-1.68	3.746E-02
TRPT1	tRNA phosphotransferase 1	1.50	3.746E-02
AHNAK2	AHNAK nucleoprotein 2	1.55	3.746E-02
PSG4	pregnancy specific beta-1-glycoprotein 4	1.50	3.746E-02
MMP1	matrix metallopeptidase 1	-2.05	3.746E-02
RAB4B	RAB4B, member RAS oncogene family	1.46	3.746E-02
FAM111B	family with sequence similarity 111 member B	-1.55	3.746E-02
METRNL	meteorin like, glial cell differentiation regulator	1.46	3.755E-02
IER3	immediate early response 3	1.38	4.004E-02
MAN1B1	mannosidase alpha class 1B member 1	1.45	4.004E-02
ARL13B	ADP ribosylation factor like GTPase 13B	-1.46	4.004E-02
EGR1	early growth response 1	1.48	4.004E-02
RRAS	RAS related	1.49	4.004E-02
ZNF784	zinc finger protein 784	1.48	4.004E-02
RUSC2	RUN and SH3 domain containing 2	1.45	4.004E-02
FDCSP	follicular dendritic cell secreted protein	1.63	4.004E-02
BTG2	BTG anti-proliferation factor 2	1.38	4.074E-02
CADM2-AS1	CADM2 antisense RNA 1	1.38	4.074E-02
LINC01133	long intergenic non-protein coding RNA 1133	1.61	4.149E-02

ADAMTS3	ADAM metallopeptidase with thrombospondin type 1 motif 3	-1.44	4.149E-02
ACOX2	acyl-CoA oxidase 2	-1.39	4.188E-02
GPAT3	glycerol-3-phosphate acyltransferase 3	-1.47	4.188E-02
NCOA5	nuclear receptor coactivator 5	-1.37	4.188E-02
NEU1	neuraminidase 1	1.37	4.188E-02
PTPRH	protein tyrosine phosphatase, receptor type H	1.64	4.188E-02
S100A16	S100 calcium binding protein A16	1.42	4.188E-02
NAXE	NAD(P)HX epimerase	1.42	4.271E-02
PCYOX1L	prenylcysteine oxidase 1 like	1.38	4.271E-02
CENPL	centromere protein L	-1.42	4.356E-02
MKNK2	MAP kinase interacting serine/threonine kinase 2	1.37	4.393E-02
PCK2	phosphoenolpyruvate carboxykinase 2, mitochondrial	1.73	4.393E-02
TYRP1	tyrosinase related protein 1	-1.71	4.393E-02
NELFE	negative elongation factor complex member E	1.38	4.393E-02
WBP1	WW domain binding protein 1	1.39	4.393E-02
CERCAM	cerebral endothelial cell adhesion molecule	1.43	4.413E-02
GCLM	glutamate-cysteine ligase modifier subunit	-1.39	4.452E-02
RFX5	regulatory factor X5	1.37	4.472E-02
TMEM200A	transmembrane protein 200A	-1.56	4.589E-02
ETHE1	ETHE1, persulfide dioxygenase	1.68	4.589E-02
SMARCAD1	SWI/SNF-related, matrix-associated actin-dependent regulator of chromatin, subfamily a, containing DEAD/H box 1	-1.46	4.589E-02
FBXO43	F-box protein 43	-1.40	4.589E-02

AP4E1	adaptor related protein complex 4 epsilon 1 subunit	-1.44	4.669E-02
ECT2	epithelial cell transforming 2	-1.53	4.686E-02
LINC01139	long intergenic non-protein coding RNA 1139	1.46	4.697E-02
CUEDC2	CUE domain containing 2	1.48	4.890E-02
RNF123	ring finger protein 123	1.47	4.895E-02
NME9	NME/NM23 family member 9	-1.53	4.895E-02

8 References

1. Batra H, Antony VB. The pleural mesothelium in development and disease. Front Physiol. 2014;5:1–6.
2. Mutsaers SE. The mesothelial cell. Int J Biochem Cell Biol. 2004;36(1):9–16.
3. Mutsaers SE. Mesothelial cells: Their structure, function and role in serosal repair. Respirology. 2002;7:171–91.
4. Que J, Wilm B, Hasegawa H, Wang F, Bader D, Hogan BLM. Mesothelium contributes to vascular smooth muscle and mesenchyme during lung development. Proc Natl Acad Sci U S A. 2008;105(43):16626–30.
5. Wu M, Smith CL, Hall JA, Lee I, Luby-Phelps K, Tallquist MD. Epicardial Spindle Orientation Controls Cell Entry into the Myocardium. Dev Cell. 2010;19(1):114–25.
6. Wilm B, Ipenberg A, Hastie ND, Burch JBE, Bader DM. The serosal mesothelium is a major source of smooth muscle cells of the gut vasculature. Development. 2005;132(23):5317–28.
7. Dixit R, Ai X, Fine A. Derivation of lung mesenchymal lineages from the fetal mesothelium requires hedgehog signaling for mesothelial cell entry. Dev. 2013;140:4398–406.
8. Kawanishi K. Diverse properties of the mesothelial cells in health and disease. Pleura and Peritoneum. 2016;1(2):79–89.
9. Morrisey EE, Hogan BLM. Preparing for the First Breath: Genetic and Cellular Mechanisms in Lung Development. Dev Cell. 2010;18(1):8–23.
10. Yap TA, Aerts JG, Popat S, Fennell DA. Novel insights into mesothelioma biology and implications for therapy. Nat Rev Cancer. 2017;17(8):475–88.
11. Hi BL, Ha H. Mechanisms of epithelial-mesenchymal transition of peritoneal mesothelial cells during peritoneal dialysis. J Korean Med Sci. 2007;22(6):943–945.
12. Von Gise A, Stevens SM, Honor LB, Oh JH, Gao C, Zhou B, et al. Contribution of fetal, but not adult, pulmonary mesothelium to mesenchymal lineages in lung homeostasis and fibrosis. Am J Respir Cell Mol Biol. 2016;54(2):222–230.
13. Kawaguchi M, Bader DM, Wilm B. Serosal mesothelium retains vasculogenic potential. Dev Dyn. 2007;236(11):2973–9.
14. Cano E, Carmona R, Muñoz-Chápuli R. Wt1-expressing progenitors contribute to multiple tissues in the developing lung. Am J Physiol - Lung Cell Mol Physiol. 2013;305(4):L322–32.
15. Winters NI, Thomason RT, Bader DM. Identification of a novel developmental mechanism in the generation of mesothelia. Dev. 2012;139(16):2926–34.
16. Rinkevich Y, Mori T, Sahoo D, Xu PX, Bermingham JR, Weissman IL. Identification and prospective isolation of a mesothelial precursor lineage giving rise to smooth muscle cells and fibroblasts for mammalian internal organs, and their vasculature. Nat Cell Biol. 2012;14(12):1251–60.
17. Kachali C, Eltoum I, Horton D, Chhieng DC. Use of mesothelin as a marker for mesothelial cells in cytologic specimens. Semin Diagn Pathol. 2006;23(1):20–4.
18. Kaneko C, Niimi H, Shinzato M, Shamoto M. Comparative studies of the same adenocarcinoma cells, macrophages, and mesothelial cells by light microscopy, scanning

electron microscopy, and transmission electron microscopy. Diagn Cytopathol. 1994;11(4):333–42.

19. Katkova LE, Baturina GS, Bondar AA, Jagirdar RM, Hatzoglou C, Gourgoulianis KI, et al. Benign Pleural Mesothelial Cells Have Higher Osmotic Water Permeability than Malignant Pleural Mesothelioma Cells and Differentially Respond to Hyperosmolality. Cell Physiol Biochem. 2019;52(4):869–78.

20. Rennard SI, Jaurand MC, Bignon J. Role of pleural mesothelial cells in the production of the submesothelial connective tissue matrix of lung. Am Rev Respir Dis. 1984;130(2).

21. Mutsaers SE, Birnie K, Lansley S, Herrick SE, Lim CB, Prêle CM. Mesothelial cells in tissue repair and fibrosis. Front Pharmacol. 2015;6(113).

22. Yang H, Rivera Z, Jube S, Nasu M, Bertino P, Goparaju C, et al. Programmed necrosis induced by asbestos in human mesothelial cells causes high-mobility group box 1 protein release and resultant inflammation. Proc Natl Acad Sci U S A. 2010;107(28):12611–6.

23. Mutsaers SE, Whitaker D, Papadimitriou JM. Stimulation of mesothelial cell proliferation by exudate macrophages enhances serosal wound healing in a murine model. Am J Pathol. 2002;160(2):681–692.

24. Antony VB, Owen CL, Hadley KJ. Pleural mesothelial cells stimulated by asbestos release chemotactic activity for neutrophils in vitro. Am Rev Respir Dis. 1989;139:199–206.

25. Mutsaers SE, Wilkosz S. Structure and function of mesothelial cells. Cancer Treat Res. 2007;134:1–19.

26. Lechner JF, Tokiwa T, LaVeck M, Benedict WF, Banks-Schlegel S, Yeager H, et al. Asbestos-associated chromosomal changes in human mesothelial cells. Proc Natl Acad Sci U S A. 1985;82(11):3884–8.

27. Mutsaers EE, Whitaker D, Papadimitriou JM. Changes in the concentration of microvilli on the free surface of healing mesothelium are associated with alterations in surface membrane charge. J Pathol. 1996;180(3):333–9.

28. Jonjić N, Peri G, Bernasconi S, Sciacca FL, Colotta F, PierGiuseppe P, et al. Expression of adhesion molecules and chemotactic cytokines in cultured human mesothelial cells. J Exp Med. 1992;176(4):1165–74.

29. Liao D, Wang Q, He J, Alexander DB, Abdelgied M, El-Gazzar AM, et al. Persistent Pleural Lesions and Inflammation by Pulmonary Exposure of Multiwalled Carbon Nanotubes. Chem Res Toxicol. 2018;31:1025–1031.

30. Bernstein DM, Rogers RA, Sepulveda R, Kunzendorf P, Bellmann B, Ernst H, et al. Evaluation of the fate and pathological response in the lung and pleura of brake dust alone and in combination with added chrysotile compared to crocidolite asbestos following short-term inhalation exposure. Toxicol Appl Pharmacol. 2015;283:20–34.

31. Foley-Comer AJ, Herrick SE, Al-Mishlab T, Prêle CM, Laurent GJ, Mutsaers SE. Evidence for incorporation of free-floating mesothelial cells as a mechanism of serosal healing. J Cell Sci. 2002;115:1383–9.

32. Carmona R, Cano E, Grueso E, Ruiz-Villalba A, Bera TK, Gaztambide J, et al. Peritoneal repairing cells: A type of bone marrow derived progenitor cells involved in mesothelial regeneration. J Cell Mol Med. 2011;15(5):1200–9.

33. Owens MW, Grimes SR. Pleural mesothelial cell response to inflammation: Tumor necrosis factor- induced mitogenesis and collagen synthesis. Am J Physiol - Lung Cell

Mol Physiol. 1993;

34. Hillegass JM, Miller JM, MacPherson MB, Westbom CM, Sayan M, Thompson JK, et al. Asbestos and erionite prime and activate the NLRP3 inflammasome that stimulates autocrine cytokine release in human mesothelial cells. Part Fibre Toxicol. 2013;10(39).
35. Shukla A, MacPherson MB, Hillegass J, Ramos-Nino ME, Alexeeva V, Vacek PM, et al. Alterations in gene expression in human mesothelial cells correlate with mineral pathogenicity. Am J Respir Cell Mol Biol. 2009;
36. Griffith DE, Miller EJ, Gray LD, Idell S, Johnson AR. Interleukin-1-mediated release of interleukin-8 by asbestos-stimulated human pleural mesothelial cells. Am J Respir Cell Mol Biol. 1994;10(3):245–52.
37. Acencio MMP, Soares B, Marchi E, Silva CSR, Teixeira LR, Broaddus VC. Inflammatory Cytokines Contribute to Asbestos-Induced Injury of Mesothelial Cells. Lung. 2015;193:831–7.
38. Zolak JS, Jagirdar R, Surolia R, Karki S, Oliva O, Hock T, et al. Pleural mesothelial cell differentiation and invasion in fibrogenic lung injury. Am J Pathol. 2013;182(4):1239–1247.
39. Hanna A, Pang Y, Bedrossian CWM, Dejmek A, Michael CW. Podoplanin is a useful marker for identifying mesothelioma in malignant effusions. Diagn Cytopathol. 2010;
40. Sahn SA. Pleural Effusions of Extravascular Origin. Clin Chest Med. 2006;
41. Namvar S, Woolf AS, Zeef LAH, Wilm T, Wilm B, Herrick SE. Functional molecules in mesothelial-to-mesenchymal transition revealed by transcriptome analyses. J Pathol. 2018;245(4):491–501.
42. Owens S, Jeffers A, Boren J, Tsukasaki Y, Koenig K, Ikebe M, et al. Mesomesenchymal transition of pleural mesothelial cells is PI3K and NF-KB dependent. Am J Physiol - Lung Cell Mol Physiol. 2015;308(12):L1265–L1273.
43. Decologne N, Kolb M, Margetts PJ, Menetrier F, Artur Y, Garrido C, et al. TGF-β1 Induces Progressive Pleural Scarring and Subpleural Fibrosis. J Immunol. 2007;179(9):6043–51.
44. Davila RM, Crouch EC. Role of mesothelial and submesothelial stromal cells in matrix remodeling following pleural injury. Am J Pathol. 1993;142(2):547–55.
45. Gaudio E, Rendina EA, Pannarale L, Ricci C, Marinozzi G. Surface morphology of the human pleura. A scanning electron microscopic study. Chest. 1988;93(1):149–53.
46. Peng M-J, Wang N-S, Vargas FS, Light RW. Subclinical Surface Alterations of Human Pleura. Chest. 1994;
47. Wang NS. Anatomy of the pleura. Clin Chest Med. 1998;19(2):229–40.
48. Zocchi L. Physiology and pathophysiology of pleural fluid turnover. Eur Respir J. 2002;20:1545–1558.
49. Mitzner W, Loube J, Venezia J, Scott A. Self-organizing pattern of subpleural alveolar ducts. Sci Rep. 2020;10.
50. Miserocchi G, Venturoli D, Negrini D, Del Fabbro M. Model of pleural fluid turnover. J Appl Physiol. 1993;75(4):1798–806.
51. Markov AG, Amasheh S. Tight junction physiology of pleural mesothelium. Front Physiol. 2014;

52. Allen SJ, Fraser JRE, Laurent UBG, Reed RK, Laurent TC. Turnover of hyaluronan in the rabbit pleural space. J Appl Physiol. 1992;73:1457–60.

53. Nie HG, Tucker T, Su XF, Na T, Peng J Bin, Smith PR, et al. Expression and regulation of epithelial Na+ channels by nucleotides in pleural mesothelial cells. Am J Respir Cell Mol Biol. 2009;

54. Sironi C, Bodega F, Porta C, Monaco A, Zocchi L, Agostoni E. Na+-glucose cotransporter is also expressed in mesothelium of species with thick visceral pleura. Respir Physiol Neurobiol. 2008;161(3):261–6.

55. Irvin CG, Bates JHT. Measuring the lung function in the mouse: The challenge of size. Respiratory Research. 2003.

56. Shinohara H. Distribution of lymphatic stomata on the pleural surface of the thoracic cavity and the surface topography of the pleural mesothelium in the golden hamster. Anat Rec. 1997;

57. Basil MC, Katzen J, Engler AE, Guo M, Herriges MJ, Kathiriya JJ, et al. The Cellular and Physiological Basis for Lung Repair and Regeneration: Past, Present, and Future. Cell Stem Cell. 2020;26(4):482–502.

58. Cigognetti M, Lonardi S, Fisogni S, Balzarini P, Pellegrini V, Tironi A, et al. BAP1 (BRCA1-associated protein 1) is a highly specific marker for differentiating mesothelioma from reactive mesothelial proliferations. Mod Pathol. 2015;28(8):1043–57.

59. Chapel DB, Schulte JJ, Husain AN, Krausz T. Application of immunohistochemistry in diagnosis and management of malignant mesothelioma. Transl Lung Cancer Res. 2020;9.

60. Fels Elliott DR, Jones KD. Diagnosis of Mesothelioma. Surgical Pathology Clinics. 2020.

61. Carbone M, Adusumilli PS, Alexander HR, Baas P, Bardelli F, Bononi A, et al. Mesothelioma: Scientific clues for prevention, diagnosis, and therapy. CA Cancer J Clin. 2019;69(5):402–29.

62. Nowak AK, Forde PM. Immunotherapy trials in mesothelioma — promising results, but don’t stop here. Nat Rev Clin Oncol. 2019;16:726–728.

63. Saunders J, Ashton M, Hall C, Laird B, MacLeod N. Pain management in patients with malignant mesothelioma: Challenges and solutions. Lung Cancer Targets Ther. 2019;10:37–46.

64. Ordóñez NG. Deciduoid mesothelioma: Report of 21 cases with review of the literature. Mod Pathol. 2012;25:1481–1495.

65. Ordóñez NG. Mesothelioma with signet-ring cell features: Report of 23 cases. Mod Pathol. 2013;26:370–384.

66. Sato A, Torii I, Okamura Y, Yamamoto T, Nishigami T, Kataoka TR, et al. Immunocytochemistry of CD146 is useful to discriminate between malignant pleural mesothelioma and reactive mesothelium. Mod Pathol. 2010;23(11):1458–66.

67. Odgerel CO, Takahashi K, Sorahan T, Driscoll T, Fitzmaurice C, Yoko-O M, et al. Estimation of the global burden of mesothelioma deaths from incomplete national mortality data. Occup Environ Med. 2017;

68. Ito A, Hagiyama M, Mimura T, Matsumoto M, Wakayama T, Iseki S, et al. Expression

of cell adhesion molecule 1 in malignant pleural mesothelioma as a cause of efficient adhesion and growth on mesothelium. Lab Investig. 2008;

69. Treasure T, Lang-Lazdunski L, Waller D, Bliss JM, Tan C, Entwisle J, et al. Extra-pleural pneumonectomy versus no extra-pleural pneumonectomy for patients with malignant pleural mesothelioma: clinical outcomes of the Mesothelioma and Radical Surgery (MARS) randomised feasibility study. Lancet Oncol. 2011;
70. Vogelzang NJ, Rusthoven JJ, Symanowski J, Denham C, Kaukel E, Ruffie P, et al. Phase III study of pemetrexed in combination with cisplatin versus cisplatin alone in patients with malignant pleural mesothelioma. J Clin Oncol. 2003;
71. Lapidot M, Freyaldenhoven S, Bueno R. New concepts in the treatment of malignant pleural mesothelioma. J Thorac Dis. 2018;10(3):1283–5.
72. Ricciardi S, Cardillo G, Zirafa CC, Carleo F, Facciolo F, Fontanini G, et al. Surgery for malignant pleural mesothelioma: An international guidelines review. Journal of Thoracic Disease. 2018. p. S285–S292.
73. Wolf AS, Daniel J, Sugarbaker DJ. Surgical Techniques for Multimodality Treatment of Malignant Pleural Mesothelioma: Extrapleural Pneumonectomy and Pleurectomy/Decortication. Semin Thorac Cardiovasc Surg. 2009;21(2):132–48.
74. Wolf AS, Flores RM. Updates in Staging and Management of Malignant Pleural Mesothelioma. Surg Oncol Clin N Am. 2020;29(4):603–12.
75. de Gooijer CJ, Borm FJ, Scherpereel A, Baas P. Immunotherapy in Malignant Pleural Mesothelioma. Frontiers in Oncology. 2020.
76. Scherpereel A, Mazieres J, Greillier L, Lantuejoul S, Dô P, Bylicki O, et al. Nivolumab or nivolumab plus ipilimumab in patients with relapsed malignant pleural mesothelioma (IFCT-1501 MAPS2): a multicentre, open-label, randomised, non-comparative, phase 2 trial. Lancet Oncol. 2019;20(2):239–53.
77. Dual immunotherapy prolongs survival while avoiding chemotherapy in malignant pleural mesothelioma. 2020. Available from: https://www.iaslc.org/DualImmunotherapy-Prolongs-Survival-While-AvoidingChemotherapy-in-Malignant-Pleural-Mesothelioma
78. Lievense LA, Sterman DH, Cornelissen R, Aerts JG. Checkpoint blockade in lung cancer and mesothelioma. Am J Respir Crit Care Med. 2017;196(3):274–282.
79. Røe OD, Anderssen E, Helge E, Pettersen CH, Olsen KS, Sandeck H, et al. Genome-wide profile of pleural mesothelioma versus parietal and visceral pleura: The emerging gene portrait of the mesothelioma phenotype. PLoS One. 2009;4(8):e6554.
80. Plasschaert LW, Žilionis R, Choo-Wing R, Savova V, Knehr J, Roma G, et al. A single-cell atlas of the airway epithelium reveals the CFTR-rich pulmonary ionocyte. Nature. 2018;
81. Travaglini KJ, Nabhan AN, Penland L, Sinha R, Gillich A, Sit R V, et al. A molecular cell atlas of the human lung from single cell RNA sequencing. bioRxiv. 2019;
82. Reyfman PA, Walter JM, Joshi N, Anekalla KR, McQuattie-Pimentel AC, Chiu S, et al. Single-cell transcriptomic analysis of human lung provides insights into the pathobiology of pulmonary fibrosis. Am J Respir Crit Care Med. 2019;199(12):1517–36.
83. Adams TS, Schupp JC, Poli S, Ayaub EA, Neumark N, Ahangari F, et al. Single Cell RNA-seq reveals ectopic and aberrant lung resident cell populations in Idiopathic

Pulmonary Fibrosis. bioRxiv. 2019;

84. Habermann AC, Gutierrez AJ, Bui LT, Yahn SL, Winters NI, Carla L, et al. Single-cell RNA-sequencing reveals profibrotic roles of distinct epithelial and mesenchymal lineages in pulmonary fibrosis. bioRxiv. 2019;6.

85. Bueno R, Stawiski EW, Goldstein LD, Durinck S, De Rienzo A, Modrusan Z, et al. Comprehensive genomic analysis of malignant pleural mesothelioma identifies recurrent mutations, gene fusions and splicing alterations. Nat Genet. 2016;48:407–416.

86. Sneddon S, Rive CM, Ma S, Dick IM, Allcock RJN, Brown SD, et al. Identification of a CD8+ T-cell response to a predicted neoantigen in malignant mesothelioma. Oncoimmunology. 2020;

87. Sugarbaker DJ, Richards WG, Gordon GJ, Dong L, De Rienzo A, Maulik G, et al. Transcriptome sequencing of malignant pleural mesothelioma tumors. Proc Natl Acad Sci U S A. 2008;105(9):3521–6.

88. Bott M, Brevet M, Taylor BS, Shimizu S, Ito T, Wang L, et al. The nuclear deubiquitinase BAP1 is commonly inactivated by somatic mutations and 3p21.1 losses in malignant pleural mesothelioma. Nat Genet. 2011;43:668–72.

89. Bianchi AB, Mitsunaga SI, Cheng JQ, Klein WM, Jhanwar SC, Seizinger B, et al. High frequency of inactivating mutations in the neurofibromatosis type 2 gene (NF2) in primary malignant mesotheliomas. Proc Natl Acad Sci U S A. 1995;92(24):10854–10858.

90. Carbone M, Ferris LK, Baumann F, Napolitano A, Lum CA, Flores EG, et al. BAP1 cancer syndrome: malignant mesothelioma, uveal and cutaneous melanoma, and MBAITs. J Transl Med. 2012;10(179).

91. Betti M, Aspesi A, Biasi A, Casalone E, Ferrante D, Ogliara P, et al. CDKN2A and BAP1 germline mutations predispose to melanoma and mesothelioma. Cancer Lett. 2016;378(2):120–30.

92. Carbone M, Flores EG, Emi M, Johnson TA, Tsunoda T, Behner D, et al. Combined Genetic and Genealogic Studies Uncover a Large BAP1 Cancer Syndrome Kindred Tracing Back Nine Generations to a Common Ancestor from the 1700s. PLoS Genet. 2015;11.

93. Testa JR, Cheung M, Pei J, Below JE, Tan Y, Sementino E, et al. Germline BAP1 mutations predispose to malignant mesothelioma. Nat Genet. 2011;43(10):1022–1025.

94. Hylebos M, Van Camp G, Van Meerbeeck JP, De Beeck KO. The genetic landscape of malignant pleural mesothelioma: Results from massively parallel sequencing. J Thorac Oncol. 2016;11(10):1615–26.

95. Armstrong JF, Pritchard-Jones K, Bickmore WA, Hastie ND, Bard JBL. The expression of the Wilms' tumour gene, WT1, in the developing mammalian embryo. Mech Dev. 1993;40(1–2):85–97.

96. Husain AN, Colby T V., Ordóñez NG, Allen TC, Attanoos RL, Beasley MB, et al. Guidelines for pathologic diagnosis of Malignant Mesothelioma: 2017 Update of the consensus statement from the International Mesothelioma Interest Group. Archives of Pathology and Laboratory Medicine. 2018.

97. Gulyás M, Hjerpe A. Proteoglycans and WTI as markers for distinguishing adenocarcinoma, epithelioid mesothelioma, and benign mesothelium. J Pathol. 2003;199(4):479–87.

98. Zamora M, Männer J, Ruiz-Lozano P. Epicardium-derived progenitor cells require β-catenin for coronary artery formation. Proc Natl Acad Sci U S A. 2007;104(46):18109–14.

99. Shield PW, Koivurinne K. The value of calretinin and cytokeratin 5/6 as markers for mesothelioma in cell block preparations of serous effusions. Cytopathology. 2008;19(4):218–23.

100. Cury PM, Butcher DN, Fisher C, Corrin B, Nicholson AG. Value of the mesothelium-associated antibodies thrombomodulin, cytokeratin 5/6, calretinin, and CD44H in distinguishing epithelioid pleural mesothelioma from adenocarcinoma metastatic to the pleura. Mod Pathol. 2000;13(2):107–12.

101. Kennedy AD, King G, Kerr KM. HBME-1 and antithrombomodulin in the differential diagnosis of malignant mesothelioma of pleura. J Clin Pathol. 1997;50(10):859–862.

102. Fetsch PA, Simsir A, Brosky K, Abati A. Comparison of three commonly used cytologic preparations in effusion immunocytochemistry. Diagn Cytopathol. 2002;26(1):61–6.

103. Inamura K. Update on immunohistochemistry for the diagnosis of lung cancer. Cancers. 2018.

104. Hwang HC, Pyott S, Rodriguez S, Cindric A, Carr A, Michelsen C, et al. BAP1 immunohistochemistry and p16 FISH in the diagnosis of sarcomatous and desmoplastic mesotheliomas. Am J Surg Pathol. 2016;

105. Marchevsky AM, Khoor A, Walts AE, Nicholson AG, Zhang YZ, Roggli V, et al. Localized malignant mesothelioma, an unusual and poorly characterized neoplasm of serosal origin: best current evidence from the literature and the International Mesothelioma Panel. Mod Pathol. 2020;33(2):281–96.

106. Tsuji S, Tsuura Y, Morohoshi T, Shinohara T, Oshita F, Yamada K, et al. Secretion of intelectin-1 from malignant pleural mesothelioma into pleural effusion. Br J Cancer. 2010;

107. Bhalla R, Siddiqui MT, Mandich D, Cartun RW, Fiel-Gan MD, Nassar A, et al. Diagnostic utility of D2-40 and podoplanin in effusion cell blocks. Diagn Cytopathol. 2007;35(6):342–7.

108. Patel A, Borczuk AC, Siddiqui MT. Utility of Claudin-4 versus BerEP4 and B72.3 in pleural fluids with metastatic lung adenocarcinoma. J Am Soc Cytopathol. 2020;9(3):146–51.

109. Matsuura R, Kaji H, Tomioka A, Sato T, Narimatsu H, Moriwaki Y, et al. Identification of mesothelioma-specific sialylated epitope recognized with monoclonal antibody SKM9-2 in a mucin-like membrane protein HEG1. Sci Rep. 2018;8.

110. Tsuji S, Washimi K, Kageyama T, Yamashita M, Yoshihara M, Matsuura R, et al. HEG1 is a novel mucin-like membrane protein that serves as a diagnostic and therapeutic target for malignant mesothelioma. Sci Rep. 2017;

111. Matsuda M, Ninomiya H, Wakejima R, Inamura K, Okumura S, Mun M, et al. Calretinin-expressing lung adenocarcinoma: Distinct characteristics of advanced stages, smoker-type features, and rare expression of other mesothelial markers are useful to differentiate epithelioid mesothelioma. Pathol Res Pract. 2020;16(3).

112. Naso JR, Tsuji S, Churg A. HEG1 is a Highly Specific and Sensitive Marker of Epithelioid Malignant Mesothelioma. Am J Surg Pathol. 2020;44(8):1143–8.

113. Guo G, Chmielecki J, Goparaju C, Heguy A, Dolgalev I, Carbone M, et al. Whole-exome

sequencing reveals frequent genetic alterations in BAP1, NF2, CDKN2A, and CUL1 in malignant pleural mesothelioma. Cancer Res. 2015;

114. Hung YP, Dong F, Dubuc AM, Dal Cin P, Bueno R, Chirieac LR. Molecular characterization of localized pleural mesothelioma. Mod Pathol. 2020;

115. Nasu M, Emi M, Pastorino S, Tanji M, Powers A, Luk H, et al. High incidence of somatic BAP1 alterations in sporadic malignant mesothelioma. J Thorac Oncol. 2015;10(4):565–76.

116. Wang L-M, Shi Z-W, Wang J-L, Lv Z, Du F-B, Yang Q-B, et al. Diagnostic accuracy of BRCA1-associated protein 1 in malignant mesothelioma: a meta-analysis. Oncotarget. 2017;8(40):68863–68872.

117. Hida T, Hamasaki M, Matsumoto S, Sato A, Tsujimura T, Kawahara K, et al. Immunohistochemical detection of MTAP and BAP1 protein loss for mesothelioma diagnosis: Comparison with 9p21 FISH and BAP1 immunohistochemistry. Lung Cancer. 2017;

118. Yoshimura M, Kinoshita Y, Hamasaki M, Matsumoto S, Hida T, Oda Y, et al. Highly expressed EZH2 in combination with BAP1 and MTAP loss, as detected by immunohistochemistry, is useful for differentiating malignant pleural mesothelioma from reactive mesothelial hyperplasia. Lung Cancer. 2019;130:187–93.

119. Ishizumi T, McWilliams A, MacAulay C, Gazdar A, Lam S. Natural history of bronchial preinvasive lesions. Cancer and Metastasis Reviews. 2010.

120. Daniels JMA, Sutedja TG. Detection and minimally invasive treatment of early squamous lung cancer. Ther Adv Med Oncol. 2013;5:235–248.

121. Bono F, Lombardi M. Prominent in situ component in a pleural malignant mesothelioma. Int J Surg Pathol. 2015;23:127–9.

122. Whitaker D, Henderson DW, Shilkin KB. The concept of mesothelioma in situ: Implications for diagnosis and histogenesis. Semin Diagn Pathol. 1992;9(2):151–61.

123. Churg A, Galateau-Salle F, Roden AC, Attanoos R, von der Thusen JH, Tsao MS, et al. Malignant mesothelioma in situ: morphologic features and clinical outcome. Mod Pathol. 2020;33(2):297–302.

124. Cagle PT, Churg A. Differential diagnosis of benign and malignant mesothelial proliferations on pleural biopsies. Arch Pathol Lab Med. 2005;129(11):1421–7.

125. Jaurand MC, Kaplan H, Thiollet J, Pinchon MC, Bernaudin JF, Bignon J. Phagocytosis of chrysotile fibers by pleural mesothelial cells in culture. Am J Pathol. 1979;94(3):529–538.

126. Wu YJ, Rheinwald JG. A new small (40 kd) keratin filament protein made by some cultured human squamous cell carcinomas. Cell. 1981;25(3):627–35.

127. Thiollet J, Jaurand MC, Kaplan H, Bignon J, Hollande E. Culture procedure of mesothelial cells from the rat parietal pleura. Biomed Express. 1978;

128. Aronson JF, Cristofalo VJ. Culture of epithelial cells from the rat pleura. In Vitro. 1981;17:61–70.

129. Ke Y, Reddel RR, Gerwin BI, Reddel HK, Somers ANA, McMenamin MG, et al. Establishment of a human in vitro mesothelial cell model system for investigating mechanisms of asbestos-induced mesothelioma. Am J Pathol. 1989;134(5):979–991.

130. La Rocca PJ, Rheinwald JG. Anchorage-independent growth of normal human

mesothelial cells: A sensitive bioassay for EGF which discloses the absence of this factor in fetal calf serum. Vitr Cell Dev Biol. 1985;21(1):67–72.

131. Connell ND, Rheinwald JG. Regulation of the cytoskeleton in mesothelial cells: Reversible loss of keratin and increase in vimentin during rapid growth in culture. Cell. 1983;34:245–53.

132. Murphy JOE, Rheinwald JG. Intraperitoneal injection of genetically modified, human mesothelial cells for systemic gene therapy. Hum Gene Ther. 1997;8(16):1867–79.

133. Calabrò L, Sigalotti L, Fonsatti E, Bertocci E, Di Giacomo AM, Danielli R, et al. Expression and regulation of B7-H3 immunoregulatory receptor, in human mesothelial and mesothelioma cells: Immunotherapeutic implications. J Cell Physiol. 2011;226(10):2595–600.

134. Duhig EE, Kalpakos L, Yang IA, Clarke BE. Mesothelial markers in high-grade breast carcinoma. Histopathology. 2011;59:957–64.

135. Liaw YS, Yu CJ, Shun CT, Lee YC, Kuo SH, Luh KT, et al. Expression of integrins in human cultured mesothelial cells: The roles in cell-to-extracellular matrix adhesion and inhibition by RGD-containing peptide. Respir Med. 2001;95(3):221–6.

136. Kawai N, Ouji Y, Sakagami M, Tojo T, Sawabata N, Yoshikawa M, et al. Isolation and culture of pleural mesothelial cells. Exp Lung Res. 2019;

137. Acencio MMP, Vargas FS, Marchi E, Carnevale GG, Teixeira LR, Antonangelo L, et al. Pleural mesothelial cells mediate inflammatory and profibrotic responses in talc-induced pleurodesis. Lung. 2007;

138. Orengo AM, Spoletini L, Procopio A, Favoni RE, De Cupis A, Ardizzoni A, et al. Establishment of four new mesothelioma cell lines: Characterization by ultrastructural and immunophenotypic analysis. Eur Respir J. 1999;

139. Zhou X, Zhu L, Lizarraga R, Chen Y. Human airway epithelial cells direct significant rhinovirus replication in monocytic cells by enhancing ICAM1 expression. Am J Respir Cell Mol Biol. 2017;57(2):216–225.

140. Ordõez NG. Pleomorphic mesothelioma: Report of 10 cases. Mod Pathol. 2012;

141. Blum W, Pecze L, Felley-Bosco E, Worthmüller-Rodriguez J, Wu L, Vrugt B, et al. Establishment of immortalized murine mesothelial cells and a novel mesothelioma cell line. Vitr Cell Dev Biol - Anim. 2015;51(7):714–21.

142. Stylianou E, Jenner LA, Davies M, Coles GA, Williams JD. Isolation, culture and characterization of human peritoneal mesothelial cells. Kidney Int. 1990;37(6):1563–70.

143. Lokmic Z, Ng ES, Burton M, Stanley EG, Penington AJ, Elefanty AG. Isolation of human lymphatic endothelial cells by multi-parameter fluorescence-activated cell sorting. J Vis Exp. 2015;(99):e5269.

144. Lenihan C, Rogers C, Metcalfe AD, Martin YH. The effect of isolation and culture methods on epithelial stem cell populations and their progeny-toward an improved cell expansion protocol for clinical application. Cytotherapy. 2014;16(12):1750–9.

145. Happle C, Meyer-Decking L, Dreier A, Wetzke M, Gläsener S, Grychtol R, et al. Improved protocol for simultaneous analysis of leukocyte subsets and epithelial cells from murine and human lung. Exp Lung Res. 2018;

146. Yung S, Li FK, Chan TM. Peritoneal mesothelial cell culture and biology. Perit Dial Int. 2006;26(2):162–73.

147. Dauleh S, Santeramo I, Fielding C, Ward K, Herrmann A, Murray P, et al. Characterisation of cultured mesothelial cells derived from the murine adult omentum. PLoS One. 2016;11(7):e0158997.

148. Shukla A, Barrett TF, MacPherson MB, Hillegass JM, Fukagawa NK, Swain WA, et al. An extracellular signal-regulated kinase 2 survival pathway mediates resistance of human mesothelioma cells to asbestos-induced injury. Am J Respir Cell Mol Biol. 2011;

149. Fernandes-Silva H, Correia-Pinto J, Moura RS. Canonical sonic hedgehog signaling in early lung development. J Dev Biol. 2017;5(1).

150. Jiang J, Hui C chung. Hedgehog Signaling in Development and Cancer. Dev Cell. 2008;15(6):801–12.

151. Chen Y, Jiang J. Decoding the phosphorylation code in Hedgehog signal transduction. Cell Res. 2013;23:186–200.

152. Fulmer D, Toomer KA, Glover J, Guo L, Moore K, Moore R, et al. Desert Hedgehog-Primary Cilia Cross Talk Shapes Mitral Valve Tissue by Organizing Smooth Muscle Actin. Dev Biol. 2020;463(1):26–38.

153. Pala R, Alomari N, Nauli SM. Primary cilium-dependent signaling mechanisms. Int J Mol Sci. 2017;18(11):2272.

154. Breslow DK, Hoogendoorn S, Kopp AR, Morgens DW, Vu BK, Kennedy MC, et al. A CRISPR-based screen for Hedgehog signaling provides insights into ciliary function and ciliopathies. Nat Genet. 2018;50:460–471.

155. Duran I, Taylor SP, Zhang W, Martin J, Qureshi F, Jacques SM, et al. Mutations in IFT-A satellite core component genes IFT43 and IFT121 produce short rib polydactyly syndrome with distinctive campomelia. Cilia. 2017;

156. Taylor SP, Dantas TJ, Duran I, Wu S, Lachman RS, Nelson SF, et al. Mutations in DYNC2LI1 disrupt cilia function and cause short rib polydactyly syndrome. Nat Commun. 2015;

157. Liu B, Chen S, Cheng D, Jing W, Helms JA. Primary cilia integrate hedgehog and Wnt signaling during tooth development. J Dent Res. 2014;93(5):475–482.

158. Pusapati G V., Kong JH, Patel BB, Krishnan A, Sagner A, Kinnebrew M, et al. CRISPR Screens Uncover Genes that Regulate Target Cell Sensitivity to the Morphogen Sonic Hedgehog. Dev Cell. 2018;

159. He M, Subramanian R, Bangs F, Omelchenko T, Liem KF, Kapoor TM, et al. The kinesin-4 protein Kif7 regulates mammalian Hedgehog signalling by organizing the cilium tip compartment. Nat Cell Biol. 2014;

160. Corbit KC, Aanstad P, Singla V, Norman AR, Stainier DYR, Reiter JF. Vertebrate Smoothened functions at the primary cilium. Nature. 2005;437:pages1018–1021.

161. Goetz SC, Anderson K V. The primary cilium: A signalling centre during vertebrate development. Nat Rev Genet. 2010;11:331–344.

162. Kim J, Kato M, Beachy PA. Gli2 trafficking links Hedgehog-dependent activation of Smoothened in the primary cilium to transcriptional activation in the nucleus. Proc Natl Acad Sci U S A. 2009;106(51):21666–71.

163. Tang JY, Xiao TZ, Oda Y, Chang KS, Shpall E, Wu A, et al. Vitamin D3 inhibits hedgehog signaling and proliferation in murine basal cell carcinomas. Cancer Prev Res. 2011;44(5):744–751.

164. Hadden MK. Hedgehog and Vitamin D Signaling Pathways in Development and Disease. In: Vitamins and Hormones. 2016.

165. Linder B, Weber S, Dittmann K, Adamski J, Hahn H, Uhmann A. A functional and putative physiological role of calcitriol in Patched1/Smoothened interaction. J Biol Chem. 2015;290(32):19614–28.

166. Faria AVDS, Akyala AI, Parikh K, Brüggemann LW, Spek CA, Cao W, et al. Smoothened-dependent and -independent pathways in mammalian noncanonical Hedgehog signaling. J Biol Chem. 2019;

167. Goodrich L V., Milenković L, Higgins KM, Scott MP. Altered neural cell fates and medulloblastoma in mouse patched mutants. Science (80-). 1997;277:1109–13.

168. Alfaro AC, Roberts B, Kwong L, Bijlsma MF, Roelink H. Ptch2 mediates the Shh response in Ptch1-/- cells. Dev. 2014;141:3331–9.

169. Ringuette R, Atkins M, Lagali PS, Bassett EA, Campbell C, Mazerolle C, et al. A Notch-Gli2 axis sustains Hedgehog responsiveness of neural progenitors and Müller glia. Dev Biol. 2016;411(1):85–100.

170. Katoh Y, Katoh M. Integrative genomic analyses on GLI1: Positive regulation of GLI1 by Hedgehog-GLI, TGFβ-Smads, and RTK-PI3K-AKTsignals, and negative regulation of GLI1 by Notch-CSL-HES/HEY, and GPCR-Gs-PKA signals. Int J Oncol. 2009;35(1):187–92.

171. Sharma N, Nanta R, Sharma J, Gunewardena S, Singh KP, Shankar S, et al. PI3K/AKT/mTOR and sonic hedgehog pathways cooperate together to inhibit human pancreatic cancer stem cell characteristics and tumor growth. Oncotarget. 2015;6(31):32039–60.

172. Shi Q, Li S, Li S, Jiang A, Chen Y, Jiang J. Hedgehog-induced phosphorylation by CK1 sustains the activity of Ci/Gli activator. Proc Natl Acad Sci U S A. 2014;111(52):E5651–E566.

173. Pelullo M, Zema S, Nardozza F, Checquolo S, Screpanti I, Bellavia D. Wnt, Notch, and TGF-β pathways impinge on hedgehog signaling complexity: An open window on cancer. Front Genet. 2019;10.

174. Javelaud D, Pierrat MJ, Mauviel A. Crosstalk between TGF-β and hedgehog signaling in cancer. FEBS Lett. 2012;586(4):2016–25.

175. Dennler S, André J, Verrechia F, Mauviel A. Cloning of the human GLI2 promoter: Transcriptional activation by transforming growth factor-β via SMAD3/β-catenin cooperation. J Biol Chem. 2009;284(46):31523–31.

176. Sadam H, Liivas U, Kazantseva A, Pruunsild P, Kazantseva J, Timmusk T, et al. GLI2 cell-specific activity is controlled at the level of transcription and RNA processing: Consequences to cancer metastasis. Biochim Biophys Acta - Mol Basis Dis. 2016;1862:46–55.

177. Tang YA, Chen Y feng, Bao Y, Mahara S, Yatim SMJM, Oguz G, et al. Hypoxic tumor microenvironment activates GLI2 via HIF-1α and TGF-β2 to promote chemoresistance in colorectal cancer. Proc Natl Acad Sci U S A. 2018;

178. Bai CB, Auerbach W, Lee JS, Stephen D, Joyner AL. Gli2, but not Gli1, is required for initial Shh signaling and ectopic activation of the Shh pathway. Development. 2002;129:4753–61.

179. Jones EA, Sajid MI, Shenton A, Evans DG. Basal Cell Carcinomas in Gorlin Syndrome:

A Review of 202 Patients. J Skin Cancer. 2011;

180. Umehara F, Tate G, Itoh K, Yamaguchi N, Douchi T, Mitsuya T, et al. A novel mutation of desert hedgehog in a patient with 46, XY partial gonadal dysgenesis accompanied by minifascicular neuropathy. Am J Hum Genet. 2000;

181. Peng T, Frank DB, Kadzik RS, Morley MP, Rathi KS, Wang T, et al. Hedgehog actively maintains adult lung quiescence and regulates repair and regeneration. Nature. 2015;526.

182. Amankulor NM, Hambardzumyan D, Pyonteck SM, Becher OJ, Joyce JA, Holland EC. Sonic hedgehog pathway activation is induced by acute brain injury and regulated by injury-related inflammation. J Neurosci. 2009;29:10299–308.

183. Kong Y, Peng Y, Liu Y, Xin H, Zhan X, Tan W. Twist1 and snail link hedgehog signaling to tumor-initiating cell-like properties and acquired chemoresistance independently of ABC transporters. Stem Cells. 2015;33(4):1063–74.

184. Chen X, Shi C, Cao H, Chen L, Hou J, Xiang Z, et al. The hedgehog and Wnt/β-catenin system machinery mediate myofibroblast differentiation of LR-MSCs in pulmonary. Cell Death Dis. 2018;9.

185. Metcalfe C, Siebel CW. The Hedgehog Hold on Homeostasis. Cell Stem Cell. 2015;17(5):505–6.

186. Watkins DN, Berman DM, Burkholder SG, Wang B, Beachy PA, Baylin SB. Hedgehog signalling within airway epithelial progenitors and in small-cell lung cancer. Nature. 2003;422:313–317.

187. Fendrich V, Oh E, Bang S, Karikari C, Ottenhof N, Bisht S, et al. Ectopic overexpression of Sonic Hedgehog (Shh) induces stromal expansion and metaplasia in the adult murine pancreas. Neoplasia. 2011;

188. Tape CJ, Ling S, Dimitriadi M, McMahon KM, Worboys JD, Leong HS, et al. Oncogenic KRAS Regulates Tumor Cell Signaling via Stromal Reciprocation. Cell. 2016;

189. Yuan Z, Goetz JA, Singh S, Ogden SK, Petty WJ, Black CC, et al. Frequent requirement of hedgehog signaling in non-small cell lung carcinoma. Oncogene. 2007;26:1046–1055.

190. Varnat F, Duquet A, Malerba M, Zbinden M, Mas C, Gervaz P, et al. Human colon cancer epithelial cells harbour active HEDGEHOG-GLI signalling that is essential for tumour growth, recurrence, metastasis and stem cell survival and expansion. EMBO Mol Med. 2009;

191. Li H, Lui N, Cheng T, Tseng HHK, Yue D, Giroux-Leprieur E, et al. Gli as a Novel Therapeutic Target in Malignant Pleural Mesothelioma. PLoS One. 2013;

192. Whitson RJ, Lee A, Urman NM, Mirza A, Yao CY, Brown AS, et al. Noncanonical hedgehog pathway activation through SRF-MKL1 promotes drug resistance in basal cell carcinomas. Nat Med. 2018;24:271–281.

193. Bonilla X, Parmentier L, King B, Bezrukov F, Kaya G, Zoete V, et al. Genomic analysis identifies new drivers and progression pathways in skin basal cell carcinoma. Nat Genet. 2016;48(4):398–406.

194. Kasper M, Regl G, Frischauf AM, Aberger F. GLI transcription factors: Mediators of oncogenic Hedgehog signalling. Eur J Cancer. 2006;42(4):437–45.

195. Hui M, Cazet A, Nair R, Watkins DN, O'Toole SA, Swarbrick A. The Hedgehog signalling pathway in breast development, carcinogenesis and cancer therapy. Breast Cancer Research. 2013.

196. Eichberger T, Sander V, Schnidar H, Regl G, Kasper M, Schmid C, et al. Overlapping and distinct transcriptional regulator properties of the GLI1 and GLI2 oncogenes. Genomics. 2006;

197. Hutchin ME, Kariapper MST, Grachtchouk M, Wang A, Wei L, Cummings D, et al. Sustained Hedgehog signaling is required for basal cell carcinoma proliferation and survival: Conditional skin tumorigenesis recapitulates the hair growth cycle. Genes Dev. 2005;

198. Grachtchouk M, Mo R, Yu S, Zhang X, Sasaki H, Hui CC, et al. Basal cell carcinomas in mice overexpressing Gli2 in skin. Nat Genet. 2000;24(3):216–7.

199. Shi Y, Moura U, Opitz I, Soltermann A, Rehrauer H, Thies S, et al. Role of hedgehog signaling in malignant pleural mesothelioma. Clin Cancer Res. 2012;

200. Meerang M, Bérard K, Felley-Bosco E, Lauk O, Vrugt B, Boss A, et al. Antagonizing the hedgehog pathway with vismodegib impairs malignant pleural mesothelioma growth in vivo by affecting stroma. Mol Cancer Ther. 2016;15(5):1095–105.

201. Coni S, Di Magno L, Canettieri G. Determination of acetylation of the gli transcription factors. In: Methods in Molecular Biology. 2015.

202. Lim CB, Prêle CM, Cheah HM, Cheng YY, Klebe S, Reid G, et al. Mutational Analysis of Hedgehog Signaling Pathway Genes in Human Malignant Mesothelioma. PLoS One. 2013;8(6):e66685.

203. Incardona JP, Gaffield W, Kapur RP, Roelink H. The teratogenic Veratrum alkaloid cyclopamine inhibits Sonic hedgehog signal transduction. Development. 1998;

204. Byrne EFX, Sircar R, Miller PS, Hedger G, Luchetti G, Nachtergaele S, et al. Structural basis of Smoothened regulation by its extracellular domains. Nature. 2016;535:517–22.

205. Wang C, Wu H, Katritch V, Han GW, Huang XP, Liu W, et al. Structure of the human smoothened receptor bound to an antitumour agent. Nature. 2013;497:338–343.

206. Atwood SX, Sarin KY, Whitson RJ, Li JR, Kim G, Rezaee M, et al. Smoothened Variants Explain the Majority of Drug Resistance in Basal Cell Carcinoma. Cancer Cell. 2015;27:342–353.

207. Lauth M, Bergström Å, Shimokawa T, Toftgård R. Inhibition of GLI-mediated transcription and tumor cell growth by small-molecule antagonists. Proc Natl Acad Sci U S A. 2007;104(20):8455–8460.

208. Benvenuto M, Masuelli L, De Smaele E, Fantini M, Mattera R, Cucchi D, et al. In vitro and in vivo inhibition of breast cancer cell growth by targeting the Hedgehog/GLI pathway with SMO (GDC-0449) or GLI (GANT-61) inhibitors. Oncotarget. 2016;23(7):9250–70.

209. Agyeman A, Jha BK, Mazumdar T, Houghton JA. Mode and specificity of binding of the small molecule GANT61 to GLI determines inhibition of GLI-DNA binding. Oncotarget. 2014;5:4492–503.

210. Zhang R, Wu J, Ferrandon S, Glowacki KJ, Houghton JA. Targeting GLI by GANT61 involves mechanisms dependent on inhibition of both transcription and DNA licensing. Oncotarget. 2016;7(49):80190–80207.

211. Fu J, Rodova M, Roy SK, Sharma J, Singh KP, Srivastava RK, et al. GANT-61 inhibits pancreatic cancer stem cell growth in vitro and in NOD/SCID/IL2R gamma null mice xenograft. Cancer Lett. 2013;330(1):22-32.

212. Srivastava RK, Kaylani SZ, Edrees N, Li C, Talwelkar SS, Xu J, et al. GLI inhibitor GANT-61 diminishes embryonal and alveolar rhabdomyosarcoma growth by inhibiting Shh/AKT-mTOR axis. Oncotarget. 2014;

213. Tong W, Qiu L, Qi M, Liu J, Hu K, Lin W, et al. GANT-61 and GDC-0449 induce apoptosis of prostate cancer stem cells through a GLI-dependent mechanism. J Cell Biochem. 2018;

214. Lim CB, Prêle CM, Baltic S, Arthur PG, Creaney J, Neil Watkins D, et al. Mitochondria-derived reactive oxygen species drive GANT61-induced mesothelioma cell apoptosis. Oncotarget. 2015;6(3):1519–1530.

215. Filippakopoulos P, Qi J, Picaud S, Shen Y, Smith WB, Fedorov O, et al. Selective inhibition of BET bromodomains. Nature. 2010;468:1067–1073.

216. Tang Y, Gholamin S, Schubert S, Willardson MI, Lee A, Bandopadhayay P, et al. Epigenetic targeting of Hedgehog pathway transcriptional output through BET bromodomain inhibition. Nat Med. 2014;

217. Zanellato I, Colangelo D, Osella D. JQ1, a BET Inhibitor, Synergizes with Cisplatin and Induces Apoptosis in Highly Chemoresistant Malignant Pleural Mesothelioma Cells. Curr Cancer Drug Targets. 2017;18(8):816–28.

218. Moestrup KS, Andersen MS, Jensen KB. Isolation and in vitro characterization of epidermal stem cells. Methods Mol Biol. 2017;1553:67–83.

219. Beckett P, Edwards J, Fennell D, Hubbard R, Woolhouse I, Peake MD. Demographics, management and survival of patients with malignant pleural mesothelioma in the National Lung Cancer Audit in England and Wales. Lung Cancer. 2015;88:344–8.

220. Churg A, Galateau-Salle F. The separation of benign and malignant mesothelial proliferations. In: Archives of Pathology and Laboratory Medicine. 2012.

221. Ysasi AB, Wagner WL, Valenzuela CD, Kienzle A, Servais AB, Bennett RD, et al. Evidence for pleural epithelial-mesenchymal transition in murine compensatory lung growth. PLoS One. 2017;12(5):e0177921.

222. Churg A, Hwang H, Tan L, Qing G, Taher A, Tong A, et al. Malignant mesothelioma in situ. Histopathology. 2018;72:1033–8.

223. Liu K, Newbury PA, Glicksberg BS, Zeng WZD, Paithankar S, Andrechek ER, et al. Evaluating cell lines as models for metastatic breast cancer through integrative analysis of genomic data. Nat Commun. 2019;10.

224. Blanquart C, Jaurand MC, Jean D. The Biology of Malignant Mesothelioma and the Relevance of Preclinical Models. Frontiers in Oncology. 2020.

225. Butler CR, Hynds RE, Gowers KHC, Lee DDH, Brown JM, Crowley C, et al. Rapid expansion of human epithelial stem cells suitable for airway tissue engineering. Am J Respir Crit Care Med. 2016;194:156–68.

226. Lertkiatmongkol P, Liao D, Mei H, Hu Y, Newman PJ. Endothelial functions of platelet/endothelial cell adhesion molecule-1 (CD31). Curr Opin Hematol. 2016;23(3):253–9.

227. Kumar A, Bhanja A, Bhattacharyya J, Jaganathan BG. Multiple roles of CD90 in cancer. Tumor Biol. 2016;37:11611–11622.

228. Turini S, Bergandi L, Gazzano E, Prato M, Aldieri E. Epithelial to mesenchymal transition in human mesothelial cells exposed to asbestos fibers: Role of TGF-β as

mediator of malignant mesothelioma development or metastasis via EMT event. Int J Mol Sci. 2019;

229. Falk P, Angenete E, Bergström M, Ivarsson ML. TGF-β1 promotes transition of mesothelial cells into fibroblast phenotype in response to peritoneal injury in a cell culture model. Int J Surg. 2013;

230. Pantazi E, Gemenetzidis E, Trigiante G, Warnes G, Shan L, Mao X, et al. GLI2 induces genomic instability in human keratinocytes by inhibiting apoptosis. Cell Death Dis. 2014;5(1):e1028.

231. Huang L, Walter V, Hayes DN, Onaitis M. Hedgehog-GLI signaling inhibition suppresses tumor growth in squamous lung cancer. Clin Cancer Res. 2014;20(6):1566–74.

232. Han L, Jiang J, Ma Q, Wu Z, Wang Z. The inhibition of heme oxygenase-1 enhances the chemosensitivity and suppresses the proliferation of pancreatic cancer cells through the SHH signaling pathway. Int J Oncol. 2018;52(6):2101–9.

233. Kawagishi H, Xiong J, Rovira II, Pan H, Yan Y, Fleischmann BK, et al. Sonic hedgehog signaling regulates the mammalian cardiac regenerative response. J Mol Cell Cardiol. 2018;

234. Mille F, Tamayo-Orrego L, Lévesque M, Remke M, Korshunov A, Cardin J, et al. The Shh receptor Boc promotes progression of early medulloblastoma to advanced tumors. Dev Cell. 2014;31(1):34–47.

235. Jenkins D. Hedgehog signalling: Emerging evidence for non-canonical pathways. Cell Signal. 2009;21(7):1023–34.

236. Chenna V, Hu C, Khan SR. Synthesis and cytotoxicity studies of Hedgehog enzyme inhibitors SANT-1 and GANT-61 as anticancer agents. J Environ Sci Heal - Part A Toxic/Hazardous Subst Environ Eng. 2014;49:641–7.